

**Peptide-tethered Naphthalene Diimide and  
Peptide Amphiphile-Based Functional Soft  
Materials and Metal Nanocluster-Based  
Nanohybrids**

---

---

**THESIS SUBMITTED FOR THE DEGREE OF DOCTOR  
OF PHILOSOPHY (SCIENCE)  
OF  
JADAVPUR UNIVERSITY**

---

**DIPAYAN BAIRAGI, M. Sc.**  
**School of Biological Sciences**  
**Indian Association for the Cultivation of Science**  
**Jadavpur, Kolkata -700032, India**



## CERTIFICATE FROM THE SUPERVISOR

This is to certify that the thesis entitled “**Peptide-tethered Naphthalene Diimide and Peptide Amphiphile-Based Functional Soft Materials and Metal Nanocluster-Based Nanohybrids**” submitted by **Sri Dipayan Bairagi**, who got his name registered on 30.08.2018 for the award of Ph. D. (Science) Degree of Jadavpur University, is absolutely based upon his own work under the supervision of **Prof. Arindam Banerjee** and that neither this thesis nor any part of it has been submitted for any degree/diploma or any other academic award anywhere before.

*A. Banerjee* 21.11.2022

Prof. Arindam Banerjee

प्रो. अरिंदम बनर्जी / Prof. Arindam Banerjee  
वरिष्ठ प्रध्यापक / Senior Professor  
जैविक विज्ञान शाखा / School of Biological Sciences  
इण्डियन एसोसियेशन फॉर द कल्चिवेशन ऑफ साइन्स  
Indian Association for the Cultivation of Science  
यादवपुर, कोलकाता - 700032 / Jadavpur, Kolkata - 700032, INDIA

[Signature of the Supervisor(s) & date with official seal]





## DECLARATION


The research work embodied in this thesis entitled **“Peptide-tethered Naphthalene Diimide and Peptide Amphiphile-Based Functional Soft Materials and Metal Nanocluster-Based Nanohybrids”** being submitted to Jadavpur University, Kolkata, has been carried out at the Indian Association for the Cultivation of Science, Jadavpur, under the supervision of Prof. Arindam Banerjee, Senior Professor, School of Biological Sciences, Indian Association for the Cultivation of Science. This work is original and has not been submitted in part or in full, for any degree or diploma to this or any other university.

DIPAYAN BAIRAGI

Index No. **154/18/Chem./26**




---



*Dedicated to  
The Cradle of My Research  
Works,  
IACS*

---





## Table of Contents

<i>Abstract</i> .....	xi-xii
<i>Preface</i> .....	xiii-xv
<i>Acknowledgement</i> .....	xvii-xix
<i>Abbreviations</i> .....	xxi-xxii
<i>Chapter 1:</i>	
<b>General Introduction</b> .....	1-128
<i>Chapter 2:</i>	
<b>Materials and Methods</b> .....	131-136
<i>Chapter 3:</i>	
<b>Self-Assembling Peptide-Based Hydrogel: Regulation of Mechanical Stiffness and Thermal Stability and 3D Cell Culture of Fibroblasts</b> .....	137-170
<i>Chapter 4:</i>	
<b>In-situ Formation of a Nano-Hybrid of Silver Nano-Dots and Peptide Nanofibers in a Silver-Based Metallogel: Elucidating Their Potential for Antimicrobial Activities</b> .....	171-202
<i>Chapter 5:</i>	
<b>Peptide-Appended Core-substituted Naphthalenediimides: Exploration of Aggregation and Semiconducting Property</b> .....	203-226
<i>Chapter 6:</i>	
<b>A Nanohybrid Containing Cyan-Emitting Copper Nanoclusters and TiO<sub>2</sub> Nanoparticles: Tuning of Optoelectronic Properties</b> .....	227-249
<i>List of Publications</i> .....	251



## ABSTRACT

Index No: **154/18/Chem./26**

Thesis Title: **“Peptide-tethered Naphthalene Diimide and Peptide Amphiphile-Based Functional Soft Materials and Metal Nanocluster-Based Nanohybrids”**

Name of the Candidate: **Dipayan Bairagi**

This thesis in general discusses several functional nanomaterials and nanohybrids. More specifically it contains soft materials designed from peptide amphiphiles as well as peptide-conjugated naphthalene diimide and their potential applications in eukaryotic cell culture, designing antimicrobial agents and semiconducting materials. The final part of the thesis describes enhancement of optoelectronic property in a new fluorescent copper nanocluster and titanium dioxide nanoparticle-based nanohybrid system. Peptide amphiphiles containing Histidine in one end, have potential for aggregate in various ways. A histidine-based amphiphile forms clear hydrogel in the pH range of 5.5 to 8.5. The morphology, mechanical strength and thermal stability of this hydrogel is tuned to make this hydrogel capable of acting as a matrix to grow NIH-3T3 fibroblasts and RAW264.7 murine macrophages. This tuning is made possible by making a two-component hydrogel with the peptide amphiphile and succinic acid. The probable model of self-aggregation is proposed using data from powder XRD and FT-IR signatures. Another histidine-based peptide amphiphile is found to form strong metallogel in presence of silver nitrate salt. By varying the photo-reduction conditions, it is possible to synthesize both few-atom silver nanoclusters and silver nanoparticles from the same metallogel. Enhancement of gel-strength in nanomaterial-included hydrogels can be traced to the fact that all the nanomaterials grow along the hydrogel fibers, thus, facilitating cross-linking between the nano-fibers. These hydrogels are potential antimicrobial agents. Reactive oxygen species (ROS) produced by the nanomaterials, are identified as the main reason of bacteria death. The next study deals with a naphthalene diimide molecule having peptide amphiphiles attached to its imide position and hydrocarbon chain attached to its core. The aggregation study reveals that this molecule shows H and J-type

aggregation when non-polar solvents are gradually added to the monomer solvent chloroform. The solvent induced aggregation initially affects H aggregation but finally J aggregation is seen over 9:1 hydrocarbon solvent to chloroform solvent ratio. The morphology changes from nanorods (H aggregate) to nanofibers (J aggregate) in the self-assembly. This molecule is further studied to investigate its semiconducting nature. The current output of this material is tuned by adding various benzene-based  $\pi$ -systems. It is found that more electron rich  $\pi$ -systems makes hybrid systems that show enhancement of current. In the last study, a nanohybrid is formulated using copper nanocluster and  $\text{TiO}_2$  nanoparticles and it is characterized by spectroscopic analysis. Positively charged nanoclusters sit inside the Lewis-acidic pore of  $\text{TiO}_2$ . The photocurrent and dark current of  $\text{TiO}_2$  nanoparticles are improved significantly by the nanocluster. Systematic variation of their weight ratio vividly demonstrated that 10% w/w  $\text{TiO}_2$ -Cu NC hybrid was the most effective current generator. The mechanism of the enhancement is discussed from valence-band XPS and diffused reflectance spectroscopic studies.



## PREFACE

The research embodied in the present thesis entitled “**Peptide-tethered Naphthalene Diimide and Peptide Amphiphile-Based Functional Soft Materials and Metal Nanocluster-Based Nanohybrids**” deals with the synthesis, characterization and gelation studies of several synthetic self-assembling short-peptides and peptide conjugated naphthalene diimide based soft materials and their various applications.

Investigations described in this thesis have been carried out by the author in the School of Biological Sciences, **Indian Association for the Cultivation of Science**, Jadavpur, Kolkata-700032, India during the time of **2016-2022** under the supervision of *Prof. Arindam Banerjee*. The entire work has been described and summarized within the six chapters of this thesis.

**Chapter 1** is the general introduction which provides the comprehensive literature survey on structure and application of self-aggregated super-structures of peptide amphiphiles. This chapter highlights structural features of amino acid and peptide based supramolecular gels and their different applications. It also reviews current works on rylene dye (naphthalene diimide) based soft materials and their different applications. It is concluded by discussion on metal nanoclusters with an emphasis on copper nanoclusters and nanohybrid materials based on them.

**Chapter 2** describes the reagents and instruments used, and the experimental procedures followed to perform the entire work embodied in this thesis.

**Chapter 3** describes a histidine-containing peptide-based amphiphile which forms a transparent hydrogel within a pH range of 5.5 to 8.5 in phosphate buffer solution. Interestingly, thermal stability and mechanical stiffness are modulated by incorporating different types of dicarboxylic acids into the hydrogels. Inclusion of succinic acid with the molar ratio 2:1 (peptide: dicarboxylic acid) yields improved properties compared to the other tested dicarboxylic acids like oxalic, malonic, glutaric and octanedioic acids. Transmission electron microscopic (TEM) images show the assembly of nanospheres is responsible for the hydrogel obtained from the assembly of native peptide. However, a morphological transformation takes

place from nanosphere to nanofibers, when the peptide gels with succinic acid. 1. Gel stiffness is enhanced considerably upon the addition of succinic acid to amphiphile with 2:1 molar ratio. The two-component gel consisting of peptide and succinic acid has been successfully used for three-dimensional cell culture using mouse fibroblast cell line (NIH-3T3).

**Chapter 4** describes the formation of both silver nanoclusters and nanoparticles from a silver-based metallogel. To form this gel, a histidine containing peptide amphiphile is synthesized which forms metallogel in presence of  $\text{AgNO}_3$  in 2:1 molar ratio. Higher concentration of metal forms soluble complex. The metallogel is photo reduced in to different conditions to synthesize a blue light emitting silver nanocluster and silver nanoparticles separately. Transmission electron microscopic (TEM) images show that the nanoclusters and nanoparticles are grown along the nanofibers of the peptide amphiphile. The nanomaterials have significantly increased the rheological properties XRD and FT-IR studies reveal interactions between peptide amphiphiles and the nanomaterials. These nanohybrid systems show extremely efficient antimicrobial properties for both Gram-positive and Gram-negative bacteria. Interestingly, they show compatibility with NIH 3T3 cells, thus it can be concluded that silver nanocluster and nanoparticle decorated peptide amphiphile nanofibers are biocompatible to eukaryotes but inhibits bacteria growth. Inter-cellular generation of reactive oxygen species are responsible for killing of bacteria as seen by DCFDA probe.

**Chapter 5** explores the self-assembly of dipeptide-tethered naphthalene diimide. The monomer under consideration has two dipeptides in its imide positions and a  $\text{C}_{12}$  alkyl amine is added to the core position of the  $\pi$ -conjugated system. The monomer itself is a fluorescent material that has an emission maximum at 560 nm (yellow) in chloroform. It shows solvent dependent aggregation when we add an anti-solvent which is defined as a solvent in which the monomer is insoluble. Interestingly the monomer aggregates in H-type formation until chloroform:hexane is 10:90. As we further increase the amount of hexane J-type aggregation occurs. The phenomenon is well described using FT-IR spectroscopy. Further the current-voltage study shows that addition of electron donating benzene substitutes (aniline, anisole and 4-methoxy phenol) in the aggregate increases the current value due to formation of long charge-separated species.

**Chapter 6** deals with a nanohybrid material formed by combining a copper nanocluster with photoactive TiO<sub>2</sub> nanocrystals. Nanohybrid materials are designed to cover up the weaknesses of individual components. In this current work an environment friendly synthesis was exploited to produce a cyan-emitting copper nanocluster (Cu NC) with a quantum yield of 8.7%. This negatively charged nanocluster was successfully used to make a nanohybrid with anatase titanium dioxide mesoporous nanoparticles having Lewis-acidic pores. The nanohybrid formation was characterized by time correlated single photon counting studies (TCSPC), solid state UV-visible absorption spectroscopy and valence band X-Ray photoelectron spectroscopy. A systematic increase of Cu NC loading on the TiO<sub>2</sub> showed an increase of current from a range of 10<sup>-7</sup> A (in native TiO<sub>2</sub>) to 10<sup>-4</sup> A (1:10 Cu NC-TiO<sub>2</sub> hybrid). Interestingly, the photocurrent response of TiO<sub>2</sub> also dramatically improved from 8.9×10<sup>-3</sup> mA to 4.1 mA in 1:10 Cu NC-TiO<sub>2</sub> hybrid. Systematic variation of their weight ratio vividly demonstrated that 10% w/w TiO<sub>2</sub>-Cu NC hybrid was the most effective current generator, keeping the semiconducting and photovoltaic nature intact. The increase in photocurrent can be attributed to the long-lived electron-hole separation in the nanohybrid system.

Each chapter from chapter 3 to 6 begins with a short 'Introduction' followed by 'Experimental Section', 'Results and discussion' and 'Conclusion'. For convenience, 'References' are given at the end of each chapter. List of publications has been appended at the end of the thesis.



## ACKNOWLEDGEMENT

I would like to acknowledge my gratefulness to many wonderful people for their contribution, support, and guidance towards my Ph.D. dissertation.

At this moment of accomplishment, first and foremost, I would like to express my sincere gratitude towards my Ph. D. supervisor, Professor Arindam Banerjee, for providing me with the opportunity to pursue Ph. D. I am much obliged to him for his constant support and guidance. He provides me with ample academic liberty in his lab to conduct research work of my interest, that enables me to explore the fascinating field of supramolecular chemistry. I am deeply beholden for his untiring determination and patience, which helps to channelize my performance in right perspective. His own zeal for continuing the high standards of research that this lab has maintained over the years, has always inspired me and set a good example for me in my career.

I gratefully acknowledge University Grant Commission (UGC) as well as Indian Association for the Cultivation of Science (IACS) for taking care of my doctoral fellowship for the last 6 years.

The state-of-the-art central instrumental facilities along with the friendly and cordial atmosphere rank IACS among the very best in the country to enrol as a Ph. D. scholar. I feel extremely fortunate to have the opportunity to work at this institute and to be a part of the IACS family which has taken care of me through thick and thin.

I also want to thank Jadavpur University, for allowing me to get registered as a Ph. D. candidate.

I consider myself lucky enough to have experienced such a friendly lab environment with cooperative lab mates during my Ph. D. tenure. It is because of them that I have never felt alone or depressed during my struggles in this once in a lifetime journey to become the doctor of philosophy. It is from the bottom of my heart that I acknowledge all the wonderful souls that I met in the lab since I joined. Senior labmates Dr. Abhishek Baral, Dr. Kingshuk Basu, Dr. Nibedita Nandi, Dr. Subir Paul, Dr. Kousik Gayen, my friends Mr. Biplab Mondal, Mr. Biswanath Hansda and Mr. Soumyajit Hazra who are about to write their own thesis too, and the juniors Mr. Niladri Hazra, Mr. Purnadas Ghosh and Ms. Tanushree Mondal helped me immensely in planning and executing my experiments. Seniors have always come up with inspiring and innovative solutions whenever I felt stuck. I

am especially thankful to Kousik da to help me explore new horizons of supramolecular chemistry. A special mention is necessary for Soumyajit who made a lot of experiments possible. Without those, I could have been well behind in my research output. Biplab and Biswanath has always been persistent supports in many aspects of my day-to-day research works. Without such huge supports from past and present lab mates it would have been almost impossible for me to complete my work smoothly.

I would like to express my gratitude to all the faculty members of our department, School of Biological Sciences, Prof. Prasanta Kumar Das, Prof. Rupa Mukhopadhyay, Dr. Siddhartha Sankar Jana, Dr. Dipak Kumar Sinha, Dr. Prosenjit Sen and Dr. Benu Brata Das and Dr. Ritesh Ranjan Pal for helping me in several matters including the departmental instruments and other department related issues.

It is my pleasure to thank our departmental staffs, Mr. Sovan Mallick, Mr. Gour Chandra Bairagi, Mr. Prasenjit Ghosh and Mr. Ashoke Kumar for their cordial help.

A special mention goes to the Research Scholars' Association (RSA) of IACS. The way RSA has truly become the face of the scholars and students of this institute, is truly phenomenal. They have always stood for the students' rights- financial, academical, experimental all the aspects are taken care of. RSA keeps the campus life vibrant by organizing cultural and sporting event. I could always rejuvenate myself thanks to the RSA.

Collaborators played a big role in my doctoral research projects. Thus, my sincere gratitude goes with Prof. Ian W. Hamley and Dr. Deepak Kumar Sinha. I am immensely grateful to Mr. Parijat Biswas for his contribution in the biological experiments of my very first publication from this laboratory.

I am also thankful to friends and colleagues of IACS from other labs who had always opened their door for any experimental helps. I would like to thank lab members of Prof. Asim Bhowmik, Prof. Narayan Pradhan, Prof Parthasarathi Dastidar, Prof. Prasanta Kumar Das and Prof. Abhishek Dey.

My research involves lot of instrumental techniques. Thus, the technical help from Mrs. Chapma Bag, Dr. Sasanka Majhi, Mr. Chinmoy Chakraborty, Mr. Sumit Roy, Mr. Sachin Roy, Mr. Nirmalya Dutta, Mr. Arunim Paul, Mr. Supriya Chakraborty, Mr. Arup Das, Mr. Chanchal Kumar Das, Dr. Bholanath Mondal, Mr. S. K. Sarkar,

Mr. Goutam Biswas, as well as help from glassware, electrical and engineering section is deeply acknowledged.

The note of acknowledgement can never be complete without one's family. I am forever indebted to my grandmother Smt. Sita Tanti whose loving presence and selfless care have protected me since my childhood. My parents Sri Bijan Kumar Bairagi and Smt. Krishna Bairagi are two huge pillars of whatever success I have enjoyed in my life. They remain my constant support, source of inspiration and care-giver till date. No amount of thankfulness can really gauge the depth of their sacrifice for their child. I am grateful to have you both in my life. I would like to end this vote of thanks by saying how grateful I am to my beloved wife Mrs. Ragini Singh. She had been my go-to-person to whine about all the frustration of paper-rejections, failed experiments and my own inefficiency at certain matters. Her support and love have pushed me through the muddy road of a Ph.D.scholar. She actively helped me out in organizing and writing down this thesis and saved me from quite a bulk of the work.

Dipayan Bairagi

Indian Association for the Cultivation of Science

Jadavpur





## Abbreviations

Abbreviations used for amino acids, peptides, derivatives, substituent, reagents, experimental tools, etc. are largely in accordance with the recommendations of the IUPAC-IUB commission on Biochemical Nomenclature, 1974, *Pure and Applied Chemistry*, **40**, 315-331. Other symbols, nomenclature, etc. are based on the list in *J. Biol. Chem.*, 1989, 669-671. Protein amino acids are of L-configuration unless otherwise indicated. Standard three letter coding is used for all amino acids. Additional abbreviations used in this thesis are listed below.

Ala	Alanine
AFM	Atomic force microscope
Arg	Arginine
AU	Absorbance units
a.u.	Arbitrary units
Boc	Tertiary butyloxycarbonyl
Bz	Benzyl
$\delta$	Chemical shift
d	Doublet
DCC	<i>N,N'</i> -dicyclohexylcarbodiimide
DCU	<i>N,N'</i> -dicyclohexylurea
DMF	Dimethyl formamide
DMSO	Dimethyl sulfoxide
ESI	Electro spray ionization
FE-SEM	Field emission scanning electron microscope
Fmoc	N-fluorenyl-9-methoxycarbonyl
FT-IR	Fourier transform-Infra red
HCOOH	Formic acid
h	Hours
HR	High resolution
HRMS	High resolution mass spectrometry
HR-TEM	High resolution transmission electron microscope
<i>J</i>	Coupling constant
M	Molar

m	Multiplate
Me	Methyl
MeOH	Methanol
MHz	Megahertz
μm	Micrometer
MS	Mass spectrometry
Nap	Naphthyl
nm	nanometer
NMR	Nuclear magnetic resonance
PBI	Perylenebisimide
NDI	Naphthalenediimide
Ph	Phenyl
pH	The negative logarithm hydrogen-ion activity ( $-\log_{10} [\text{H}_3\text{O}^+]$ )
Phe	Phenyl alanine
PL	Photoluminescence
PXRD	Powder X-Ray Diffraction
s	Singlet (in NMR)
s	Seconds
SEM	Scanning electron microscopy
SAXRD	Small angle X-ray diffraction
t	Triplet
TEM	Transmission electron microscope
TFA	Trifluoroacetic acid
TLC	Thin layer chromatography
TMS	Tetramethylsilane
UV/Vis	Ultraviolet/visible spectroscopy
Val	Valine
WAXS	Wide angle X-ray scattering
XRD	X-ray diffraction
Trp	Tryptophan
β-Ala	β-alanine

# CHAPTER 1

---

## General Introduction





## 1.1. Self-assembly: The stepping stone of the Supramolecular Chemistry

The seamless working of nature's processes is built on how the smallest of molecular entities come together to create bigger structures and this hierarchical process goes on from the quarks to the galaxies. As science tries to unravel the mysteries of natural processes, it gradually comes to light that, molecules more often than not work in unison. This natural process of 'coming together and function as a whole' is nothing but molecular self-assembly (Figure 1.1). The chemistry of reaction and interaction at a level beyond single molecule is defined as Supramolecular Chemistry. Nobel Prize winner for his work in this field in 1987, Jean-Marie Lehn was the first person to define Supramolecular chemistry as 'chemistry beyond the molecule'<sup>1</sup>. According to Professor Lehn, supramolecular chemistry 'aims at designing and implementing functional chemical systems based on molecular components held together by non-covalent intermolecular forces.'<sup>1</sup> Thus, it is understood that studies included in supramolecular chemistry is nothing but studies conducted to understand the self-assembly processes and edit or mimic such processes to develop new functional superstructures. Although the academically recognised field of supramolecular chemistry is young, the studies comprising of supramolecular interactions based on weak forces can date back to earliest days of chemistry. A fascinating self-assembled structure is cell membrane where simple lipid molecules come together to create a highly specific membrane system where membrane proteins remain embedded.<sup>2</sup> In modern days, discovery of DNA double helix in 1953 is one of the most celebrated studies of self-assembled system. The double helix uses  $\pi$ - $\pi$  stacking and hydrogen bonding interaction between complementary base pairs to hold its structure.<sup>3</sup> Moreover, the structure uses hydrogen bonding between neighbouring water molecule and the phosphate group of the DNA bases.

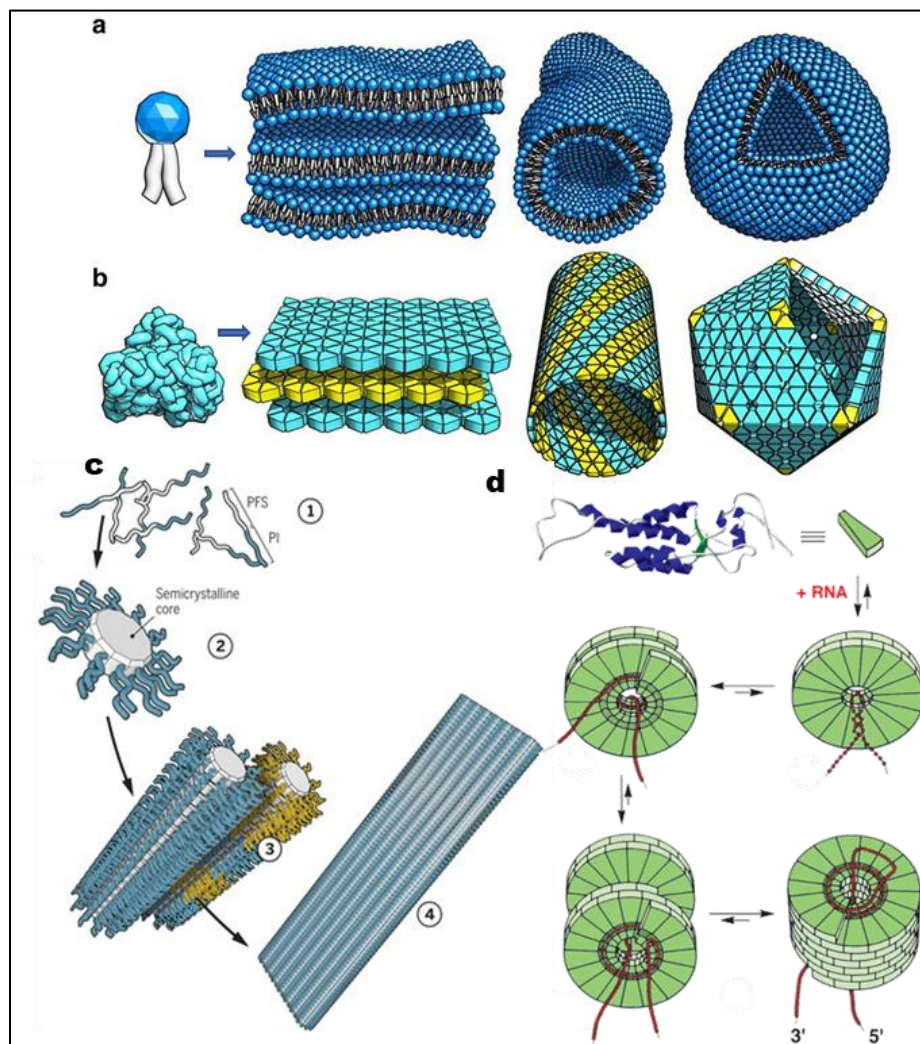


**Figure 1.1** Representing various self-assembly systems starting from individual units. (a) Lipid monomers form lamellar, tubular and vesicular superstructures. (b) Proteins form crystalline lamellar, helical tubular and regular icosahedral structures. (Adopted from S. Yang, Y. Yan, J. Huang, A. V. Petukhov, L. M. J. Kroon-Batenburg, M. Drechsler, C. Zhou, M. Tu, S. Granick and L. Jiang, *Nat. Commun.*, 2017, **8**, 15856). (c) Crystallization induced self-assembly of a block co-polymer into semi crystalline discs which assemble into rods that finally forms 2D sheets. (Adopted from M. Ballauff, *Science*, 2016, **352**, 656-657). (d) Tobacco mosaic virus assembles through individual protein sub-units associating with viral RNA yielding a two-disc architecture. This grows further to slipped disc structure via a conformation change. (Adopted from L. M. Greig and D. Philp, *Chem. Soc. Rev.*, 2001, **30**, 287-302).

Since the discovery of the double helix, the field of supramolecular chemistry was flooded with the works of Pedersen, Lehn and Cram. Charles Pedersen's discovery of crown ethers<sup>4</sup> in 1967, Jean-Marie Lehn's synthesis of first cryptands<sup>5</sup> in 1969 and experiments done by Donald Cram using spherand hosts elaborating the

importance of preorganisation<sup>6</sup> in self-assembly paved the path to a new field—rather a new outlook to a pre-existing phenomenon. Later in 1989 Robson and Hoskins utilised coordination bond to synthesize coordination polymer.<sup>7</sup> In 1983, Nuzzo and Allara fabricated self-assembling monolayer of alkanethiols on gold surface.<sup>8</sup> Self-assembly continues to be the primary strategy to organize supramolecular superstructures using the non-covalent interactions. This is a useful strategy to design nanostructures like nanospheres, nanowires, nanorods, vesicles, bilayers, micelles etc. to macroscopic objects such as helical fibres or 2D sheets.<sup>9-11</sup> As self-assembly techniques erase the boundaries between chemistry, biology and material sciences, the research output has grown by leaps and bounds in the past decades.

Scientists have put up a lot of effort in the development of pre-programmed systems in which small molecular building blocks converge by itself to produce a much larger, more complicated assembled system. The idea of ‘pre-programming’ contains all the information necessary to selectively produce the desired superstructure with the help of their molecular building blocks (in terms of size, shape, symmetry, and the electronic properties of their binding sites). So, we can define self-assembly as *the spontaneous and reversible association of molecules or ions to form larger, more complex supramolecular entities according to the intrinsic information contained in the molecules themselves*. Thus, self-assembly occurs under thermodynamic control with the system converging to the thermodynamically most stable state.<sup>12</sup> Self-assembly processes can be subdivided in two parts depending on their thermodynamic stability. The first one is the static self-assembly which is either in a local or global equilibrium and consequently, does not dissipate any energy. Examples of such system are self-assembly of ribosome or nanofibers formed through peptide self-assembly. (Figure 1.2) The second type of self-assembly system is dynamic self-assembly where the aggregation occurs only due to dissipation of energy. Live cells are complex example of such systems.<sup>13</sup> (Figure 1.2) Supramolecular self-assembly is directed by molecular recognitions. It is fundamentally a spontaneous and reversible association of molecular components known as tectons,<sup>14</sup> under the intermolecular (Or intra-molecular) control of non-covalent interactions such as coordination interactions, hydrogen bonds, and dipolar interactions. The reversible nature of

self-assembly is key to convergence of the resulting system into thermodynamically most stable state. In the living system, this process incorporates the potential for self-healing. Fundamentally, self-assembly is a convergent process in which a number of components assemble into, ideally, a single final, stable structure. The self-organization is the tool through which molecules evolved through inanimate matter to finally organize into a way to finally create living systems.

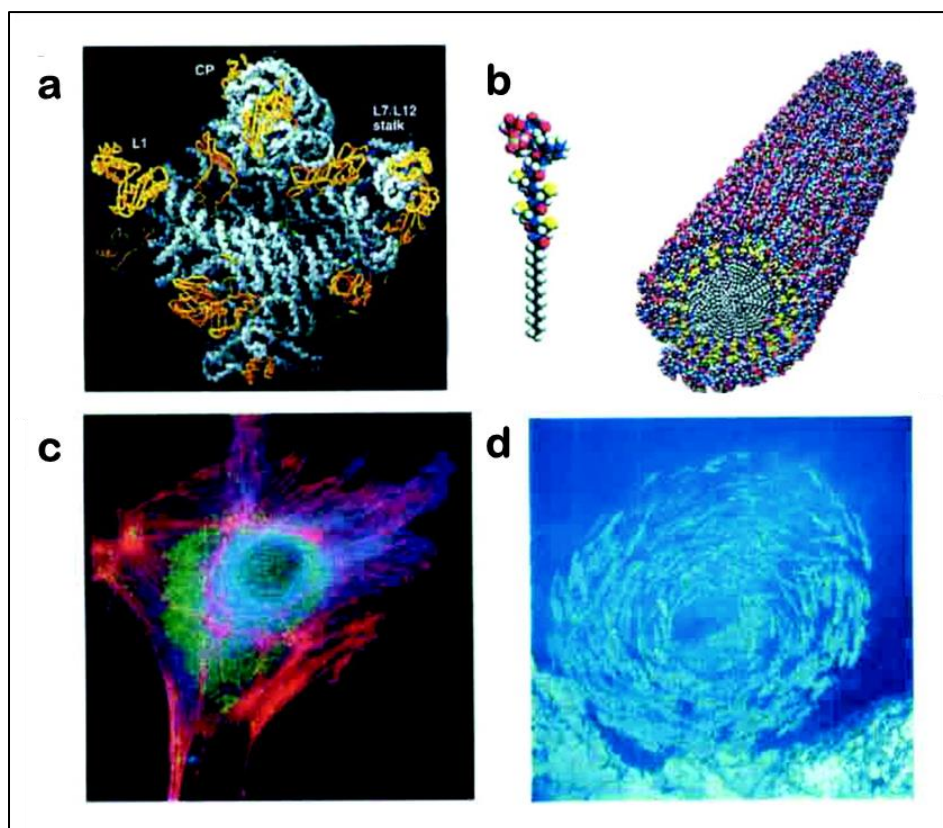


**Figure 1.2** Representing Examples of static self-assembly (a) ribosome crystal structure, (b) self-aggregated nanofibers formed from peptide amphiphiles. Examples of dynamic self-assembly (c) a fluorescently labeled cell, (d) Belousov-Zhabotinski reaction shows reaction-diffusion waves. (Adopted from M. Whitesides George and B. Grzybowski, *Science*, 2002, **295**, 2418-2421).

### 1.1.1. Interacting Forces in Supramolecular Self-assembly

Self-assembly creates larger and more complicated structures by bringing the molecules close to each other and but the question remains, “What brings them



together?” However big the self-assembled superstructures may be, the forces that hold them together are weak non-covalent interactions. Self-assembly is always brought in by weak forces such as ionic bonding, hydrogen bonding, metal coordinate bonds, dipole-dipole interactions, Van der Waals forces and hydrophobic interactions. (Figure 1.3)

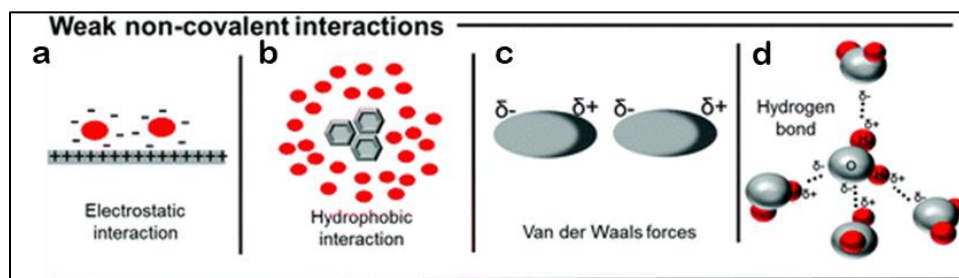


**Figure 1.3** Schematic representation of different non-covalent forces responsible for self-aggregation. (a) Electrostatic attraction between charged particles and oppositely charged 2D surface, (b) Hydrophobic interaction creates aggregation among hydrophobic moieties in a hydrophilic environment. (c) Dipole-dipole attraction of Van der Waals forces. (d) Hydrogen bonding in water molecules via  $O \cdots H - O$  mode. (Adopted from S. Casalini, C. A. Bortolotti, F. Leonardi and F. Biscarini, *Chem. Soc. Rev.*, 2017, **46**, 40-71).

The term non-covalent interactions encompass various types of intermolecular interactions each with a different energy profile as depicted in table 1. The non-covalent interaction provides the room for synthesis of numerous types of architecturally different supramolecules with compelling features which is not attainable by conventional covalent synthesis method. The presence of non-covalent interactions first came into light in 1873 when Johannes Diderik van der Waals established them but Nobel laureate Hermann Emil Fischer is credited with the establishment of philosophical roots of supramolecular chemistry. In 1890, Fischer proposed the very famous “Lock and key” model for the enzyme-substrate complex interaction thus paving way for the molecular recognition and host-guest chemistry. To understand the interaction chemistry of supramolecules. We need to understand the non-covalent interactions in depth.

\

**Table 1.1** Energy of various non-covalent bonds involved in supramolecular chemistry.

Types of Interaction	Bond Energy (kJ/mol)
Hydrogen bond	10-65
Ion-dipole	50-200
Dipole-dipole	5-50
Cation- $\pi$	5-80
$\pi$ - $\pi$	0-50
Metal-ligand	0-400
Van der Waals force	<5
Metal-ligand	0-400

### 1.1.1.1. Hydrogen Bonding

Hydrogen bond is a weak electrostatic attractive force that exists between a hydrogen atom covalently bonded to a very electronegative atom, X and a lone pair of electrons on another small, electronegative atom, Y. The atoms X and H are covalently bonded and are a polar bond due to X being an electronegative moiety. X-H is known as Hydrogen bond donor. Hydrogen bonding is established between Hydrogen and X, Y will have to be the atoms F, O or N. The atom Y consists of lone pairs the bond between the H and Y becomes more electronegative with increasing electronegativity of X atom. Hydrogen bonds found in nature are of two types- intermolecular and intramolecular hydrogen bonds. They are weaker in nature as compared to covalent bonds and the common example of hydrogen bond in acetic acid dimer where the O-H...O bond is established. Another important hydrogen bonding to be noted is N-H...O found in various secondary superstructure including parallel  $\beta$ -sheets, alpha helices and the bases found in DNA double stranded helix forms complementary hydrogen base pairs such as Adenine=thymine and Cytosine  $\equiv$  Guanine.

### 1.1.1.2. Ionic bonds

Ionic bond formation occurs between ions of opposite charges and is thus a type of electrostatic interaction formed as a result of complete transfer of electrons from a less electronegative atom to a highly electronegative atom. Ionic bonds are thus directional in nature. Ionic bond is commonly seen between metals and non-metals as they have high electronegativity difference. Example of Ionic bond in supramolecular chemistry is supramolecular ionic networks which is formed by the interactions of multicationic and multianionic molecules and are fluidic in nature. An example of a common ionic liquid is tetradecyl(trihexyl)phosphonium chloride which has a melting point below 20 °C.

### **1.1.1.3. van der Waals forces**

There are three types of van der Waals forces:

- a. Dipole-dipole interactions – these interactions occur between two molecules having temporary dipole and the interaction is built between the positive end of one molecule and negative side of another molecule and they are oriented in such a manner to facilitate this.
- b. Dipole- induced dipole interactions – A permanent dipole induces a transient dipole in a nearby molecule by distorting its electron distribution.
- c. Induced dipole-induced dipole interactions – In an atom, electrons remain in constant motion, and the motion of electrons on one atom influences the motion of the electrons in the other atom and at any point of time there exist an imbalance of charge distribution in the nucleus thus an instantaneous dipole is established which influences the electron cloud in the neighbouring atoms. Similarly, a transient dipole molecule can induce dipole in the neighbouring molecule. This interaction is very weak.

### **1.1.1.4. Hydrophobic interaction**

Hydrophobic interaction is commonly found in non-polar substances which causes them to cluster together to reduce the contact with water. The interaction between the water molecule is more favourable than the interaction between the non-polar substance and water molecule. When non-polar molecules interact with an aqueous

environment the water molecule surround it forming a cage like structure, reducing the entropy but enough energy is not available bring this process to completion and hence the water molecules release into the environment from increasing the entropy. This phenomenon drives the hydrophobic effect. Example of hydrophobic effect in supramolecular assembly is self-assembly of peptide amphiphile (PA) molecules<sup>15</sup>

### 1.1.1.5. Coordination interaction

Interaction through coordination covalent bonds is of extreme importance in metal directed self-assemblies. This is an interaction where the donor shares two electrons equally with the vacant orbital of the acceptor. Coordination polymers, metal organic framework, peptide metallogeles<sup>15</sup> are some examples of assemblies that utilize coordination bond.

### 1.1.1.6. $\pi$ - $\pi$ stacking

Another weak non-covalent interaction is known as  $\pi$ - $\pi$  stacking can be seen among molecules with aromatic groups. In peptide, it can be seen mainly in the peptide nanostructures that assemble by peptides contain aromatic amino acids, such as phenylalanine, tyrosine, and tryptophan. Due to the limited solubility of molecules containing aromatic groups,  $\pi$ - $\pi$  interactions are very stable in water. Moreover, it can show growth in specific direction. Example of such interaction is common in rylene dye derivatives. Details discussion on them can be found elsewhere in his thesis.

## 1.2. Assembly of Supramolecular polymers via non-covalent forces

In the general polymers the monomers are linked by via covalent bond but for supramolecules the covalent bond no longer holds significance and the main force of interaction between the monomers is H-bonding,  $\pi$ - $\pi$  stacking, hydrophobic effect etc. which are highly directional and non-covalent in nature. The term ‘Supramolecular Polymers’ can be more explicitly defined as, “*polymeric arrays of monomeric units that are brought together by reversible and highly directional secondary interactions, resulting in polymeric properties in dilute and*

concentrated solution as well as in the bulk. The directionality and strength of the supramolecular bonding are important features of systems that can be regarded as polymers and that behave according to well-established theories of polymer physics.”<sup>16</sup> (Figure 1.4) Hence, from the thermodynamic point of view the supramolecular polymerisation is a process in which the monomers are linked together via non-covalent interactions which are relatively weaker than covalent interactions. (Figure 1.4) Thus, the supramolecular polymers are less robust mechanically and chemically as compared to polymers formed by covalent interactions. This property of being less robust mechanically and chemically is advantageous to the supramolecular polymers as it makes room for easy processing, recyclability, self-healing, stimuli responsiveness, and other evolvable properties. The supramolecular polymers are superior than the conventional polymers in lot many ways and it can be reflected the diverse types of self-assembled supramolecular nanostructures available in nature which are assembled from their respective monomers after their aggregation through specific non-covalent interactions.

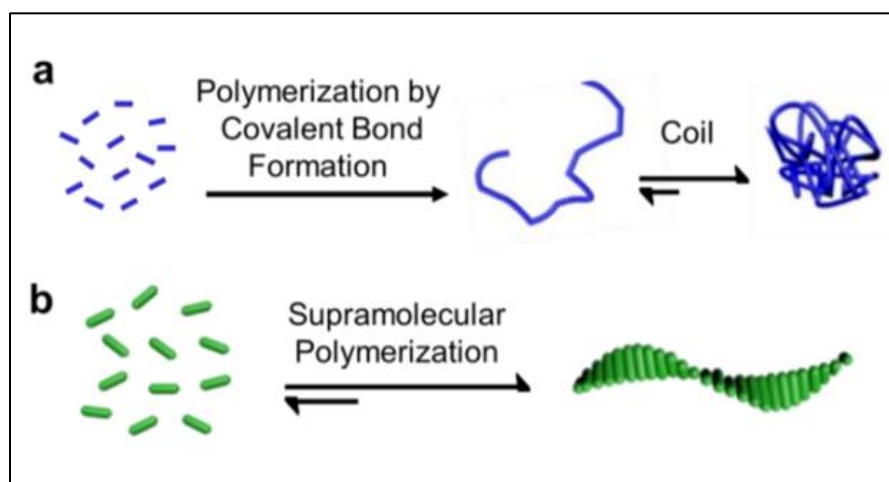


**Figure 1.4** Schematic representation of (a) covalent polymerization which is characterized by irreversible formation process and covalent bond formation between the monomers. (b) Supramolecular polymerization which takes place due to non-covalent forces and the process is a reversible one. (Adopted X. Hou, C. Ke, Y. Zhou, Z. Xie, A. Alngadh, D. T. Keane, M. S. Nassar, Y. Y. Botros, C. A. Mirkin, J. F. Stoddart, *Chem. Eur. J.* 2016, **22**, 12301).

Synthetic supramolecular polymers are able to combine the best of both worlds: bioinspired functionality from natural systems with the accessibility and mouldable characteristics of synthesised materials. As a result, synthetic molecules enable fabrication of robust supramolecular materials with promising applications.<sup>17</sup> Here, some of the important categories of synthetic supramolecular polymers, classified by their primary binding motif, are discussed briefly.

### 1.2.1. Multiple Hydrogen bonded motifs

The first type of non-covalent- multiple hydrogen bond was reported by Lehn and his co-workers and has been a major inspiration for the synthesis of supramolecular polymers since then.] In 1994, Lee and Griffin moved to supramolecular architectures using a single hydrogen bond between a carboxylic acid and a pyridine arranged through single hydrogen bond.<sup>18</sup> The supramolecular arrangement yields to fibrous arrangement with rheological properties owing to the ionic character of the bond between an acid and pyridine Wuest and coworkers introduced one-dimensional aggregates based on hydrogen bonds in the crystalline state.<sup>19</sup> They used an array of double hydrogen-bonded monomers that formed polymeric arrays in the crystal. Interestingly polymeric arrays are not always the product. In different conditions, dimer formation took place too (Figure 1.5). In a next step, Lehn moved to the liquid crystalline phase using a triple-hydrogen bonded strategy in 1990.<sup>20</sup> Here, his group synthesized two complementary monomeric units (A-A and B-B), assembled them into a (A-A:B-B)<sub>n</sub> polymeric structure, and observed chiral fiber-like architectures with electron microscopy. The rather low association constant of the triple-hydrogen bonded units was overcome by the directionality of their linear arrangement in the liquid-crystalline phase.

In 1997, E. W. Meijer and co-workers synthesised supramolecular polymeric materials using quadruple hydrogen-bonding 2-ureido-4[1H]-pyrimidinone (UPy) unit (Figure 1.5), having higher binding constant and possessed tuneable macroscopic rheological and material properties.<sup>21</sup> d. The molecule is very easy to synthesize in one step from commercially available precursor molecules or in three steps from methyl acetate. At that time, it represented the first example of a (self-

complementary) quadruple hydrogen bonding unit. The analysis of the binding strength was much more difficult than the synthesis of UPy, as it is so high.

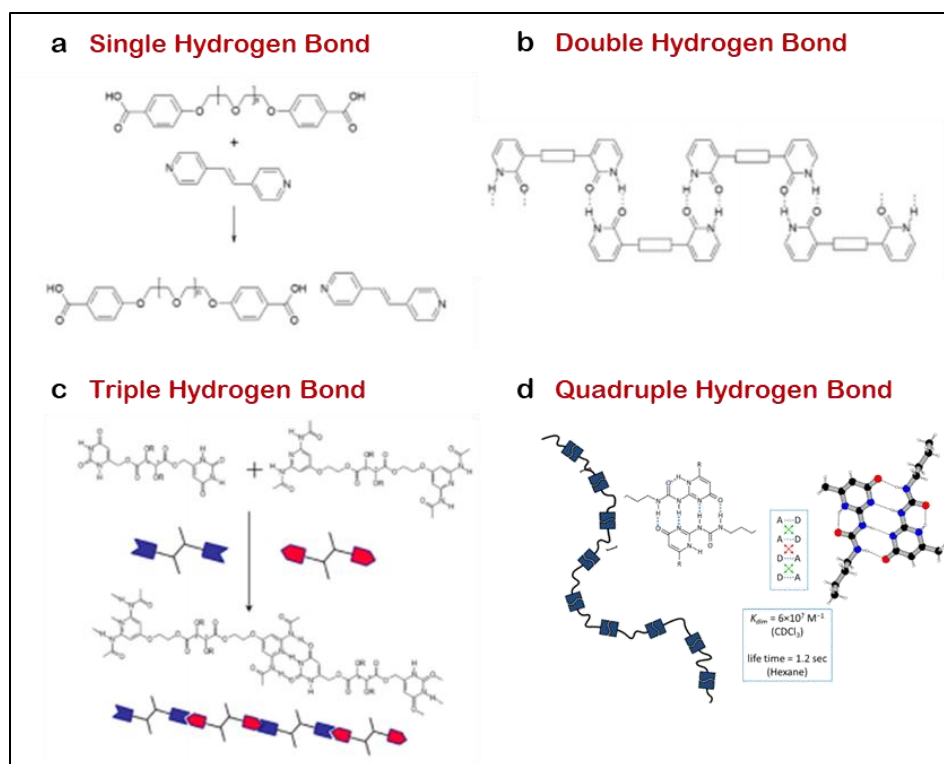


**Figure 1.5** Supramolecular polymer network extended by H-bonding association, (a) Propagation of network through single  $N\cdots H-O$  bond developed by Griffin and co-workers, (Adopted from C. M. Lee, C. P. Jariwala, A. C. Griffin, *Polymer*, 1994, **35**, 4550–4554). (b) through double  $N-H\cdots O=C$  hydrogen bond formulized by Wuest and co-workers (Adopted from Y. Ducharme, J. D. Wuest, *J. Org. Chem.*, 1988, **53**, 5787–5789) and (c) triple hydrogen bonded network developed by Lehn and co-workers. (Adopted from C. Fouquey, J. M. Lehn, A. M. Levelut, *Adv. Mater.*, 1990, **2**, 254–257) (d) Meijer and co-worker developed UPy-based supramolecular network which utilizes four H-bonds thus possessing a very high association constant. (Adopted from R. P. Sijbesma, F. H. Beijer, L. Brunsveld, B. J. Folmer, J. H. Hirschberg, R. F. Lange, J. K. Lowe, E. W. Meijer, *Science*, 1997, **278**, 1601–1604).

**1.2.2. Large  $\pi$ -conjugated surfaces:** Self-assembly of  $\pi$ -conjugated systems can be extremely strong, due to a combination of hydrophobic and  $\pi$ - $\pi$  interactions. The  $\pi$ - $\pi$  systems offers a range of features such as robustness, extensive  $\pi$ - electron delocalisation, well ordered columnar structures which can be put to advance functional applications. The driving force of aggregation grows

approximately linearly with increasing size of the hydrophobic surface and results in the formation of remarkably stable polymers. The property of stacking interaction enables the electronic coupling between the molecules' delocalized  $\pi$ -electrons and it confers interesting optical and electronic properties which can be exploited in areas such as sensing and solar heat conversion. these  $\pi$ -conjugated molecules absorb (and sometimes emit) light in the UV/vis or near-IR range and their spectral properties are sensitive to aggregation. Using spectroscopic techniques quantitative analysis of polymerization and distinction between H and J aggregation can be executed. One of the prominent example of  $\pi$ -conjugated system is perylene dyes which find a variety of biological applications due to their ability to form water soluble compound as they accommodate ionic or non-ionic substituents with multiple polar groups into the core-region, imide- or ortho-positions of perylene bismide (PDI) self-assembly.<sup>22</sup> These ionic groups help in lowering the  $\pi$ - $\pi$  aggregation by shielding the inner perylene chromophores. Würthner and co-workers contributed significantly in understanding the mechanism of PDI self- assembly and its various applications.<sup>22</sup> It can be employed for live cell imaging as their absorption and emission range is beyond 500nm thus reducing the auto-fluorescence of the background cells.<sup>22</sup> Other than PDIs, large  $\pi$ -surface containing molecules utilized by several researchers in the studies includes naphthalene diimide (NDI) and oligo(phenylenevinylene) (OPV)<sup>23</sup> based supramolecular polymers



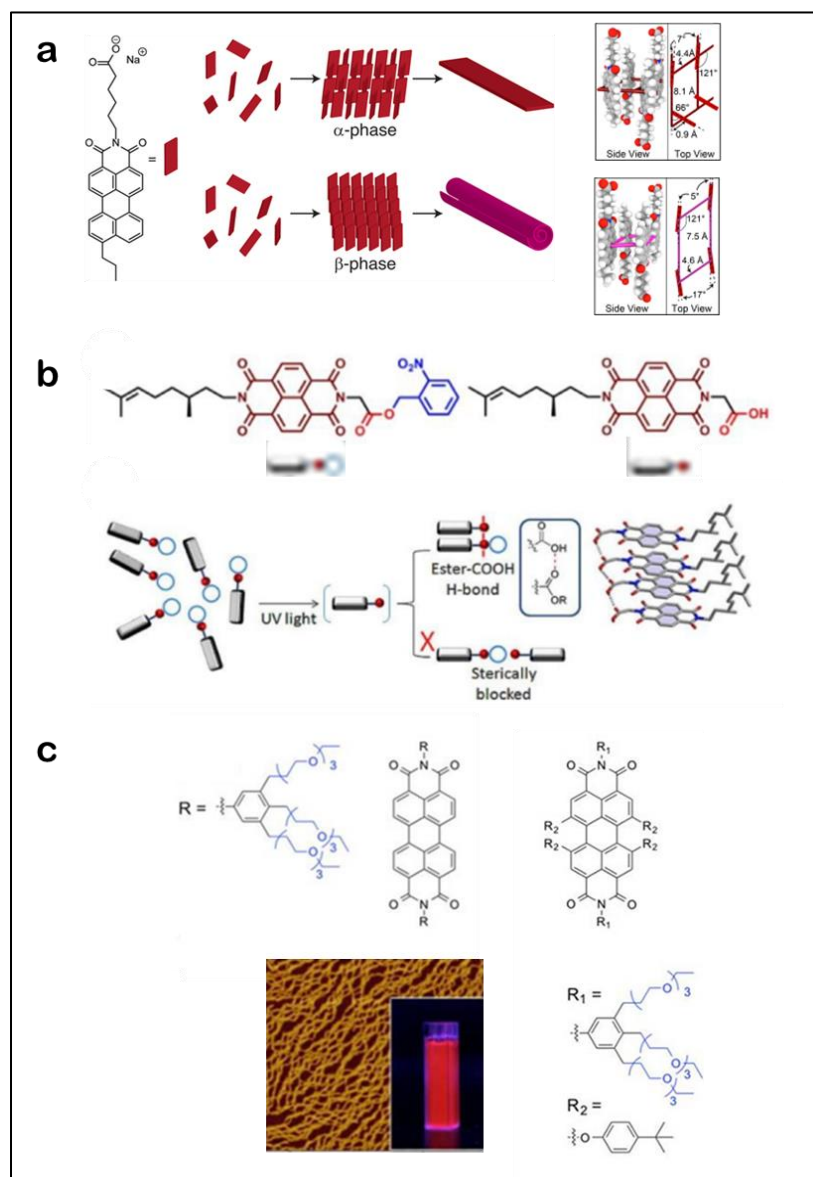


**Figure 1.6** Examples of Supramolecular polymeric network formation through  $\pi$ -conjugated systems. (a) Schematic representation of the crystallization of a perylene monoimide chromophore amphiphile into two different modes of  $\pi$ -stacking namely, kinetic  $\alpha$ -phase and thermodynamically more stable  $\beta$ -phase through thermal annealing. (Adopted from R. V. Kazantsev, A. J. Dannenhoffer, A. S. Weingarten, B. T. Phelan, B. Harutyunyan, T. Aytun, A. Narayanan, D. J. Fairfield, J. Boekhoven, H. Sai, A. Senesi, P. I. O'Dogherty, L. C. Palmer, M. J. Bedzyk, M. R. Wasielewski and S. I. Stupp, *J. Am. Chem. Soc.*, 2017, **139**, 6120-6127). (b) A NDI-based monomer with photo-labile ortho-nitrobenzyl (ONB) protected carboxylic acid group dictates the  $\pi$ -stacking assembly even as photoirradiation decomposes the nitrobenzene part. (Adopted from D. S. Pal and S. Ghosh, *Eur. J. Chem.*, 2018, **24**, 8519-8523.) (c) Two different PBI-based molecules co-assemble through  $\pi$ -stacking to form nanofibers. (Adopted from D. Görl, X. Zhang, V. Stepanenko and F. Würthner, *Nat. Commun.*, 2015, **6**, 7009)

**1.2.3. Host-guest system:** The host-guest interaction was the foundation of supramolecular chemistry as the discovery of cryptands and crown ethers by Lehn, Cram, and Pedersen expanded the supramolecular chemistry horizon.<sup>17</sup> The host-guest interactions include interaction between two molecules as the name suggests, between the host and guest molecule. Guest molecule recognises the cavity in the host molecule and forms a very strong supramolecular complex based on complementarity and size fit between them. The interaction is specific in terms of size, shape, charge, and polarity and can thus, be used in the formation of directed supramolecular synthesis. One of the key synthetic molecules used in host-guest systems, cyclodextrins (CD), are cyclic oligomers assembled out of six ( $\alpha$ ), seven ( $\beta$ ) or eight ( $\gamma$ ) glucopyranose units, linked by  $\alpha$ -(1-4)-glycosidic linkages, named  $\alpha$ -,  $\beta$ -, and  $\gamma$ -cyclodextrins, respectively. CDs can form multiple complexes with different types of organic guest molecules which forms cognate pair for the cavity and display different binding affinities. The pioneering work of Harada and co-workers in reporting the role of CDs in assembling aqueous supramolecular polymers. Adamantane is a strong guest for the  $\beta$ -CD cavity, with an association constant of  $10^4 \text{ M}^{-1}$ , while similar affinities are found for phenol and phenylalanine guests in  $\alpha$ -CD.<sup>23,24</sup>

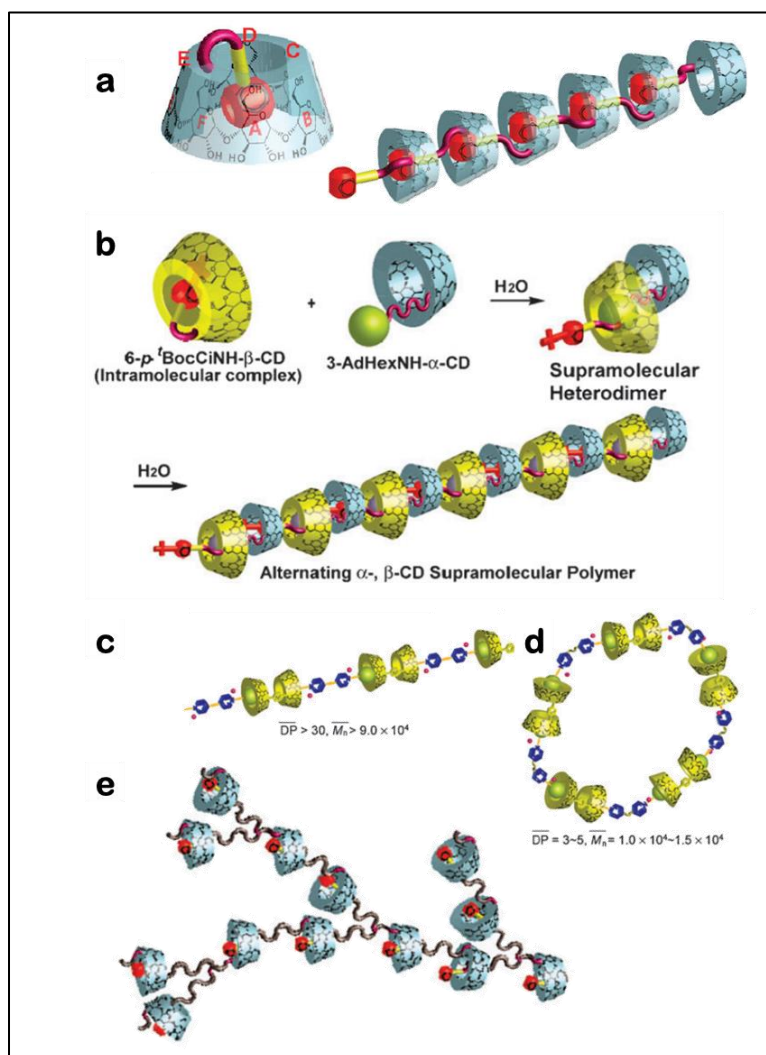


**Figure 1.7** Monomers and supramolecular polymer networks (SPNs) formed by their association through host-guest interactions. (a) When a hydrocinnamoyl group was attached to  $\beta$ -Cyclodextrin at the C6 position, the  $\beta$ -Cyclodextrin and hydrocinnamoyl group formed an intramolecular complex where the benzene ring acts as a guest to the host  $\beta$ -Cyclodextrin cavity. Supramolecular polymers known as daisy chain structure is formed when the guest part (cinnamoyl group) was attached to one of the secondary hydroxyl groups of CD (the wider side). (Adopted from M. Miyauchi, Y. Kawaguchi and A. Harada, *J. Inclusion Phenom. Macrocyclic Chem.*, 2004, **50**, 57–62) (b) When *t*-Boc cinnamoyl-CD, which forms intramolecular complexes, and  $\alpha$ -CD bearing an adamantane group were mixed in a 1 : 1 ratio in water, they formed a block copolymer with alternate  $\alpha$  and  $\beta$  monomers. (Adopted from M. Miyauchi and A. Harada, *J. Am. Chem. Soc.*, 2004, **126**, 11418–11419) (c) When a  $\beta$ -CD dimer and an adamantane dimer were mixed in aqueous solutions, they formed a supramolecular polymer when the linker is rigid, and (d) gave cyclic supramolecular oligomers when the linker is flexible. (Adopted from K. Ohga, Y. Takashima, H. Takahashi, Y. Kawaguchi, H. Yamaguchi and A. Harada, *Macromolecules*, 2005, **38**, 5897–5904. (e) Branched supramolecular polymers formed by bifunctional cyclodextrin derivatives. (Adopted from W. Deng, H. Yamaguchi, Y. Takashima and A. Harada, *Angew. Chem., Int. Ed.*, 2007, **46**, 5144–5147).

### 1.2.4. Peptide Amphiphiles:

Peptide Amphiphiles (PA) constitutes of four different domains (Figure 1.8) and undergoes self-assembly to produce functional peptide Amphiphile. The four different domains have different functional role to play, domain 1 is the hydrophobic part consisting of long alkyl chain, domain 2 is the Hydrogen bonding motif which forms intermolecular assemblies through hydrogen bond, domain 3 consists of peptide with polar side chains and domain 4 is an epitope which interacts with specific protein and also mediates cell adhesion. They aggregate to form high aspect ratio fibers. The bioactive part of the amphiphile remains at the outer portion of the peptide fibrils and lipophilic tail is buried inside the core (Figure 1.8). The charged peptide amphiphile monomers remains dissolved in water due to intermolecular columbic repulsion and neutralization of their charges through pH change causes self-aggregation that ultimately forms various superstructures such as nanotube, nanofibers (Figure 1.8), twisted nanoribbons and others. The structural integrity of the fibrils can be attributed to the  $\beta$ -sheet forming domain which forbids the assembling like micelles. These  $\beta$ -sheet domains are tunable and by altering the peptide sequence of this area we can improve upon the gel strength The chiral centre attached to the long chain have been found to induce helicity in the fibers.<sup>25</sup> Perturbation from symmetry in molecules leads to aggregation in chiral fashion which is ultimately reflected in microscopic chirality. However, in this context it is worth to be noted that such chiral induction is highly dependent on the corresponding gelator, solvent system and sometimes on the handedness of a particular amino acid in the peptide sequence.<sup>26</sup> Peptide amphiphile is one of the prime foci of this thesis and is discussed in detail in subsequent sections.

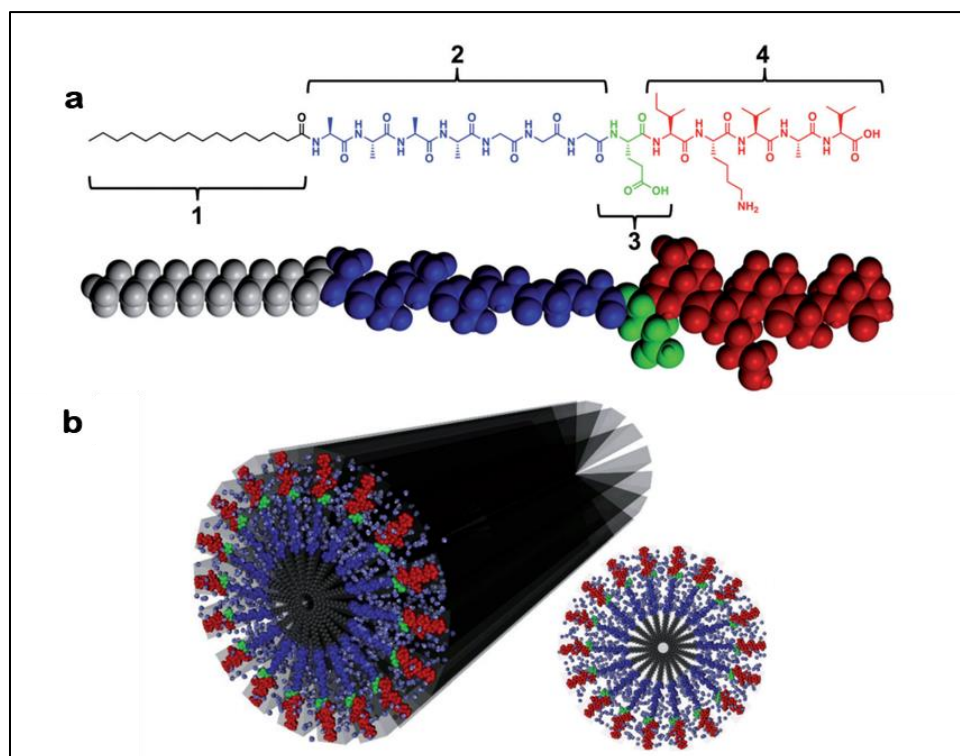


**Figure 1.8** A self-assembled nanofiber formation from a peptide amphiphile. (a) The representative peptide amphiphile illustrates four rationally devised domains. Domain 1 represents the lyophilic chain, Domain 2 consists of short peptide sequence of consecutive residues with neutral side chains to enhance  $\beta$ -sheet formation through H-bonding, Domain 3 is very short sequence of charged amino acid residues to enhance solubility of the amphiphile in water and finally the Domain 4 consists of the epitope sequence with interacts with proteins or adhere to cells. (b) Graphical representation of the self-assembly of the peptide amphiphile molecules into nanofibers. The cross section of these fibers elucidates the molecular self-assembly with clarity. (Adopted from M. J. Webber, E. J. Berns and S. I. Stupp, *Isr. J. Chem.*, 2013, **53**, 530-554).

### 1.3. Peptides to nanomaterials through supramolecular organisation

Peptides are one of the most abundant biomolecules occurring in nature that aggregate in diversified nanostructures. They play an essential role in fundamental physiological processes and are indispensable for many biochemical reactions. The diverse functionality of peptides can be attributed to their building blocks – amino

## General Introduction

acids. Amino acids, by virtue of their enormous range of properties essentially create infinite functional and structural potential in the peptide sequences.

There are 20 protein forming  $\alpha$ -amino acids found in nature and possess L-configuration.<sup>27</sup> Two or more  $\alpha$ -amino acids are joined by peptide bonds and are called peptide residues. The peptide bond is established between the carboxyl group of one amino acid and the amine group of another amino acid by the condensation reaction. These peptide bonds are susceptible to enzymatic cleavage known as proteolysis.<sup>28</sup> The amino acids are optically active except for glycine and thus occur in nature in two types of stereoisomers L and D. All  $\alpha$ -amino possess different types of side chain groups known as R groups. The functional diversity of amino acids is attributed by these R group and are classified as polar charged or uncharged and hydrophobic amino acids. (Figure 1.9) The peptides composed of D-amino acids are more stable than L-amino acids in terms of proteolytic cleavage and thus are more used in biomaterials designing.<sup>29</sup>

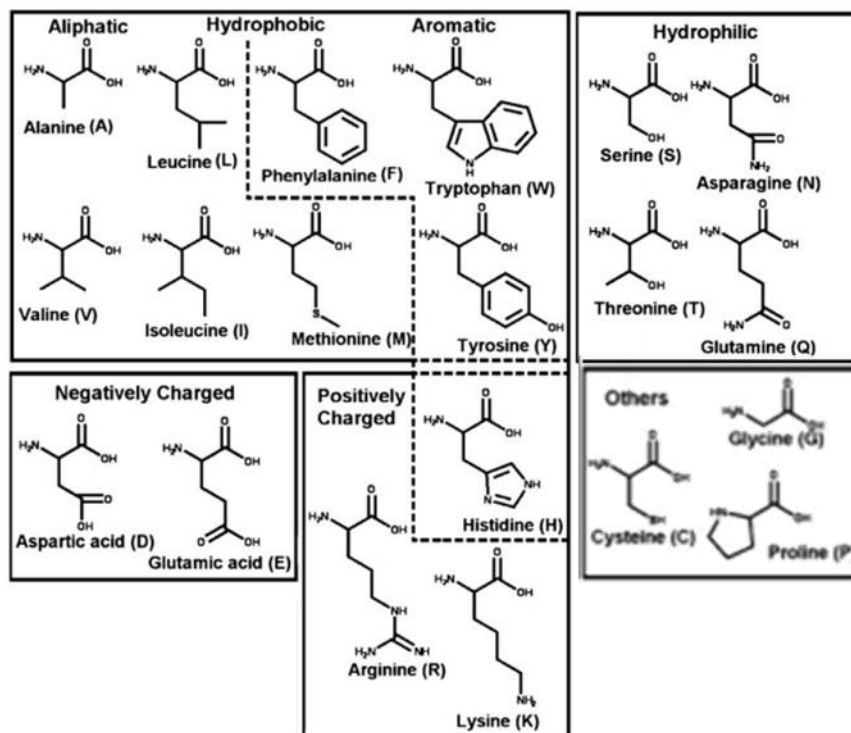


**Figure 1.9** Chemical structures of proteinogenic amino acids classified according to the nature of their side chains. (Adopted from R. V. Ulijn and A. M. Smith, *Chem. Soc. Rev.*, 2008, **37**, 664-675)

In this thesis, we will be focussing extensively on histidine utilising its multifaceted properties. Histidine is the most versatile amino acid of all the 20 amino acids found in nature due to its unique molecular structure and thus it plays various roles in protein architecture and bioactivities.<sup>30,31,32</sup> Histidine is composed of imidazole ring with an acidic ionization constant of  $pK_a = 6.5$  a coordinating ligand of metallic cations (for example,  $Ca^{2+}$  and  $Zn^{2+}$ ); and a hydrogen bond donor and acceptor. It exists in two protonation forms, neutral form and the protonated form and thus have complex molecular interactions.<sup>33</sup> (Figure 1.10) shows the functional group of histidine and its interaction functions along with optimised structures of histidine in neutral form A and in the protonated form B.

Histidine exhibits five types of interactions with the other amino acids and metallic cations of the proteins. 1. Cation- $\pi$  interaction- the imidazole ring of the histidine is aromatic and can take part in cation- $\pi$  interaction in by interacting with metallic cations or organic cations such as protonated amino acid  $Lys^+$  and  $Arg^+$ .<sup>34</sup> The protonated form of Histidine itself acts as a cation and interacts with other aromatic acids such as Phe, Tyr and Trp.<sup>35,36</sup> 2.  $\pi$ - $\pi$  stacking interaction- The imidazole structure of histidine side chain is a conjugative  $\pi$ -plane, which can make  $\pi$ - $\pi$  stacking interactions with the aromatic side chains of other amino acids such as Phe, Tyr, and Trp.<sup>37,38</sup> 3. Hydrogen- $\pi$  interaction- hydrogen- $\pi$  bond is formed between the polar hydrogen atom of histidine with other aromatic amino acids in 'T' orientation.<sup>39</sup> 4. Coordinate bond interaction- The basic nitrogen atom in the imidazole of histidine has a lone electron pair that make it a coordinate ligand of metallic cations, such as  $Zn^{2+}$  and  $Ca^{2+}$ .<sup>40</sup> 5. Hydrogen bond interaction- The polar hydrogen atom of the imidazole is a hydrogen-bond donor, and the basic nitrogen atom is a hydrogen-bond acceptor<sup>41,42</sup> (Figure 1.10).



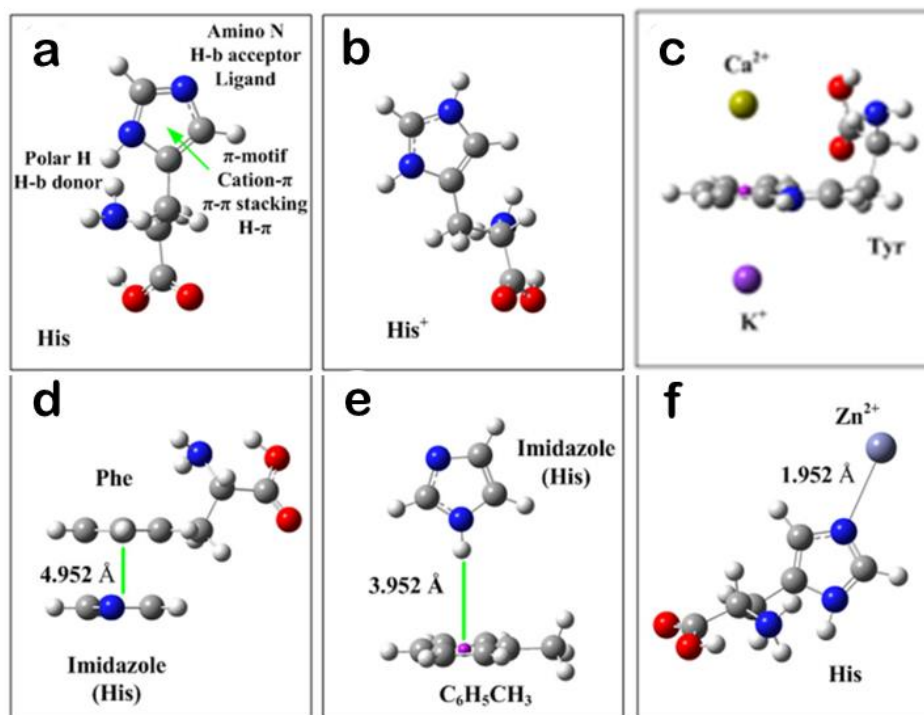


**Figure 1.10** Different interaction of histidine. (a) The optimized geometry and the forces of histidine (His) contributed in different interactions. (b) The optimized geometry of protonated histidine (His<sup>+</sup>). The protonated imidazole take part in electrostatic interactions or in the cation- $\pi$  interactions with aromatic moieties. (c) The structure of possible cation- $\pi$  interactions from either below or above the aromatic plane. (d) Parallel  $\pi$ - $\pi$  stacking interaction between phenylalanine and histidine (simplified as the imidazole). (e) The hydrogen- $\pi$  interaction structure formed between an aromatic system and polar hydrogen connected to nitrogen of imidazole and oriented perpendicularly to the  $\pi$ -plane. (f) The coordinate bonding between metallic cation and imidazole of histidine. (Adopted from S.-M. Liao, Q.-S. Du, J.-Z. Meng, Z.-W. Pang and R.-B. Huang, *Chem. Cent. J.*, 2013, 7, 44-44).

Due to the limitations of  $\alpha$ -amino acids in biomaterial  $\omega$ -amino acids can be used in exchange of  $\alpha$ -amino acids to construct bioactive peptide sequences as it confers more flexibility to the peptide backbone due to it having variable number of methylene units separating the two functional groups.<sup>43, 44</sup>  $\beta$ -Alanine ( $\beta$ -Ala),  $\gamma$ -amino butyric acid ( $\gamma$ -Abu), and  $\delta$ -amino valeric acid ( $\delta$ -Ava) are consecutive members of a homologous series of  $\omega$ -amino acid (Figure 1.11).  $\beta$ -Ala is the only naturally occurring  $\beta$ -amino acid with diverse biological function to play. It plays an important as a neurotransmitter in the visual system and binds with the receptor shared by the glycine and  $\gamma$ -amino butyric acid ( $\gamma$ -Abu).  $\beta$ -Ala is one of the



constituents of the naturally occurring dipeptides anserine ( $\beta$ -alanyl-N-methyl-L-histidine) and carnosine ( $\beta$ -alanyl-L-histidine).<sup>45-47</sup> Dipeptides anserine and carnosine are localised in the muscle cells which is innervated by the post-synaptic membrane and thus take part in transmission of nerve signals to the muscles and also have role to play in muscular metabolism. GABA also known as  $\gamma$ -amino butyric acid is an inhibitory neurotransmitter found in the mammalian brain.<sup>48, 49</sup> The proteolytic instability of the biomaterials can be enhanced by the incorporation of unusual amino acids (non-proteinaceous) such as  $\delta$ -Amino valeric acid ( $\delta$ -Ava) derived from rumen ciliate protozoa, in the bovine pancreatic trypsin inhibitor by substituting it with Gly-Gly segment, thus reducing the inhibiting tendency.<sup>50</sup> A very interesting and pivotal example of biologically active tripeptide GSH which is formed by the unusual peptide bond  $\gamma$ -peptide in place of the  $\alpha$ -peptide bond and is a potent antioxidant found in living system. The presence of the unusual peptide linkage in GSH makes it less susceptible to the peptidase degradation.<sup>51, 52</sup> Inspired by this tactics employed by nature many functional supramolecular systems have been designed with  $\omega$ -amino acids to achieve proteolytic stable biomaterials.<sup>53</sup> Moreover,  $\omega$ -amino acids containing large number of methylene units like 11-aminoundecanoic acid have been used to make flexible soft materials.<sup>54</sup>

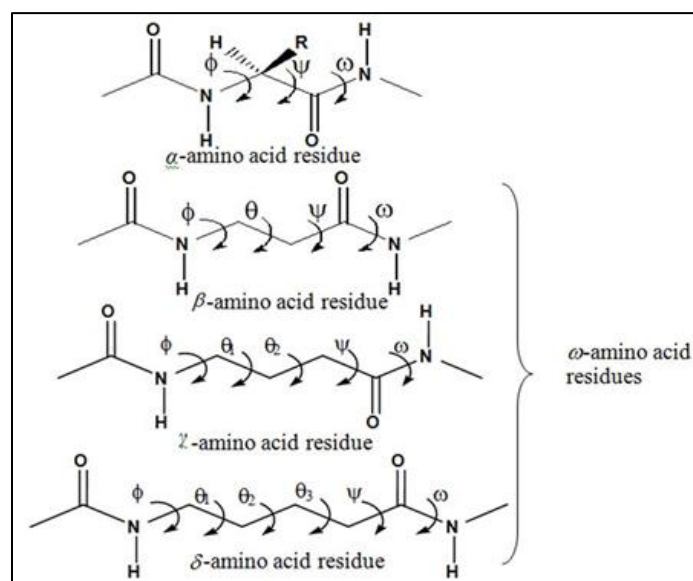


**Figure 1.11**  $\alpha$  and  $\omega$ -amino acid residues and their important torsional angles (adapted from A. Banerjee and P. Balaram, *Curr. Sci.*, 1997, **73**, 1067-1077).

Thus, we see, amino acids with various functional motifs are threaded together in a poly-peptide chain. The amide bond that is responsible for this covalent threading, is also unique because it contains a hydrogen bond donor group in terms of N-H and an acceptor in the form of C=O. Hence, polypeptide chains can form extensive intramolecular and intermolecular H-bonds to create higher order supramolecular structures known as secondary structures.

### 1.3.2. Secondary structures of peptides

The regular folding patterns along a peptide chain in a protein are known as secondary structures. Important, abundant and recognizable secondary structures found in proteins are helices,  $\beta$ -strands and reverse turns. The simplest form of two secondary and super-secondary structures common in all protein structures are  $\alpha$ -helix and  $\beta$ -sheet. Different variations of these basic structures give rise to more variation into peptide secondary structures, like parallel and anti-parallel  $\beta$ -sheets,  $\beta$ -turns, loops,  $3_{10}$  helix,  $\pi$ -helix and many other complex structural motifs including, helix-turn-helix,  $\beta$ -hairpin,  $\beta$ - $\alpha$ - $\beta$  and others.

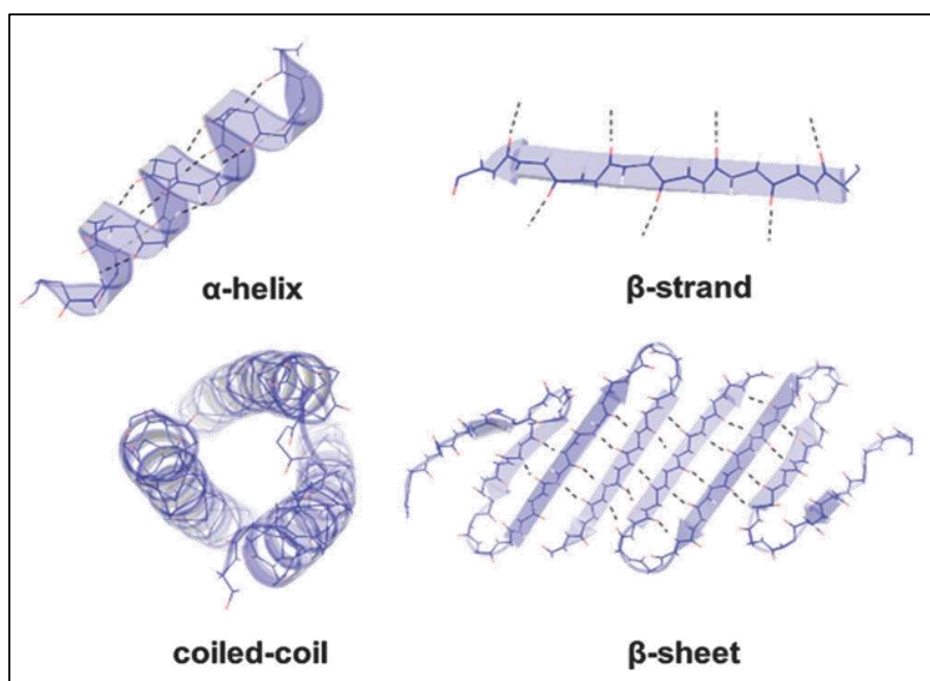


**Figure 1.12**  $\alpha$ -Helix and  $\beta$ -strand protein folding elements and their assembled states – coiled coils and  $\beta$ -sheets. Dotted lines indicate hydrogen bonds. (Adopted from E. De Santis and M. G. Ryadnov, *Chem. Soc. Rev.*, 2015, **44**, 8288-8300).

### 1.3.2.1. Alpha helices/coiled coils

$\alpha$ -helix is a right-handed helical structure adopted by the protein backbone. It is formed by the formation of hydrogen bonds between the C=O of one amino acid and the amide of  $i+4$  amino acid residues. (Figure 1.12) Thus, all the NH and C=O groups are joined together, except the first three NH groups and the last three C=O groups at the ends of the  $\alpha$  helix.<sup>55</sup>  $\alpha$  helices vary in length ranging from four to five to over 40 amino acid residues. The average length of  $\alpha$  helices is around 10 residues corresponding to the three helical turns. The  $\alpha$ -helices can be used for the purpose of self-assembly as components of coiled coils (Figure 1.12) which was first proposed by Pauling, Corey and Crick.<sup>56,57</sup> Coiled coil is made up of at least two helices with hydrophobic core buried inside. For the coiled coils to be a stable structure the first and fourth residues of the heptad should be hydrophobic. As such, aliphatic side chains (L, I, V) create a stripe down one face of the helix which is buried through the interactions with another helix to form the coiled coil also known as leucine zippers. Incorporation of hydrophilic residue in the hydrophobic core offers specificity. The fifth and seventh residues of the heptads are generally charged and helps in complementing the charge on the facing helix and also helps in bonding with another partner in a heterodimeric system. More intricate structures involving multiple helices in interaction with multiple neighbours is also reported. Classic example of coiled-coiled structure includes stimuli-responsive hydrogels made up of proteins having leucine zipper motifs.<sup>58</sup> Wilson and his co-workers designed a fibrous coiled-coil structure using sticky end assembly. All natural coils form blunt assemblies but SAF-p1 and SAF-p2 a heterodimeric parallel coiled coil has a staggered hydrophobic interface.<sup>59</sup> Thus, due to the staggering a peptide sticky end is available to participate in interacting with another peptide and promotes the structure along the long axis of the coiled-coil. Arginine residues were incorporated in the hydrophobic core of the SPF-p2 peptide to form salt bridge with the aspartic acid residue present in the coiled-coil interface.<sup>60</sup> The first example of the designed polar assembly system was studied using fluorophores and it was reported that at near equilibrium the self-assembly occurs in a polar fashion by addition of molecules to only end of the fibres.<sup>61</sup>

### 1.3.2.2. $\beta$ -sheets and $\beta$ -hairpins

$\beta$ -strands are the most predominant structural component of proteins after alpha helices. The  $\beta$  strand is generally composed of 5-10 residues and assumes conformational angles of  $\phi$ ,  $\psi$  angles close to  $-120^\circ$ ,  $140^\circ$ . They are located at the upper left quadrant of Ramachandran plot.<sup>62</sup> The two or more  $\beta$ -strands join together to form  $\beta$ -sheets which are formed by the interaction between the non-contiguous amino acids in the polypeptide chain, unlike  $\alpha$ -helix which is comprised of one contiguous segment of the chain.  $\beta$ -strands lack intra-segmental hydrogen bonds but use Hydrogen bonds to interact with the neighbouring  $\beta$ -strand and thus forms sheets (Figure 1.12) which run parallel or anti-parallel to each other. Pauling and Corey in 1950's identified parallel and antiparallel  $\beta$ -sheets.<sup>63</sup> The C=O of one strand forms hydrogen bonds with adjacent strand. The  $\beta$ -strand appears pleated because of the alternate positioning of the  $C\alpha$  atom above and below the plane of the  $\beta$ -sheets. The sidechains follow this pattern, pointing alternately above and below the  $\beta$  sheet structure. The amino acids in the aligned  $\beta$ -strands can run in the same direction to form the parallel  $\beta$ -pleated sheets or the amino acid residues in successive strands can run through in opposite direction to produce the antiparallel  $\beta$ -pleated sheets. Antiparallel  $\beta$ -sheets tends to be more stable intrinsically because of the presence of narrowly spaced Hydrogen bonds with maximum peptide bond dipole, that alternate with widely spaced ones. In the parallel  $\beta$ -sheets the evenly spaced hydrogen bonds bridges the  $\beta$  strands at an angle. Both parallel and anti-parallel  $\beta$ -sheets have all possible backbone hydrogen bonds barring the two outside strand of  $\beta$  sheets as they have only one neighbouring  $\beta$  strand each which may form hydrogen bonds with water molecules.  $\beta$ - sheets can be assembled into long fibrous protein structures as seen in neurodegenerative amyloid diseases such as Alzheimer's and Parkinson's disease.<sup>64</sup> the characteristic feature of most  $\beta$ -sheet include the alternating pattern of the hydrophobic and hydrophilic residues which upon being assembled into sheets gives rise to hydrophobic and hydrophilic faces. A fibrous system having a pattern of hydrophobic amino acids and complementary charges in between the peptides can be created and an example of such system is (RADA)<sub>4</sub>.<sup>65</sup>

The hydrogels made up of this peptide sequence has a very interesting property as reported by Zhang and his group that after subjecting the hydrogel to mechanical stress despite the destruction of the gross morphology the supramolecular structure remains intact as confirmed by comparing the circular dichroism data of before and after sonication.<sup>66</sup> Different types of hierarchical can be formed from  $\beta$ -sheet peptides, which have been classed as tapes, ribbons, fibrils and fibres, all of which vary in the number of sheets that pack together to form the final structure.<sup>67</sup> The organisation of these structures depend upon the peptide concentration as well as salt concentration and varies linearly with the peptide concentration for a given peptide sequence.<sup>68</sup>

$\beta$ -hairpins can be used as an alternate to  $\beta$ -sheets, they are made up of two short  $\beta$ -sheet sequences linked by a turn sequence.  $\beta$ -hairpins can be used to stack peptides in a manner so that they interact with each other which is sometimes unattainable in the  $\beta$ -sheets as they consist of repetitive amino acids sequence and hence have a tendency to be aligned out of order leaving no room for interaction with another peptide. The  $\beta$ -hairpins composed of natural amino acid can associate to form hydrogels at higher pH.<sup>69</sup>

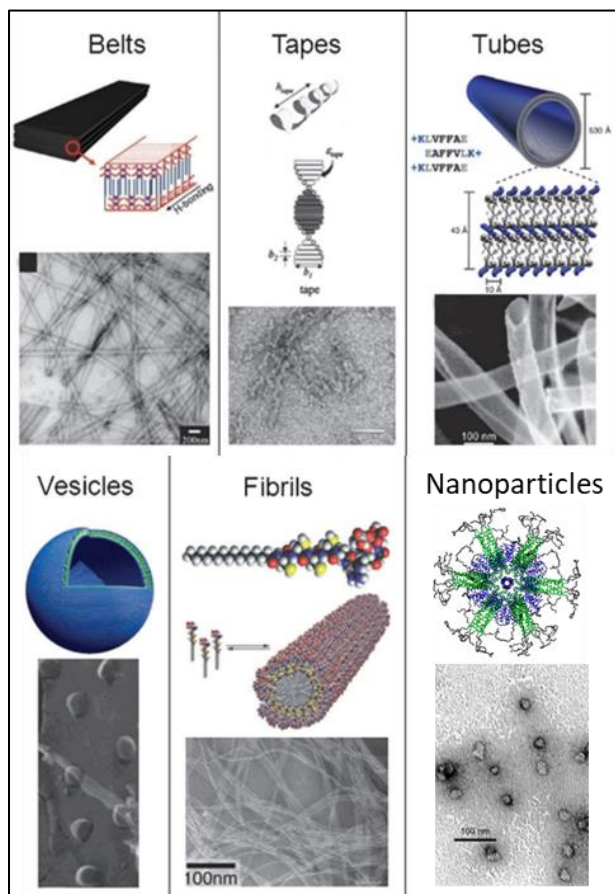


**Figure 1.13** Various nanostructures like nanobelts, nanotapes, nanotubes, vesicles, nanofibers and nanoparticles formed by peptide self-assembly are shown in both cartoon form as well as electron microscopic images. (Adopted from K. H. Smith, E. Tejeda-Montes, M. Poch and A. Mata, *Chem. Soc. Rev.*, 2011, **40**, 4563 and N. J. Sinha, M. G. Langenstein, D. J. Pochan, C. J. Kloxin and J. G. Saven, *Chem. Rev.*, 2021, **121**, 13915-13935).

### 1.3.3. Peptide nanostructures

The last couple of years witnessed remarkable growth in self-assembly field. Peptides and amino acid derivatives exhibit biocompatible, biodegradable, non-toxic and tunable properties which makes them an excellent choice as a molecular building block in synthesising various nanoscale structures. Various nanostructures including nanobelts, tapes, nanotubes, nanovesicles, nanorodes, nanofibrils and others (Figure 1.13) are obtained from the self-assembling amino acids and peptides and find variety of applications.<sup>70</sup>

### 1.3.3.1. Vesicles

Vesicles are bilayer, spherical, hollow assemblies constituted of amphiphilic molecules. Vesicles size can be fine tunes by altering the chain length and composition of the building blocks.<sup>71</sup> Hydrophobic domains are packed between the hydrophilic domains protruding in the outer environment as well as interacting with the inner aqueous environment and hence are capable of entrapping the hydrophilic molecules in the interior aqueous phase and the hydrophobic molecules in the hydrophobic part of the bilayer.<sup>72</sup> the hydrophobicity of the peptide tails determines the structure adopted by the peptide assembly- nanotubes or vesicles.

The peptide building blocks provides the prospect of designing vesicles highly sensitive to local environmental condition such as pH, redox potential, enzymes, or external stimulus such as ultrasound waves , light and magnetic field.<sup>73</sup> The example includes cationic vesicles derived from a polypeptide having a poly (L- glutamate) backbone and hydrophilic poly (2-aminoethyl methacrylate hydrochloride) PAMA. It is pH sensitive and is thus suitable to be used as delivery vehicle for genes and therapeutic drugs as the side chain is loaded with Doxorubicin hydrochloride (DOX.HCl) which releases the cargo upon pH change due to the protonation of PAMA side chains.<sup>74</sup> Poly(l-lysine hydrochloride)(PLL) and poly(gamma-benzyl-d7-l-glutamate) copolypeptides were also shown to form pH- and temperature-sensitive vesicles, when combined with pDNA.<sup>75</sup> In this case, the pDNA was partially condensed on the PLL phase and partially encapsulated inside the vesicle, resulting in an enhanced protection.

### 1.3.3.2. Micelles

Peptide-based micelles are closed monolayer structures consisting of hydrophobic inner core surrounded by a hydrophilic outer shell. They are used widely in the biomedicine domain and are prepared by the direct dissolution and solvent switch method. They are formed spontaneously above the critical micellar concentrations (CMC) and is temperature sensitive.<sup>76,77</sup>

Self-assembled peptide micelles can be used for diagnosis disease such as cancers. Example of such a self-assembled micelle that was used to detect cancer cells with

furin expression was an amphiphilic peptide RVRRRFFF coupled with nitrobenzoxadiazole fluorophore (NBD) as RVRRR serves as the cleavage site for furin.<sup>78</sup> The increase in fluorescence was noted when the C-3 micelle were taken up by the cancer cells and hence they can serve as early indicator of certain cancers.

Amphiphilic peptide-based conjugates made up of fibrin-binding peptide, CREKA, or a fluorescently labeled CREKA conjugate (Cy7-CREKA) like a cationic head group, a PEG<sub>2000</sub> spacer, and a 1,2-distearoyl-sn-glycero-3-phosphoethanolamine (DSPE) hydrophobic tail, formed micelles that served for theranostic systems in cancer such as glioblastoma and atherosclerosis.<sup>79, 80</sup>

### 1.3.3.3. Nanofibers and Nanobelts

Nanofibers are 5-20nm wide cylindrical structures with a length up to microns. They can be loaded with high amounts of bioactive molecules such as nucleic acid because of the high surface-to-volume ratio. Nanofibers are formed due to the self-assembly of ionic self-complementary peptides, collagen-triple helical peptides and amyloid peptides.<sup>81</sup> Secondary structures and side-chain interactions are vital in conferring stability to the nanofibers and thus can be tweaked to enhance the nanofiber formation. Amino-acids sequences are altered keeping in mind the hydrophobic-hydrophilic balance. Nanofibers composed of short amphiphilic peptides have more of hydrophobic amino acids such as Isoleucine (Ile) and their tendency to form of forming  $\beta$ -sheet structure.<sup>82</sup> Nanofiber assembly is also promoted by the collapse of hydrophobic alkyl chain. An amphiphilic peptide NH<sub>2</sub>-KIWFQNR-COOH with cationic residues at both the termini promotes the elongation of nanofibers by  $\beta$ -sheet pairing and  $\beta$ -stacking.<sup>83</sup> Gold nanocluster are incorporated in peptide based nanofibers (PNFs) to enhance their luminescence efficiency. The example of such PNF includes incorporation of HAuCl<sub>4</sub> in the amphiphilic peptide (RGDAEAKAEAKCCYYCCAEAKAEAKRGD), where the luminescence of AuNCs was augmented 70-fold.<sup>84</sup> PNFs can also be used as nanoprobe in magnetic resonance imaging (MRI) with the help of chelation of gadolinium ions.

Stupp and co-workers substantiated the formation of wide nanobelts having short alternating hydrophobic-hydrophilic peptide amphiphile and a flat structure. They can be conformed to produce twisted ribbons by altering the concentration of the



amphiphile. Stable  $\beta$ -sheets were also formed with only four amino acid residues by Stupp and his team.<sup>25</sup>

#### 1.3.3.4. Nanotubes

Nanotubes are three dimensional, highly ordered hollow cylinders made up of amphiphilic building blocks.<sup>85</sup> Peptide nanotubes (PNT) are versatile in nature as the head group can be manipulated to suit broad range of applications. The amino acids are present on the outer surface of the PNTs and the hydrophobic alkyl groups are oriented towards the core. The pH of the solution and the hydrophobicity of peptide monomers dictates the PNT formation and dimensions.<sup>86,87</sup>

Ghadiri and coworkers first designed the cyclic polypeptides that spontaneously self-assembled into long channel structure.<sup>88</sup> These channel structures had hydrophobic residues exposed on the outer surface and thus could attach lipid bilayer.<sup>88</sup> The cyclic cyclo-(d-Trp-Tyr) formed nanotubular assemblies in the presence of pDNA, mediating an enhanced in vitro and in vivo duodenal permeability for the pDNA. Thus projecting them as potential oral gene delivery system for the genetic treatment of diseases associated with duodenum, stomach, liver, and kidney.<sup>89</sup> The peptide-polymer or peptide-lipid hybrid nanotubes consisting of consist of a peptide core and a covalently attached polymeric or lipid coating have been extensively studied as promising nontoxic nanostructures for biomedical applications.<sup>90</sup>

### 1.4. Self-assembly of peptide-conjugated rylenediimides

$\pi$ - conjugated molecules have enjoyed increasing interests in the scientific community over the last couple of decades, owing to widespread applications of these molecules in chemistry and material sciences. Rylene dyes are a special class of  $\pi$ - conjugated organic molecule, built on the naphthalene framework. Their assembling patterns are sought after due to exciting optoelectronic properties. perylenediimides (PDIs) is one of the most extensively studied rylene dyes. In recent days, Naphthalenediimides (NDIs) which are the lowest possible homologues among the rylene dye family, have experienced heightened interest. Self-assembly of NDIs have been extensively utilized in the current research work.

## General Introduction

NDIs possess high electron affinity, good charge carrier mobility, and excellent thermal and oxidative stability, making them promising candidates for applications in organic electronics, photovoltaic devices, and flexible displays. Moreover, in terms of self-assembling capacity, high  $\pi$ -acidity and large  $\pi$ -surface area of these compounds, make them susceptible towards several stacking interactions. NDIs have also been extensively studied due to their potential real-world uses across a wide variety of applications including supramolecular chemistry, sensing, host-guest complexes for molecular switching devices, such as catenanes and rotaxanes, ion-channels, catalysis, and medicine and as non-fullerene accepters in solar cells.

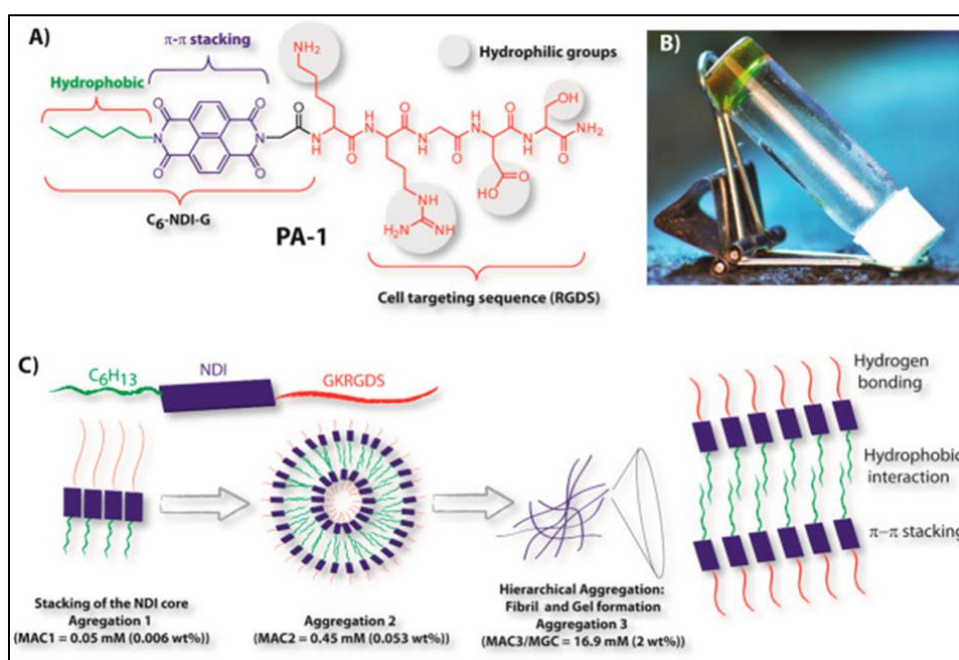


**Figure 1.14** An NDI-conjugated peptide amphiphile hydrogelator shows how its different component helps in gradual self-assembly to form final hydrogel. (a) Elucidation of structural role of each component in self-assembly, (b) Inverted vial image of the hydrogel, (c) Hierarchical assembly of the NDI-peptide amphiphile into nanofibers utilising non-covalent interactions. (Adopted from N. Singha, P. Gupta, B. Pramanik, S. Ahmed, A. Dasgupta, A. Ukil and D. Das, *Biomacromolecules*, 2017, **18**, 3630-3641).

Amino acid and peptides are among the most crucial self-assembling units due to their biocompatibility and mouldability. Another added advantage of using them is their capacity to produce hydrogen bonding interaction of amide units (CO-NH) and van der Waals interaction from the hydrophobic side chains of amino acids to form various well defined nanoarchitectures. Last two decades have experienced

surge of new peptide-based molecules being utilized as efficient biomaterials in the field of tissue engineering, cell culture, sensing and others.  $\pi$ -conjugated organic chromophoric molecules with covalently attached peptides have emerged as a very active area of research since last few years. Among the  $\pi$ -conjugated molecules, rylene dyes provide desired molecular properties such as  $\pi$ -acidity, planarity and excellent charge carrier mobility. To explore the self-assembling behavior of naphthalenedianhydride (NDA) /perylenedianhydride (PDA) in various solvent systems, amino acids or synthetic peptides have been covalently conjugated at the imide position of NDA/PDA to produce naphthalenediimides (NDI)/ perylenediimide (PDI) (Figure 1.14). The self-assembling nature of amino acid/peptide appended NDIs/PDI is the most important characteristic and it has the capability to form various well-defined self-organized nanostructures like nanofiber, nanotube, nanoribbon, nanosheet with tunable properties (Figure 1.14). These molecules self-assemble through hydrogen bonding interactions of amide (CO-NH), hydrophobic interaction of side chain of amino acid and  $\pi$ - $\pi$  interactions between NDA/PDA chromophore to form fluorescent aggregates or gel in different solvent systems with many interesting applications.

#### 1.4.1. Naphthalenediimides (NDIs) and nature of their self-assembly

While perylenediimide and the higher rylene analogues are proven candidates for opto-electronic material, Naphthalenediimide (NDI), the smallest possible homologue, has attracted scientists' attention until very recently. They are coveted for their outstanding optical properties. NDIs are a neutral, planar, redox-active, chemically robust, electron-deficient class of  $\pi$ -conjugated aromatic compound and they are capable of self-organization through  $\pi$ - $\pi$  stacking and they can be incorporated into larger multicomponent assemblies through intercalation and have been used for a variety of applications, ranging from biomedicine to electronics.<sup>91-93</sup> 1,4,5,8-naphthalenetetracarboxylic dianhydride (NDA) is main precursor for the synthesis of many different kinds of NDI derivatives and have significance for the production of industrially relevant Dyes Pigm..

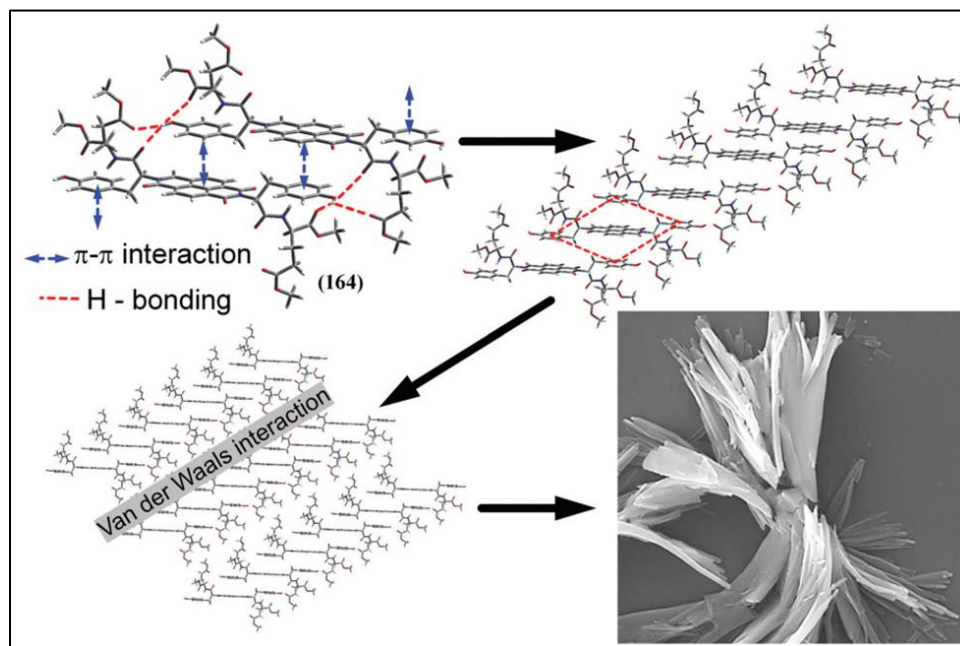


**Figure 1.15** An NDI-bola amphiphile containing peptide sequence of Tyrosine-Glutamic acid self-aggregates using  $\pi$ - $\pi$  interaction, H-bonding as well as Van der Waals interaction to form nanoflower architecture. The significance of all the non-covalent forces is elucidated from this example. (Adopted from S. P. Goskulwad, D. D. La, R. S. Bhosale, M. Al Kobaisi, L. A. Jones, S. V. Bhosale and S. V. Bhosale, *ChemistrySelect*, 2018, **3**, 1460–1465).

The moot point of utility of NDI is that various kinds of functional motifs can be incorporated through their imide positions. Moreover, the core positions of the naphthalene moiety can be further functionalized to synthesize electronically important materials. NDI-based molecules are generally soluble in moderately polar organic solvents such as chloroform, dichloromethane, tetrahydrofuran etc. The monomers absorb in the UV region of the absorption spectra, smaller than 400 nm. Functionalization with the long or branched alkyl chain or alkoxy (bolaamphiphiles) groups enhance their solubility in organic non-polar or polar solvents while the hydrophobic effect in the complementary polar or non-polar solvents respectively brings the aromatic monomer close to each other, promoting aromatic stacking.<sup>94, 95</sup> Substitution with alkyl and alkoxy based amphiphiles at naphthalenediimide are employed in the molecular design to tune their self-organization, whereas substituents containing  $\pi$ -cloud produce additional aromatic interactions (Figure 1.15). It should be noted that the functionalization *via* the diimide nitrogen yields naphthalenediimide which does not show fluorescence.

Thus, these compounds are not very useful in their monomeric state. Effective attempts have been made to overcome their low quantum yield, including functionalization in the core position and aggregation induced enhance emission (AIEE) of NDI based molecules. Tang and co-workers have introduced aggregation-induced enhanced emission (AIEE) strategy to increase the fluorescence quantum yield of chromophoric assemblies.<sup>96-98</sup> However, the AIEE phenomenon takes place on molecules which are not planar and has the freedom to undergo free-rotation about the bond connecting the chromophore and backbone moieties, like ethylene or silole. Aggregation restricts free rotation of these moieties thus blocks the non-radiative pathways and subsequently increase in fluorescence intensity takes place. Aggregation induced enhance emission of naphthalenediimide containing molecules is reported by various research group across the globe.

It should be noted that the naphthalenediimide emit depending on the way they pack in the aggregated state. Multiple non-covalent interactions, such as  $\pi$ - $\pi$  stacking, hydrogen bonding, and Van der Waals interaction dictates the nature of self-aggregation of the NDI based nano-architecture (Figure 1.15). It is commonly noted that the aggregated superstructures exhibit unique optical, electronic and charge-transport properties.<sup>99, 100</sup> A couple of forms are seen to be taken by NDIs or PDIs in self-assembled form, namely, H-type (face to face) and J-type (edge to edge) depending on the relative alignment of the transition dipole moments of adjacent molecules. These two states are primarily spectroscopic states. J aggregation shows a red shift of the maximum absorption band with respect to the monomer. Structurally, a head to tail arrangement of the associated molecules is observed with a longitudinal displacement. The H-aggregate, on the other hand, is characterized by a blue (hypsochromic) shift of the absorption maxima of the monomer. It can be understood that a parallel or side by side orientation of the stacked molecules is responsible for this kind of spectroscopic output.<sup>101</sup>

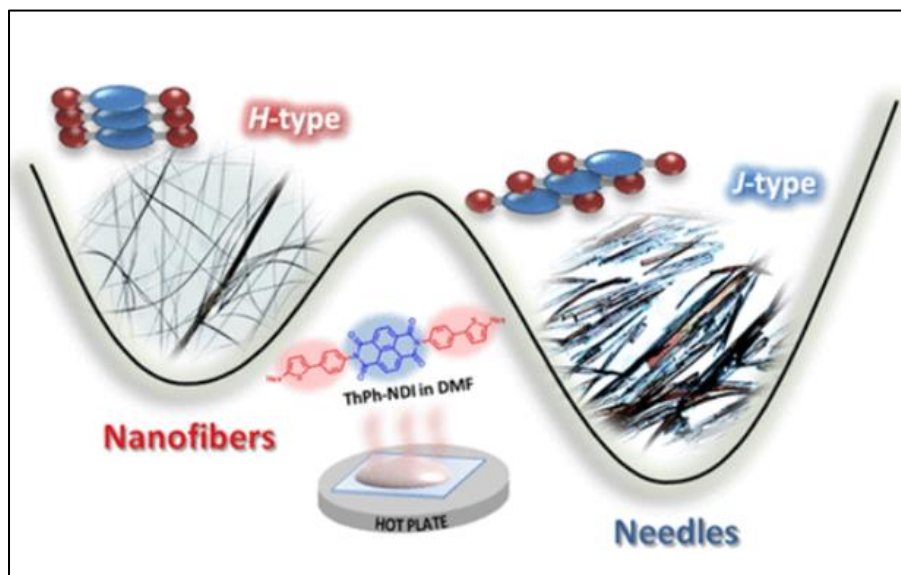


**Figure 1.16** Pictorial demonstration of formation of both J-aggregate and H-aggregate from a single monomer. H-aggregation is the kinetically trapped state and nanofiber morphology is obtained in this process whereas the thermodynamic product is a J-aggregation which finally leads to needle-like nanostructure. (Adopted from M. Zangoli, M. Gazzano, F. Monti, L. Maini, D. Gentili, A. Liscio, A. Zanelli, E. Salatelli, G. Gigli, M. Baroncini and F. Di Maria, *ACS Appl Mater Interfaces*, 2019, **11**, 16864–16871).

Maria and coworker have reported a phenyl-thiophene conjugated naphthalenediimide semiconductive material and the monomer is trapped two different kind of crystalline states by cleverly varying the physical conditions.<sup>102</sup> The solvent evaporation rate promotes the development of extremely elaborated hierarchical self-assembled structures. Slow solvent evaporation produces needle-shaped crystals (polymorph  $\alpha$ ) which forms through J aggregation and rapid solvent evaporation produces nanofibers (polymorph  $\beta$ ) with H aggregates (Figure 1.16).

#### 1.4.2. Anion- $\pi$ interaction

Anion-  $\pi$  interaction is a specific non-covalent interaction between the lone-pair electron of an anion and a electron deficient extended  $\pi$ -system having a strong positive quadrupole moment. Intuitively a repulsive interaction, establishment of this non-covalent force has been done on the early 21<sup>st</sup> century.



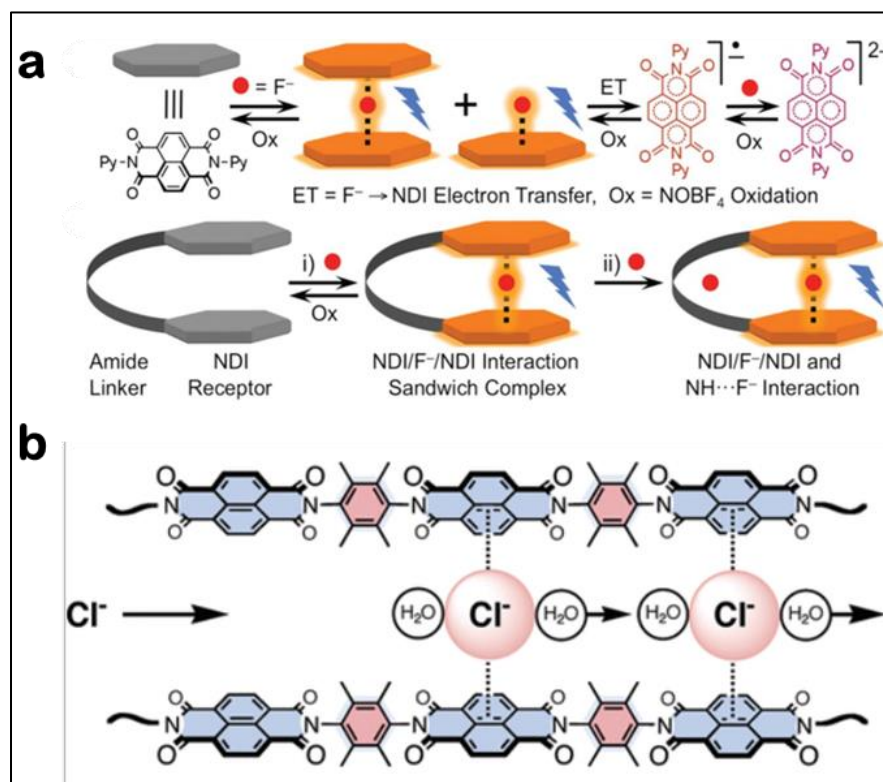


**Figure 1.17** (a) Graphical presentation of anion- $\pi$  interactions between  $F^-$  and NDI receptor. Step wise  $F^-$  recognition by preorganized NDI receptors through (i)  $\pi$ -anion- $\pi$  and (ii) H-bonding interactions (Adopted from S. Guha and S. Saha, *J. Am. Chem. Soc.*, 2010, **132**, 17674–17677). (b) Schematic representation of the NDI-based anion- $\pi$  slide for transmembrane anion transport (Adopted from V. Gorteau, G. Bollot, J. Mareda, A. Perez-Velasco and S. Matile, *J. Am. Chem. Soc.*, 2006, **128**, 14788-14789).

Saha and coworkers demonstrated an unprecedented example of a supramolecular anion- $\pi$  interaction involving fluoride ion and  $\pi$ -electron deficient colorless naphthalene diimide (NDI) receptors (Figure 1.17a).<sup>103</sup> Strong electronic interactions between lone-pair electrons of  $F^-$  ion and  $\pi^*$ -orbitals of the NDI unit produces an orange-colored  $NDI^{\cdot-}$  radical anion. Further addition of  $F^-$  ion creates pink colored NDI dianion. No such color change was noticed by the interaction of NDI receptor and other anions with  $F^-$ ,  $Cl^-$ ,  $Br^-$ ,  $I^-$ ,  $NO_2^-$ ,  $NO_3^-$ ,  $PF_6^-$ ,  $AcO^-$ , and  $H_2PO_4^-$  anions as tetra-*n*-butylammonium (TBA) salts. This study selectivity and sensitivity detects the  $F^-$  ion at nM concentration in 85:15 DMSO/ $H_2O$  solutions over the other anions.<sup>103</sup> Matile and coworkers were able to put the NDI-system to work in a biomimetic application. They designed a series of shape-persistent oligo-naphthalenediimides and proved their suitability for chloride- selective

transmembrane transport by multi-ion hopping (Figure 1.17b). This phenomenon is possible due to “anion–p slides” which depends on the design of the end groups of these oligo-naphthalenediimide systems.<sup>104</sup>

### 1.4.3. Amino acid-tethered naphthalenediimide aggregates

Gavindraju and coworkers successfully demonstrated the chirality transcription and enhancement by employing the homochiral and heterochiral peptide conjugates of NDI derivative (Figure 1.18). The homochiral moieties showed 1D fibrous aggregate with opposite chirality, whereas the heterochiral moieties show zero-dimensional organization.<sup>105</sup> Banerjee and coworkers reported a peptide appended naphthalene diimide (NDI) based molecule that self-assembles to form a fluorescent J-aggregates in aqueous media and showed a remarkable yellow fluorescence in solid state (Figure 1.18a). Interestingly, that molecule showed H<sup>+</sup> ion concentration-dependent change in the emission property in aqueous medium. These properties of the molecule can be used for development of authentication tools for security purposes as a rewritable fluorescence color code.<sup>106</sup> In another report they described a synthetic peptide-based NDI molecule that was found to form fluorescent H-aggregated species in the self-assembled state in a chloroform and methylcyclohexane mixture (Figure 1.18b). The computational study proved that the transition from S<sub>2</sub> (second excited state) to S<sub>0</sub> (ground energy state) is responsible for the fluorescence as S<sub>1</sub> is a dark state.<sup>107</sup>

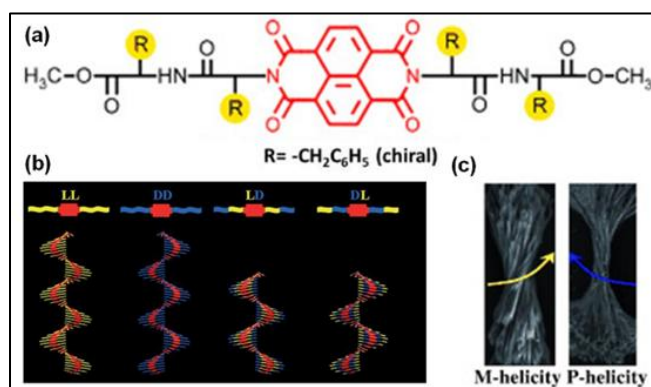


**Figure 1.18** (a) Molecular structures of homochiral (LL and DD), heterochiral (LD and DL) peptide conjugates of NDIs. (b) Schematic representation of left-handed (LL and LD) and right-handed (DD and DL) chiral supramolecular assemblies. (c) FE-SEM images of self-assembled structures of homochiral peptide conjugates of NDIs LL (left) and DD



(right) formed in water/DMSO (85:15) (Adopted from M. Pandeewar, M. B. Avinash and T. Govindaraju, *Chem - A Eur J*, 2012, **18**, 4818–4822)

Lin and coworkers have reported the first example of the NDI-containing hydrogelators without aromatic rings in the side chains of amino acids, and this indicates the aromatic amino acid residue is not a necessary component for the structural design of NDI-capped small molecule hydrogelators.<sup>108</sup> They suggested that the combination of equimolar ratio of NDI-Serine and NDI-Lysine can be used to promote the formation of a supramolecular hydrogel (Figure 1.19a). Using this approach, the cell viability ratios of newly discovered hydrogelators can also be improved compared with those of NDI-dipeptides.

Parquette and co-workers reported an Fmoc functionalized NDI derivative that formed antiparallel  $\beta$ -sheet structure (Figure 1.19c). The intermolecular  $\pi$ - $\pi$  interaction of the NDI and fluorene units facilitated the dimer formation and flat nanobelt assemblies and thereby resulted in the formation of hydrogels.<sup>109</sup>

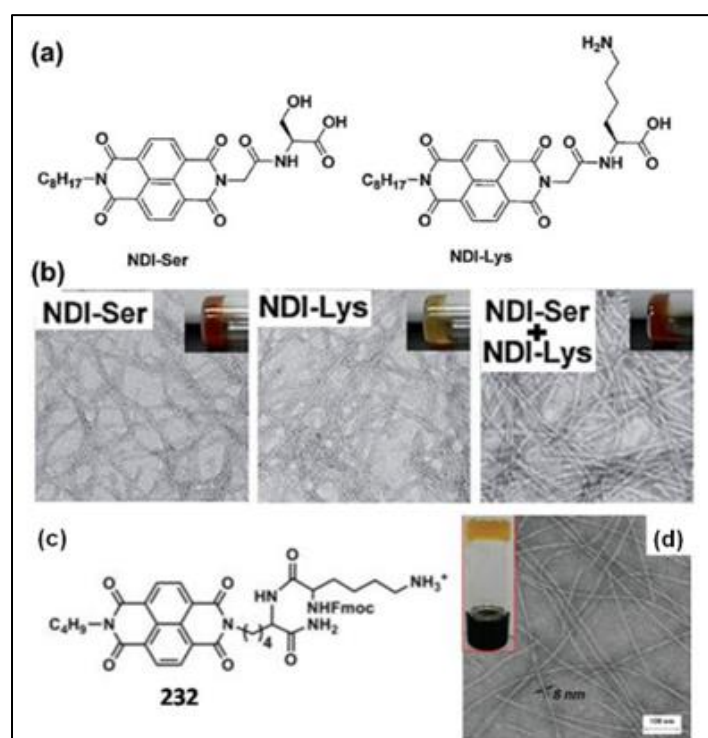


**Figure 1.19** (a) Chemical structures of NDI-Ser and NDI-Lys. (b) image of self-supportive hydrogel (in inset) and negative stained TEM images of NDI-Ser, NDI-Lys and NDI-Ser + NDI-Lys (1:1). (Adopted from L. -H. Hsu, S. -M. Hsu, F. -Y. Wu, Y. -H. Liu, S. R. Nelli, M. - Y. Yeh and H. -C. Lin, *RSC Adv.*, 2015, **5**, 20410-20413). (c) Structure of the dipeptide-NDI gelator (d) The TEM image of nanobelts formed by the gelator 232 in water;

*inset shows the hydrogel (Adopted from H. Shao, J. R. Parquette, Chem. Commun., 2010, 4285).*

Banerjee and co-workers reported a fluorescent hydrogel derived from peptide appended naphthalene diimide bola-amphiphile (P) and primary amines with long alkyl chains at physiological pH 7.46 (Figure 1.21a). NDI-containing peptide amphiphile alone does not form gel in aqueous medium. However, the NDI molecule forms two component yellow fluorescent J-aggregate in aqueous medium in the presence of long alkyl chains primary amines with the molar ratio of NDI: long chain amine 1:2. Moreover, these two-component hydrogel exhibits good semiconducting behavior in their respective co-assembled states.<sup>110</sup>

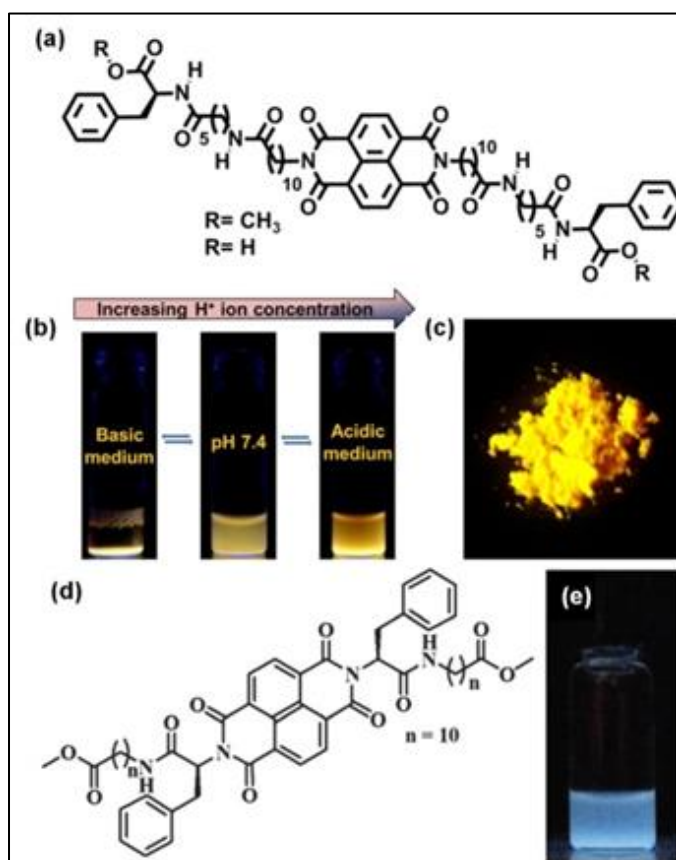


**Figure 1.20** (a) Chemical structure of peptide appended NDIs. (b) Photographs of compound ( $R=H$ ) in phosphate buffer solution pH 7.4, under acidic and basic conditions under UV light ( $\lambda_{max} 365$  nm). (c) Solid state fluorescence of the NDI ( $R=H$ ) obtained from the same buffer solution (Adopted from S. Basak, N. Nandi, S. Paul and A. Banerjee, *ACS Omega*, 2018, **3**, 2174–2182). (d) Chemical structure of peptide appended NDI. (e) Photograph of this molecule in  $CHCl_3$ : MCH = 10: 90 solvent mixture under UV light (365 nm) (Adopted from S. Basak, N. Nandi, K. Bhattacharyya, A. Datta and A. Banerjee, *PhysChemChemPhys*, 2015, **17**, 30398–30403)

The same research group also reported a morphology dependent modulation of semiconducting property of a dipeptide appended naphthalenediimide. The NDI molecule is self-assembled to form soluble aggregate with nano-vesicular structures in aqueous phosphate buffer medium of pH 7.5. Interestingly, the molecule form hydrogels with nanofibrillar network structure in the presence of glucono- $\delta$ -lactone at pH 4.7 or  $\text{Ru}^{3+}$  solution at pH 4.6. The soluble aggregates and glucono- $\delta$ -lactone based hydrogel were found to form J-aggregates with greenish blue fluorescence (Figure 1.21b). The soluble aggregates and both gels showed magnificent current conduction and photoswitching properties. The photoconductivity and photocurrent gain in the GDL and  $\text{Ru}^{3+}$  mediated gels were several orders higher than NDI soluble aggregate.<sup>111</sup>

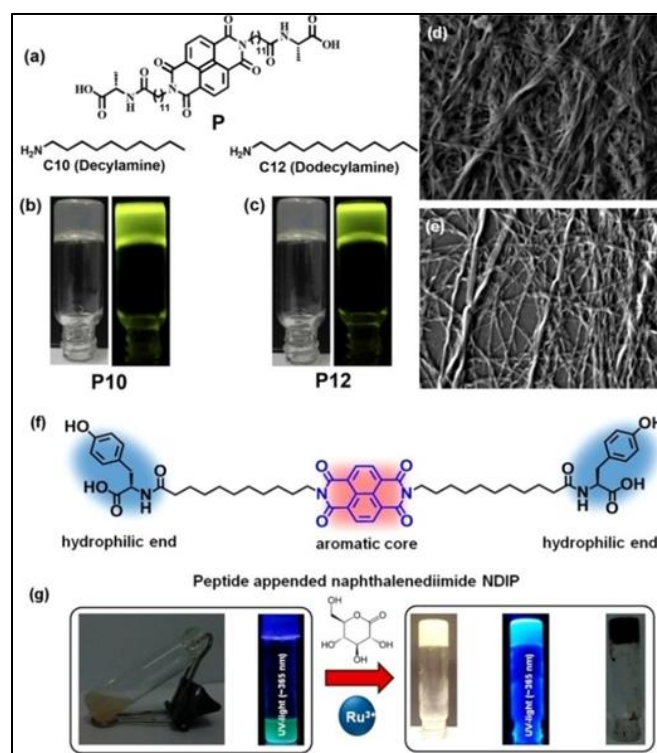


**Figure 1.21** (a) Chemical structures NDI bolamphiphile (P), decylamine (C10) and dodecylamine (C12). (b and c) Photographs of two-component hydrogels with C10 and C12 at a molar ratio 1:2. FE-SEM images of the two component hydrogels in presence of (d) P10 and (e) P12. (f) Chemical structure of the NDIP. (Adopted from N. Nandi, S. Basak, S. Kirkham, I. W. Hamley and A. Banerjee, *Langmuir*, 2016, **32**, 13226–13233) (g) The NDI molecule forms fluorescent aggregates at pH 7.5 buffer medium which turns into gels upon addition of in situ acid generator GDL and metal ions. (Adopted from K. Basu, B.

Mondal, A. Das Mahapatra, N. Nandi, D. Basak and A. Banerjee, *J. Phys. Chem. C*, 2019, **123**, 20558–20566)

Banerjee's group have reported an aggregation induced drastic change in the emission and gel formation of appended peptide based self-assembled molecule depending on the solvent composition (chloroform: methylcyclohexane). The gelator peptide NF (Figure 1.22) shows an interesting property called antisolvent gelation in the mixed solvent system, i. e., the molecule itself exhibits very feeble fluorescence in solution state, while it emits a bright yellow color in the aggregated gel state in the chloroform and methylcyclohexane mixture (Figure 1.22). UV-vis and fluorescence spectroscopic data suggest the presence of J-type aggregates in the self-assembled state and the gel also shows an excellent semiconducting behavior.<sup>112</sup>

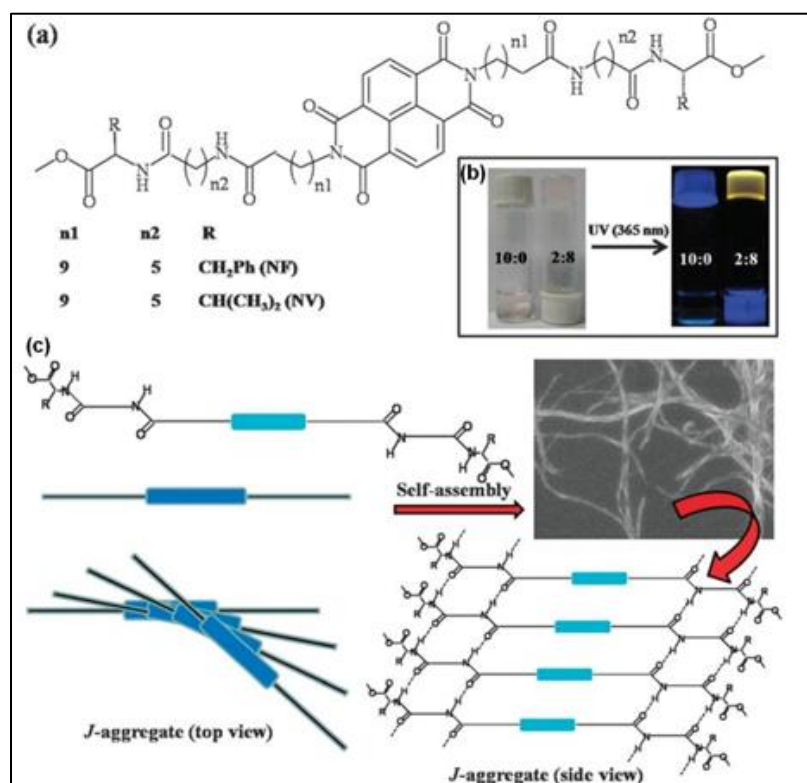


**Figure 1.22** (a) Chemical structure of monomer NF. (b) Photographs of NF in pure chloroform and in gel state in the chloroform and MCH mixture (2:8) in daylight and under UV light. (c) A probable self-assembled packing model of NF (Adopted from S. Basak, J. Nanda and A. Banerjee, *Chem. Commun.*, 2013, **49**, 6891-6893).

Ulijn and co-workers reported a biocatalytic self-assembly of NDI based acceptors and various di-alkoxy/hydroxyl-naphthalene (DAN/DHN) donors into two-component 1D chiral charge-transfer nanofibers in aqueous medium that ultimately leads to a gel formation (Figure 1.23).<sup>113</sup> They showed thermolysin-catalyzed condensation to form NDI conjugated dipeptide acceptor that was further assembled with a donor to form enhanced long-range charge-transfer complex in gel state. The presence of the catalyst in the system ensured that any disruption of the system through external factors can be dynamically corrected through the fully reversible nature of this system.

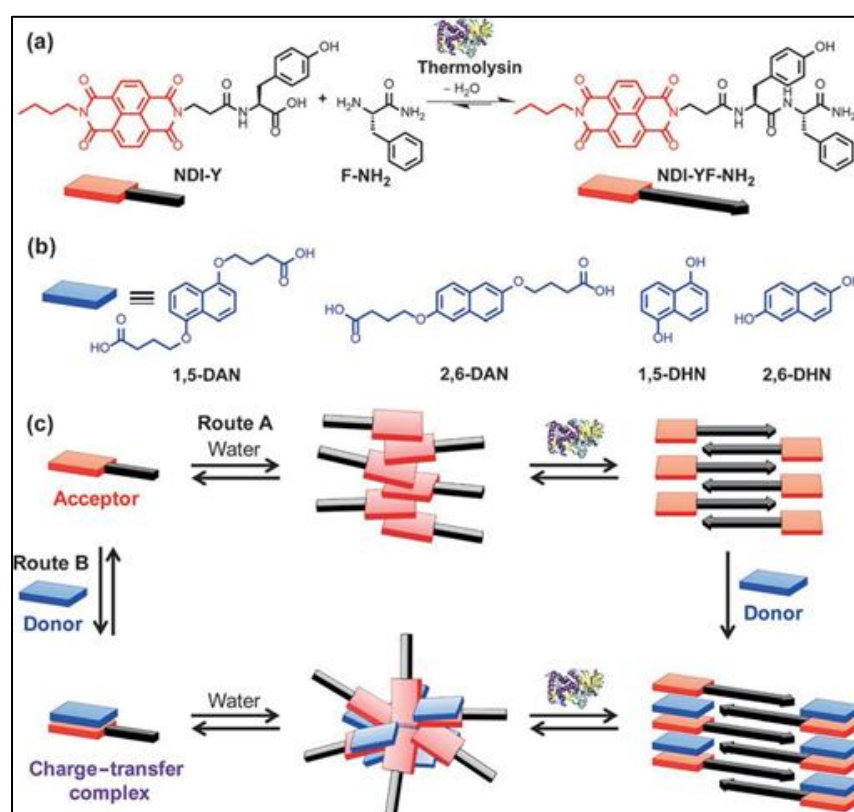


**Figure 1.23** (a) Thermolysin-catalyzed condensation of NDI-dipeptide conjugate. (b) Molecular structures of various DAN/DHN donors. (c) Schematic illustration of differential supramolecular organization in the presence and absence of various DAN/DHN donors. (Adopted from S. K. M. Nalluri, C. Berdugo, N. Javid, P. W. J. M. Frederix and R. V. Ulijn, *Angew. Chem. Int. Ed.*, 2014, **53**, 5882-5887).

Ardoña et. al. reported a multi-chromophoric hydrogelator system by combining three distinct  $\pi$ -electron units (oligo(p-phenylenevinylene, OPV), quater-



thiophene, and NDI) within peptidic 1-D nanostructures to create localized energy gradients in aqueous environments (Figure 1.24).<sup>114</sup> The combination of photonic donor–acceptor pair and electron donor-acceptor pair within one nanostructure enables potentially simultaneous and/or sequential energy- and electron-transfer events and it allows for the creation of localized electric fields between the donor and acceptor units that result from charge separation. Using this strategy, the kinetics of the assembly and the degree of self-sorting could be varied through the choice of the assembly trigger, which changes the kinetics of acidification. The hydrolysis of glucono- $\delta$ -lactone (GdL) provides a slow pH drop that allows for stepwise triggering of peptide components into essentially self-sorted nanostructures based on subtle pKa differences, whereas HCl addition leads to a rapid formation of mixed components within a nanostructure.

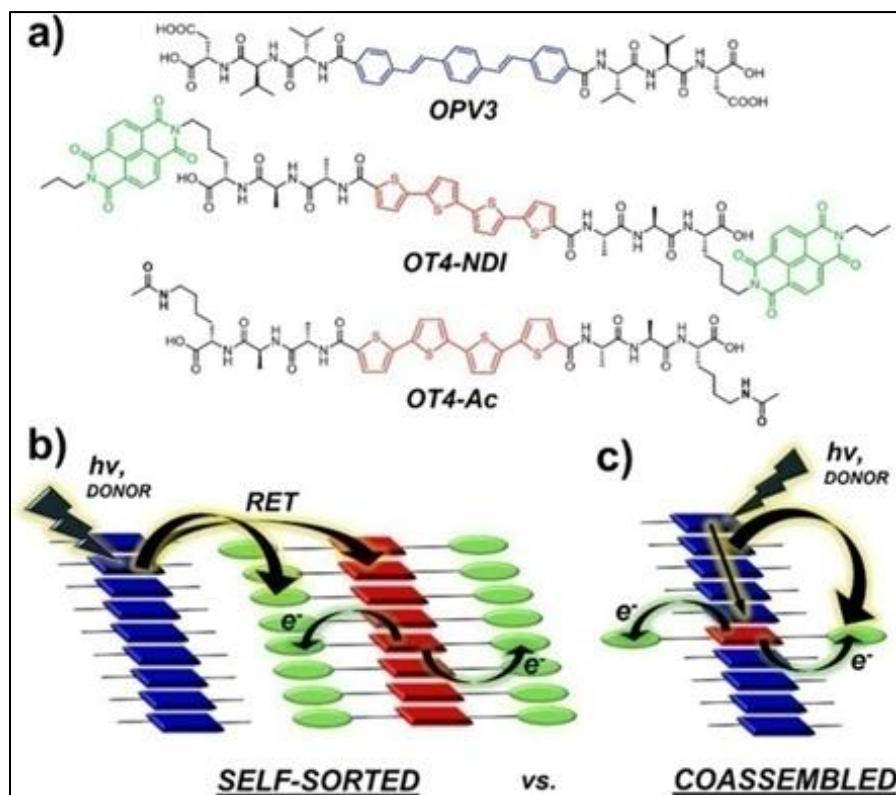


**Figure 1.24** (a) Molecular structures of OPV, quarter-thiophene and NDI conjugated peptides. (b) and (c) diagrams of resonance-energy transfer (RET) and electron-transfer within a two-component peptidic nanostructure with three  $\pi$ -electron units (Adopted from H. A. M. Ardoña, E. R. Draper, F. Citossi, M. Wallace, L. C. Serpell, D. J. Adams and J. D. Tovar, *J. Am. Chem. Soc.*, 2017, **139**, 8685-8692).

Singha et. al. reported asymmetric NDI-capped peptide based amphiphile that forms hydrogel (Figure 1.25) following a three-step aggregation mechanism involving  $\pi$ - $\pi$  stacking, hydrophobic interactions, and hydrogen bonding.<sup>115</sup> They have noticed that extremely smaller aggregates with low population of the molecules were formed at a very low concentration, followed by spherical aggregates with increasing concentration, and eventually further hierarchical aggregation leads to the formation of fibrous network. The compound showed stronger aggregation upon increasing the pH of the solution and using this approach, they were able to exploit this property to determine the pH at different cellular locations.

Liu and coworkers have designed a chiral dipeptide substituted naphthalenediimide and investigated its radical formation abilities as well as the circularly polarized luminescence (CPL) activity. The chiral dipeptide form two enantiomeric molecules termed L-NDI-GE or D-NDI-GE upon conjugation with NDI unit. The compounds formed gels in methanol or mixed DMF/water systems. Interestingly, upon irradiation with UV light the gel formed  $\text{NDI}^{\cdot-}$  radical anions and both neutral and radical anion gels showed CD and CPL (Figure 1.25). The neutral assemblies exhibited the luminescence dissymmetry factor  $g_{lum}$  in the order of  $10^{-3}$  whereas the radical anion showed  $g_{lum}$  enhanced by 2 orders of magnitude to  $10^{-1}$ .<sup>116</sup>



**Figure 1.25** Graphical presentation for the formation of  $\text{NDI}\bullet^-$  radical anions. The L-NDI-GE forms the organogel by molecular self-assembly and it emit left-handed CPL; enhancing and reversing the CPL of L-NDI-GE organogel upon formation  $\text{NDI}\bullet^-$  radical anions by UV irradiation. (Adopted from Y. Wang, Y. Jiang, X. Zhu and M. Liu, *J. Phys. Chem. Lett.*, 2019, **10**, 5861–5867)

### 1.5. Soft materials

Pierre-Gilles de Gennes in 1970s first described the term ‘Soft matter’ and hence is regarded as the father of the soft matter.<sup>117</sup> Soft materials can be defined as the substance having physical state intermediate of solid and liquid. The physical state of these materials is heavily influenced by the external stimuli such as temperature, pressure, applied electric or magnetic field.

Soft materials are an integral part of our lives and as most of the biological matter belong to the soft matter category such as the cell membrane which helps in maintaining the integrity of the cell and carries out vital functions at physiological level. It includes gels, polymers, liquid crystals, colloids, foams and granular material (Figure 1.26). Soft materials have unique feature of both solid and liquid states and it exhibits fluidity and mobility of liquids and long-range order of solids. One of the most common examples of our day-to-day life soft material is Liquid Crystal Display (LCD) which is in the intermediate of liquid and crystalline state that renders it the unique property. Colloids can also be classified as soft materials (Figure 1.26); they are a dispersion medium in which dispersed particles remains in a continuous phase. examples of such a medium includes blood, paint, butter, milk etc.



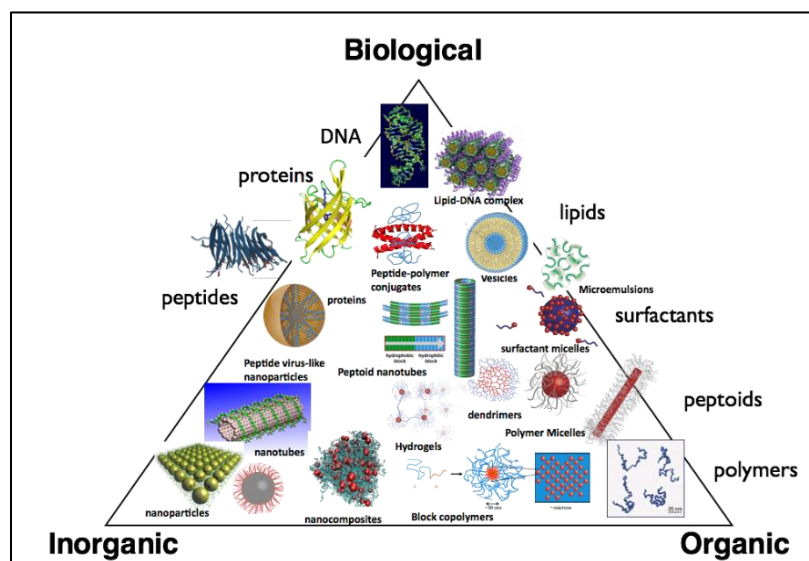


*Figure 1.26 Graphics elaborating diversity of soft materials arranged in a triangular arrangement where the three extremes are biological, inorganic and organic materials. (Adopted from website of University of Oslo Bio<sup>3</sup>)*

## 1.6. Functional soft materials- Supramolecular gels

Supramolecular gels are hard to be defined as they comprise of various types of materials. Dr. Dorothy himself stated that the “colloidal condition, the “gel”, easier to recognize than to define”.<sup>118</sup> Gels are formed when molecules with certain structural features self-assemble in a solvent and to form supramolecular assemblies which immobilizes the entire solvent. Gels are composed of two components a gelator in small quantity and a fluid component. In the past decade, gels have been extensively studied due to their wide applications in the field of Material Sciences.<sup>119</sup> Industries such as that of cosmetic, oil and technology, food, textile and healthcare exploits gels. They are also utilized in optoelectronics, hybrid materials, tissue engineering as well as regenerative medicines (Figure 1.27).

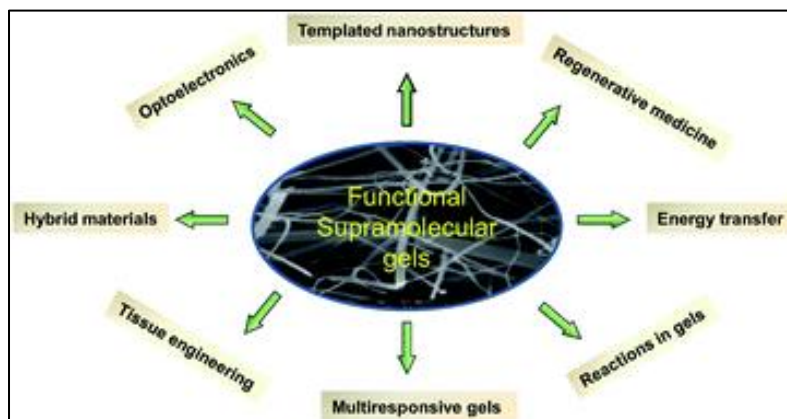


**Figure 1.27** Supramolecular gels can show various functionality like their role in regenerative medicine, catalysis, optoelectronics etc. (Adopted from S. Banerjee, R. K. Das and U. Maitra, *J. Mater. Chem.*, 2009, **19**, 6649-6687).

Low molecular weight gelator (LMWG) discovered in the early nineteenth century have been extensively studied in recent times. LMWG are stabilized by the non-covalent interactions like hydrogen bond,  $\pi$ - $\pi$  interaction, hydrophobic interaction and ionic interaction which are sensitive to external stimuli like pH, heat and mechanical force. Hence, there exist a dynamic equilibrium in between the sol-gel and gel-sol transformations of a supramolecular gels. This is advantageous to these gels and is not reported in case of polymer gels.<sup>120</sup> Although low molecular weight organogels are often seemed to be underrated in comparison to their aqueous counterpart in terms of applications, these gels are not only 'smart materials', but are versatile and have plentiful applications. Ajayaghosh and his co-workers first developed oligo-p-phenylenevinylene (OPV) containing  $\pi$ -organogelators via cooperative effect of H-bonding and  $\pi$ -stacking. This low molecular weight organogelators forms self-supporting soft-solid in aliphatic hydrocarbon solvents such as hexane, decane, dodecane, cyclohexane, petrol, diesel, and kerosene, when dissolved in small quantities (<2 mM) at room temperature.<sup>121</sup>

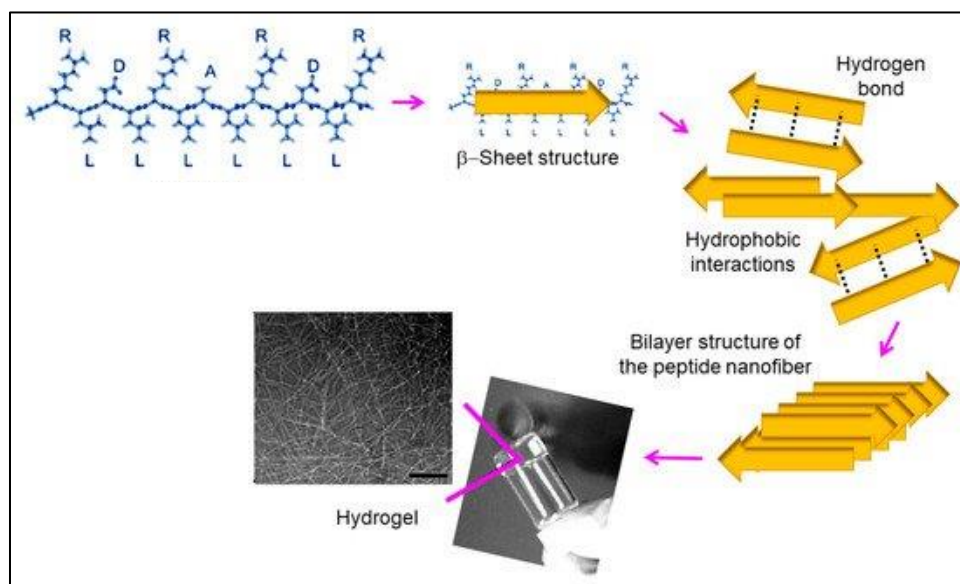


**Figure 1.28** 10 Schematic showing the assembly pattern from molecular level to macroscopic level during gelation. The process can affect all levels of the assembly. The molecular structure can be changed but the emergent phenomena resulting from those changes have been so far difficult to predict and control. The step-by-step processes of non-covalent interaction finally forms self-supporting gel consisting of nanofibrous morphology. (Adopted from J. Tsukamoto, K. Naruse, Y. Nagai, S. Kan, N. Nakamura, M. Hata, M. Omi, T. Hayashi, T. Kawai and T. Matsubara, *Tissue Eng. Part A*, 2017, **23**, 1394-1402).

The formation of gels occurs through a network of fibers which begins by the self-assembly of individual molecules. One-dimensional non-covalent attractive forces such as the hydrogen-bonding and  $\pi$ -stacking interactions are the driving force and the formed nanostructures should facilitate the fabrication of the one-dimensional fibers. In aqueous environment the driving force is the hydrophobic interaction. The next step is the cross-linking of the fibers due to entanglement and branching. These cross-links have non-covalent features which renders reversibility to the supramolecular gels.

### 1.6.1. Classification of gels

The classification of gels can be done in several ways based on origin, the nature of the gelator, the solvent and the interactions that are in play as the driving force behind gelation. The classification of gels is given below (Figure 1.29).

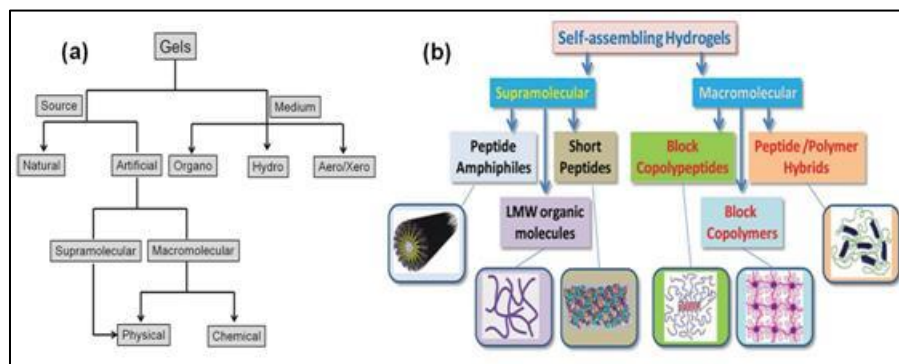


**Figure 1.29** (a) Classification of gels (adopted from N. M. Sangeetha and U. Maitra, *Chem. Soc. Rev.*, 2005, **34**, 821) and (b) classification of self-assembling hydrogels (adopted from C. Chassenieux and C. Tsitsilianis, *Soft Matter*, 2016, **12**, 1344–1359).

One of the primary classes of gels is organogels which entrap organic solvent inside its solid network. There are many types of organogels produces such as benzylidene protected sugar-based organogelators which selectively gels the oil phase from the oil-water mixture at room temperature and hence can be used for oil-spill remediation for marine entity.<sup>122</sup> Maitra and his co-workers have synthesized cholesterol based hydrogels as cholesterol acts as an excellent gelator due to its hydrophobic core. These gels were not sensitive to the external stimulus change despite bearing cationic character.<sup>123</sup> Upon comparison with the natural anionic bile salts it was found that the critical aggregation concentration was lower as compared to the bile salt aggregates. Maitra and his group also synthesized luminescent based hydrogels having lanthanide (III) cholates (Figure 1.30) and upon being dried to a xerogel it did not lose its fluorescent character. It is used as a luminescent coating on a glass surface.



**Figure 1.30** (a) Photographs of Lanthanide (III) cholate gels under UV irradiation of 365 nm (from left to right): Eu(III) cholate (5/15 mM) doped with 6mM pyrene, Tb(III) cholate (5/15 mM), Tb(III)–Eu(III) cholate (4.9/0.1/15 mM) and Tb(III)–Eu(III) cholate (4/1/15 mM).

*mM) all doped with 400mM DHN. Photographs of the thin films drop cast from the suspensions of xerogels under UV irradiation of 365 nm of (b) Tb(III) cholate (5/15 mM), (c) Tb(III) cholate (5/15 mM) + 400 mM DHN, (d) Tb(III)–Eu(III) cholate (4/1/15 mM) + 400mM DHN and (e) Eu(III) cholate (5/15 mM) + 6mM pyrene [DHN-2,3-dihydroxynaphthalene] (Adapted from S. Banerjee, R. Kandanelli, S. Bhowmik and U. Maitra, *Soft Matter*, 2011, 7, 8207–8215)*

The other type of gels are hydrogels which hold water inside the gel network. Unlike the conventional polymeric hydrogels that are mainly based on covalently cross-linked networks of polymers (i.e., gellant), the networks in supramolecular hydrogels are formed due to non-covalent interactions between the hydrogelator. Considering that water is the unique solvent to maintain life forms on earth, it is important and necessary to distinguish water from organic solvents. Because supramolecular hydrogels are a type of relatively simple heterogeneous system that consists of a large amount of water, it is not surprising that the applications of hydrogels and hydrogelator in life science have advanced most significantly.<sup>39</sup> Several small organic molecules form hydrogels in aqueous medium. Some of them are discussed below.

Banerjee and his research group have reported a hydrogelator where they performed the derivatization of perylene bisimide core with L-tyrosine (Figure 1.31). The hydrogelator self-assemble to form a gel which is responsive to pH changes and semiconducting in nature. The hydrogel exhibited excellent photo-switching behavior and therefore can be applied as a soft photodetector.<sup>124</sup> This work demonstrate how hydrogels too can be utilized in photovoltaic activities.

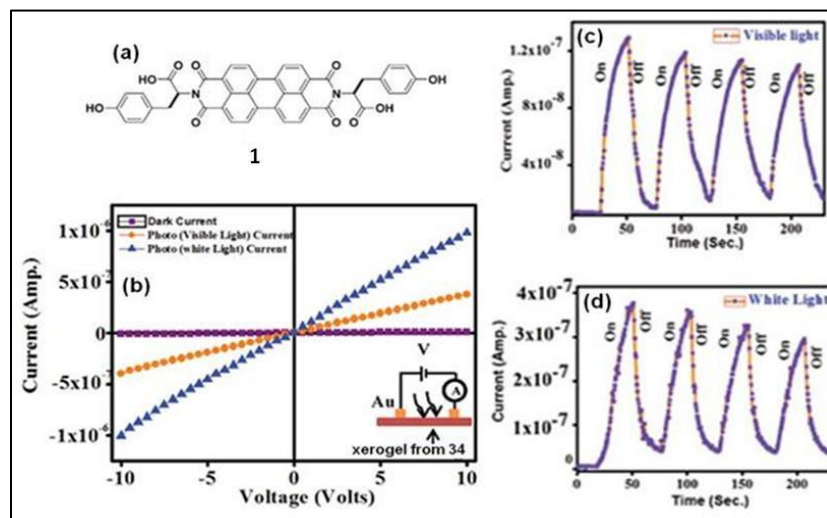


**Figure 1.31** (a) Chemical structure of the gelator molecule. (b)  $I$ - $V$  plots in dark, visible and white light conditions of the xerogel made by hydrogel; Inset: A schematic representation of the circuit diagram for  $I$ - $V$  measurements. (c) and (d) Transient photo-response by turning on/off visible and white light illumination of a representative conductor device made of the xerogel, respectively (adapted from S. Roy, D. K. Maiti, S. Panigrahi, D. Basak and A. Banerjee, *RSC Adv.*, 2012, **2**, 11053-11060).

In terms of formation of gels, it can be further classified in three different ways depending on the alteration of ratio of different components to tailor the properties of the gels.<sup>125</sup> Most work in this field has been focussed on the two added components which can be divided as follows:

1. Two-component gel phase materials where neither of the compounds can form gels alone but they self-assemble in combination to yield a gel. For example Zinic' and coworkers have reported studies on a peptide-based co-gel system that consists of a mixture of (S,S)-bis(LeuOH) oxalamide ((S,S)-14) and (S,S)-bis(leucinol) oxalamide ((S,S)-15) (Fig. 7a). An equimolar ratio of (S,S)-14 and (S,S)-15 was shown to gel up to 7 times more p-xylene than either component alone, suggesting the presence of a synergistic gelation effect with these two components.<sup>126</sup>
2. Two gelator component gels where both the compounds gelators. In this system there are two extremes, a) both gelators interact with each other to form co-fibers or b) the two gelators self-sort resulting in two different nanofibers within the gel. For example, Smith and co-workers investigated a series peptide-based dendrimers (which are essentially the covalent equivalents of their dendron-aliphatic diamine complexes) to show that self-sorting gels can be achieved via a change in Dendron

size (generation 1–3) or dendron chirality (D or L-lysine used as dendron building block). However, these systems, changing the shape of the dendrimer by varying the length of the aliphatic diamine resulted in mixed assemblies of the two components.<sup>127</sup>

3. Gelator plus additive component gels where one compound is a gelator and the other molecule is non-gelating and is designed to impact the gels thermomechanical or functional properties by, for example, impacting the assembly of the gelator. For example, a tripeptide containing an oligo-methylene group was found to form hydrogels at the two pH extremes (in presence of an acid or a base); however, it does not form a hydrogel at neutral pH. This property to obtain a hydrogel of the peptide in the presence of an organic acid, citric acid.<sup>128</sup>

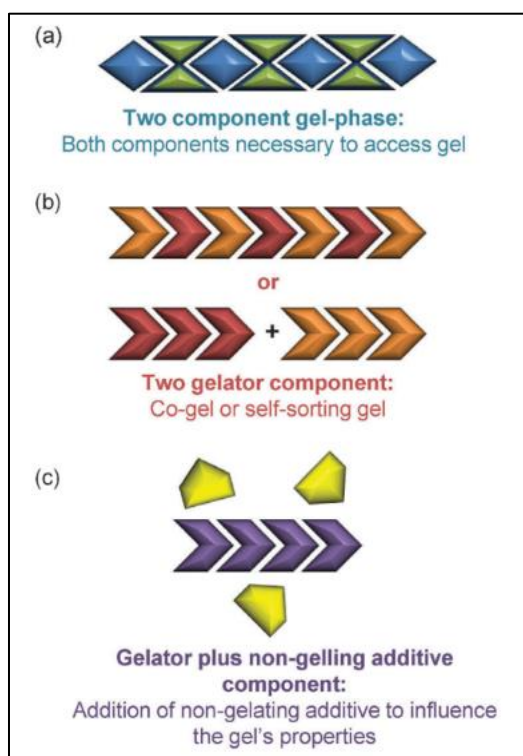


**Figure 1.32** Classification of gels in terms of gelator components (adopted from L. E. Buerkle and S. J. Rowan, *Chem. Soc. Rev.*, 2012, **41**, 6089-6102).



## 1.6.2. Amino acid and peptide hydrogels

Proteins such as insulin form hydrogels and peptides being the building block of the protein can form hydrogels autonomously as they are the building blocks of proteins. It was established by Namba and coworkers who found that the terminal position of flagellin gelates water at a concentration  $> 15\text{mg/ml}$ .<sup>129</sup> In fact, even ultra-short peptides,<sup>130, 131</sup> such as dipeptides, is capable of forming gels upon self-assembly. The Phe-Phe motif has become much popular as the most useful minimalist building block in peptide self-assembly towards the fabrication of various nanostructures and supramolecular gels (Figure 1.33). This motif can be easily recognized as a very effective yet simple fragment efficaciously used by several research groups for driving self-assembly. The pioneered work by Gazit's group on the nanofibers formed by the self-assembly of diphenylalanine<sup>132, 133</sup> has prompted researchers to explore the ability of small peptide fragments to self-assemble in different solvents. Replacing the first Phe residue with Ile yields hydrogel with a fine networked nanostructure.<sup>134</sup> Replacing the Phe residue of Ile-Phe with, conformational rigidness  $\alpha$ ,  $\beta$ -dehydrophenylalanine ( $\Delta\text{Phe}$ ) has yielded the stronger hydrogel at physiological condition with an injectable application.<sup>135</sup>

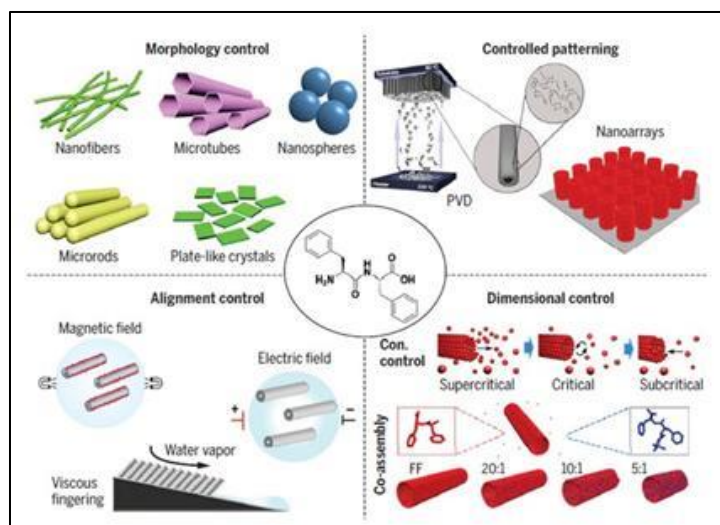


**Figure 1.33** Modulation of self-assembly of the Phe-Phe moiety by variation of different methodologies. (Adopted from K. Tao, P. Makam, R. Aizen and Ehud Gazit, *Science*, 2017, **358**, 885).



The gelation properties of the peptide gels can be tuned by modifying some moieties such as the N-terminal protective group such as benzoylcarbonyl<sup>136</sup> can be introduced to lessen the repulsive effect of it as well as promote gelation and introduction of some more H-bonding,  $\pi$ -stacking and hydrophobic interaction in the molecules also helps in enhancing the gelation capability. Bolaamphiphilic amino acid based molecules with benzoylcarbonyl N-terminus protection was been found to form organogels.<sup>137</sup> Hexafluoro derivative of the benzoylcarbonyl derivative is even better motif for gelation when a phenyl alanine residue is present at the N-terminus of the peptide and these kind of peptides show sequence specific gelation.<sup>138</sup> Pyrene, a fluorescent polyaromatic hydrocarbon, can be a good candidate to induce enough hydrophobicity in peptides and amino acid to trigger their self-assembly.<sup>139, 140</sup>

One of the most intensively studied Low Molecular Weight Gels (LMWGs) is Fmoc-diphenylalanine (Fmoc-Phe-Phe). Adams and Firth stated that the overall hydrophobicity of the molecule helps in the gelation. The gelation can be altered by the controlled change in the pH of the aqueous medium of the gelator<sup>141</sup>, by applying the FmocFF to a silica water surface<sup>142</sup>, or slowly adding water to solution of the hydrogelator in DMSO.<sup>143</sup> Fleming et. al. demonstrated the importance of the methoxy linker connected with the Fmoc moiety in comparison to analogous alkyl fluorenyl linkers in Fmoc-tyrosine-leucine (YL) dipeptide moiety (Figure 1.34).<sup>144</sup> In this work, both the linker length and flexibility are proposed to be imperative; aromatic-aromatic interactions have been found to be heavily dependent on which linker is present, with short linkers facilitating robust aromatic stacking and H-bonding interactions by restricting the conformation. Naphthalene moiety is also frequently employed to achieve strong aromatic-aromatic interaction in peptide based gelators.<sup>145</sup> 2-(naphthalen-2-yl) acetic acid is one such naphthalene-based moiety which has been applied by researchers for designing peptides capable of gels assembling.<sup>146-148</sup> Zhang et. al. reported a dipeptide derivative made by conjugating 2-(naphthalen-2-yl) acetic acid with Phe-Phe residue (NapFF)(Figure 1.34).<sup>149</sup> In this gelator molecule, the naphthalenyl group provides the hydrophobic interaction to enhance self-assembly in an aqueous environment, while the dipeptide backbone acts as both hydrogen bond acceptors and hydrogen bond donors. They have demonstrated NapFF as an effective hydrogelator that

forms a hydrogel at a concentration of 0.8% (w/v), with the gel–sol transition temperature at about 323 K (Figure 1.34). Adams and his co-workers used 2-naphthol to construct several naphthalene-based dipeptide derivatives<sup>150</sup> with an ether bond.<sup>151</sup> They reported that the hydrogelation of these naphthalene-dipeptide could be controlled by reducing the pH value with the hydrolysis of glucono delta-lactone (GdL). They choose GdL for pH control because its hydrolysis to gluconic acid allows a slow and uniform pH change.

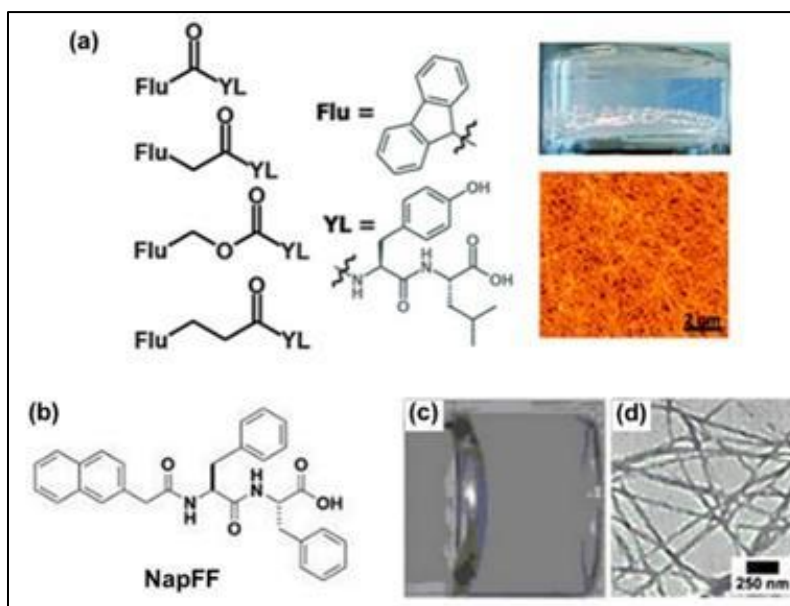


**Figure 1.34** (a) Chemical structures of the fluorenyl based hydrogelator and the pictorial images of the gel and corresponding AFM images (Adopted from S. Fleming, S. Debnath, P. W. J. M. Frederix, T. Tuttle and R. V. Ulijn, *Chem. Commun.*, 2013, **49**, 10587-10589). (b) Chemical structure of hydrogelator NapFF. (c) Vial picture and (d) TEM image of the hydrogel NapFF (Adopted from Y. Zhang, Y. Kuang, Y. Gao and B. Xu, *Langmuir*, 2011, **27**, 529–537).

A series of peptides can be gelated, simple tri and tetra peptides can also form sheet like assembly. In a significant work, Tuttle and Ulijn have recently introduced an improved version of Coarse Grained molecular simulation protocol for screening tripeptides for their aggregation behaviour and this computational method has been applied to a huge number of gene-encoded tripeptides ( $203 = 8000$ )<sup>152</sup> By this study a set of design rules that promote aggregation has been described: to attain maximum aggregation propensity score (a) the aromatic amino acid residue should be placed at the 2 or 3 position of the peptide (b) the hydrogen-bonding residues

should be placed at position 1 (N-terminus) and (c) negative residues at position 3 (C-terminus). Experimental finding also matches well with the theoretical prediction, unprotected tripeptides with KYF, KYY, KFF and KYW have been found to form hydrogels in absence of any organic solvents.<sup>153</sup>

Marchesan and her co-workers systematically investigated tripeptides containing one D-amino acid residue at the N-terminal and they found that chirality plays a critical role in the morphology of the nanofiber networks of the resulting hydrogels. The authors observed that the tripeptides VFF and FFV fail to form supramolecular gels, while <sup>D</sup>VFF and <sup>D</sup>FFV form hydrogels (Figure 1.35) at 0.67% (w/v) at physiological pH.<sup>154</sup> Pochan and Schneider have investigated another class of amphiphilic peptides with  $\beta$ -hairpin-like structure showing folding dependent gelation due to intramolecular folding pattern.<sup>69, 155, 156</sup> A peptide molecule consisting of alternative valine and lysine residues at the two arms of a hairpin and a D-proline residue at the central position undergoes pH triggered hydrogelation only in presence of certain folding conditions. They have designed another type of  $\beta$ -hairpin with dissimilar arm length with an exchangeable  $\beta$ -strand region that can enjoy swapping with another exchangeable  $\beta$ -strand of another peptide.<sup>157</sup>

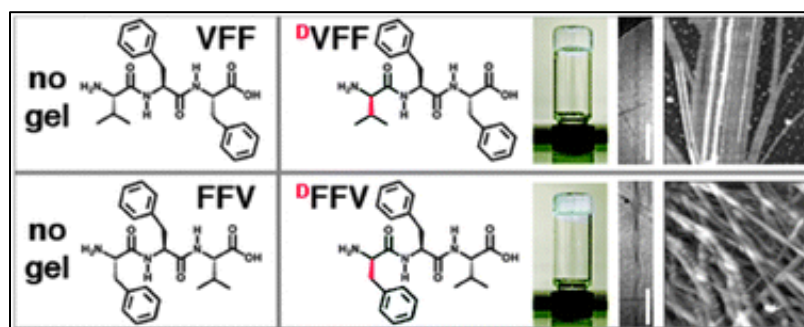


**Figure 1.35** Change of chirality of the N-end amino acid turns non-gelators VFF and FFV into hydrogelators <sup>D</sup>VFF and <sup>D</sup>FFV. The self-supporting hydrogels from <sup>D</sup>VFF and <sup>D</sup>FFV exhibit nanofibrillar network in their corresponding AFM images (adapted from S. Marchesan, C. D. Easton, F. Kushkaki, L. Waddington and P. G. Hartley, *Chem. Commun.*, 2012, **48**, 2195–2197)

### 1.6.3. Hydrogels based on peptide amphiphile

The peptide amphiphile is an important class of hydrogelators composed of peptide chain attached to a long hydrocarbon chain which enhances van der Waals interaction in self-assembly process. The design of peptide amphiphile (PA) is discussed previously in this thesis earlier. Based on a rational design scheme and decorated with various functional epitopes peptide amphiphile form mostly  $\beta$ -pleated sheets. These  $\beta$ -sheets self-assembles to form various nanostructures (Figure 1.36). The hydrogel based on PAs are generally observed to form nanofibers or nanobelts. Discussion of structural variety of PAs that deviates from the classic design, are important. This thesis further contains two original research works based of peptide amphiphile.

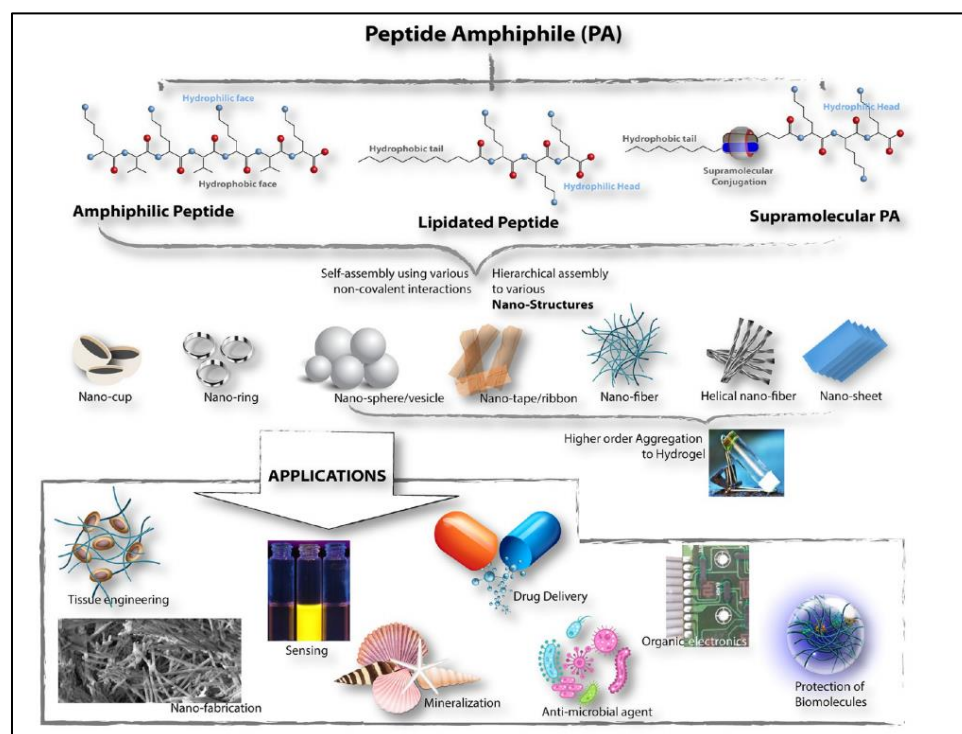


**Figure 1.36** Schematic presentation of sub-division of peptide amphiphiles, the nanostructures they adopt in suitable aggregating conditions and various applications in which the nano-assemblies are utilized. (Adopted from A. Dasgupta and D. Das, *Langmuir*, 2019, **35**, 10704-10724).

Peptide amphiphiles can be classified into three categories: (1) amphiphilic peptides, (2) lipidated peptide amphiphiles, and (3) supramolecular peptide

amphiphile conjugates. In this section, these different classes of PAs are discussed with respect to the structural aspect.

Amphiphilic peptides (1) are a class of PAs which are made of amino acids only.<sup>158</sup> In principle, such PAs are made of a combination of hydrophobic and hydrophilic amino acids. Nature utilizes this phenomenon to create membrane proteins which are capable of folding in such a way as to create an entirely hydrophobic surface with a hydrophilic interior, thereby enabling themselves to assimilate into the lipid bilayer of membranes.<sup>159</sup> Several peptide-based toxins and antibiotics are functional through this mechanism.<sup>160,161</sup> A similar amphipathic mechanism is also adopted for the construction of cell-penetrating as well as antimicrobial peptides, and in recent years, there has been a surge in preparing such sequences.<sup>162, 163</sup> Peptides comprising repetitive dyads of hydrophobic and hydrophilic residues often tend to adopt  $\beta$ -pleated sheetlike structures. Such sequences create two faces of a  $\beta$ -strand, a hydrophobic one where all of the hydrophobic side chains are directed while the other face comprises the polar side chains of the amino acids (Figure 1.36). While constructing all amino acid PAs, this is the most common platform. A plethora of such peptides and their self-assemblies are reported in the literature. A series of such PAs (**1-3**, Figure 1.37) are reported by Zhang et al.<sup>164</sup> In all of these peptides, the amphiphilicity was generated by the alternate use of hydrophilic and hydrophobic amino acid residues. These sequences self-assemble into nanofibers, and a higher-order aggregation of the nanofibers leads to hydrogelation. Another interesting subclass of such PAs is the 20 amino acid sequence developed by Schnieder et al.<sup>69</sup> By introducing a <sup>D</sup>Pro-<sup>L</sup>Pro linker in between two stretches of alternating lysine and valine, a type II  $\beta$ -turn is created (**4**, Figure 1.37). These peptides are highly soluble in water or low pH and remain as a low-viscosity liquid. In this state, the peptide adopts no particular secondary structure and remains as random coils due to electrostatic repulsion of the cationic groups. However, at basic pH, as the solubility of the peptide decreases because of the deprotonation of the free amines, the peptides folds in such a fashion as to create antiparallel  $\beta$ -sheet structures involving a  $\beta$ -hairpin in the <sup>D</sup>Pro-<sup>L</sup>Pro region. The folded peptide intermolecularly self-assembles to form a hydrogel.<sup>69</sup>

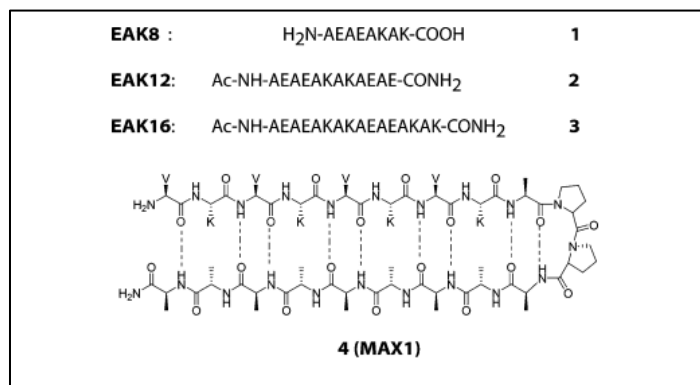


**Figure 1.37** Chemical structures of some important amphiphilic peptides (Adopted from S. Zhang, T. Holmes, C. Lockshin and A. Rich, *Proc. Natl. Acad. Sci.*, 1993, **90**, 3334-3338 and J. P. Schneider, D. J. Pochan, B. Ozbas, K. Rajagopal, L. Pakstis and J. Kretsinger, *J. Am. Chem. Soc.*, 2002, **124**, 15030-15037).

Lipidated Peptide Amphiphiles (2) are the class of PAs which are the most abundant in the literature.<sup>165, 166</sup> They have a fairly simple design pioneered by Stupp and coworkers in search of a diverse rational design of amphiphiles.<sup>167</sup> post-translational modification of signal transduction proteins with lipid groups is common. One or two lipid groups (palmitoyl, farnesyl, and geranylgeranyl) get attached to the C-terminal amino acids of the proteins, which help them to anchor at the cell membrane.<sup>168</sup> In general, designer peptide amphiphiles in general comprise the hydrocarbon chains at the N-terminal and the peptide sequence at the C-terminal serves as the polar headgroup. However, examples of PAs are also available where the N-terminal is conjugated with a polar charged group (quaternary ammonium) while the C-terminal is connected to hydrocarbon chains.<sup>169</sup> Structurally, these groups of amphiphiles resemble typical phospholipids or surfactants. They self-assemble above a critical aggregation concentration (CAC) similar to the critical micelle concentration (CMC) of a surfactant. Below the CAC, the molecules remain in the monomeric state.

An excellent example of a single tail lipidated PA was reported by Stupp et al.<sup>170</sup> There are five different structural elements in the design of the PA (**5**, Figure 1.38). A palmitoyl group at the N-terminal acting as the hydrophobic part and connected to the second region containing four cysteine residues, providing an oxidative polymerization site. Then comes a flexible linker of three glycine residues



followed by the fourth section, a single phosphorylated serine residue. The presence of the phosphoserine residue is for binding with calcium ions and promoting mineralization. The fifth and final region is a cell-targeting RGD motif.

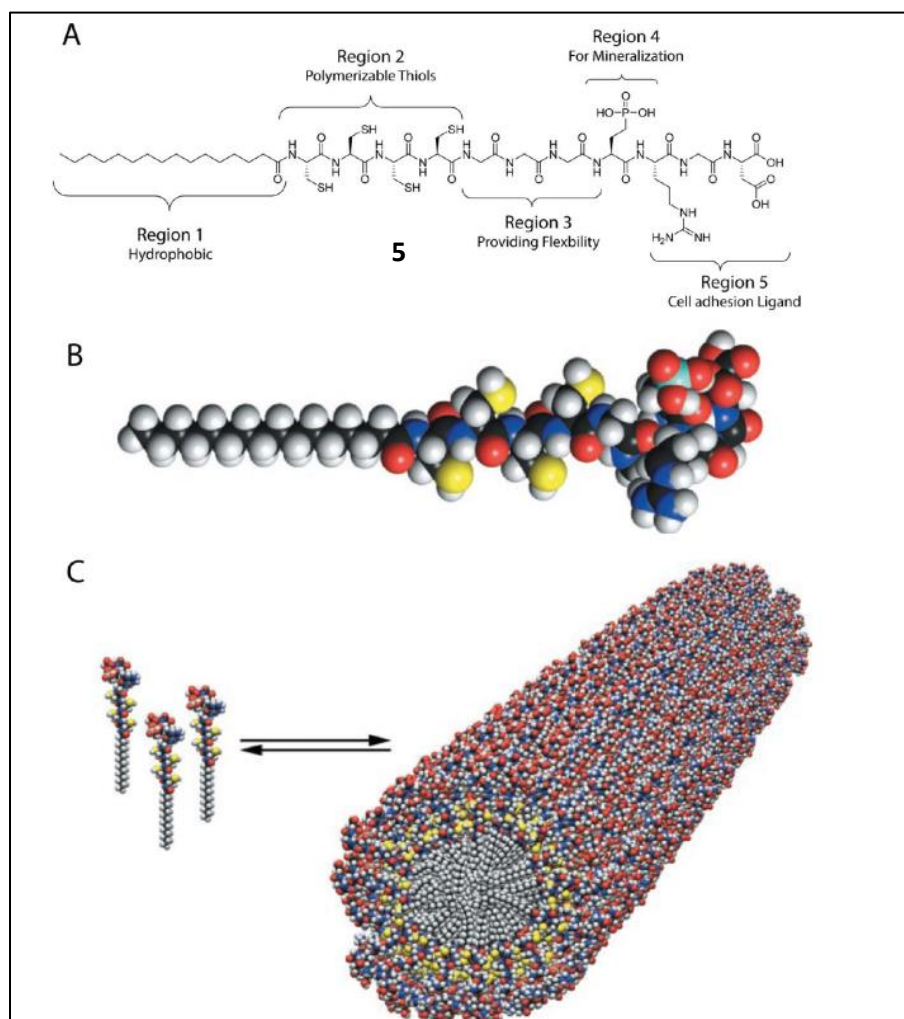


**Figure 1.38** (a) Chemical structure of peptide amphiphile 5 highlighting five key structural features. (b) Molecular model of the PA showing the overall conical shape of the molecule on going from the narrow hydrophobic tail to the bulkier peptide region. (c) Schematic showing cylindrical micelle formation through the self-assembly of 5. (Adopted from J. D. Hartgerink, E. Beniash and S. I. Stupp, *Science*, 2001, **294**, 1684-1688).

Another interesting design to promote the self-assembly of lipidated PAs comes from the introduction of aromatic groups in between the peptide sequence and the hydrocarbon chains. The use of fused aromatic groups such as naphthalene,

pyrene, Fmoc, and arylenediimides (ADIs) in short peptides is a common approach to the construction of peptide-based hydrogels.<sup>171, 172</sup> The introduction of such aromatic groups enhances the hydrophobicity and provides the possibility of strong  $\pi$ - $\pi$  stacking between the molecules. ADIs are a common choice for this purpose, not only for their  $\pi$ - $\pi$  stacking ability but also because of the fact that these groups have tremendous potential in applications in organic electronics and chemosensor development.<sup>173</sup> The presence of an aromatic moiety as the hydrophobic group

An interesting design strategy of peptide amphiphile is to add aromatic moiety in the hydrophobic part of the molecule. In a work done by Das and co-workers, the PA contained lysine as the polar headgroup, and the pyrene-butanoic acid-connected FF unit acts as the hydrophobic region.<sup>174</sup> In water, the PA possibly forms micelle-like aggregates, which then go through higher-order aggregation to produce disklike structures (Figure 1.39). However, no hydrogel formation was observed even at a very high concentration. Interestingly, the addition of a dicationic NDI molecule in an equimolar ratio resulted in a self-supporting hydrogel (Figure 1.39). Detailed NIOSY analyses revealed an unusual combination of the cation- $\pi$  and charge-transfer interactions between PA and NDTA, resulting in the hydrogel. It is interesting that a portion of the pyrene ring is involved in the CT interaction with NDI while the other part of the group experiences a cation- $\pi$  interaction with the cationic group of NDTA.

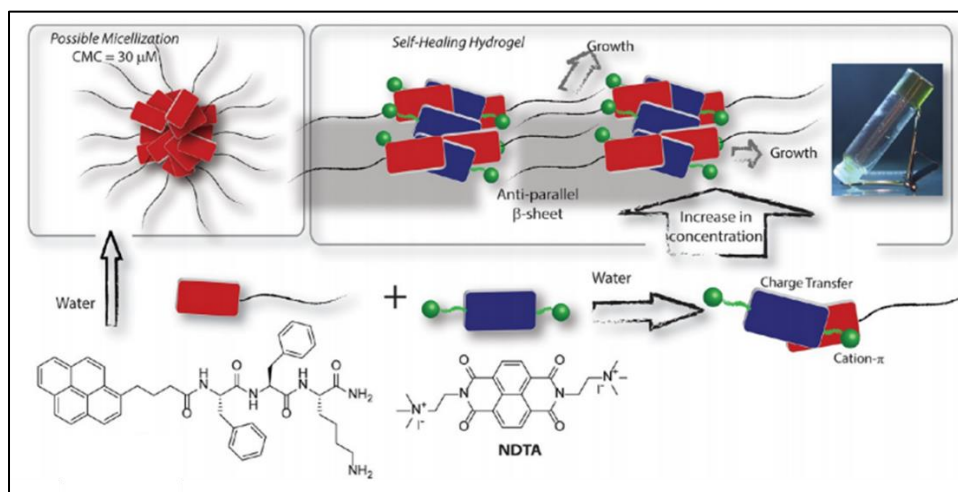


**Figure 1.39** Chemical structure and self-assembly of a pyrene containing PA with lysine headgroup without NDTA and hydrogel formation with NDTA and formation of charge



*transfer complex. (Adopted from B. Pramanik, S. Ahmed, N. Singha, B. K. Das, P. Dowari and D. Das, Langmuir, 2019, 35, 478-488).*

Supramolecular Amphiphiles (3) has emerged through combination of traditional amphiphiles and supramolecular chemistry.<sup>175</sup> In contrast to traditional amphiphiles, in this case, an amphiphilic structure is constructed by combining two separate molecules through supramolecular interactions or dynamic covalent bonds. This approach provides the flexibility to construct various amphiphilic structures from one particular component. Moreover, supramolecular amphiphiles are very useful in the fabrication of soft materials with high structural complexity and stimuli responsiveness.<sup>175</sup>

## **1.7. Strategy of peptide gelation**

In supramolecular gels the non-covalent interactions are weak in nature and they can be broken and reformed in response to the various external stimuli such as heat, pH of the medium, external chemicals, sonication, mechanical force and irradiation by light. Moreover, the presence of functional groups with specific physical or chemical responses allows them to external stimuli beside the non-covalent interactions.

### **1.7.1. Metal Induced gelation**

Metals are good candidates for triggering self-assembly process of peptides. Metal ions sometimes act a mere additive to improve the properties of gel materials and in some cases the metal ions are essential component for the gelation to occur. Banerjee and co-workers have reported a series of amphiphilic tyrosine based self-healable, multi-stimuli responsive metallo-hydrogels. Formation of these hydrogels is highly selective to Ni<sup>2+</sup> ions. (Figure 1.40). The self-healing property and the stiffness of these metallo-hydrogels can be tuned by varying the chain length of the corresponding gelator amphiphile.<sup>176</sup>

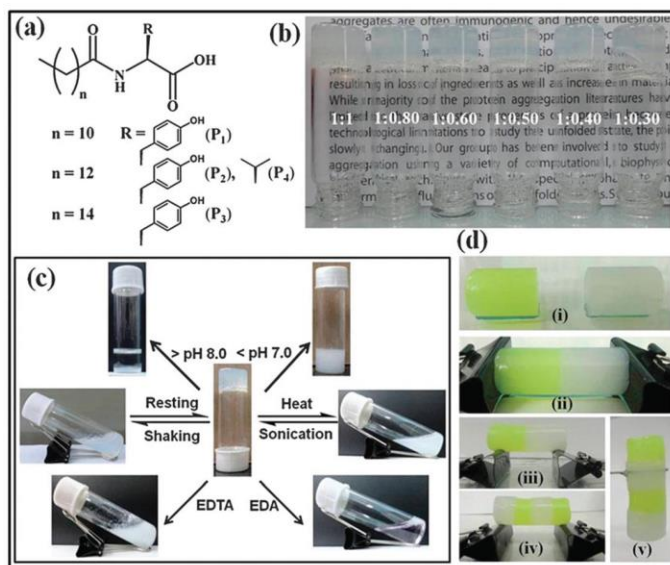


**Figure 1.40** (a) Chemical structures of the amphiphiles ( $P_1$ – $P_4$ ). (b) Glass vial Pictures of metallo-hydrogels obtained by different proportions of the  $P_3$  and nickel salt ( $\text{NiCl}_2$ ). (c) Multi-stimuli responsive hydrogel of  $P_3$ . (d) Self-healing behavior (i–v) of the metallo-hydrogel. (Adopted from S. Basak, J. Nanda and A. Banerjee, *Chem. Commun.*, 2014, **50**, 2356–2359).

Halder and co-workers reported that the iron (III) complex of 4-biphenylcarboxy capped diphenylalanine formed a stable gel in water.<sup>177</sup> The gelation was selective for Fe (III) and complexes with other metal ions such as Cd, Cu, Zn, Cr, Ni, Hg, Mg, Mn, Pb, and Pd failed to form metallogel (Figure 1.41). Interestingly, the gelation behaviour was also dependent on the capping and of the n-terminus of the peptide residue and no gel formation was observed in case of Boc and acetyl capped diphenylalanine (Figure 1.41).

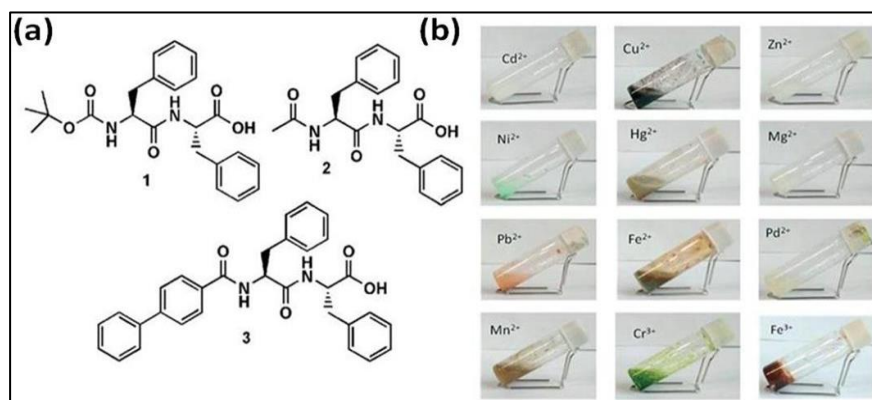


**Figure 1.41** (a) The chemical structure of the peptides 1–3. (b) Different metal ion induced hydrogelation of peptide 2. (Adopted from S. Sasmal, K. Maji, D. Díaz Díaz and D. Haldar, *CrystEngComm*, 2019, **21**, 4289–4297).

Xu and co-workers have reported that by incorporating a bipyridine motif into a tripeptide-based hydrogelator actually collapse its ability towards gel formation. Surprisingly, the same compound formed nanofibers with a ruthenium (II) tris(bipyridine) complex that forms a stable hydrogel.<sup>178</sup> The ruthenium complex offers a geometrical control to pre-arrange the peptide prior to the self-assembly. This metallo-hydrogelator not only formed a hydrogel but also exhibits gel-sol transition upon oxidation of the metal centre. The metal complex imparted optical, electronic, redox, or magnetic properties to supramolecular hydrogels.

Liu and co-workers reported a L-histidine ester terminated bolaamphiphile (BolaHis) molecule that forms a stable hydrogel and self-assembled into single-walled nanotubes in the acidic environment in 8 N sulphuric acid or hydrochloric acid. The molecule also forms hydrogel in presence of copper (II) ion with one-molecular thickness nanofibers. Interestingly, both hydrogels exhibit unique single-walled nanotubes and nanofibers. (Figure 1.42)<sup>179</sup>

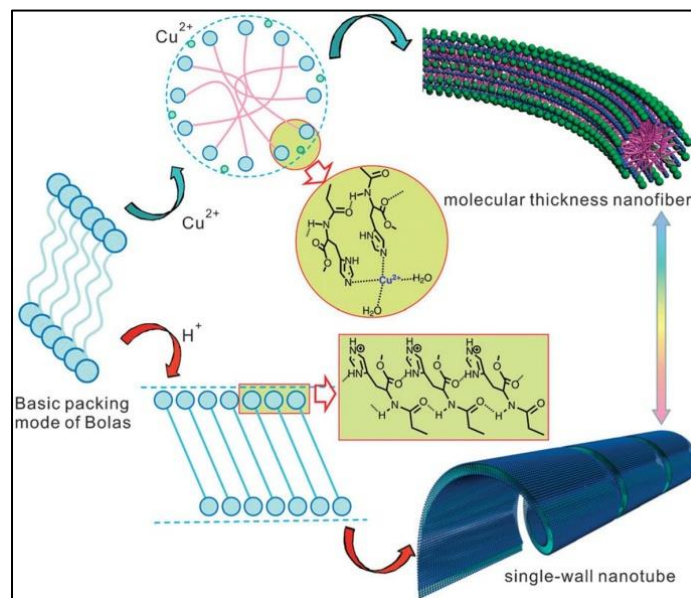


**Figure 1.42** Graphical illustration of the self-assembly of Bola His with  $Cu^{2+}$  and  $H^+$ . (Adopted from Y. Liu, T. Wang, Z. Lib and M. Liu, *Chem. Commun.*, 2013, **49**, 4767-4769).

They also reported metallogels of an amphiphilic L-histidine derivative with  $Fe^{3+}$ . Interestingly, upon resting the hydrogel at the room temperature, the gel undergoes shrinkage that 90% of ferric ion containing water was expelled from the gel.

Song and his co-workers synthesized biometallohydrogel with broad-spectrum antimicrobial activities and tuneable mechanical properties based on biocompatible amino acid coordinated self-assembly with  $Ag^+$  (Figure 1.43). The high directionality and anchoring ability of the coordination interactions allow  $Ag^+$  to be fixed within the amino acid nanofiber hydrogels, where the  $Ag^+$ -Fmoc-amino acid coordination complexes act as precursors for producing AgNPs through a mild mineralization process. In situ mineralization of AgNPs ensures the controlled spatial distribution of AgNPs in the hydrogel matrix, which is of key importance for sustainable release of  $Ag^+$ , improved antimicrobial efficacy and tuneable mechanical properties (Figure 1.43).<sup>180</sup>

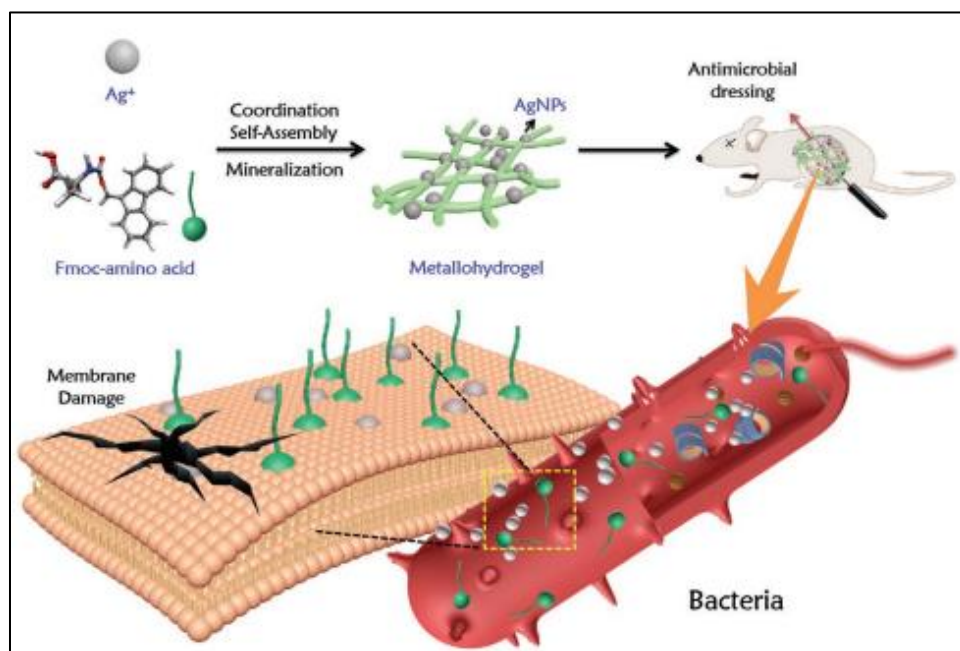


**Figure 1.43** Graphical representation of silver mineralization from a Fmoc-based metallohydrogel with  $\text{Ag}^+$  (Adopted from J. Song, C. Yuan, T. Jiao, R. Xing, M. Yang, D. J. Adams and X. Yan, *Small*, 2020, **16**, 1907309).

Banerjee and his group synthesised a histidine-based amphiphile containing a C14 fatty acyl chain, N-histidyl N'-myristyl ethyl amine (AM1, 14.7 mM) forms hydrogels in the presence of  $\text{Fe}^{3+}$  (within the range 1.47 to 4.41 mM) and  $\text{Hg}^{2+}$  (within the range 3.67 to 11.02 mM) ions (Figure 1.44) in aqueous dispersions at pH 6.6 (27 °C). The imidazole ring of the histidine residue plays a vital role to interact with these metal ions. The thermal and mechanical stability of these metallo-hydrogels can be tuned by changing the proportion of amphiphile to metal ion ratio (1:0.1 to 1:0.3 for  $\text{Fe}^{3+}$ -containing gel and 1:0.25 to 1:0.75 for  $\text{Hg}^{2+}$ -containing gel). Both, the amphiphiles and the metal ion induced hydrogels reveal catalytic activity of p-nitrophenyl esters hydrolysis for the acetyl, n-butyl and n-octyl esters (Figure 1.44). Ferric ion containing metallo-hydrogel exhibits higher catalytic activity than the corresponding AM1 aggregate in the absence of metal ions.<sup>181</sup>

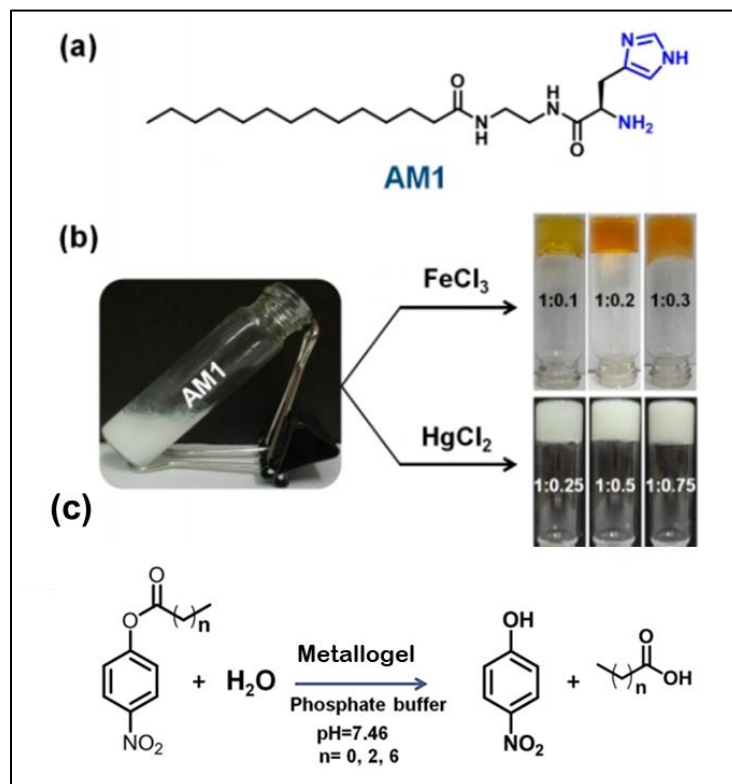


**Figure 1.44** (a) Chemical structure of amphiphilic AM1, (b) metal induced gelation of AM1 using FeCl<sub>3</sub> and HgCl<sub>2</sub> and (c) the catalytic activity of these metallo gels in hydrolysis reaction. (Adopted from I. K. Gayen, K. Basu, D. Bairagi, V. Castelletto, I. W. Hamley and A. Banerjee, *ACS Appl. Bio Mater.*, 2018, **1**, 1717-1724).

### 1.7.2. Enzyme-assisted gelation

Enzymes are basic molecular catalysts of life. Specific enzyme can be used for removal of a selective group of a peptide and after removal of that particular group that peptide can self-assemble into gel. The enzyme that assists peptide bond cleavage are generally called hydrolase. During the mid of last century, it has been found that the hydrolysing protein can act in reverse way under some specific circumstances i.e., they can assist peptide bond formation also. It is still difficult to synthesize natural polypeptides by a chemoenzymatic approach, however, chemoenzymatic synthesis offers a flexible and more specific method for peptide synthesis.<sup>182, 183</sup> Enzymes have recently emerged as tools to achieve this by converting non-assembling peptide precursors into self-assembling building blocks under stable pH, ionic strength and temperature condition. Peptide based systems that are responsive to enzymes can make them useful in biological

situations, for example taking advantage of an early enzyme in blood clotting. It may help prevent blood loss, if a liquid can be switched to a gel. Enzyme-assisted self-assembly can be achieved either by catalysing the synthesis of a self-assembly molecule, or by removing a blocking group from a molecule to facilitate assembly.

Another example of an enzyme assisted self-assembly system is reversed hydrolysis. In that case, a protease was used to drive the self-assembly of peptide hydrogelators via coupling of non-assembling precursors. A range of Fmoc-amino acids and FF or LL were used to synthesise Fmoc- tripeptide derivatives (Figure 1.45)<sup>183</sup> This method relies on an enzymatic step that is thermodynamically ‘up-hill’, which is driven thermodynamically by the self-assembly process (Figure 1.45). It is thought that the fully reversible nature of this method will help prevent formation of kinetic aggregates and favour the thermodynamically stable assembly, thereby paving the way to a self-assembled structure with fewer defects.

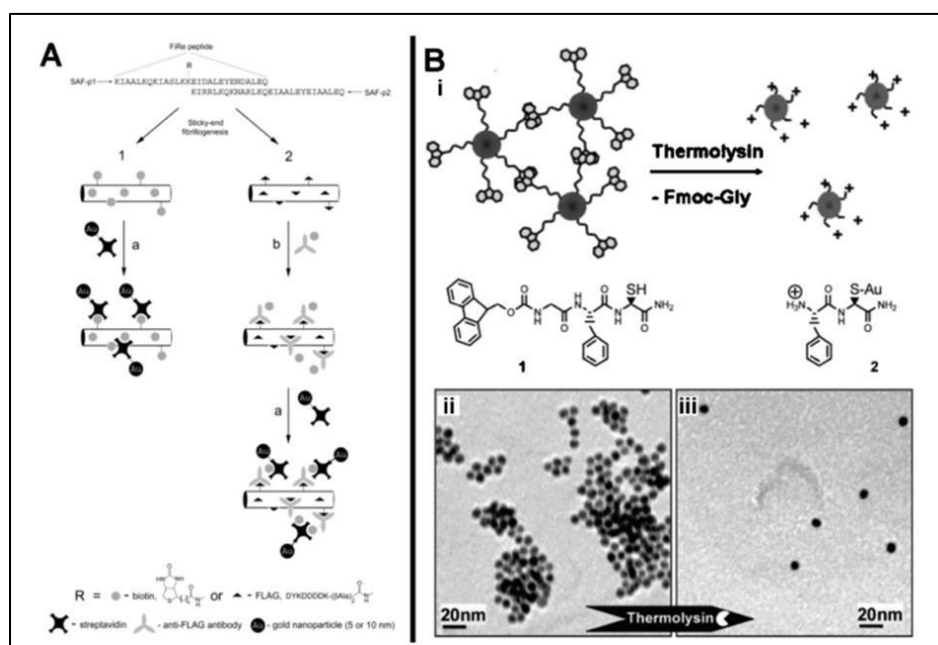


**Figure 1.45:** Schematic of the modification of the coiled-coil SAF system by the addition of biotin or FLAG peptides to an exposed lysine residue. The biotin was then used to bind streptavidin labelled with gold particles or in the case of the FLAG peptide, antibody labelled with biotin that the bound streptavidin labelled with gold (A). Schematic of gold particles coated with a Fmoc peptide containing a protease-sensitive sequence. With the peptide intact the gold particles cluster, after cleavage with the protease, thermolysin in this case, the gold particles should disperse (a). Electron microscopy results show this to be the case with clusters of particles prior to cleavage (b) and a dispersion afterwards (c). (Adopted from M. G. Ryadnov and D. N. Woolfson, *J. Am. Chem. Soc.*, 2004, **126**, 7454–7455)



There is an example of an enzyme assisted conformational transformation from a O-acyl to N-acyl conversion through a peptide cleavage. In this system a  $\beta$ -sheet forming peptide sequence have been attached to a side chain of serine, threonine or cysteine and a short capping peptide is attached to the amino group. This capping peptide is designed to be cleaved off by a specific protease (Figure 1.46). Once this occurs, a chemical rearrangement happens that repositions the desired peptide chain onto the amino group leaving the normal serine, threonine or cysteine side chain present (Figure 1.46). Due to this chemical rearrangement after the action of the protease the process is irreversible.<sup>184</sup>

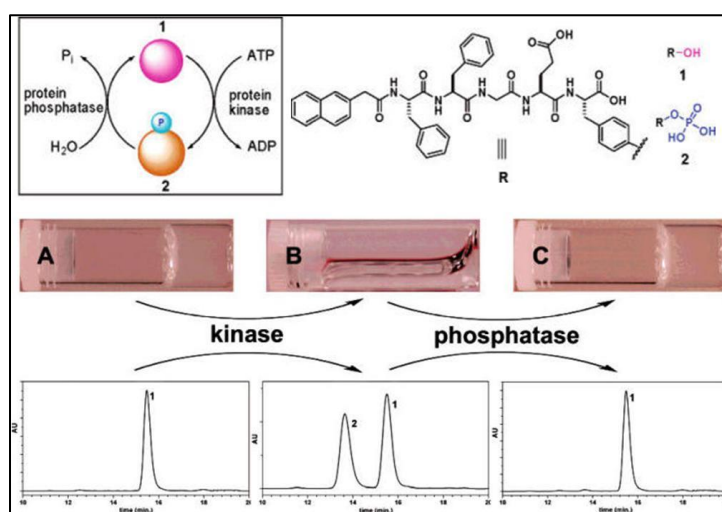


**Figure 1.46:** Reversible modification of the subunits of a gel by a phosphatase/kinase reaction where the addition of a phosphate group to the tyrosine of the molecule causes the gel to disassemble, addition of a phosphatase removes the phosphate group and triggers gelation again. (Adopted from, Z. M. Yang, G. L. Liang, L. Wang and B. Xu, *J. Am. Chem. Soc.*, 2006, **128**, 3038-3043.)

A reversible system using two enzymes that catalyse opposite reactions (phosphorylation/dephosphorylation) was demonstrated to control the gel-sol transition of a peptide in a highly controlled manner. The peptide used is a naphthalene linked to FFGY, this peptide is a gel in water (Figure 1.47), in the presence of adenosine triphosphate, kinase adds a phosphate group to the tyrosine residue, resulting in a transition to a solution. The further addition of a phosphatase results in the removal of the phosphate and to trigger gelation.<sup>185</sup> The use of enzymes in self-assembly adds a level of control over the self-assembly process



and is therefore expected to play a key role in the future development of more complex structures with fewer defects.

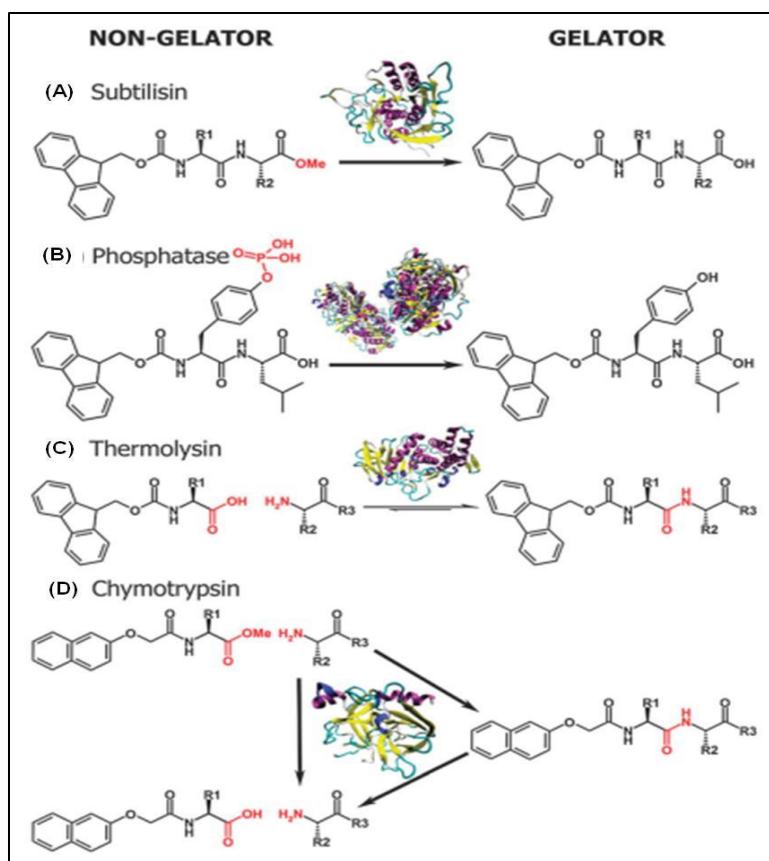


**Figure 1.47:** Summary of reported enzyme responsive hydrogelation examples including: (A) subtilisin methyl ester cleavage; (B) phosphatase phosphate cleavage; (C) thermolysin amide bond condensation and (D) chymotrypsin non-equilibrium (temporary) assembly. (Adopted from S. Fleming and R. V. Ulijn, *Chem. Soc. Rev.*, 2014, **43**, 8150-8177)

### 1.7.3. pH-sensitive gelation

Hayes and his co-workers reported a structurally simple urea-based LMWG bearing two carboxylic acids that formed robust, pH-responsive hydrogels with outstanding dye scavenging properties (Figure 1.48).<sup>186</sup> The compound was completely soluble in basic media and can be converted into a hydrogel on acidification. These nanofibers interact selectively with positively charged dyes such as methylene blue and methyl violet and this property was successfully utilized in dye scavenging. Smith and co-workers have reported a hydrazide functionalized molecule DBS-CONHNH<sub>2</sub> which was a pH-tolerant hydrogelators that formed hydrogels within pH range 2-11.5 (Figure 1.48).<sup>187</sup>

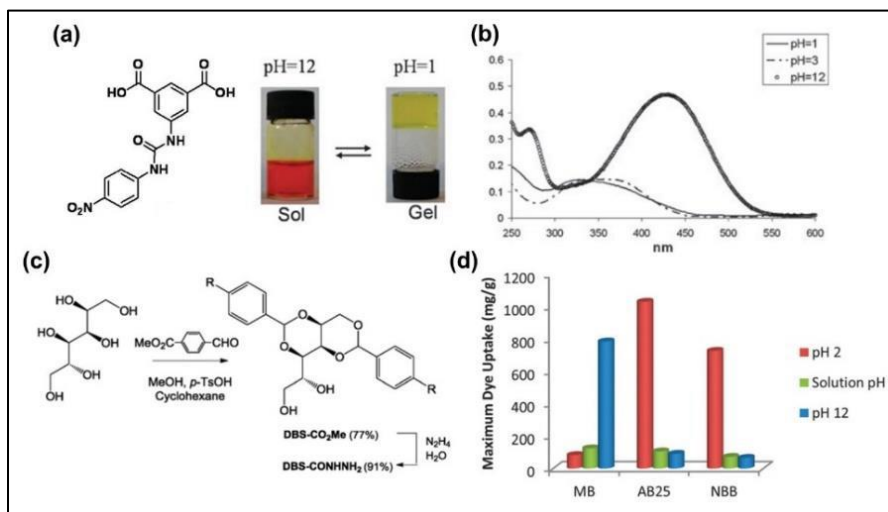


**Figure 1.48** (a) The chemical structure of the urea based gelator (left) and the vial pictures containing an aqueous solution of the gelator and the subsequent hydrogel formed upon acidification (right). (b) UV-vis spectra of the gelator at different pH values. (Adopted from F. Rodríguez-Llansola, B. Escuder, J. F. Miravet, D. Hermida-Merino, I. W. Hamley, C. J. Cardin and W. Hayes, *Chem. Commun.*, 2010, **46**, 7960-7962). (c) Synthesis of novel hydrogelator DBS-CONHNH<sub>2</sub>. (d) Maximum dye adsorption by DBS-CONHNH<sub>2</sub> under different conditions of pH. (Adopted from B. O. Okesola and D. K. Smith, *Chem. Commun.*, 2013, **49**, 11164-11166).

These gels obtained from the gelator showed very high level of dye adsorption capacity for different types of dyes under various conditions of pH. Furthermore, changing of pH can be used to control various dye adsorption-desorption procedure. The interaction of acids and bases in low polarity organic media has also been used to prepare multi-component organogels in which gel formation has been achieved after the formation of an ionic pair.

#### 1.7.4. Thixotropic properties

‘The term Thixotropic’, can be defined as the “ reversible reduction and recovery of elastic modulus, yield stress and viscosity isothermally upon the application and removal of a destructive shear strain.”<sup>188</sup> This type of reversible mechanotropic property occurs as a consequence of structural (microscopic) reorganizations of the self-assembled aggregates. This is because of the loss or gain of weak intermolecular interactions (such as H-bonding,  $\pi$ - $\pi$  stacking, electrostatic forces, and London dispersion forces). By this virtue, thixotropic gels offer widespread

applications in fields starting from smart and adaptive materials, detergents, lubricants, paints and foods, to drug control and release, and tissue engineering, attracting attention from both academia and industry.

In a recent review, Weiss and his co-workers specifically focused on the correlations between thixotropic and structural properties of molecular gels having crystalline fibrillar networks (SAFINs) (Figure 1.49).<sup>189</sup> They indicated that the formation of thixotropic molecular gels and their recovery (after the application of destructive strain) are dependent on the type and strength of intermolecular interactions in the SAFINs of the gelator molecules. While applying destructive strain, those interactions at or near junction zones are weakened, damaged or disordered preferentially, without disassembling the individual fibers.

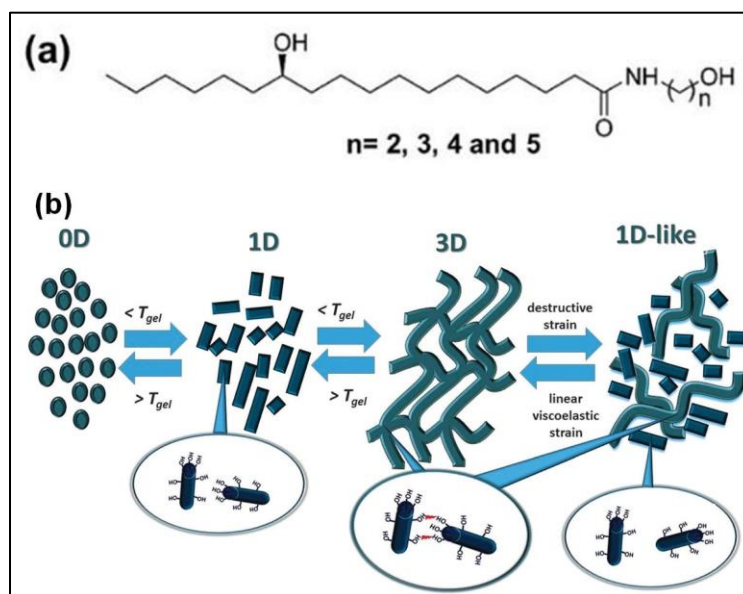


**Figure 1.49** (a) The chemical structure of aliphatic thixotropic molecular gelators. (b) Graphical representation of a possible mechanism for mechanotropic destruction and reformation of self-assembled fibrillar networks. (Adopted from V. A. Mallia and R. G. Weiss, *Soft Matter*, 2015, **11**, 5010-5022).

Banerjee and co-workers reported tripeptide-based hydrogel at physiological pH and temperature. This hydrogel exhibits thixotropy property and used for entrapment and sustained release of an antibiotic vancomycin and vitamin B12 at physiological pH and temperature for about 2 days (Figure 1.50).<sup>190</sup>

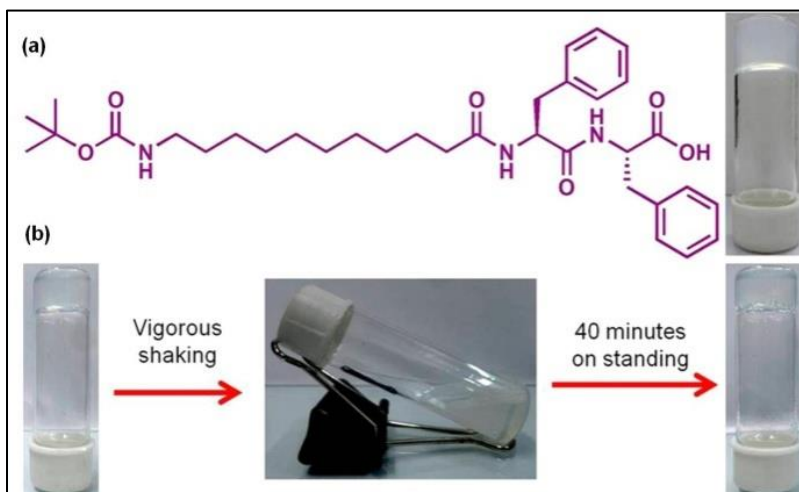


**Figure 1.50** (a) Chemical structure of the gelator and the hydrogel at pH 7.46. (b) thixotropic nature of the hydrogel. (Adopted from A. Baral, S. Roy, A. Dehsorkhi, I. W. Hamley, S. Mohapatra, S. Ghosh, and A. Banerjee, *Langmuir*, 2014, **30**, 929–936).

Dey and coworkers reported a poly (vinyl alcohol) (PVA) embedded hybrid hydrogel of a  $\beta$ -amino acid-containing Fmoc-protected tripeptide at physiological pH and room temperature. The tripeptide-based pure hydrogel was found to be unstable after half an hour addition but after addition of PVA, it increased the temporal and mechanical stability of the hydrogel and the gel becomes thixotropic in nature. The thixotropic nature of the hydrogel has been exploited to entrap and release doxorubicin, an anticancer drug, under physiological conditions. (Figure 1.51)<sup>191</sup>

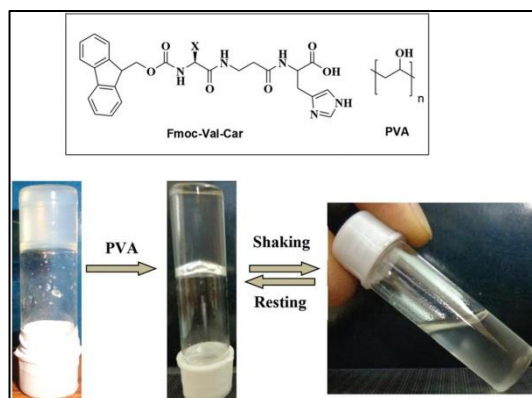


**Figure 1.51** Chemical structures of Fmoc-Val-Car and PVA and the appearance of Fmoc-Val-Car hydrogels in the presence and absence of PVA. (Adopted from R. D. Mahapatra, J. Dey and R. G. Weiss, *Soft Matter*, 2019, **15**, 433-441).

## 1.8. Peptide Hydrogel as functional materials

### 1.8.1. Hydrogels as extracellular matrix

Cell cultures on a 2D surface or in liquid suspension is a well-explored field of study. In spite of advantages of these methods, they are unable to mimic real environment of cells inside tissue systems. The tissue system consists of the cells and the extra-cellular matrix (ECM). The signalling and responsiveness between cells and cell to ECM is a matter of great interest as it can unveil mechanism of carcinogenic tumor<sup>192</sup> and have application in regenerative medicines.<sup>193</sup> Supramolecular hydrogels assembled from amino acids and peptide-derived hydrogelators have shown great potential as biomimetic three-dimensional (3D) extracellular matrices because of their merits over conventional polymeric hydrogels, such as non-covalent or physical interactions, controllable self-assembly, and biocompatibility. These merits enable hydrogels to be made not only by using external stimuli, but also under physiological conditions by rationally designing gelator structures, as well as in situ encapsulation of cells into hydrogels for 3D culture.<sup>192</sup>

In the 1990s, Zhang et al. reported peptide-based gelators with 16 amino acids, EAK16-II (Ac-NH-AEAEAKA-KAEAEAKAK-CONH<sub>2</sub>), which adopted a  $\beta$ -sheet configuration by self-complementary ionic interactions between positively charged lysines and negatively charged glutamic acids, together with hydrophobic interactions of alanines to form the ordered nanofibers at neutral pH.<sup>164</sup> Gelation occurs when the complementary charges neutralized each other at pH 7. Since this discovery, many peptide hydrogelators are designed using complementary charged peptide residues. Since then, similar peptides were designed to make 3D nanofibrous scaffolds capable of supporting cell growth, such as RAD16-I (AcNRADARAD-ARADARADA-CN<sub>2</sub>) and RAD16-II (AcNRARADADARA-RADADA-CN<sub>2</sub>) oligopeptide with positively and negatively charged residues. Both could self-assemble into hydrogels in physiological solution (Figure 1.52).<sup>194</sup> The stiffness of the nanofibrous (Figure 1.52) hydrogel could be tuned by altering concentration of gelators. Human umbilical vein endothelial cells (HUVECs) suspended in ionic solution were implanted in the hydrogels. The tunable stiffness of the hydrogels can direct the differentiated cellular behavior, which is useful for vascular networks engineering in 3D.<sup>195</sup> RAD16-I hydrogel was also investigated

as matrix scaffold that allowed ovarian cancer cells to reside in a 3D microenvironment similar to cellular niches in vivo, and was found to promote 3D cell adhesion and migration.<sup>196</sup> Moreover, cells in such hydrogels could maintain their cell functions after culture.

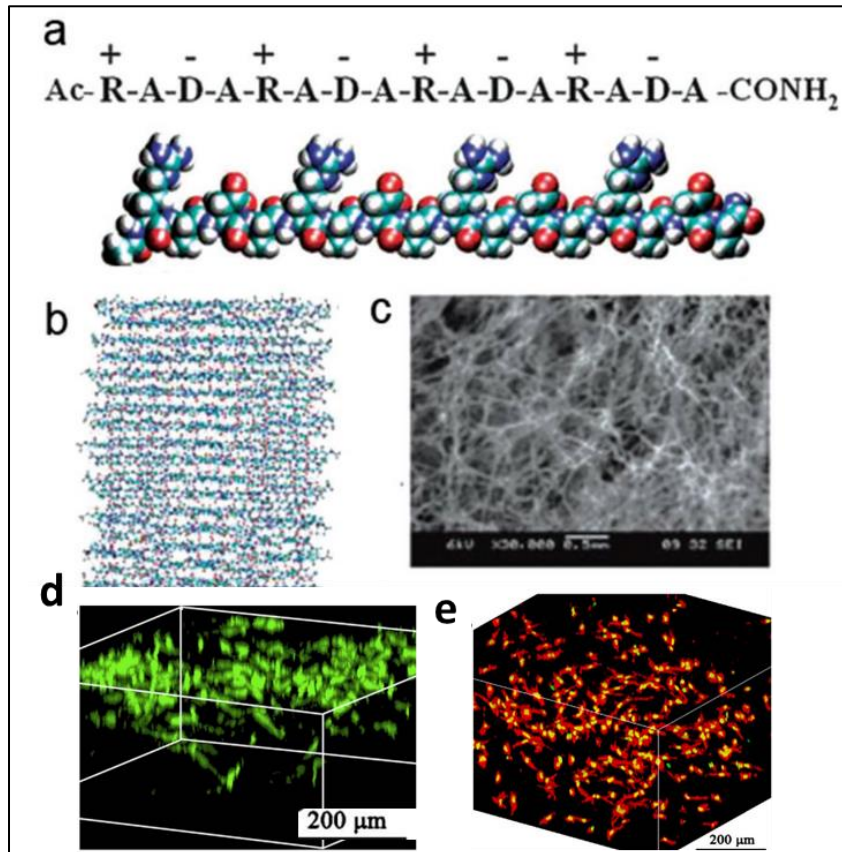


**Figure 1.52** (a) Amino acid sequence and molecular model of RAD16-I. (b) Hundreds of individual peptides self-assembly into a nanofiber. (c) SEM image of RAD16-I nanofibrous scaffold. (d) Laser confocal scanning microscopy images of bone cells. (e) HUVECs show the cell migrated several hundred microns into the peptide scaffold. (Adopted from Y. Yanlian, K. Ulung, W. Xiumei, A. Horii, H. Yokoi and Z. Shuguang, *Nano Today*, 2009, **4**, 193-210).

Similarly, K(SL)<sub>3</sub>RG(SL)<sub>3</sub>KGRGDS peptide can be dissolved in deionized water with sucrose and the charge of lysine-containing peptides may be screened by negatively charged heparin to form a hydrogel with the encapsulated dental pulp stem cells (DPSCs) and growth factors, e.g., vascular endothelial growth factor (VEGF).<sup>197</sup> Figure 1.53 displays DPSC cell in 3D after in vitro seeding into hydrogels. The cells appear elongated with stretched-out shapes and in contact



with neighboring cells. The cell clusters in the hydrogel can produce collagen as their own ECM to replace the synthetic carrier (Figure 1.53b). Further histologic analysis of *in vivo* transplantation shows that DPSC in the peptide hydrogels with growth factors (GFs) can form a vascularized soft connective tissue as dental pulp (Figure 1.53c–f). The cells can further degrade the hydrogel and replace it by a collagenous ECM (Figure 5d and e). Cells at the cell-dentin interface appear flat and have an intimate association with the dentin wall, where cellular processes extend into the dentinal tubules (Figure 1.53e). This custom-made, bioactive ECM at hand is able to support the formation of a vascularized soft connective tissue similar to dental pulp after transplantation *in vivo*. Owing to the striking resemblance between hydrogels and soft tissues, this supramolecular hydrogel is a promising material for dental treatment.<sup>197</sup>

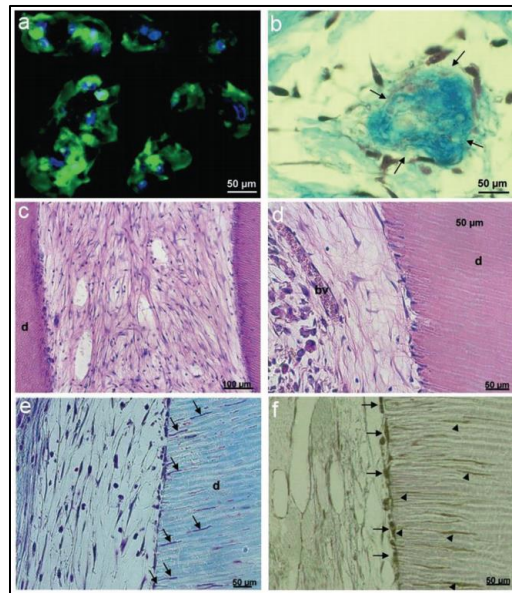


**Figure 1.53** DPSC morphology in  $K(SL)_3RG(SL)_3KGRGDS$  peptide-based 3D hydrogels. (a) Confocal microscopy shows that cells are stretched out and display cell-cell contacts. (b) Histologic Masson's trichrome stain reveals collagen deposition. (c) After 5 weeks of *in vivo* transplantation, DPSC have formed a pulp-like soft connective tissue. (d) Higher magnification shows blood vessels and a cell layer in intimate association with the dentin wall. (e) The cells extend processes into the dentinal tubules (arrows), a characteristic of odontoblast cell morphology. (f) The cell layer adjacent to the dentin as well as the cellular processes stain positive for dentin sialoprotein. (Adopted from K. M. Galler, J. D. Hartgerink, A. C. Cavender, G. Schmalz and R. N. D'Souza, *Tissue Eng Part A*, 2012, **18**, 176-184).

## General Introduction

Ulijn and co-workers reported aromatic short dipeptides based on 9-fluorenyl methoxy-carbonyl (Fmoc) (Figure 1.54a, Fmoc-FF and Fmoc-RGD).<sup>198, 199</sup> Powders of Fmoc peptides were dissolved in alkali (pH = 10.0 for Fmoc-FF) or acid solutions (pH = 3.0 for Fmoc-RGD) and then neutralized to pH 7.0 to make bioactive 3D hydrogels through hydrogen bonds and  $\pi$ - $\pi$  interactions. Cells could be in situ encapsulated inside the hydrogels by mixing Fmoc-peptide solution and cell suspension (Figure 1.54b). The hydrogel was found to promote aggregation of the encapsulated dermal fibroblasts through RGD integrin binding (Figure 1.54c–e).

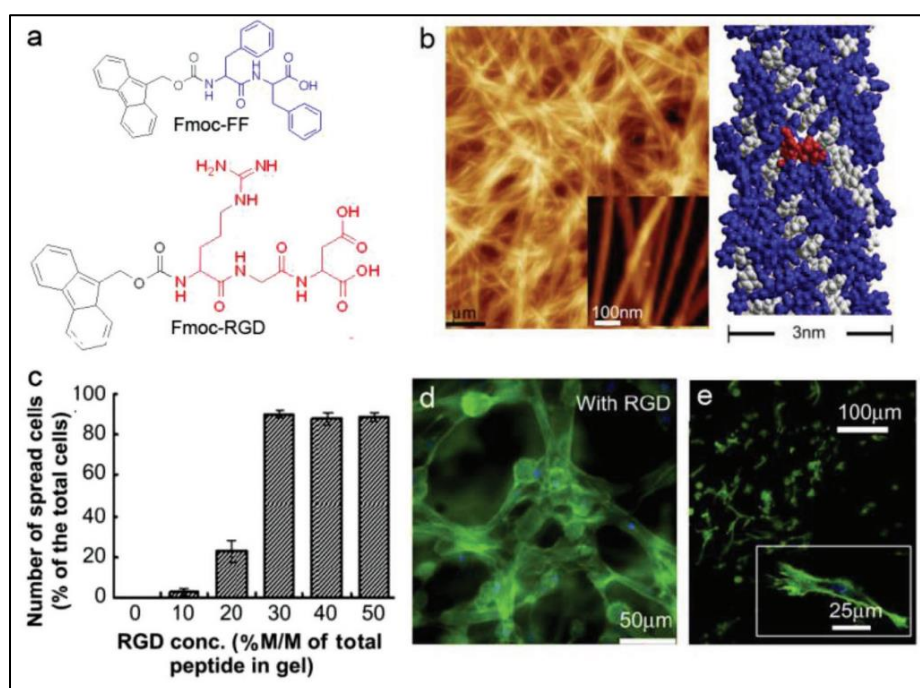


**Figure 1.54** (a) The chemical structures of the Fmoc-FF and Fmoc-RGD. (b) Left panel: AFM of nanofibers; right panel: RGD sequences are presented on the fiber surface. (c) The Fmoc-RGD concentration influenced cell spreading. (d) (HDFa) were well spread on hydrogel fibers. (e) Integrin blocking experiment. (Adopted from M. Zhou, A. M. Smith, A. K. Das, N. W. Hodson, R. F. Collins, R. V. Ulijn and J. E. Gough, *Biomaterials*, 2009, **30**, 2523-2530).

Xu et al. established a class of enzyme-triggered self-assembly based on amino acid derived precursors.<sup>200</sup> Tyrosine phosphate was coupled to the C-terminal of a  $\beta$ -amino acid derivative to give a precursor which could be hydrolyzed into hydrogelator after treatment with a phosphatase (Figure 1.55b). The mixture of



precursor and phosphatase was injected into a mouse and the in vivo gelation ability of this hydrogelator was evaluated (Figure 1.55c and d). The excellent biostability rendered the hydrogels as promising candidate for biomedical applications.

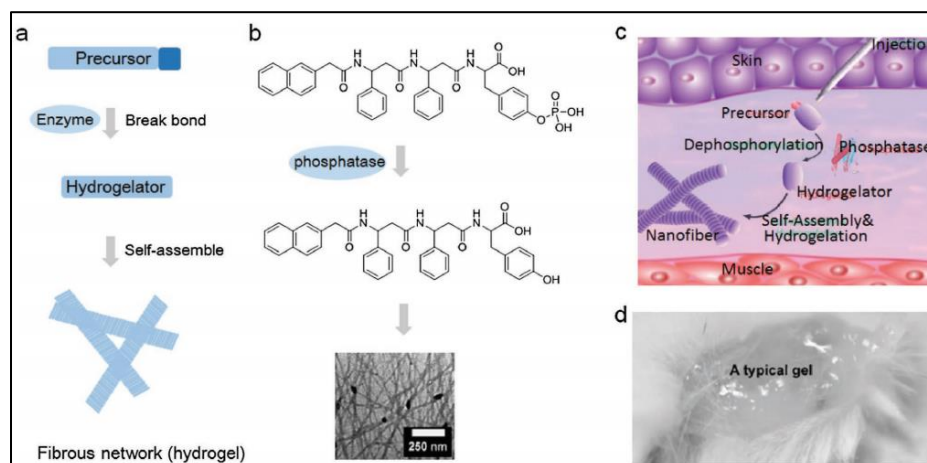


**Figure 1.55** (a) Illustration of enzyme-instructed self-assembly to form supramolecular hydrogels via bond cleavage. (b) Molecular structures of the precursor and its corresponding hydrogelators, and the TEM image of the self-assembled nanofibers. (c) Illustration of the formation of a supramolecular hydrogel in vivo. (d) A typical hydrogel formed at the injection site of a mouse. (Adopted from F. Zhao, C. S. Weitzel, Y. Gao, H. M. Browdy, J. Shi, H. C. Lin, S. T. Lovett and B. Xu, *Nanoscale*, 2011, **3**, 2859-2861.)

In a recent work, Sun and co-workers have designed an extracellular matrix called PGmatrix using a peptide sequence called h9e (FLIVI-GSII-GPGGDGPGGD).<sup>201</sup> The peptide forms strong hydrogel when dissolved in an acidic solution or when a neutral solution of the gelator is treated with calcium ions.<sup>202</sup> Examination of MS/MS spectra obtained for different calcium adducts of the h9e peptides (shows that in  $[M + Ca]^{2+}$  ion calcium is most likely coordinated by the carboxyl group of the internal D residue is and solvated by the C-terminal D. The PGmatrix has shown a superior Human induced pluripotent stem cells (hiPSCs) maintenance than traditional 2D cultures. The cells remained inside the gel in spheroid form. The spheroids in the universal peptide hydrogel are viable (85–96%) and show superior pluripotency and differentiation potential based on multiple bio-markers (Figure 1.56). Cell performance is influenced by the degradability of the hydrogel but not by gel strength. Without post-printing crosslinking aided by UV or visible lights or chemicals, various patterns are easily extruded from a simple star to a

kidney-like organ shape using the universal peptide hydrogel bioink (Figure 1.56) showing acceptable printability.<sup>201</sup>

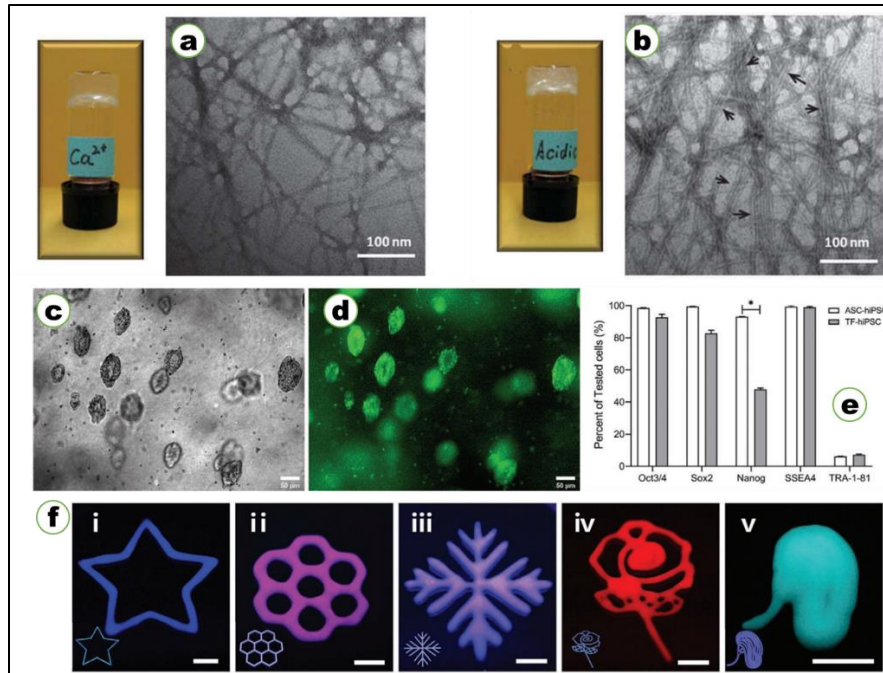


**Figure 1.56** (a) The h9e peptide forms porous hydrogel in presence of  $Ca^{2+}$  ions, (b) it forms more robust hydrogel in acidic medium, (c) The brightfield image and (d) fluorescence images of the cultured hiPSCs, (e) Flow cytometric analysis of two hiPSC lines cultured in 3D PGmatrix demonstrated high expression of Oct3/4, SOX2, NANOG, and SSEA4 but low expression of TRA-1-81. (f) Bioprinted PGmatrix constructs (3%) of different patterns. Scale bar. 5mm. (Adopted from H. Huang, J. Shi, J. Laskin, Z. Liu, D. S. McVey and X. S. Sun, *Soft Matter*, 2011, **7**, 8905-8912; Q. Li, G. Qi, X. Liu, J. Bai, J. Zhao, G. Tang, Y. S. Zhang, R. Chen-Tsai, M. Zhang, D. Wang, Y. Zhang, A. Atala, J.-Q. He and X. S. Sun, *Adv. Funct. Mater.*, 2021, **31**, 2104046).

## 1.8.2 Antimicrobial Hydrogels

Infectious disease remains a major threat to public health, and new antimicrobial agents is an utmost priority to fight against the multi-drug-resistant bacteria. The discovery of antimicrobial peptides has stimulated the use of self-assembly of peptide amphiphiles to develop antibacterial hydrogels. Schneider, Pochan and their co-workers reported a twenty-amino acid containing lysine-rich amphiphilic peptide (MAX1) based mechanically rigid hydrogel (Figure 1.57).<sup>203</sup> Solvent

exposed lysine on the surface of the  $\beta$ -sheet rich fibrils interact with the outer leaflet of bacterial cell surfaces, ultimately causing the disruption of bacterial cell membrane. Thus, this gel has been proven as inherently antibacterial and shows broad-spectrum activity against both Gram-negative (*Escherichia coli* and *Klebsiella pneumoniae*) and Gram-positive (*Staphylococcus epidermidis*, *Staphylococcus aureus* and *Streptococcus pyogenes*) bacteria without accumulating any exogenous antimicrobial agents. By systematically replacing the lysine residues MAX1 with arginine they developed second-generation (MARG1) that can be shear-thin delivered by syringe allowing easy administration (Figure 1.57).<sup>204</sup> The gel is highly active against the multidrug resistant bacteria while this is in contact with the peptide gel surface as evident from the live/dead assays (Figure 1.57). Hydrogel developed from self-assembling  $\beta$ -hairpin peptide having high content of arginine residue has also been reported and this hydrogel is active against *S. aureus*, *E. coli*, and *P. aeruginosa*, while being cytocompatibility towards mammalian cells.<sup>205</sup>

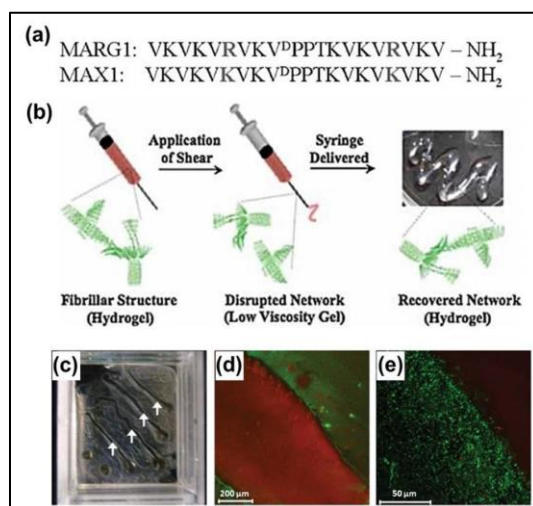


**Figure 1.57** (a) Amino acid sequences of MARG1 and MAX1. (b) Injectable  $\beta$ -Hairpin peptide hydrogels. (c) MARG1 hydrogel shear-thin delivered to a bed of MRSA. (d) Laser scanning confocal images of live/dead viability assays (e) Magnification of agar-hydrogel border where individual cocci are evident. (Adopted from D. A. Salick, D. J. Pochan and J. P. Schneider, *Adv. Mater.*, 2009, **21**, 4120-4123).

Chen and Li et al. reported the preparation of biocompatible hydrogels with antimicrobial activity against Gram-positive bacteria by taking advantage of the

intermolecular aromatic-aromatic interactions of Fmoc and the phenyl group.<sup>206</sup> They generated a hydrogel based on the co-assembly of a hydrogelators Fmoc-Phe (Fmoc-F) and an antibacterial building block Fmoc-Leu (Fmoc-L) and found that the co-assembled (Fmoc-F+Fmoc-L) supramolecular hydrogel is bactericidal against Gram-positive bacteria via a mechanism involving cell wall and membrane disruption (Figure 1.58). As the hydrogel is biocompatible with normal mammalian cells, the authors suggested that this type of antibacterial hydrogel could potentially serve as an antimicrobial coating in clinical devices and wound dressings or a topical agent for the treatment of clinical skin and wound infections mainly caused by Gram-positive bacteria such as *Staphylococcus aureus*.

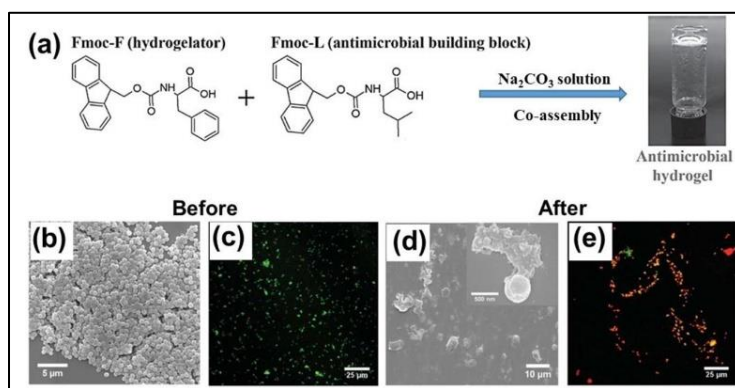


**Figure 1.58**(a) Antimicrobial hydrogel based on the co-assembly of Fmoc-F and Fmoc-L. (b) and (d) Representative SEM images and (c) and (e) overlapping fluorescence images for the LIVE/DEAD bacterial staining assay of *S. aureus* before and after contact with the co-assembled hydrogel for 2 h. (Adopted from I. Irwansyah, Y.-Q. Li, W. Shi, D. Qi, W. R. Leow, M. B. Y. Tang, S. Li and X. Chen, *Adv. Mater.*, 2015, **27**, 648–654).

A very simple long-chain amino acid containing dipeptide-based hydrogelators, reported from Banerjee's group, was found to form a proteolytically stable, mechano-sensitive hydrogel exhibiting remarkable and selective antimicrobial activity against Gram-negative bacteria. This thixotropic nature bestows an injectable property on the hydrogel and this can be utilized to inject by using a syringe. Furthermore, the hydrogel exhibits remarkable antibacterial activity against Gram-negative bacteria *Escherichia coli* and *Pseudomonas aeruginosa* (Figure 1.59).<sup>110</sup> They have also demonstrated that a small change in the molecular

structure of the gelator peptide not only turns the gelator into a non-gelator molecule under similar conditions, but also has a significant negative impact on its bactericidal character.

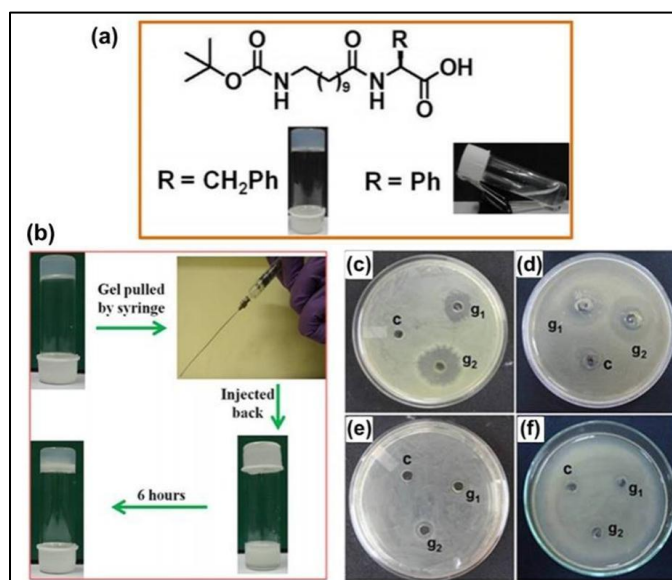


**Figure 1.59** (a) Chemical structures of dipeptides (b) Illustration of the injectable hydrogel. (c)-(f) Determination of the effect of hydrogel on Gram-negative and Gram-positive bacteria by agar-diffusion assay method: various bacteria [(c) *Escherichia coli*, (d) *Pseudomonas aeruginosa*, (e) *Staphylococcus aureus*, and (f) *Bacillus subtilis*] were spread on an Agar plate. (Adopted from A. Baral, S. Roy, S. Ghosh, D. Hermida-Merino, I. W. Hamley and A. Banerjee, *Langmuir*, 2016, **32**, 1836-1845).

A series of simple long-chain phenylalanine-containing dipeptide-based hydrogelators are reported by Banerjee and co-workers.<sup>207</sup> They have designed five hydrogelators by varying the chain length containing the free amine group. These gelators form fibrillar hydrogels at pH 6.6. The gel strength and gel recovery time have been successfully modulated by varying the alkyl chain length of the N-terminally located amino acid residues. Similarly, the thermal stability of these hydrogels has been nicely tuned by altering the alkyl chain length of the N-terminally located amino acid residues. All of these hydrogelators were studied for antibacterial activity and interestingly, among all gelators in the series only the gel obtained from the longer alkyl chain containing gelators (P4 and P5 in the Figure 1.60) than the other gelator analogues exhibit potential antibacterial activity against Gram positive (*Staphylococcus aureus* and *Bacillus subtilis*) as well as Gram negative (*Escherichia coli*) bacteria (Figure 1.60).<sup>207</sup> Both of these hydrogels



also show negligible lytic effect against human erythrocytes. Furthermore, these hydrogels show significant stability towards proteolytic enzymes present inside the cells, thus enhancing the hydrogel's applicability for practical purposes in future.

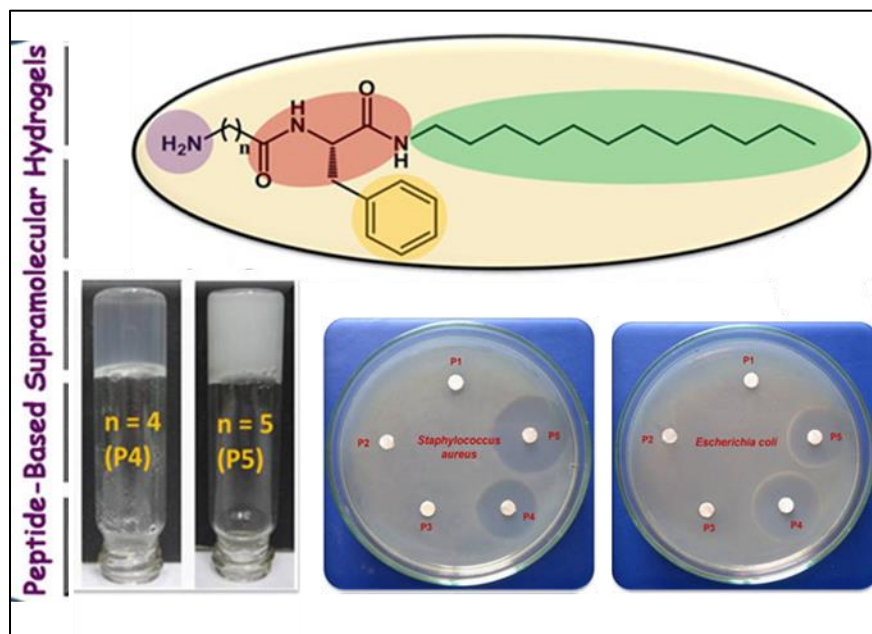


**Figure 1.60** The general chemical structure of the hydrogelators. Hydrogels formed with P4 and P5 shows antimicrobial activities against both gram-positive and gram-negative bacteria. (Adopted from N. Nandi, K. Gayen, S. Ghosh, D. Bhunia, S. Kirkham, S. K. Sen, S. Ghosh, I. W. Hamley and A. Banerjee, *Biomacromolecules*, 2017, **18**, 3621-3629).

Metal ion-induced peptide assembly is an interesting field. As compared to traditional antibacterial  $\text{Ag}^+$ , rare earth metal ions possess the advantage of antibacterial performance with photostability and low toxicity. In a recent work, Xu and co-workers have designed a new peptide Fmoc-FFWDD-OH which could form a stable hydrogel induced by rare earth metal ions, including  $\text{Tb}^{3+}$ ,  $\text{Eu}^{3+}$ , and  $\text{La}^{3+}$  (Figure 1.61).<sup>208</sup> The mechanical properties were characterized by rheological measurements, and they exhibited elasticity-dominating properties. Transmission electron microscopy (TEM) images showed a large number of nanoscale fiber structures formed in the hydrogel.<sup>208</sup> Circular dichroism (CD) spectra, Fourier transform infrared (FT-IR) spectra, ThT assays, and X-ray diffraction (XRD) pattern illustrated the formation mechanism of the fiber structure. The rare earth ion-induced peptide hydrogel was proved to possess good antibacterial

performance on *Escherichia coli* with excellent biocompatibility. The introduction of rare earth metal ions may have some potential applications in the biological antibacterial and medical fields.

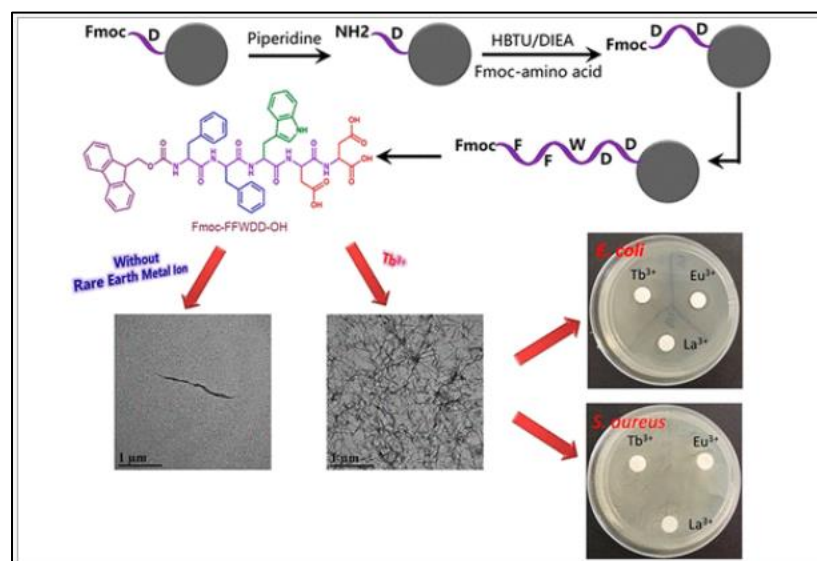


**Figure 1.61** Schematic presentation of solid-state synthetic strategy of the peptide gelator *Fmoc-FFWDD-OH*. The gelation takes place in presence of rare earth metal cations  $Tb^{3+}$ ,  $Eu^{3+}$  and  $La^{3+}$ . The metallogels show good antibacterial effect on *E.coli*. (Adopted from W. Xu, Z. Zhang, X. Zhang, Y. Tang, Y. Niu, X. Chu, S. Zhang and C. Ren, *Langmuir*, 2021, **37**, 12842-12852).

### 1.8.3. Catalytic activity of Hydrogels

Peptide based hydrogels are highly ordered arrays of peptide molecules; scientists have used these materials in catalysing various typical organic reactions as well as a biocatalyst. Some research groups showed that a histidine containing peptide hydrogel act as an artificial enzyme that mimic the activity of the natural enzyme like esterase. Esterase enzyme plays an important role inside the body to break down the drugs molecules into corresponding smaller fragments. The esterase-like activity of the peptide-based gel has been checked by taking a model substrate, *p*-nitrophenyl ester.<sup>209-214</sup>

Miravet and Escuder reported a (L)-proline-based supramolecular hydrogelator that affords a supramolecular hydrogel at a concentration of 0.25% (w/v). This hydrogel has a remarkable efficiency as a heterogeneous organocatalyst for a direct aldol reaction with high stereoselectivity (up to 90% ee) and also with easy

recovery and regeneration of the catalyst (Figure 1.62).<sup>209</sup> In another study, they reported covalently appended imidazole based supramolecular hydrogel that showed the esterase like activity and able to hydrolyse the *p*-nitrophenyl acetate (*p*-NPA) as well as inactivated esters, and L and D-phenylalanine methyl esters. The ordered arrangement of the catalytic centres upon self-assembly of molecules into a fibrillar network is taken advantage to attain improved catalytic activity when compared to the non-aggregating analogue. (Figure 1.62)

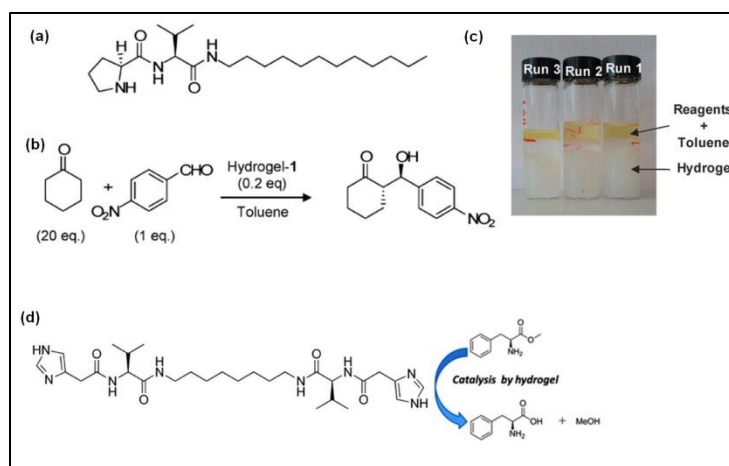


**Figure 1.62** (a) Molecular structure of the L-proline based hydrogelator. (b) Catalytic role of the hydrogel in aldol reaction. (c) Macroscopic feature of the catalytic system used for several runs (Adopted from F. Rodríguez-Llansola, J. F. Miravet and B. Escuder, *Chem. Commun.*, 2009, 7303-7305). (d) Molecular structure of imidazole containing gelator that showing hydrolysis of (L)-phenylalanine methyl ester. (Adopted from N. Singh, M. P. Conte, R. V. Ulijn, J. F. Miravet and B. Escuder, *Chem. Commun.*, 2015, **51**, 13213-13216).

Stupp and co-workers demonstrated the esterase like activity of  $\beta$ -sheet forming peptide amphiphile by using a 2,4-dinitrophenyl acetate (DNPA) as a substrate (Figure 1.63). At the terminal of the peptide molecule contains two histidine residues linked to a lysine residue and form a gel pH above 6.5 that indicates high-aspect-ratio of nanofibers. They also showed that hydrolysis reaction took place on the surface of cylindrical nanostructures formed by aggregation of peptide amphiphile due to the higher number of active site at the surface.<sup>211</sup>



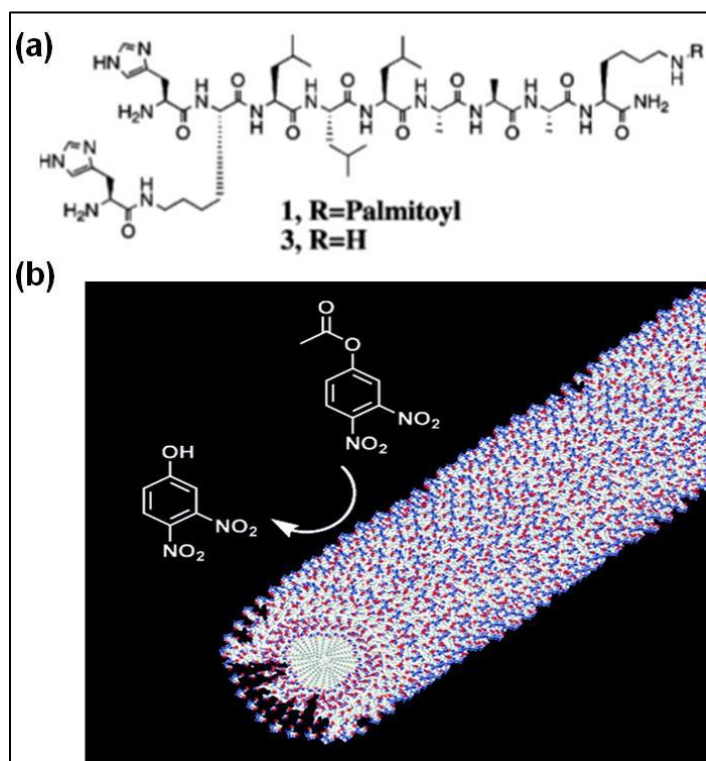


**Figure 1.63**(a) Chemical structure of histidine containing peptide amphiphile (b) The Graphical image shows the hydrolysis of dinitrophenyl ester at the surface of cylindrical structure formed by peptide amphiphile. (M. O. Guler and S. I. Stupp, *J. Am. Chem. Soc.* 2007, **129**, 12082-12083).

Liang and co-workers designed an artificial hydrolytic catalyst via co-assembly of histidine and arginine based short peptides. They synthesized three peptide amphiphile and one of the molecules contains histidine residue as a active site but in other two molecules histidine was absent. They demonstrated that the peptide molecule exhibited much higher catalytic efficiency (when the assembled hydrolase catalytic sites were embedded in a matrix of peptide nanofibers) than that of the peptide nanofibers without any catalytic sites. This suggests that a well-ordered nanostructure is an attractive scaffold for developing new artificial enzymes. (Figure 1.64)<sup>212</sup>

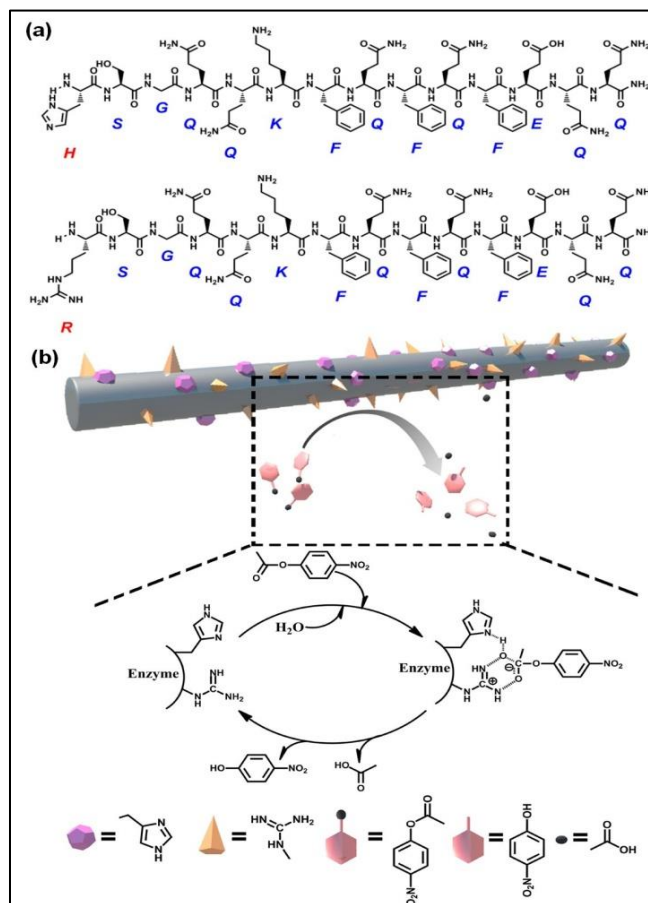


**Figure 1.64** (a) Chemical structure of histidine and arginine containing peptide amphiphile (b) schematic representation of possible mechanisms for the cleavage of *p*-nitrophenyl acetate (PNPA) catalyzed by histidine-arginine based co-assembled nanofibers. (Adopted from C. Zhang, X. Xue, Q. Luo, Y. Li, K. Yang, X. Zhuang, Y. Jiang, J. Zhang, J. Liu, G. Zou, and Xing-J. Liang, *ACS Nano*, 2014, **8**, 11715–11723).

## 1.9. Metal nanoclusters

### 1.9.1. Nano: The size perspective

After identification of existence of a gold particle that behaves differently than its larger counterparts in interacting with lights, the major challenge is determination of its size. The invention of transmission electron microscopy (TEM) by Knoll and Raska in 1931 was an important asset, as the size of the synthesized nanoparticles could be precisely measured. J. Turkevich, in a pioneering work,<sup>215</sup> synthesized gold nanoparticles by employing citrate ions and gold salt in aqueous solution.

TEM imaging of these gold nanoparticles suggests that the size of the synthesized gold particles was 10-20 nm.<sup>215</sup>

Thus, the word “nano”, from the Greek “nanos” (or Latin “nanus”) become the key of modern science to which everyone is looking up. “Nano” refers to the  $10^{-9}$  power, or one billionth. In these terms, it refers to a meter, or a nanometer, which is on the scale of atomic diameter. A typical carbon-carbon bond length, or the spacing between these atoms in a molecule, are in the range of 0.12-0.15 nm, ten hydrogen atoms are about 1 nm, a DNA double-helix has a diameter around 2 nm, a cell membrane is about 9 nm thick, a virus is about 70 nm long, and a red blood cell is 5000 nm in diameter. A single particle of smoke is in the order of 1000 nm. A human hair is about 50,000-1,00,000 nm across (Figure 1.63).

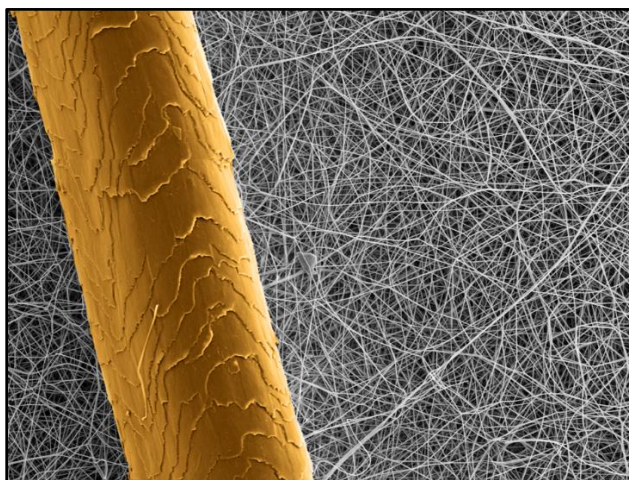


**Figure 1.63** Comparison between nanofibres with a single human hair (in yellow) (Adopted from [www.exceedfilter.com](http://www.exceedfilter.com)).

For example, if a block of gold is cut into smaller and smaller pieces it would still have the same color, melting temperature, etc. But at certain ranges of the nanoscale, gold particles behave differently.<sup>216</sup> A sheet of paper is about 100,000 nm thick. Figure 1.64 describes the size variation from a single atom to a human hair. Generally, nanoscale refers to measurements of 1-100 nm.

Now, after getting the idea of the size, the important question is what is special in the size and why it is important. When objects are below 100 nm in size, they can exhibit unexpected chemical and physical properties. The optical, electrical, mechanical, magnetic, and chemical properties can be systematically

manipulated by adjusting the size, composition, and shape of this class of materials on the sub-100 nm length scale.

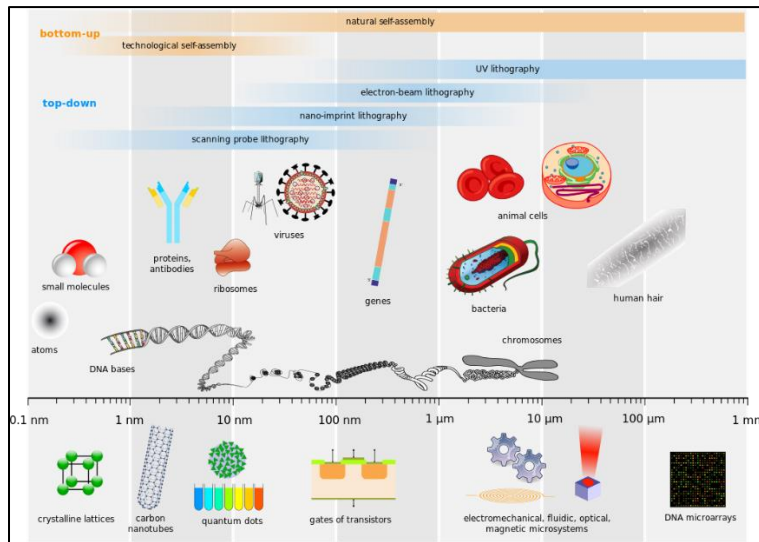


**Figure 1.64** Comparison of length scale of different objects starting from a human hair to much smaller materials ending up to a single atom (Adopted from [www.commonswikimedia.org](http://www.commonswikimedia.org)).

For example, if a block of gold is cut into smaller and smaller pieces it would still have the same color, melting temperature, etc. But at certain ranges of the nanoscale, gold particles behave differently.<sup>216</sup> The properties of materials with nanometric dimensions are significantly different from the bulk materials due to the increase in surface area/volume ratio. Optical and electronic properties of nanomaterials would be different from their bulk counterpart. In nanomaterials the catalytic property is also enhanced than their bulk counterpart due to greater surface area. Catalytic efficiency of nano dimensional materials increases because more surface area ensures its greater contact with the substrate molecules.

### 1.9.2. Nanomaterial and Nanoparticle: Definition

Nanomaterial is a research area that takes a material science-based approach to nanotechnology. It deals material with morphological features on the nanoscale. The European Commission approved the following definition of a nanomaterial: “A natural, incidental or manufactured material containing particles, in an unbound state or as an aggregate or as an agglomerate and where, for 50% or more of the

particles in the number size distribution, one or more external dimensions is in the size range 1 nm – 100 nm.”

In nanotechnology, a particle is defined as nanoparticles when its size remains between 1 and 100 nm. Nanoparticle research is currently an area of immense scientific interest due to a wide variety of potential applications in biomedical, optical and electronic fields.

### 1.9.3. Development in metallic nanostructures field

The method (using citrate as reducing agent as well as stabilizer for gold nanoparticles) developed by J. Turkevich<sup>215</sup> was further modified by G. Frens and it has since become a common method that is utilized even now a days for preparing citrate-capped gold nanoparticles of >10 nm diameter.<sup>217, 218</sup> The early synthesis of some of the metal nanoparticles followed this approach of using some kind of stabilizer to prevent the nanoparticles from aggregation due to collisions in the solution state. The common stabilizers used are surfactants, amphiphilic polymers, ligands, and even solvent molecules if they can bind to nanoparticle surfaces.<sup>219</sup> An early example of producing magnetic nanoparticles was proposed by Hess *et al.* to prepare Co-colloid of 10-100 nm. In this method,  $\text{Co}_2(\text{CO})_8$  was heated to a high temperature in the presence of dispersant polymer.<sup>220</sup> The generation of metal nanoparticles by thermal decomposition of metal-organic precursor in the presence of a stabilizer became a common approach for the synthesis of Fe, Co, Ni, and Cd metal nanoparticles.<sup>221</sup> Better size control of metal nanoparticles was achieved using another process where high concentration of reducing agents like citrate or sodium borohydride were used. Synthesis of phosphine protected gold nanoparticles was developed by Schmid *et al.* by using excess  $\text{NaBH}_4$ , where the size of gold nanoparticles was ~1.4 nm.<sup>222</sup> “Brust-Schiffin method” reported a quite popular method for synthesis of gold nanoparticle in 1994. This method was motivated by the thiol self-assembled-monolayer (SAM) on metal surfaces.<sup>223, 224</sup> This was the first report of using thiol as a capping ligand for the synthesis of gold nanoparticles. The Brust’s method involves two steps where the first step involves the phase transfer of gold salt by using a phase transfer agent (surfactant) and subsequently the Au(I) thiolate polymer was reduced by  $\text{NaBH}_4$  to form nanoparticles. The use of excess reducing

agent (typically 10 times the gold salt) helped in narrowing the size distribution. This nanoparticle system was highly stable due to the strong interaction of thiol with the gold surface and the van der Waals interactions. The size of the nanoparticle can be effectively controlled by the ratio of precursor gold salt to alkanethiol. Due to their extraordinary stability, these thiol-protected nanoparticles can be even isolated and stored in powder form and further re-dispersed in any desired solvent. This was in strong contrast to the behavior of the earlier mentioned gold colloid in solution that was stabilized by charge stabilization.<sup>225</sup>

Development of nanoparticles has shown the most fundamental phenomenon of a nanoparticle is the surface plasmon resonance (SPR). SPR of particles with size below 2 nm is surprising. This was because of the purity of the isolated nanoparticles. The high molar absorptivity coefficient of plasmonic nanoparticle will dominate the spectral feature of smaller nanoparticles. So, the intriguing question is how the spectral properties of nanoparticle changes, when their size is smaller than 2 nm? When the size of nanoparticles is below 2 nm, the metal core possesses only a countable number of atoms (up to ~200) and such ultrasmall particles behave as clusters of atoms or like molecules. The properties of such clusters are different than the bulk metal, and also different than their larger counterparts (*i.e.*, conventional nanoparticles). Some of the clusters are also called super atoms as they show some of the properties like atoms. It would be interesting to know at what size (*i.e.*, precise number of atoms) the gold nanoparticles start showing quantum confinement.

Free electron model throws light in determining the limiting size of the nanoclusters as the quantum size regime can be estimated using this model. As the size of the particle becomes smaller, the average spacing ( $\delta$ ) of the electronic energy levels becomes considerable and  $\delta$  increases with decreasing size. The average spacing ( $\delta$ ) can be roughly expressed as

$$\delta = \frac{E_f}{N}$$

where  $E_f$  refers to the Fermi energy and  $N$  is the number of metal atoms, since  $N$  can be expressed as  $\propto d^3$  ( $d$  is the nanoparticle diameter). So, the spacing is inversely proportional to the cube of particle diameter. If room temperature

thermal energy ( $k_B T$ ) is used as a criterion for considering quantum confinement, then the following relation is obtained:

$$\delta = k_B T$$

after substituting the value of Fermi energy for gold,  $E_f = 5.5$  eV into the equation we can get the critical number of gold atom to be 220 atoms. The number of atom and the particle volume are related as

$$N = (59 \text{ nm}^{-3}) V$$

This gives the value of equivalent diameter to be  $\sim 2$  nm. Thus, for nanoparticles below 2 nm the electronic energy quantization will dominate and the collective plasmon mode will no longer be supported. To differentiate such ultrasmall particles from conventional plasmonic nanoparticles, they are often called nanoclusters. Here, when the size of the particle is decreased down to a few atoms, the size approaches the Fermi wavelength of electrons leading to break up of the continuous density of states into discrete energy levels. This leads to the outcome of dramatically different optical, electrical and chemical properties compared to larger nanoparticles.

#### 1.9.4. Importance and scopes of metallic nanoclusters

In the smallest size regime, metal clusters become “molecular species”,<sup>226-229</sup> and discrete states with strong fluorescence can be observed.<sup>230</sup> The nanoclusters provide the “missing link” between atomic and nanoparticle behavior in noble metals, these highly fluorescent noble metal nanoclusters smoothly link the optical and electronic structure transitions from atoms to nanoparticles with observable free electron behavior and also offer new opportunities for creating new biological labels,<sup>231, 232</sup> energy transfer pairs, and other light emitting sources in nanoscale electronics. As the size of the nanocluster is confined within the quantum regime, they are often called quantum clusters.<sup>233</sup> Sub-nanometer-sized metal nanoclusters (gold/silver/platinum) display molecule-like properties and they have discrete size-dependent electronic state.<sup>234</sup> Their distinct molecule-like electronic transition resulted in fascinating properties including fluorescence,<sup>235</sup> redox-like charging behavior,<sup>234</sup> ferromagnetism<sup>236</sup> and unique size- and shape-dependent catalytic,



## General Introduction

optical, electrical, magnetic, and chemical properties that are often different from their bulk (Figure 1.65).<sup>237, 238</sup> They found prospective applications in bioassays and biolabeling,<sup>239</sup> sensing,<sup>240</sup> single molecular spectroscopy,<sup>241</sup> catalysis,<sup>240, 242</sup> and nanoelectronics.<sup>234</sup>

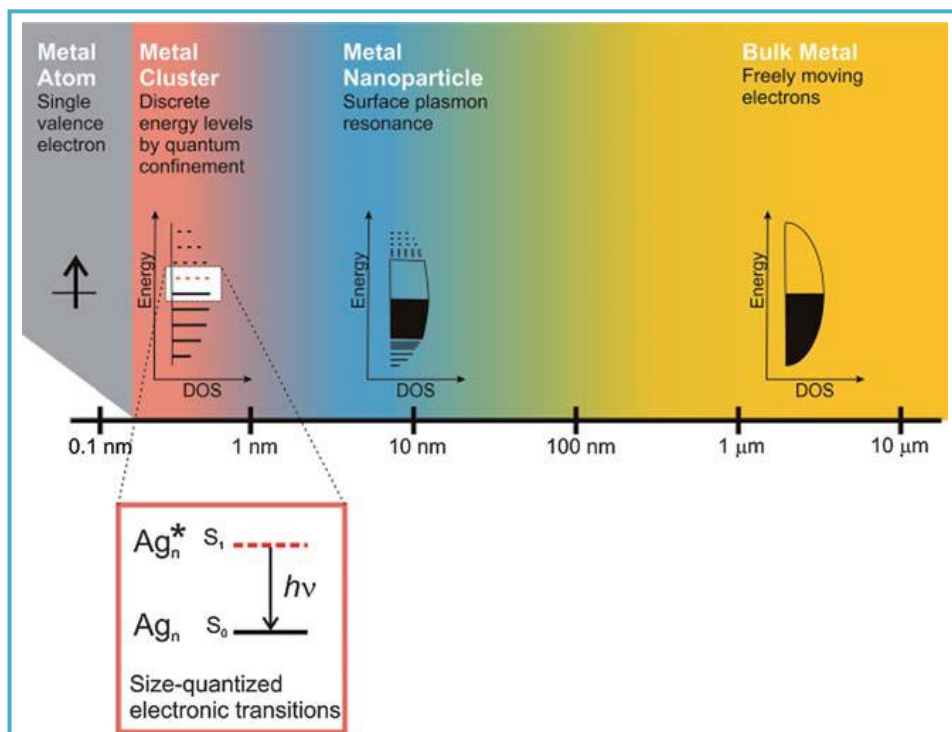


**Figure 1.65** The effect of size on metals. Whereas bulk metal and metal nanoparticles have a continuous band of energy levels, the limited number of atoms in metal nanoclusters results in discrete energy levels, allowing interaction with light by electronic transitions between energy levels. Metal nanoclusters bridge the gap between single atoms and nanoparticles (Adopted from I. Diez and R. H. A. Ras, *Nanoscale*, 2011, **3**, 1963-1970).

A strong fluorescent emission can often be observed upon excitation of these nanoclusters in the UV–visible range.<sup>235</sup> They also exhibit size,<sup>243</sup> ligand,<sup>244</sup> solvent<sup>245</sup> and temperature<sup>246</sup> dependent fluorescence properties. The final chapter of this thesis deals with synthesis of copper nanoclusters and their applications in a hybrid system.



### 1.9.5. Fluorescent Copper Nanoclusters

Fluorescent copper nanoparticles (CuNCs) have gradually become an active research area due to their low cost, good water solubility, wide availability and excellent optical properties.<sup>247</sup> The biggest advantage of CuNCs is their low-cost and tunable fluorescence properties compared to fluorescent gold and silver nanoparticles, resulting in the extensive synthesis and wide applications of CuNCs. Before 2010, few reports about CuNCs have been published as they are easily oxidised and difficult to be prepared. However, considerable efforts have been devoted to explore the preparation and applications of CuNCs with different emissions and good biocompatibility since 2010 and a great progress has been achieved since last few years.

Like other metal Nanoclusters fluorescent properties of the CuNCs are one of the key features of them. Recently, lots of efforts have been devoted to prepare various water-soluble CuNCs with different emissions from blue to red (Figure 1.66). The fluorescence of CuNCs is generally attributed to the electronic transitions between the occupied d bands and states above the Fermi level (ca. sp bands) or the electronic transitions between the highest occupied molecular orbital (HOMO) and the lowest unoccupied molecular orbital (LUMO).<sup>248</sup>

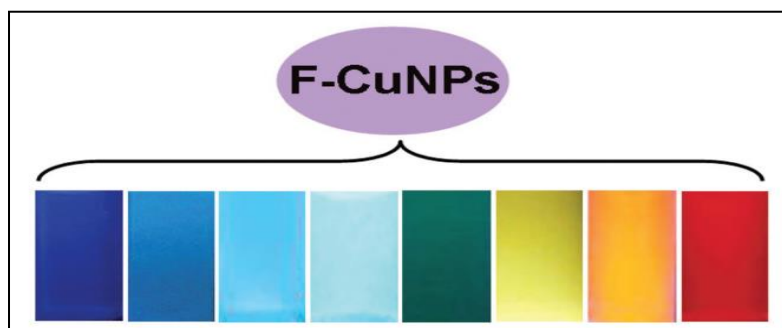


**Figure 1.66** CuNCs with different emissions from blue light to red light. (Adopted from Y. Guo, F. Cao, X. Lei, L. Mang, S. Cheng and J. Song, *Nanoscale*, 2016, **8**, 4852.)

The ligands show a significant effect on the fluorescence properties of CuNCs. For example, CuNCs stabilized by double-stranded DNA (dsDNA) exhibit bright fluorescence at 587-600 nm under excitation at 340 nm.<sup>249</sup> However, poly

(thymine) stabilized CuNCs emit red fluorescence around 615 nm with excitation at 340 nm ultraviolet (UV) light. The fluorescence intensity increases with the length of the poly T segment within single-stranded DNA (ssDNA).<sup>250</sup> Moreover, the synthetic method also significantly affects the fluorescence properties of CuNCs. For example, the bovine serum albumin (BSA)-templated CuNCs can exhibit blue and red emission due to different synthetic methods.<sup>251</sup>

### 1.9.5.1. Synthesis of Copper Nanoclusters

Stabilization of CuNCs continues to be an enigma to the scientists. The lower redox stability of Cu(0) with its lower standard reduction potential ( $E^0_{\text{Cu}^{2+}/\text{Cu(s)}} = +0.377 \text{ V}$ ) compared to other members of Group 11 noble metals, like Ag and Au ( $E^0_{\text{Ag}^+/\text{Ag(s)}} = +0.799$  and  $E^0_{\text{Au}^{3+}/\text{Au(s)}} = +1.5 \text{ V}$ ) makes such tiny sized particles very much reactive towards environmental conditions.<sup>252</sup> However, high costs of Ag and Au noble metal precursors limit their large-scale production, therefore synthesis of CuNCs is not only challenging but also interesting research field for both scientific and industrial researchers. Recently, various synthetic techniques have been developed to prepare water-soluble CuNCs with different emissions from blue to red (Figure 1.66). Generally, CuNCs are formed by the reduction of  $\text{Cu}^{2+}$  in the presence of suitable reducing agents and stabilizing agents, which can markedly affect their properties. Moreover, the stabilizing agents of CuNCs are responsible for their fluorescence emission and their sizes. Therefore, we will discuss the fabrication strategies of various CuNCs organized by the stabilizing agents used during synthesis.

#### 1.9.5.1.1. DNA oligonucleotides

DNA oligonucleotides, a kind of versatile template, have been utilized to synthesize a variety of functional nanoparticles.<sup>253-255</sup> In 2010, Mokhir's group has firstly found that dsDNA can be used as an efficient template for the formation of CuNCs in a solution of  $\text{Cu}^{2+}$  and ascorbate, and the ssDNA template cannot lead to the formation of CuNCs. The formed CuNCs exhibit excellent fluorescence centered at 587–600 nm. Interestingly, the fluorescence intensity and the size of CuNCs can be controlled by changing the length of the dsDNA template. In the procedure for the formation of CuNCs, copper(I) from the reduction of copper (II) by ascorbate can produce copper (II) and copper (0) via the disproportionation

reaction. The formed copper (0) is then clustered on dsDNA, leading to the formation of stable F-CuNPs (Figure 1.67).<sup>253</sup> This method has captured numerous scientists' interest in CuNPs. Subsequently, researchers have found that the AT sequences are better templates for the formation of dsDNA-templated CuNCs in comparison with random sequences.<sup>256</sup>

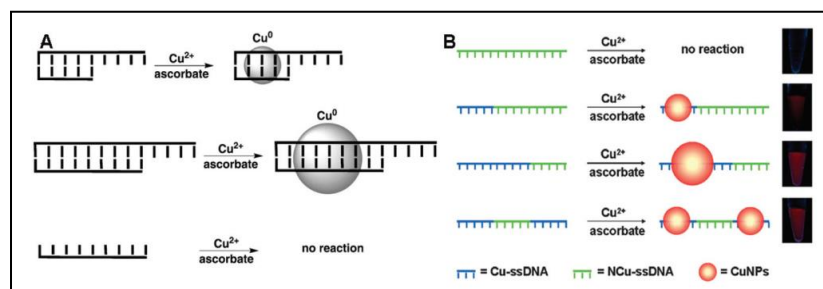


**Figure 1.67** Schematic illustration of the effect of DNA oligonucleotides on the formation of F-CuNPs. (Adopted from, A. Rotaru, S. Dutta, E. Jentsch, K. Gothelf and A. Mokhir, *Angew. Chem., Int. Ed.*, 2010, **49**, 5665–5667; Z. Qing, X. He, D. He, K. Wang, F. Xu, T. Qing and X. Yang, *Angew. Chem., Int. Ed.*, 2013, **52**, 9719–9722.)

### 1.9.5.1.2. Polymers

Polymers with various structures were used as templates for the synthesis of CuNCs. However, the first report dates back almost two decades when Zhao *et al.* used fourth-generation (G4) poly(amidoamine) (PAMAM) dendrimers with an ethylenediamine core (G4-OH) as templates to prepare a mixture of CuNCs consisting of 4 to 64 atoms in their compositions with an average diameter of less than 1.8 nm.<sup>257</sup> Highly stable and fluorescent (QY of 3.8% in ethanol) CuNCs were synthesized from the reduction of aqueous solutions of  $\text{CuSO}_4$  and polyethyleneimine (PEI) with hydrazine hydrate upon heating at 95 °C for 19 h (Figure 1.68a).<sup>258, 259</sup> When functionalized lipoic acid (LA) attached to a tuneable length of polyethylene glycol (PEG) segment was used as a template, the reduction with  $\text{NaBH}_4$  resulted in the formation of good-quality and highly fluorescent CuNCs (QY of 3.6% in water) with an average size of 2.5 nm.<sup>260</sup> The formed clusters showed long-term stability when exposed to daylight and UV irradiation. However, when a similar reaction was carried out using both dihydrolipoic acid

(DHLLA) and poly(vinylpyrrolidone) (PVP)<sup>261</sup> or just PVP alone<sup>262</sup> as capping agents and ascorbic acid as a reductant, the synthesis resulted in the formation of CuNCs with an average size of 2 nm. Polystyrene sulfonate (PSS)(Figure 1.68b)<sup>263</sup> and other multidentate polymers<sup>264</sup> as templating scaffolds were also applied in the synthesis of CuNCs. In 2012 Hui Zhang *et al.* reported the photoreductive synthesis of highly fluorescent metal nanoclusters of Cu, Ag, and Au (QYs of 2.2, 6.8, and 5.3%, respectively) in the presence of poly(methacrylic acid) functionalized with pentaerythritol tetrakis 3-mercaptopropionate (PMAA-PTMP) polymer upon UV-irradiation.<sup>265</sup> It was found that AuNCs were relatively stable as compared to copper and silver in the presence of foreign metal ions.

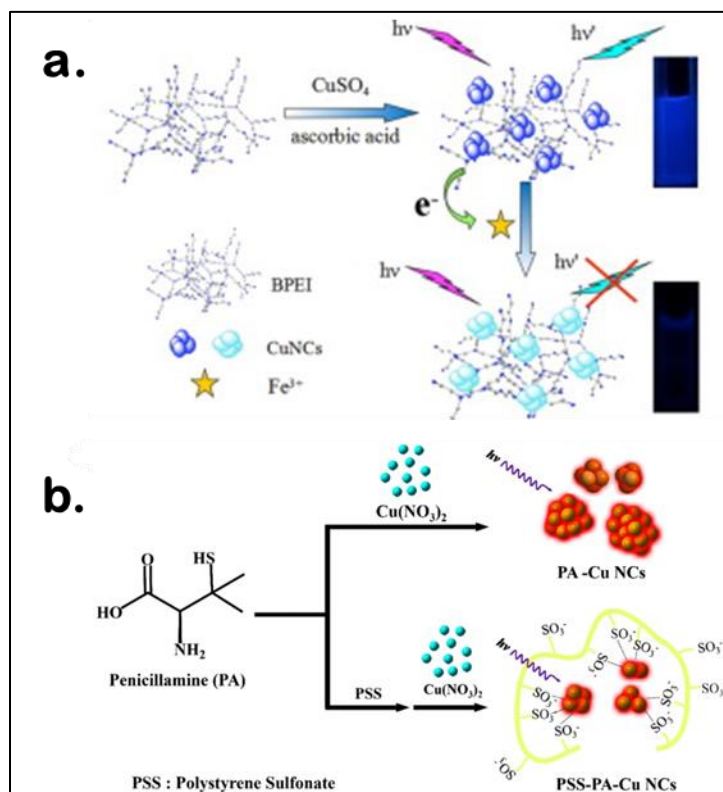


**Figure 1.68** (a) Synthesis strategy for the BPEI-CuNCs, their stability under varying pH and the mechanism of the branched polyethylenimine (BPEI)-CuNCs probe for  $Fe^{3+}$  sensing (Adopted from J. Feng, Y. Ju, J. Liu, H. Zhang and X. Chen, *Anal. Chim. Acta*, 2015, **854**, 153-160). (b) A scheme depicting a plausible mechanism for the synthesis of PSS-stabilized penicillamine (PA)-CuNCs and the photographs of the PSS-PA-CuNCs synthesized under different concentrations of PSS, from 0.005 to 0.5 wt% (Adopted from P.-C. Chen, Y.-C. Li, J.-Y. Ma, J.-Y. Huang, C.-F. Chen and H.-T. Chang, *Sci. Rep.*, 2016, **6**, 24882).

### 1.9.5.1.2. Protein

Proteins as structural biomolecules were widely used for the synthesis of versatile and biocompatible CuNCs (Figure 1.69). Among a huge number of accessible proteins, bovine serum albumin (BSA) gained considerable attention due to its availability, high-water solubility, and ability to bind various organic and inorganic substances in a noncovalent fashion. Due to the well-defined structure, containing charged amino acids and 35 thiol groups from Cys residues, BSA offers perfect albumin-binding sites for nanocluster formation.<sup>266, 267</sup> The synthesis of CuNCs involves three steps till completion. In the first step, upon mixing the reactants, at neutral pH,  $-\text{COOH}$  carboxylate groups of the protein partially dissociate and immediately form a complex with  $\text{Cu}^{2+}$ . The coordination complex resulted in the formation of a viscous paste. To enhance the solubility and further reduction with BSA, in the second reaction step, the pH of the medium needed to be increased to 12 by adding 1 M NaOH under heating at 55 °C. However, as a reducing agent, BSA is relatively weak, and to completely reduce  $\text{Cu}^{2+}$  to metallic copper, different reducing agents such as hydrogen peroxide<sup>251, 268</sup> and hydrazine hydrate ( $\text{N}_2\text{H}_4 \cdot 2\text{H}_2\text{O}$ )<sup>269-271</sup> have been proposed to facilitate the last step of the reduction process. For example, the addition of a trace amount of hydrogen peroxide not only reduces the  $\alpha$ -helix of the protein and increases the number of random and  $\delta$ -structures, but also produces  $\cdot\text{OH}$  radicals, which can break peptide bonds in BSA and reduce the ordered  $\alpha$ -helix structures. Altogether, this enhances the reduction of  $\text{Cu}^{2+}$  by the protein and leads to faster cluster formation.<sup>251</sup> On the other hand, while using hydrazine hydrate, with decreasing the pH, the  $\alpha$ -helix can be transformed to  $\delta$ -sheets and random coil structures, thus increasing the availability of functional groups ( $-\text{OH}$ ,  $-\text{NH}$  and  $-\text{COOH}$ ) that can interact with the cluster.<sup>271</sup> Other proteins such as trypsin,<sup>272</sup> human serum albumin (HSA),<sup>273</sup> transferrin,<sup>272</sup> cellulase<sup>274</sup> and lysozyme<sup>275</sup> were also reported as effective capping agents for the preparation of fluorescent copper nanoclusters. Proteins are important class of protecting group which is seen to use for NC synthesis. Use of proteins will grow more and more in coming ages.

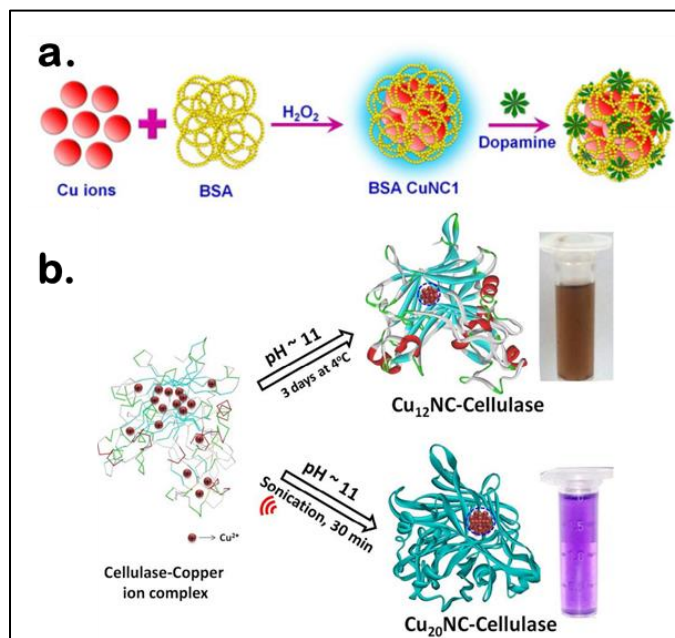


**Figure 1.69** (a) Diagrammatic illustration of the detection of dopamine using BSA CuNC synthesized in presence of H<sub>2</sub>O<sub>2</sub>. (Adopted from R. S. Aparna, J. S. A. Devi, J. Nebu, S. S. Syamchand and S. George, *J. Photochem. Photobiol. A: Chem.*, 2019, **379**, 63-71). (b) Schematic representation of reaction methods employed for the synthesis of CuNCs in cellulase solution (Adopted from A. Singh, T. Rai and D. Panda, *RSC Adv.*, 2016, **6**, 55539-55545).

### 1.9.5.1.3. Ligand assisted methods

Chen's group synthesized Cu NCs by using 2-mercapto-5-*n*-propylpyrimidine (MPP) as a protecting ligand and NaBH<sub>4</sub> as a reducing agent. Copper(II) nitrate and tetra-*n*-octylammonium bromide were co-dissolved in ethanol, followed by cooling in ice water and adding MPP and NaBH<sub>4</sub>.<sup>276</sup> After centrifugation and purification, clusters with the composition of Cu<sub>8</sub>L<sub>4</sub> (L = C<sub>7</sub>H<sub>9</sub>N<sub>2</sub>S) were obtained, as was confirmed by the electrospray ionization mass spectrometry (ESI-MS) measurements. This work inspired plenty of use of thiolate-based ligands to synthesize Cu NCs, such as GSH (Figure 1.70), penicillamine,<sup>277, 278</sup> phenylethanethiol,<sup>279</sup> dihydrolipoic acid,<sup>280</sup> mercaptobenzoic acids,<sup>281</sup> cysteamine<sup>282</sup> and 3-mercaptoptrimethoxysilane. In this context, it should be mentioned that this thesis contains work on copper nanocluster stabilised using cysteamine ligand. Both the nature of the ligands and the synthetic conditions play an important role in the structure and optical properties of the resulting Cu NCs.

Chang's group employed three isomers of mercaptobenzoic acid as ligands to synthesize Cu NCs.<sup>277</sup> Cu NCs protected by 2-mercaptobenzoic acid emitted blue light peaking at 420 nm (excited at 338 nm), with a PL QY of 13.2%. Cu NCs synthesized by using 3-mercaptobenzoic acid and 4-mercaptobenzoic acid tend to form net-like and rod-like aggregates, respectively. Different from the intense blue emission of 2-mercaptobenzoic acid protected Cu NCs, 4-mercaptobenzoic acid protected Cu NCs showed red PL (excitation peak at 324 nm and an emission peak at 646 nm), with a PL QY of only 0.5%, while 3-mercaptobenzoic acid protected Cu NCs showed even weaker red emission with a PL QY of <0.1%.<sup>276</sup>

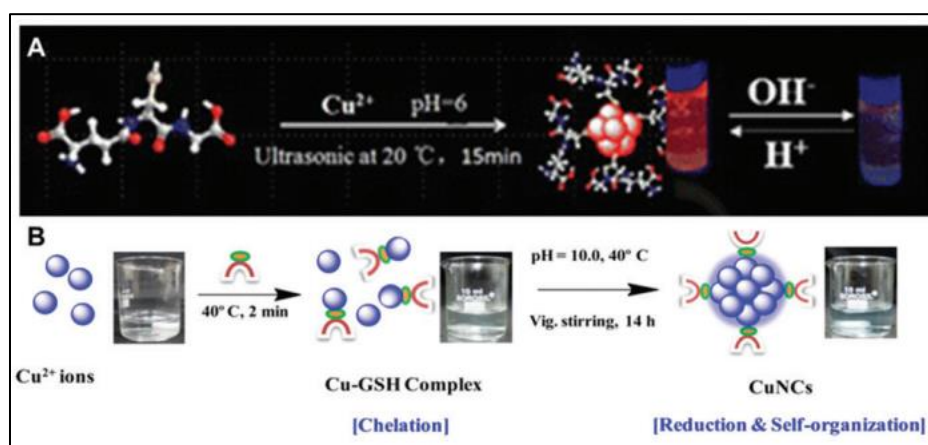


**Figure 1.70** Schematic illustration for the synthesis of Cu NCs using (a) GSH under ultrasonic treatment, and (b) GSH under heating at 40°C (Adopted from N. K. Das, S. Ghosh, A. Priya, S. Datta and S. Mukherjee, *J. Phys. Chem. C*, 2015, **119**, 24657–24664).

### 1.9.6. Nanohybrid Materials based on metal nanoclusters

The last two decades have seen flourish in synthesis and novel applications using metal nanoclusters. They are known for their various applications which are described above. Recently, it has been found that addition of various other nanomaterials with nanoclusters improve their robustness and the overall application enhances many-folds.<sup>283</sup>

Banerjee and co-workers devised a simple yet elegant strategy to make hydrogel using Fmoc protected phenylalanine. This stable and transparent hydrogel matrix is efficiently utilized to form silver nanoclusters within its matrix. The nanoclusters are preserved inside the hydrogel well. It was found that in absence of any toxic



reducing agents in a water medium, silver ions are complexed with the carboxylate group of the Fmoc-Phe-OH gelator, and they are reduced spontaneously in the presence of diffused sunlight at physiological pH (7.46) and room temperature to form silver nanoclusters (Figure 1.71). The three-dimensional structure provided by the hydrogel helps to stabilize newly formed silver nanoclusters within the hydrogel matrix. These clusters have been examined using UV-Vis, photoluminescence spectroscopy, HR-TEM, XRPD and matrix-assisted laser-desorption ionization (MALDI) mass spectrometric analysis.<sup>284</sup>

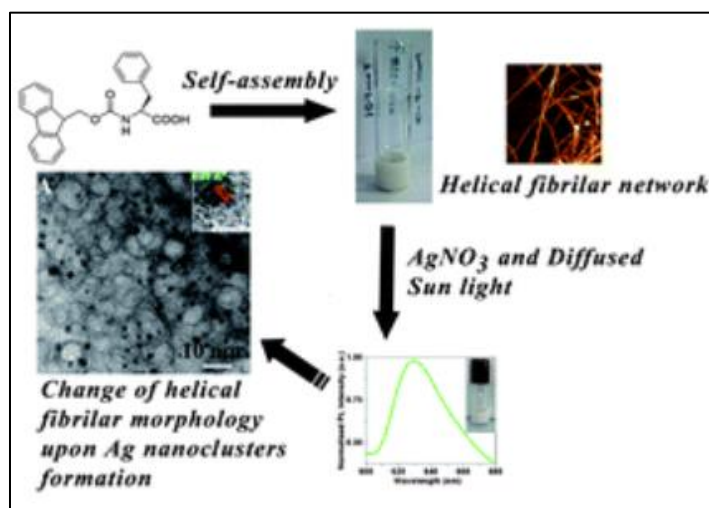


**Figure 1.71** A *N* side Fmoc protected phenylalanine forms gel having helical fibrillar network which changes after formation of silver nanoclusters inside the hydrogel in presence of silver salt and diffused sunlight. (Adopted from S. Roy and A. Banerjee, *Soft Matter*, 2011, 7, 5300-5308).

In another work by the same group, a newly synthesized blue fluorescent gold nanocluster was used in a hybrid system to create a white light emitting material. Emitting gold clusters have been tactically utilized to initiate an energy transfer process as a donor to the green emitting riboflavin (acceptor) and then riboflavin relays the energy transfer to the red emitting dye Rhodamine B in a controlled fashion to generate white light emission in a novel three component system (gold cluster, riboflavin and Rhodamine B) (Figure 1.72). The CIE coordinate of (0.32, 0.35) has been achieved for the white light emitting solution. The solution processable white light emitting material has been prepared using a non-toxic, eco-friendly solvent, in the aqueous medium. This is an early example of tri-hybrid



system where three of the component materials interacted with each other via resonance energy transfer. It can be soaked or coated over a solid surface to generate white light emission. Writing can also be achieved on the silica surface by using this new white light emitting eco-friendly solution.<sup>285</sup>

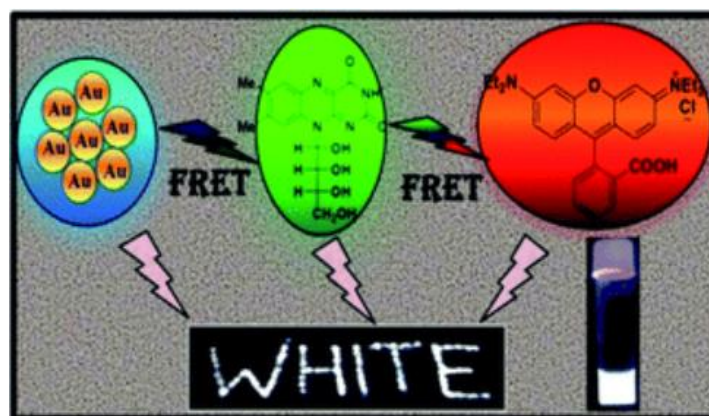


**Figure 1.72** Two FRET starting from blue-emitting gold nanocluster to green-emitting riboflavin to red-emitting rhodamine B gives rise to a white light emitting system in the triOhybrid system (Adopted from D. K. Maiti, S. Roy, A. Baral and A. Banerjee, *Journal of Materials Chemistry C*, 2014, **2**, 6574-6581).

Liu and co-workers have developed a two-component hybrid system consisting of red emitting gold nanoclusters and blue fluorescent conjugated oligomer-substituted polyhedral oligomeric silsesquioxane (POSSFF). They were connected through a FRET. By virtue of their opposite charges and good spectral overlap, efficient FRET from POSSFF to R-AuNC occurs upon electrostatic complex formation, leading to dual-emissive pink fluorescence upon donor excitation (Figure 1.73). The pink fluorescence specifically turns blue in the presence of mercury ions rather than other metal ions because of the strong metallophilic  $\text{Hg}^{2+}/\text{Au}^+$  interaction that quenches the red fluorescence from R-AuNCs (Figure 1.73). This consequently allows for visual detection and precise quantification of mercury ions with a limit of detection of  $\sim 0.1$  nM in aqueous solution. Moreover, the whole-cell permeability of the complexes and the preserved ion-selective FRET in cells make these complexes effective for multicolour intracellular sensing of mercury ion.<sup>286</sup>

Banerjee and co-worker have made a trihybrid system consisting of phenylalanine-based hydrogel nanofibers, graphene oxide (GO) nanosheet and silver nanoclusters made in-situ with the help of sunlight. This trihybrid system goes through a tetra-hybrid intermediate to reach another tri-hybrid system where the nanoclusters turn into bigger sized nanoparticles.<sup>287</sup>

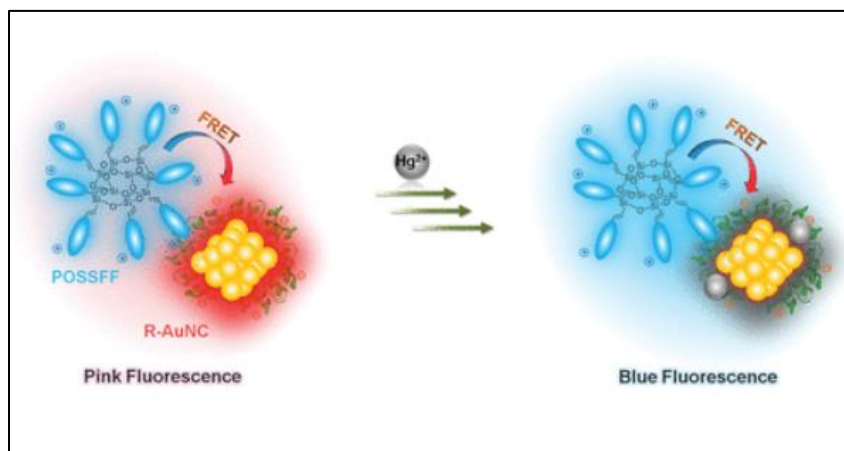


**Figure 1.73** FRET from POSSFF to the gold nanocluster enables dual fluorescence resulting on pink emission. Mercury is detected by its interaction with the nanoclusters. This quenches the nanocluster fluorescence but blue emission from POSSFF is detected (Adopted from K.-Y. Pu, Z. Luo, K. Li, J. Xie and B. Liu, *J. Phys. Chem. C*, 2011, **115**, 13069-13075).

Yu *et al.* has reported a two component nanohybrid made of 25 atom gold nanocluster and TiO<sub>2</sub> nanocrystals. This has been utilised in photochemical degradation of toxic dyes. The effects of Au<sub>25</sub>(SR)<sub>18</sub> nanoclusters on the photocatalytic activity of TiO<sub>2</sub> nanocrystals were evaluated in the reaction of photocatalytic degradation of methyl orange. The loading of Au<sub>25</sub>(SR)<sub>18</sub> nanoclusters onto TiO<sub>2</sub> results in strong visible light absorption by the composite and, more importantly, 1.6 times increase in visible light photocatalytic activity. Furthermore, the Au<sub>25</sub>(SR)<sub>18</sub>/TiO<sub>2</sub> composite nanostructure exhibits high stability in recycling tests. The Au<sub>25</sub>(SR)<sub>18</sub> nanoclusters dispersed on the TiO<sub>2</sub> surface can act as a small-band-gap semiconductor to absorb visible light, giving rise to electron-hole separation and producing singlet oxygen (<sup>1</sup>O<sub>2</sub>) (Figure 1.74). Both the generated hydroxyl radicals (HO<sup>•</sup>) and <sup>1</sup>O<sub>2</sub> are rationalized to be responsible for the decomposition of the dye.<sup>288</sup>

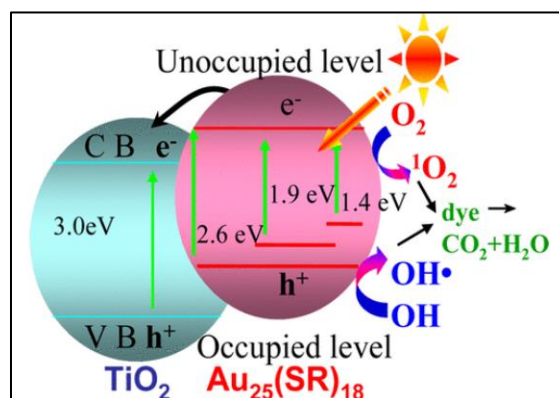


**Figure 1.74** Energy diagram of  $\text{TiO}_2$  nanocrystals and gold nanoclusters showing role of nanocluster in decreasing the energy gap and facilitating photocatalytic reduction of the dyes (Adopted from C. Yu, G. Li, S. Kumar, H. Kawasaki and R. Jin, *J. Phys. Chem. Lett.*, 2013, **4**, 2847-2852).

Banerjee's group has developed another tri-hybrid system containing gold nanoclusters recently (Figure 1.75). The work demonstrates the reduction potential of carbon dots in presence of blue LED light. The carbon dots reduce graphene oxide (GO) to reduced graphene oxide (rGO) and gold salt is reduced to gold nanoclusters. Both the carbon dots and the nanoclusters get decorated in the 2D surface of the reduced graphene oxide. This tri-hybrid system shows excellent semi conducting property and photo-current generation capability. The current gain is significantly higher when gold nanocluster is present in the system. The tri-hybrid system is also capable of degrading the warfare agent methylparaoxon (DMNP).<sup>289</sup>

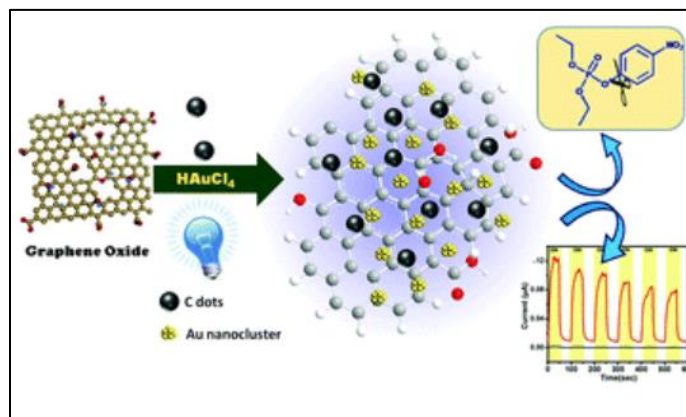


**Figure 1.75** Schematic representation of tri-hybrid formation from rGO, C dots and gold nanoclusters. This nanohybrid is utilized in degradation of DMNP as well as enhanced photocurrent production (Adopted from S. Paul, N. Hazra, S. Hazra and A. Banerjee, *J. Mat. Chem. C*, 2020, **8**, 15735-15741).

### 1.10 References:

1. J.-M. Lehn, *Proc. Natl. Acad. Sci.*, 2002, **99**, 4763-4768.
2. S. J. Singer and G. L. Nicolson, *Science*, 1972, **175**, 720-731.
3. J. D. Watson and F. H. C. Crick, *Nature*, 1953, **171**, 737-738.
4. J. Pedersen Charles, *Science*, 1988, **241**, 536-540.
5. J.-M. Lehn, *Angew. Chem., Int. Ed. Engl.*, 1988, **27**, 89-112.
6. D. J. Cram, *Angew. Chem., Int. Ed. Engl.*, 1986, **25**, 1039-1057.
7. B. F. Hoskins and R. Robson, *J. Am. Chem. Soc.*, 1989, **111**, 5962-5964.
8. R. G. Nuzzo and D. L. Allara, *J. Am. Chem. Soc.*, 1983, **105**, 4481-4483.
9. G. M. Whitesides and M. Boncheva, *Proc. Natl. Acad. Sci.*, 2002, **99**, 4769-4774.
10. R. V. Ulijn and A. M. Smith, *Chem. Soc. Rev.*, 2008, **37**, 664-675.
11. T. Li, X.-M. Lu, M.-R. Zhang, K. Hu and Z. Li, *Bioact. Mater.*, 2022, **11**, 268-282.
12. M. Whitesides George, P. Mathias John and T. Seto Christopher, *Science*, 1991, **254**, 1312-1319.
13. M. Whitesides George and B. Grzybowski, *Science*, 2002, **295**, 2418-2421.
14. P. Larpent, A. Jouaiti, N. Kyritsakas and M. W. Hosseini, *Chem. Commun.*, 2019, **55**, 91-94.
15. H. Dong, S. E. Paramonov, L. Aulisa, E. L. Bakota and J. D. Hartgerink, *J. Am. Chem. Soc.*, 2007, **129**, 12468-12472.

16. C. T. Imrie, *Trends Polym. Sci.*, 1995, **3**, 22-29.
17. E. Krieg, M. M. C. Bastings, P. Besenius and B. Rybtchinski, *Chem. Rev.*, 2016, **116**, 2414-2477.
18. C. M. Lee, C. P. Jariwala and A. C. Griffin, *Polymer*, 1994, **35**, 4550-4554.
19. Y. Ducharme and J. D. Wuest, *J. Org. Chem.*, 1988, **53**, 5787-5789.
20. C. Fouquey, J.-M. Lehn and A.-M. Levelut, *Adv. Mater.*, 1990, **2**, 254-257.
21. P. Y. Dankers, T. M. Hermans, T. W. Baughman, Y. Kamikawa, R. E. Kiełtyka, M. M. Bastings, H. M. Janssen, N. A. Sommerdijk, A. Larsen, M. J. van Luyn, A. W. Bosman, E. R. Popa, G. Fytas and E. W. Meijer, *Adv. Mater.*, 2012, **24**, 2703-2709.
22. M. Sun, K. Müllen and M. Yin, *Chem. Soc. Rev.*, 2016, **45**, 1513-1528.
23. V. Praveen, C. Ranjith, E. Bandini, A. Ajayaghosh and N. Armaroli, *Chem. Soc. Rev.*, 2014, **43**.
24. Y. Liu, Y. Yu, J. Gao, Z. Wang and X. Zhang, *Angew. Chem. Int. Ed.*, 2010, **49**, 6576-6579.
25. H. Cui, T. Muraoka, A. G. Cheetham and S. I. Stupp, *Nano Lett.*, 2009, **9**, 945-951.
26. G. Liang, Z. Yang, R. Zhang, L. Li, Y. Fan, Y. Kuang, Y. Gao, T. Wang, W. W. Lu and B. Xu, *Langmuir*, 2009, **25**, 8419-8422.
27. J. Howland, *Biochem. Educ.*, 1990, **18**, 212-212.
28. M. N. G. James, *Protein Sci.*, 1999, **8**, 693-694.
29. Q. Chen, Y. Lv, D. Zhang, G. Zhang, C. Liu and D. Zhu, *Langmuir*, 2010, **26**, 3165-3168.
30. A. Martínez, *Amino Acids*, 1995, **9**, 285-292.

31. F. Li, D. Fitz, D. G. Fraser and B. M. Rode, *Amino Acids*, 2010, **38**, 287-294.
32. A. Mrozek, J. Karolak-Wojciechowska and K. Kieć-Kononowicz, *J. Mol. Struct.*, 2003, **655**, 397-403.
33. A. Doğan, A. D. Özel and E. Kılıç, *Amino Acids*, 2009, **36**, 373-379.
34. U. D. Priyakumar, M. Punnagai, G. K. Mohan and G. N. Sastry, *Tetrahedron*, 2004, **60**, 3037-3043.
35. D. Vijay and G. N. Sastry, *Phys. Chem. Chem. Phys.*, 2008, **10**, 582-590.
36. B. L. Schottel, H. T. Chifotides and K. R. Dunbar, *Chem. Soc. Rev.*, 2008, **37**, 68-83.
37. A. Sygula, F. R. Fronczek, R. Sygula, P. W. Rabideau and M. M. Olmstead, *J. Am. Chem. Soc.*, 2007, **129**, 3842-3843.
38. C. Janiak, *J. Chem. Soc., Dalton Trans.*, 2000, 3885-3896.
39. E. A. Meyer, R. K. Castellano and F. Diederich, *Angew. Chem. Int. Ed.*, 2003, **42**, 1210-1250.
40. M. B. Smith, *March's advanced organic chemistry: reactions, mechanisms, and structure*, John Wiley & Sons, 2020.
41. S. Sirois, E. I. Proynov, J. F. Truchon, C. M. Tsoukas and D. R. Salahub, *J. Comput. Chem.*, 2003, **24**, 1110-1119.
42. M. Henry, *Chemphyschem*, 2002, **3**, 561-569.
43. I. L. Karle, A. Pramanik, A. Banerjee, S. Bhattacharjya and P. Balaram, *J. Am. Chem. Soc.*, 1997, **119**, 9087-9095.
44. *J. Chem. Educ.*, 1995, **72**, A170.
45. M. Sandberg and I. Jacobson, *J. Neurochem.*, 1981, **37**, 1353-1356.

46. V. Castelletto, C. J. C. Edwards-Gayle, F. Greco, I. W. Hamley, J. Seitsonen and J. Ruokolainen, *ACS Appl. Mater. Interfaces*, 2019, **11**, 33573-33580.
47. M. Szeftczyk, *Nanoscale*, 2021, **13**, 11325-11333.
48. J. Awapara, A. J. Landua, R. Fuerst and B. Seale, *J. Biol. Chem.*, 1950, **187**, 35-39.
49. E. Roberts and S. Frankel, *J. Biol. Chem.*, 1950, **187**, 55-63.
50. A. Banerjee and P. Balaram, *Curr. Sci.*, 1997, **73**, 1067-1077.
51. B. I. Fiser, B. z. Jójárt, M. n. Szőri, G. r. Lendvay, I. G. Csizmadia and B. I. Viskolcz, *J. Phys. Chem. B*, 2015, **119**, 3940-3947.
52. D. Ganguly, C. V. Srikanth, C. Kumar, P. Vats and A. K. Bachhawat, *IUBMB Life*, 2003, **55**, 553-554.
53. J. Nanda and A. Banerjee, *Soft Matter*, 2012, **8**, 3380-3386.
54. S. Roy, A. Baral and A. Banerjee, *Chem. Eur. J.*, 2013, **19**, 14950-14957.
55. P. J. Artymiuk and C. C. Blake, *J. Mol. Biol.*, 1981, **152**, 737-762.
56. D. J. Barlow and J. M. Thornton, *J. Mol. Biol.*, 1988, **201**, 601-619.
57. L. Pauling and R. B. Corey, *Nature*, 1953, **171**, 59-61.
58. W. A. Petka, J. L. Harden, K. P. McGrath, D. Wirtz and D. A. Tirrell, *Science*, 1998, **281**, 389-392.
59. M. J. Pandya, G. M. Spooner, M. Sunde, J. R. Thorpe, A. Rodger and D. N. Woolfson, *Biochemistry*, 2000, **39**, 8728-8734.
60. A. M. Smith, E. F. Banwell, W. R. Edwards, M. J. Pandya and D. N. Woolfson, *Adv. Funct. Mater.*, 2006, **16**, 1022-1030.



61. H. Dong, S. E. Paramonov and J. D. Hartgerink, *J. Am. Chem. Soc.*, 2008, **130**, 13691-13695.
62. G. N. Ramachandran, C. Ramakrishnan and V. Sasisekharan, *J. Mol. Biol.*, 1963, **7**, 95-99.
63. L. Pauling and R. B. Corey, *Proc. Natl. Acad. Sci. U.S.A.*, 1951, **37**, 729-740.
64. F. Chiti and C. M. Dobson, *Annu Rev Biochem*, 2006, **75**, 333-366.
65. S. Zhang, T. Holmes, C. Lockshin and A. Rich, *Proc. Natl. Acad. Sci. U.S.A.*, 1993, **90**, 3334-3338.
66. H. Yokoi, T. Kinoshita and S. Zhang, *Proc. Natl. Acad. Sci. U. S. A.*, 2005, **102**, 8414-8419.
67. A. Aggeli, I. A. Nyrkova, M. Bell, R. Harding, L. Carrick, T. C. B. McLeish, A. N. Semenov and N. Boden, *Proc. Natl. Acad. Sci.*, 2001, **98**, 11857-11862.
68. R. V. Uljijn and A. M. Smith, *Chem. Soc. Rev.*, 2008, **37**, 664-675.
69. J. P. Schneider, D. J. Pochan, B. Ozbas, K. Rajagopal, L. Pakstis and J. Kretsinger, *J. Am. Chem. Soc.*, 2002, **124**, 15030-15037.
70. K. H. Smith, E. Tejada-Montes, M. Poch and A. Mata, *Chem. Soc. Rev.*, 2011, **40**, 4563-4577.
71. K. Kita-Tokarczyk, J. Grumelard, T. Haefele and W. Meier, *Polymer*, 2005, **46**, 3540-3563.
72. T. J. Deming, *Wiley Interdiscip. Rev. Nanomed. Nanobiotechnol.*, 2014, **6**, 283-297.
73. E. G. Bellomo, M. D. Wyrsta, L. Pakstis, D. J. Pochan and T. J. Deming, *Nat. Mater.*, 2004, **3**, 244-248.

- 
74. J. Ding, C. Xiao, X. Zhuang, C. He and X. Chen, *Mater. Lett.*, 2012, **73**, 17-20.
75. H. Iatrou, H. Frielinghaus, S. Hanski, N. Ferderigos, J. Ruokolainen, O. Ikkala, D. Richter, J. Mays and N. Hadjichristidis, *Biomacromolecules*, 2007, **8**, 2173-2181.
76. V. P. Torchilin, *Pharm. Res.*, 2007, **24**, 1-16.
77. R. S. Tu and M. Tirrell, *Adv. Drug Del. Rev.*, 2004, **56**, 1537-1563.
78. X. Li, C. Cao, P. Wei, M. Xu, Z. Liu, L. Liu, Y. Zhong, R. Li, Y. Zhou and T. Yi, *ACS Appl. Mater. Interfaces*, 2019, **11**, 12327-12334.
79. E. J. Chung, Y. Cheng, R. Morshed, K. Nord, Y. Han, M. L. Wegscheid, B. Auffinger, D. A. Wainwright, M. S. Lesniak and M. V. Tirrell, *Biomaterials*, 2014, **35**, 1249-1256.
80. D. Peters, M. Kastantin, V. R. Kotamraju, P. P. Karmali, K. Gujraty, M. Tirrell and E. Ruoslahti, *Proc. Natl. Acad. Sci.*, 2009, **106**, 9815-9819.
81. S. Zhang, D. M. Marini, W. Hwang and S. Santoso, *Curr. Opin. Chem. Biol.*, 2002, **6**, 865-871.
82. S. Han, S. Cao, Y. Wang, J. Wang, D. Xia, H. Xu, X. Zhao and J. R. Lu, *Chem. Eur. J.*, 2011, **17**, 13095-13102.
83. S. Tarvirdipour, X. Huang, V. Mihali, C. A. Schoenenberger and C. G. Palivan, *Molecules*, 2020, **25**.
84. W. Zhang, D. Lin, H. Wang, J. Li, G. U. Nienhaus, Z. Su, G. Wei and L. Shang, *Bioconjugate Chem.*, 2017, **28**, 2224-2229.
85. C. Valéry, F. Artzner and M. Paternostre, *Soft Matter*, 2011, **7**, 9583-9594.
86. J. D. Hartgerink, E. Beniash and S. I. Stupp, *Proc. Natl. Acad. Sci.*, 2002, **99**, 5133-5138.

87. D. Mandal, A. N. Shirazi and K. Parang, *Org. Biomol. Chem.*, 2014, **12**, 3544-3561.
88. M. R. Ghadiri, J. R. Granja and L. K. Buehler, *Nature*, 1994, **369**, 301-304.
89. W.-H. Hsieh, S.-F. Chang, H.-M. Chen, J.-H. Chen and J. Liaw, *Mol. Pharm.*, 2012, **9**, 1231-1249.
90. S. C. Larnaudie, J. C. Brendel, I. Romero-Canelón, C. Sanchez-Cano, S. Catrouillet, J. Sanchis, J. P. Coverdale, J.-I. Song, A. Habtemariam and P. J. Sadler, *Biomacromolecules*, 2018, **19**, 239-247.
91. Y. Han, Y. Liu, J. Yuan, H. Dong, Y. Li, W. Ma, S.-T. Lee and B. Sun, *ACS Nano*, 2017, **11**, 7215-7222.
92. Q. Li, M. Peng, H. Li, C. Zhong, L. Zhang, X. Cheng, X. Peng, Q. Wang, J. Qin and Z. Li, *Org. Lett.*, 2012, **14**, 2094-2097.
93. F. Doria, M. Nadai, G. Costa, G. Sattin, C. Gallati, G. Bergamaschi, F. Moraca, S. Alcaro, M. Freccero and S. N. Richter, *Eur. J. Org. Chem.*, 2016, **2016**, 4824-4833.
94. M. B. Avinash and T. Govindaraju, *Adv. Mater.*, 2012, **24**, 3905-3922.
95. S. Ghosh, X. Q. Li, V. Stepanenko and F. Würthner, *Chemistry (Easton)*, 2008, **14**, 11343-11357.
96. Y. Hong, J. W. Y. Lam and B. Z. Tang, *Chem. Commun.*, 2009, DOI: 10.1039/B904665H, 4332-4353.
97. X. Fang, H. Ke, L. Li and M.-J. Lin, *Dyes Pigm.*, 2017, **145**, 469-475.
98. D. A. Shejul, S. M. Wagalgave, R. W. Jadhav, M. A. Kobaisi, D. D. La, L. A. Jones, R. S. Bhosale, S. V. Bhosale and S. V. Bhosale, *New J. Chem.*, 2020, **44**, 1615-1623.

- 
99. D. Vu, M. Jevric, J. M. Bjuggren, C. Wang, X. Pan, L. Thomsen, E. Gann, M. R. Andersson and C. R. McNeill, *ACS Appl. Polym. Mater.*, 2022, **4**, 3270-3282.
100. R. I. Randle, L. Cavalcanti, S. Sproules and E. R. Draper, *Mater. Adv.*, 2022, **3**, 3326-3331.
101. K. C. Deing, U. Mayerhöffer, F. Würthner and K. Meerholz, *Phys. Chem. Chem. Phys.*, 2012, **14**, 8328-8334.
102. M. Zangoli, M. Gazzano, F. Monti, L. Maini, D. Gentili, A. Liscio, A. Zanelli, E. Salatelli, G. Gigli, M. Baroncini and F. Di Maria, *ACS Appl. Mater. Interfaces*, 2019, **11**, 16864-16871.
103. S. Guha and S. Saha, *J. Am. Chem. Soc.*, 2010, **132**, 17674-17677.
104. V. Gorteau, G. Bollot, J. Mareda, A. Perez-Velasco and S. Matile, *J. Am. Chem. Soc.*, 2006, **128**, 14788-14789.
105. M. Pandeewar, M. B. Avinash and T. Govindaraju, *Chem. Eur. J.*, 2012, **18**, 4818-4822.
106. S. Basak, N. Nandi, S. Paul and A. Banerjee, *ACS Omega*, 2018, **3**, 2174-2182.
107. S. Basak, N. Nandi, K. Bhattacharyya, A. Datta and A. Banerjee, *Phys. Chem. Chem. Phys.*, 2015, **17**, 30398-30403.
108. X. Niu, G. Liu, L. Li, Z. Fu, H. Xu and F. Cui, *RSC Adv.*, 2015, **5**, 95223-95229.
109. H. Shao and J. R. Parquette, *Chem. Commun.*, 2010, **46**, 4285-4287.
110. A. Baral, S. Roy, S. Ghosh, D. Hermida-Merino, I. W. Hamley and A. Banerjee, *Langmuir*, 2016, **32**, 1836-1845.
111. S. Roy, K. Basu, K. Gayen, S. Panigrahi, S. Mondal, D. Basak and A. Banerjee, *J. Phys. Chem. C*, 2017, **121**, 5428-5435.

112. S. Basak, J. Nanda and A. Banerjee, *Chem. Commun.*, 2013, **49**, 6891-6893.
113. S. K. Nalluri, C. Berdugo, N. Javid, P. W. Frederix and R. V. Ulijn, *Angew Chem Int Ed Engl*, 2014, **53**, 5882-5887.
114. H. A. M. Ardoña, E. R. Draper, F. Citossi, M. Wallace, L. C. Serpell, D. J. Adams and J. D. Tovar, *J. Am. Chem. Soc.*, 2017, **139**, 8685-8692.
115. N. Singha, P. Gupta, B. Pramanik, S. Ahmed, A. Dasgupta, A. Ukil and D. Das, *Biomacromolecules*, 2017, **18**, 3630-3641.
116. Y. Wang, Y. Jiang, X. Zhu and M. Liu, *J. Phys. Chem. Lett.*, 2019, **10**, 5861-5867.
117. P. G. Gennes, *Soft Matter*, 2005, **1**.
118. R. G. Weiss, *J. Am. Chem. Soc.*, 2014, **136**, 7519-7530.
119. J. Raeburn, A. Zamith Cardoso and D. J. Adams, *Chem. Soc. Rev.*, 2013, **42**, 5143-5156.
120. M. Suzuki and K. Hanabusa, *Chem. Soc. Rev.*, 2010, **39**, 455-463.
121. A. Ajayaghosh and S. J. George, *J. Am. Chem. Soc.*, 2001, **123**, 5148-5149.
122. S. R. Jadhav, P. K. Vemula, R. Kumar, S. R. Raghavan and G. John, *Angew Chem Int Ed Engl*, 2010, **49**, 7695-7698.
123. S. Bhat and U. Maitra, *Tetrahedron*, 2007, **63**, 7309-7320.
124. S. Roy, D. Kumar Maiti, S. Panigrahi, D. Basak and A. Banerjee, *RSC Adv.*, 2012, **2**, 11053-11060.
125. L. E. Buerkle and S. J. Rowan, *Chem. Soc. Rev.*, 2012, **41**, 6089-6102.
126. Z. Džolić, K. Wolsperger and M. Žinić, *New J. Chem.*, 2006, **30**, 1411-1419.

127. A. R. Hirst, B. Huang, V. Castelletto, I. W. Hamley and D. K. Smith, *Chem. Eur. J.*, 2007, **13**, 2180-2188.
128. S. Paul, K. Basu, K. S. Das and A. Banerjee, *ChemNanoMat*, 2018, **4**, 882-887.
129. F. Vonderviszt, M. Sonoyama, M. Tasumi and K. Namba, *Biophys. J.*, 1992, **63**, 1672-1677.
130. C. Zhang, X. Xue, Q. Luo, Y. Li, K. Yang, X. Zhuang, Y. Jiang, J. Zhang, J. Liu, G. Zou and X.-J. Liang, *ACS Nano*, 2014, **8**, 11715-11723.
131. Y. Mu and M. Yu, *Soft Matter*, 2014, **10**, 4956-4965.
132. L. Adler-Abramovich, M. Reches, V. L. Sedman, S. Allen, S. J. B. Tandler and E. Gazit, *Langmuir*, 2006, **22**, 1313-1320.
133. L. Adler-Abramovich and E. Gazit, *Chem. Soc. Rev.*, 2014, **43**, 6881-6893.
134. N. S. de Groot, T. Parella, F. X. Aviles, J. Vendrell and S. Ventura, *Biophys. J.*, 2007, **92**, 1732-1741.
135. C. K. Thota, N. Yadav and V. S. Chauhan, *Sci. Rep.*, 2016, **6**, 31167.
136. K. Hanabusa, J. Tange, Y. Taguchi, T. Koyama and H. Shirai, *J. Chem. Soc., Chem. Commun.*, 1993, 390-392.
137. K. Hanabusa, R. Tanaka, M. Suzuki, M. Kimura and H. Shirai, *Adv. Mater.*, 1997, **9**, 1095-1097.
138. S.-M. Hsu, Y.-C. Lin, J.-W. Chang, Y.-H. Liu and H.-C. Lin, *Angew. Chem. Int. Ed.*, 2014, **53**, 1921-1927.
139. Y. Zhang, Z. Yang, F. Yuan, H. Gu, P. Gao and B. Xu, *J. Am. Chem. Soc.*, 2004, **126**, 15028-15029.
140. D. Mandal, T. Kar and P. K. Das, *Chem. Eur. J.*, 2014, **20**, 1349-1358.

141. C. Tang, A. M. Smith, R. F. Collins, R. V. Ulijn and A. Saiani, *Langmuir*, 2009, **25**, 9447-9453.
142. Y. Liu, X.-D. Xu, J.-X. Chen, H. Cheng, X.-Z. Zhang and R.-X. Zhuo, *Colloids Surf. B*, 2011, **87**, 192-197.
143. J. Raeburn, C. Mendoza-Cuenca, B. N. Cattoz, M. A. Little, A. E. Terry, A. Zamith Cardoso, P. C. Griffiths and D. J. Adams, *Soft Matter*, 2015, **11**, 927-935.
144. S. Fleming, S. Debnath, P. W. J. M. Frederix, T. Tuttle and R. V. Ulijn, *Chem. Commun.*, 2013, **49**, 10587-10589.
145. D. B. Rasale, I. Maity and A. K. Das, *Chem. Commun.*, 2014, **50**, 11397-11400.
146. L. Chronopoulou, Y. Toumia, B. Cerroni, D. Pandolfi, G. Paradossi and C. Palocci, *N. Biotechnol.*, 2017, **37**, 138-143.
147. S. Debnath, S. Roy and R. V. Ulijn, *J. Am. Chem. Soc.*, 2013, **135**, 16789-16792.
148. Y. Zhang, R. Zhou, J. Shi, N. Zhou, I. R. Epstein and B. Xu, *J. Phys. Chem. B*, 2013, **117**, 6566-6573.
149. Y. Zhang, Y. Kuang, Y. Gao and B. Xu, *Langmuir*, 2011, **27**, 529-537.
150. C. Colquhoun, E. R. Draper, E. G. B. Eden, B. N. Cattoz, K. L. Morris, L. Chen, T. O. McDonald, A. E. Terry, P. C. Griffiths, L. C. Serpell and D. J. Adams, *Nanoscale*, 2014, **6**, 13719-13725.
151. K. L. Morris, L. Chen, J. Raeburn, O. R. Sellick, P. Cotanda, A. Paul, P. C. Griffiths, S. M. King, R. K. O'Reilly, L. C. Serpell and D. J. Adams, *Nat Commun*, 2013, **4**, 1480.
152. S. J. Marrink, H. J. Risselada, S. Yefimov, D. P. Tieleman and A. H. de Vries, *J. Phys. Chem. B*, 2007, **111**, 7812-7824.



153. P. W. Frederix, G. G. Scott, Y. M. Abul-Haija, D. Kalafatovic, C. G. Pappas, N. Javid, N. T. Hunt, R. V. Ulijn and T. Tuttle, *Nat. Chem.*, 2015, **7**, 30-37.
154. S. Marchesan, C. D. Easton, F. Kushkaki, L. Waddington and P. G. Hartley, *Chem. Commun.*, 2012, **48**, 2195-2197.
155. C. Veerman, K. Rajagopal, C. S. Palla, D. J. Pochan, J. P. Schneider and E. M. Furst, *Macromolecules*, 2006, **39**, 6608-6614.
156. L. Haines-Butterick, K. Rajagopal, M. Branco, D. Salick, R. Rughani, M. Pilarz, M. S. Lamm, D. J. Pochan and J. P. Schneider, *Proc. Natl. Acad. Sci. U. S. A.*, 2007, **104**, 7791-7796.
157. R. P. Nagarkar, R. A. Hule, D. J. Pochan and J. P. Schneider, *J. Am. Chem. Soc.*, 2008, **130**, 4466-4474.
158. D. W. P. M. Löwik and J. C. M. van Hest, *Chem. Soc. Rev.*, 2004, **33**, 234-245.
159. U. Ros and A. J. García-Sáez, *The Journal of Membrane Biology*, 2015, **248**, 545-561.
160. D. A. Kelkar and A. Chattopadhyay, *Biochim. Biophys. Acta*, 2007, **1768**, 2011-2025.
161. W. Rajendra, A. Armugam and K. Jeyaseelan, *Brain Res. Rev.*, 2004, **45**, 125-141.
162. R. Qi, P. Zhang, J. Liu, L. Zhou, C. Zhou, N. Zhang, Y. Han, S. Wang and Y. Wang, *ACS Appl. Bio Mater.*, 2018, **1**, 21-26.
163. N. Rodrigues de Almeida, Y. Han, J. Perez, S. Kirkpatrick, Y. Wang and M. C. Sheridan, *ACS Appl. Mater. Interfaces*, 2019, **11**, 2790-2801.
164. S. Zhang, T. Holmes, C. Lockshin and A. Rich, *Proc. Natl. Acad. Sci.*, 1993, **90**, 3334-3338.

165. A. Trent, R. Marullo, B. Lin, M. Black and M. Tirrell, *Soft Matter*, 2011, **7**, 9572-9582.
166. I. W. Hamley, *Chem. Commun.*, 2015, **51**, 8574-8583.
167. E. Pazos, E. Sleep, C. M. Rubert Pérez, S. S. Lee, F. Tantakitti and S. I. Stupp, *J. Am. Chem. Soc.*, 2016, **138**, 5507-5510.
168. C. C. Palsuledesai and M. D. Distefano, *ACS Chem. Biol.*, 2015, **10**, 51-62.
169. K. Ariga, J.-i. Kikuchi, M. Naito, E. Koyama and N. Yamada, *Langmuir*, 2000, **16**, 4929-4939.
170. J. D. Hartgerink, E. Beniash and S. I. Stupp, *Science*, 2001, **294**, 1684-1688.
171. S. Fleming and R. V. Ulijn, *Chem. Soc. Rev.*, 2014, **43**, 8150-8177.
172. M. Kumar, N. L. Ing, V. Narang, N. K. Wijerathne, A. I. Hochbaum and R. V. Ulijn, *Nat. Chem.*, 2018, **10**, 696-703.
173. T. B. Schon, A. J. Tilley, E. L. Kynaston and D. S. Seferos, *ACS Appl. Mater. Interfaces*, 2017, **9**, 15631-15637.
174. B. Pramanik, S. Ahmed, N. Singha, B. K. Das, P. Dowari and D. Das, *Langmuir*, 2019, **35**, 478-488.
175. X. Zhang and C. Wang, *Chem. Soc. Rev.*, 2011, **40**, 94-101.
176. S. Basak, J. Nanda and A. Banerjee, *Chem. Commun.*, 2014, **50**, 2356-2359.
177. S. Sasmal, K. Maji, D. Díaz Díaz and D. Haldar, *CrystEngComm*, 2019, **21**, 4289-4297.
178. Y. Zhang, B. Zhang, Y. Kuang, Y. Gao, J. Shi, X. X. Zhang and B. Xu, *J. Am. Chem. Soc.*, 2013, **135**, 5008-5011.

- 
179. Y. Liu, T. Wang, Z. Li and M. Liu, *Chem. Commun.*, 2013, **49**, 4767-4769.
180. J. Song, C. Yuan, T. Jiao, R. Xing, M. Yang, D. J. Adams and X. Yan, *Small*, 2020, **16**, 1907309.
181. K. Gayen, K. Basu, D. Bairagi, V. Castelletto, I. W. Hamley and A. Banerjee, *ACS Appl. Bio Mater.*, 2018, **1**, 1717-1724.
182. H. Yu, H. A. Chokhawala, S. Huang and X. Chen, *Nat. Protoc.*, 2006, **1**, 2485-2492.
183. S. Toledano, R. J. Williams, V. Jayawarna and R. V. Ulijn, *J. Am. Chem. Soc.*, 2006, **128**, 1070-1071.
184. S. Dos Santos, A. Chandravarkar, B. Mandal, R. Mimna, K. Murat, L. Saucède, P. Tella, G. Tuchscherer and M. Mutter, *J. Am. Chem. Soc.*, 2005, **127**, 11888-11889.
185. Z. Yang, G. Liang, L. Wang and B. Xu, *J. Am. Chem. Soc.*, 2006, **128**, 3038-3043.
186. F. Rodríguez-Llansola, B. Escuder, J. F. Miravet, D. Hermida-Merino, I. W. Hamley, C. J. Cardin and W. Hayes, *Chem. Commun.*, 2010, **46**, 7960-7962.
187. B. O. Okesola and D. K. Smith, *Chem. Commun.*, 2013, **49**, 11164-11166.
188. J. Mewis, *J. Nonnewton. Fluid. Mech.*, 1979, **6**, 1-20.
189. V. Ajay Mallia and R. G. Weiss, *Soft Matter*, 2016, **12**, 3665-3676.
190. R. Das Mahapatra, J. Dey and R. G. Weiss, *Soft Matter*, 2019, **15**, 433-441.
191. A. Baral, S. Roy, A. Dehsorkhi, I. W. Hamley, S. Mohapatra, S. Ghosh and A. Banerjee, *Langmuir*, 2014, **30**, 929-936.
192. X.-Q. Dou and C.-L. Feng, *Adv. Mater.*, 2017, **29**, 1604062.

193. H. Hosseinkhani, P.-D. Hong and D.-S. Yu, *Chem. Rev.*, 2013, **113**, 4837-4861.
194. Y. Yanlian, K. Ulung, W. Xiumei, A. Horii, H. Yokoi and Z. Shuguang, *Nano Today*, 2009, **4**, 193-210.
195. A. L. Sieminski, A. S. Was, G. Kim, H. Gong and R. D. Kamm, *Cell Biochem. Biophys.*, 2007, **49**, 73-83.
196. Z. Yang and X. Zhao, *Int J Nanomedicine*, 2011, **6**, 303-310.
197. K. M. Galler, J. D. Hartgerink, A. C. Cavender, G. Schmalz and R. N. D'Souza, *Tissue Eng Part A*, 2012, **18**, 176-184.
198. V. Jayawarna, S. M. Richardson, A. R. Hirst, N. W. Hodson, A. Saiani, J. E. Gough and R. V. Ulijn, *Acta Biomater.*, 2009, **5**, 934-943.
199. M. Zhou, A. M. Smith, A. K. Das, N. W. Hodson, R. F. Collins, R. V. Ulijn and J. E. Gough, *Biomaterials*, 2009, **30**, 2523-2530.
200. F. Zhao, C. S. Weitzel, Y. Gao, H. M. Browdy, J. Shi, H. C. Lin, S. T. Lovett and B. Xu, *Nanoscale*, 2011, **3**, 2859-2861.
201. Q. Li, G. Qi, X. Liu, J. Bai, J. Zhao, G. Tang, Y. S. Zhang, R. Chen-Tsai, M. Zhang, D. Wang, Y. Zhang, A. Atala, J.-Q. He and X. S. Sun, *Adv. Funct. Mater.*, 2021, **31**, 2104046.
202. H. Huang, J. Shi, J. Laskin, Z. Liu, D. S. McVey and X. S. Sun, *Soft Matter*, 2011, **7**, 8905-8912.
203. D. A. Salick, J. K. Kretsinger, D. J. Pochan and J. P. Schneider, *J. Am. Chem. Soc.*, 2007, **129**, 14793-14799.
204. D. A. Salick, D. J. Pochan and J. P. Schneider, *Adv. Mater.*, 2009, **21**, 4120-4123.
205. A. S. Veiga, C. Sinthuvanich, D. Gaspar, H. G. Franquelim, M. A. Castanho and J. P. Schneider, *Biomaterials*, 2012, **33**, 8907-8916.

- 
206. I. Irwansyah, Y.-Q. Li, W. Shi, D. Qi, W. R. Leow, M. B. Y. Tang, S. Li and X. Chen, *Adv. Mater.*, 2015, **27**, 648-654.
207. N. Nandi, K. Gayen, S. Ghosh, D. Bhunia, S. Kirkham, S. K. Sen, S. Ghosh, I. W. Hamley and A. Banerjee, *Biomacromolecules*, 2017, **18**, 3621-3629.
208. W. Xu, Z. Zhang, X. Zhang, Y. Tang, Y. Niu, X. Chu, S. Zhang and C. Ren, *Langmuir*, 2021, **37**, 12842-12852.
209. F. Rodríguez-Llansola, J. F. Miravet and B. Escuder, *Chem. Commun.*, 2009, DOI: 10.1039/B916250J, 7303-7305.
210. N. Singh, M. P. Conte, R. V. Ulijn, J. F. Miravet and B. Escuder, *Chem. Commun.*, 2015, **51**, 13213-13216.
211. M. O. Guler and S. I. Stupp, *J. Am. Chem. Soc.*, 2007, **129**, 12082-12083.
212. C. Zhang, X. Xue, Q. Luo, Y. Li, K. Yang, X. Zhuang, Y. Jiang, J. Zhang, J. Liu, G. Zou and X. J. Liang, *ACS Nano*, 2014, **8**, 11715-11723.
213. A. M. Garcia, M. Kurbasic, S. Kralj, M. Melchionna and S. Marchesan, *Chem. Commun.*, 2017, **53**, 8110-8113.
214. C. Zhang, R. Shafi, A. Lampel, D. MacPherson, C. G. Pappas, V. Narang, T. Wang, C. Maldarelli and R. V. Ulijn, *Angew Chem Int Ed Engl*, 2017, **56**, 14511-14515.
215. J. Turkevich, P. C. Stevenson and J. Hillier, *Discuss. Faraday Soc.*, 1951, **11**, 55-75.
216. C. A. Mirkin, *Small*, 2005, **1**, 14-16.
217. G. Frens, *Colloid Polym Sci*, 1972, **250**, 736-741.
218. G. Frens, *Nat. Phys. Sci.*, 1973, **241**, 20-22.
219. P. C. Lee and D. Meisel, *J. Phys. Chem.*, 1982, **86**, 3391-3395.

220. P. H. Hess and P. H. Parker Jr, *J. Appl. Polym. Sci.*, 1966, **10**, 1915-1927.
221. C. H. Griffiths, M. P. O'Horo and T. W. Smith, *J. Appl. Phys.*, 1979, **50**, 7108-7115.
222. E. C. Dreaden, A. M. Alkilany, X. Huang, C. J. Murphy and M. A. El-Sayed, *Chem. Soc. Rev.*, 2012, **41**, 2740-2779.
223. C. D. Bain, E. B. Troughton, Y. T. Tao, J. Evall, G. M. Whitesides and R. G. Nuzzo, *J. Am. Chem. Soc.*, 1989, **111**, 321-335.
224. C. D. Bain and G. M. Whitesides, *Angew. Chem., Int. Ed. Engl.*, 1989, **28**, 506-512.
225. M. Brust, M. Walker, D. Bethell, D. J. Schiffrin and R. Whyman, *J. Chem. Soc., Chem. Commun.*, 1994, DOI: 10.1039/C39940000801, 801-802.
226. W. T. Wallace and R. L. Whetten, *J. Am. Chem. Soc.*, 2002, **124**, 7499-7505.
227. C. T. Campbell, S. C. Parker and D. E. Starr, *Science*, 2002, **298**, 811-814.
228. H.-P. Cheng and U. Landman, *J. Phys. Chem.*, 1994, **98**, 3527-3537.
229. L. A. Peyser, T.-H. Lee and R. M. Dickson, *J. Phys. Chem. B*, 2002, **106**, 7725-7728.
230. J. J. Velázquez, V. K. Tikhomirov, L. F. Chibotaru, N. T. Cuong, A. S. Kuznetsov, V. D. Rodríguez, M. T. Nguyen and V. V. Moshchalkov, *Opt. Express*, 2012, **20**, 13582-13591.
231. C. Félix, C. Sieber, W. Harbich, J. Buttet, I. Rabin, W. Schulze and G. Ertl, *Phys. Rev. Lett.*, 2001, **86**, 2992-2995.
232. C. Liu, X. Yang, H. Yuan, Z. Zhou and D. Xiao, *Sensors*, 2007, **7**, 708-718.

233. W. Harbich, S. Fedrigo, F. Meyer, D. M. Lindsay, J. Lignieres, J. C. Rivoal and D. Kreisler, *J. Chem. Phys.*, 1990, **93**, 8535-8543.
234. S. Chen, R. S. Ingram, M. J. Hostetler, J. J. Pietron, R. W. Murray, T. G. Schaaff, J. T. Khoury, M. M. Alvarez and R. L. Whetten, *Science*, 1998, **280**, 2098-2101.
235. J. P. Wilcoxon and B. L. Abrams, *Chem. Soc. Rev.*, 2006, **35**, 1162-1194.
236. P. Crespo, R. Litrán, T. C. Rojas, M. Multigner, J. M. de la Fuente, J. C. Sánchez-López, M. A. García, A. Hernando, S. Penadés and A. Fernández, *Phys. Rev. Lett.*, 2004, **93**, 087204.
237. G. Hodes, *Adv. Mater.*, 2007, **19**, 1307-1307.
238. C. J. Murphy, A. M. Gole, J. W. Stone, P. N. Sisco, A. M. Alkilany, E. C. Goldsmith and S. C. Baxter, *Acc. Chem. Res.*, 2008, **41**, 1721-1730.
239. J. Yu, S. A. Patel and R. M. Dickson, *Angew Chem Int Ed Engl*, 2007, **46**, 2028-2030.
240. S. Shahsavari, S. Hadian-Ghazvini, F. Hooriabad Saboor, I. Menbari Oskouie, M. Hasany, A. Simchi and A. L. Rogach, *Mater. Chem. Front.*, 2019, **3**, 2326-2356.
241. C. I. Richards, S. Choi, J. C. Hsiang, Y. Antoku, T. Vosch, A. Bongiorno, Y. L. Tzeng and R. M. Dickson, *J. Am. Chem. Soc.*, 2008, **130**, 5038-5039.
242. A. Sagadevan, A. Ghosh, P. Maity, O. F. Mohammed, O. M. Bakr and M. Rueping, *J. Am. Chem. Soc.*, 2022, **144**, 12052-12061.
243. Y.-C. Jao, M.-K. Chen and S.-Y. Lin, *Chem. Commun.*, 2010, **46**, 2626-2628.
244. Z. Wu and R. Jin, *Nano Lett.*, 2010, **10**, 2568-2573.
245. R. Zhou, M. Shi, X. Chen, M. Wang and H. Chen, *Chem. Eur. J.*, 2009, **15**, 4944-4951.

246. J. T. van Wijngaarden, O. Toikkanen, P. Liljeroth, B. M. Quinn and A. Meijerink, *J. Phys. Chem. C*, 2010, **114**, 16025-16028.
247. Y. Lu, W. Wei and W. Chen, *Chin. Sci. Bull.*, 2012, **57**, 41-47.
248. Y. Lu and W. Chen, *Chem. Soc. Rev.*, 2012, **41**, 3594-3623.
249. Z. Qing, X. He, D. He, K. Wang, F. Xu, T. Qing and X. Yang, *Angew. Chem. Int. Ed.*, 2013, **52**, 9719-9722.
250. N. Goswami, A. Giri, M. S. Bootharaju, P. L. Xavier, T. Pradeep and S. K. Pal, *Anal. Chem.*, 2011, **83**, 9676-9680.
251. C. Wang, C. Wang, L. Xu, H. Cheng, Q. Lin and C. Zhang, *Nanoscale*, 2014, **6**, 1775-1781.
252. L. Feng, Z. Huang, J. Ren and X. Qu, *Nucleic Acids Res.*, 2012, **40**, e122.
253. J. Liu, X. Zhang, M. Yu, S. Li and J. Zhang, *Small*, 2012, **8**, 310-316.
254. Q. Song, Y. Shi, D. He, S. Xu and J. Ouyang, *Chem. Eur. J.*, 2015, **21**, 2417-2422.
255. A. Rotaru, S. Dutta, E. Jentzsch, K. Gothelf and A. Mokhir, *Angew Chem Int Ed Engl*, 2010, **49**, 5665-5667.
256. Z. Qing, T. Qing, Z. Mao, X. He, K. Wang, Z. Zou, H. Shi and D. He, *Chem. Commun.*, 2014, **50**, 12746-12748.
257. M. Zhao, L. Sun and R. M. Crooks, *J. Am. Chem. Soc.*, 1998, **120**, 4877-4878.
258. Y. Ling, N. Zhang, F. Qu, T. Wen, Z. F. Gao, N. B. Li and H. Q. Luo, *Spectrochim. Acta A Mol. Biomol. Spectrosc.*, 2014, **118**, 315-320.
259. Y. Ling, J. X. Li, F. Qu, N. B. Li and H. Q. Luo, *Microchim Acta.*, 2014, **181**, 1069-1075.



260. M. Fernández-Ujados, L. Trapiella-Alfonso, J. M. Costa-Fernández, R. Pereiro and A. Sanz-Medel, *Nanotechnology*, 2013, **24**, 495601.
261. R. Ghosh, U. Goswami, S. S. Ghosh, A. Paul and A. Chattopadhyay, *ACS Appl Mater Interfaces*, 2015, **7**, 209-222.
262. Q. Tang, T. Yang and Y. Huang, *Microchim Acta.*, 2015, **182**, 2337-2343.
263. P.-C. Chen, Y.-C. Li, J.-Y. Ma, J.-Y. Huang, C.-F. Chen and H.-T. Chang, *Sci. Rep.*, 2016, **6**, 24882.
264. R. Gui, J. Sun, X. Cao, Y. Wang and H. Jin, *RSC Adv.*, 2014, **4**, 29083-29088.
265. H. Zhang, X. Huang, L. Li, G. Zhang, I. Hussain, Z. Li and B. Tan, *Chem. Commun.*, 2012, **48**, 567-569.
266. A. R.S, A. D. J.S, N. John, A. K, S. S.S and S. George, *Spectrochim. Acta A Mol. Biomol. Spectrosc.*, 2018, **199**, 123-129.
267. M. Jayasree, R. S. Aparna, R. R. Anjana, J. S. Anjali Devi, N. John, K. Abha, A. Manikandan and S. George, *Anal. Chim. Acta*, 2018, **1031**, 152-160.
268. W.-F. Lai, W.-T. Wong and A. L. Rogach, *Adv. Mater.*, 2020, **32**, 1906872.
269. F. Xu, H. Shi, X. He, K. Wang, D. He, Q. Guo, Z. Qing, L. Yan, X. Ye, D. Li and J. Tang, *Anal. Chem.*, 2014, **86**, 6976-6982.
270. H.-B. Wang, H.-D. Zhang, Y. Chen and Y.-M. Liu, *New J. Chem.*, 2015, **39**, 8896-8900.
271. Y.-R. Liu, R. Hu, T. Liu, X.-B. Zhang, W. Tan, G.-L. Shen and R.-Q. Yu, *Talanta*, 2013, **107**, 402-407.
272. W. Wang, F. Leng, L. Zhan, Y. Chang, X. X. Yang, J. Lan and C. Z. Huang, *Analyst*, 2014, **139**, 2990-2993.

273. S. Ghosh, N. K. Das, U. Anand and S. Mukherjee, *J. Phys. Chem. Lett.*, 2015, **6**, 1293-1298.
274. A. Singh, T. Rai and D. Panda, *RSC Adv.*, 2016, **6**, 55539-55545.
275. R. Ghosh, A. K. Sahoo, S. S. Ghosh, A. Paul and A. Chattopadhyay, *ACS Appl Mater Interfaces*, 2014, **6**, 3822-3828.
276. W. Wei, Y. Lu, W. Chen and S. Chen, *J. Am. Chem. Soc.*, 2011, **133**, 2060-2063.
277. X. Jia, X. Yang, J. Li, D. Li and E. Wang, *Chem. Commun.*, 2014, **50**, 237-239.
278. S. M. Lin, S. Geng, N. Li, N. B. Li and H. Q. Luo, *Talanta*, 2016, **151**, 106-113.
279. A. Ganguly, I. Chakraborty, T. Udayabhaskararao and T. Pradeep, *J. Nanopart. Res.*, 2013, **15**, 1522.
280. T. Zhou, Q. Yao, T. Zhao and X. Chen, *Talanta*, 2015, **141**, 80-85.
281. Y.-J. Lin, P.-C. Chen, Z. Yuan, J.-Y. Ma and H.-T. Chang, *Chem. Commun.*, 2015, **51**, 11983-11986.
282. M. Cui, G. Song, C. Wang and Q. Song, *Microchim Acta.*, 2015, **182**, 1371-1377.
283. J. Mu, Y. Peng, Z. Shi, D. Zhang and Q. Jia, *Mikrochim. Acta*, 2021, **188**, 384.
284. S. Roy and A. Banerjee, *Soft Matter*, 2011, **7**, 5300-5308.
285. D. K. Maiti, S. Roy, A. Baral and A. Banerjee, *J. Mat. Chem. C*, 2014, **2**, 6574-6581.
286. K.-Y. Pu, Z. Luo, K. Li, J. Xie and B. Liu, *J. Phys. Chem. C*, 2011, **115**, 13069-13075.

287. A. Biswas and A. Banerjee, *Soft Matter*, 2015, **11**, 4226-4234.
288. C. Yu, G. Li, S. Kumar, H. Kawasaki and R. Jin, *J. Phys. Chem. Lett.*, 2013, **4**, 2847-2852.
289. S. Paul, N. Hazra, S. Hazra and A. Banerjee, *J. Mat. Chem. C*, 2020, **8**, 15735-15741.



## CHAPTER 2

---

# Materials and Methods





## 2.1. Introduction

This chapter provides a detailed description of general synthetic procedures employed in this thesis for synthesis of amino acid and peptide derivatives by solution phase methods. It also provides details of all spectroscopic measurements, and many microscopic studies used in this work. The respective chapters described the specific synthetic procedures pertaining to sequences studied in this thesis.

## 2.2. Source of Chemicals and Cell-line

L-phenylalanine, 11-aminoundecanoic acid, glutathione (reduced), *tert*butyl pyrocarbonate (Boc anhydride), N,N'-dicyclohexylcarbodiimide (DCC), 1-hydroxy benzotriazole (HOBt), silver nitrate (AgNO<sub>3</sub>), chloroauric acid (HAuCl<sub>4</sub>) were purchased from Sigma Chemical Company, St. Louis Missouri, U.S.A.; Aldrich, U.S.A.; E-Merck, Germany; Lancaster, England and SRL, India. Deuterated solvents for NMR studies, CDCl<sub>3</sub> and DMSO-d<sub>6</sub> were supplied by Sigma chemical company, St. Louis Missouri, U.S.A and Cambridge Isotopic Laboratories, Massachusetts. Silica gel for TLC was obtained from E-Merck, India. Silica gel (100-200 mesh) for column chromatography was supplied by SRL, India. All other chemicals used were obtained from local manufactures like Ranbaxy, SD Fine Chemicals Pvt. Ltd., Bengal Chemical and Pharmaceutical Ltd., SRL, India, E-Merck India etc. Dulbecco's modified Eagle medium (DMEM) supplemented with 10% fetal bovine serum (FBS), penicillin, streptomycin were procured from Himedia, NIH-3T3 cells were from ATCC.

## 2.3. Experimental Procedures

**Purification of Solvents and Reagents:** The solvents used during the course of synthesis were purified as follows: Ethyl acetate and chloroform were distilled and used. Dioxane was passed through basic alumina before use. Methanol was fractionally distilled and used. Absolute methanol was prepared from distilled methanol using magnesium and iodine. Thionyl chloride was distilled from boiled linseed oil (20 mL/50 g SOCl<sub>2</sub>). Dimethyl formamide (DMF) was fractionally distilled using condenser packed with fenske helices under reduced pressure over ninhydrin (3 g/L).

**Preparation of Amino Acid Derivatives:** All amino acid methyl ester hydrochlorides used in this work were prepared by thionyl chloride absolute methanol procedure<sup>2</sup> and Boc-amino acids used in this work were prepared using Schnabel's method.<sup>3</sup> Solution Phase Peptide Synthesis: All peptides were synthesized by conventional solution-phase methods using racemization free fragment condensation strategy. The Boc group was used for N-terminal protection<sup>3</sup> and the C-terminus was protected as a methyl ester.<sup>2</sup> Couplings were mediated by N,N'-dicyclohexylcarbodiimide/1-hydroxybenzotriazole (DCC/HOBt)<sup>4</sup> Methyl ester deprotection was performed via the saponification method, and the Boc group was deprotected by 98% formic acid. The synthetic strategy was selected for most of the peptides keeping in mind that the racemization possibilities of other chiral residues in the sequence. Racemization in any step of the peptide synthesis leads to the formation of diastereomeric products. At each step of the synthesis the possibility of diastereomer formation was checked by NMR. Normally no diastereomers could be detected. Characterization and Purification of Peptides: Peptide fragments were routinely checked for homogeneity by thin layer chromatography (TLC) on silica gel using ethyl acetate-pet ether as an eluent. All the intermediates were characterized by 300, 400 and 500 MHz <sup>1</sup>H NMR spectroscopy, 75, 100 and 125 MHz <sup>13</sup>C NMR spectroscopy and mass spectrometry. All crude peptides were purified by column chromatography using silica gel (100-200 mesh size) as stationary phase ethyl acetate-pet ether mixture as eluent. The final compounds were fully characterized by 300 and 500 MHz <sup>1</sup>H NMR spectroscopy, 75 and 125 MHz <sup>13</sup>C NMR spectroscopy and mass spectrometry.

### 2.4. Spectroscopic Measurements

**NMR experiments:** All 300, 400 and 500 MHz NMR studies were carried out on a Bruker DPX spectrometer and. Coupling constants were calculated from one-dimensional experiments.

**FT-IR spectrometer:** Spectra were collected on a JASCO instrument, Model FT/IR-4200 type A. For the solution state in chloroform, NaCl cell was used. For the solution state in D<sub>2</sub>O, CaF<sub>2</sub> cell was used.



**Mass spectrometry:** Mass spectra were recorded on a Qtof Micro YA263 high-resolution mass spectrometer.

**MALDI-TOF:** MALDI-TOF MS analysis has been performed by using Applied Biosystems MALDI TOF/TOF Analyzer.

**X-Ray Photoelectron Spectroscopy:** XPS analysis of carbon dots was carried out by using an X-ray photoelectron spectroscopic (XPS, Omicron, model: 1712-62-11) method. Measurements were performed by using an Al-K $\alpha$  radiation source under 15 kV voltage and 5 mA current.

## 2.5. Microscopic Studies

**Scanning Electron Microscopy:** Morphological studies of all reported compounds were investigated using scanning electron microscope (SEM). The scanning electron microscopic studies of the peptides were done using a small amount of the solution of the corresponding compounds on microscopic slides and drying in air at room temperature. These dried samples were platinum coated and observed under microscope. The SEM studies of other peptides were taken from fibrous materials (growing from ethyl acetate or methanol-water solution by slow evaporation) after gold coating. SEM pictures were taken in a SEM apparatus (Jeol Scanning Microscope-JSM-5200 and Jeol Scanning Microscope-JSM-6700F).

**Transmission Electron Microscopy:** Transmission Electron Microscopy (TEM) was carried out to investigate the morphology of the nanostructures. Transmission electron microscopic (TEM) studies were carried out using a small amount of the solution of the corresponding compounds on a carbon coated copper grid (300 mesh) by slow evaporation and vacuum drying at 30°C for 2 days. TEM images were recorded on a JEM 2010F electron microscope and JEOL 2100 Ultra High-Resolution Field Emission Gun (UHR FEG at an accelerating voltage of 200 KV. STEM-HAADF image and EDS line scanning were recorded on a JEM 2010F electron microscope.

## 2.6. Rheological Study

Rheological experiments were done using an Advanced Rheometer AR 2000 (TA Instruments) by cone and plate geometry in a peltier plate. The cone diameter was 40 mm, cone angle 1° 59' 50", and truncation 56  $\mu$ m.

### 2.7 I-V Measurements

For I-V measurements, the DC currents were measured using Keithley source meter (model 2410). The dark I-V characteristic was performed after keeping the samples in dark for several hours. For photocurrent transient measurement, a xenon light source (model no. 66902; Newport Corp. USA) with power of 1 sun was used for the light illumination.

### 2.8 Biological Studies

**Cell culture and Microscopy:** Custom made 35 mm plastic petri dishes, with a concentric hole of diameter 10 mm, were fitted with 22x22 mm glass coverslips on the bottom using biocompatible silicone grease. A sterile rubber O-ring of diameter 12 mm was attached on top of the hole, also using silicone grease, creating a cylindrical enclosure of height ~3 mm. Then 100  $\mu$ L of the gel, pre-heated to the sol state, was poured onto the glass inside the hole and allowed to cool down and solidify. NIH 3T3 cells, cultured at 37 °C/5% CO<sub>2</sub>, in Dulbecco's modified Eagle medium (DMEM), supplemented with 10% fetal bovine serum (FBS), 100 units/ml of penicillin, and 100  $\mu$ g/ml of streptomycin were grown up to 85-90% confluence, and then harvested using 0.5 mM EDTA. 10<sup>4</sup> cells suspended in 100  $\mu$ L culture media were seeded on the gel only inside the space enclosed by the O-ring, and the dish was kept undisturbed for at least 10 minutes to allow the cells to settle. The dish was then filled with 3 mL of culture medium and stored in the cell culture incubator. Cells were then observed every 6 h using an inverted microscope (Zeiss AxioObserver Z1). Images were taken at 40x and 20x magnification using a CMOS camera (Hamamatsu Orca Flash 4.0 V2). Cells were stained with Hoechst 3342 to visualize the nucleus. Rhodamine 123 was used to stain the live cells. Hoechst 3342 and Rhodamine 123 solutions were prepared as 1  $\mu$ g/mL and 10  $\mu$ g/mL to stain the cells.

**MTT Assay:** An MTT assay<sup>5</sup> was performed to assess the viability of cells in the hydrogel environment. Mitochondrial active succinate dehydrogenase converts MTT (3-[4,5-dimethylthiazol-2-yl]-2,5-diphenyl tetrazolium bromide into purple colored formazan crystals, and its absorbance at 570nm is proportional to the

number of live cells.  $10^4$  cells were seeded for 48h, 36h, 24h and 12h from the time of addition of the MTT in a 48 well plate, with or without hydrogel. Gels of two different concentrations (1% and 2% w/v) were used to assess the effect of 2D and 3D environment on cell proliferation. Cells in each well were simultaneously treated with MTT (0.5 mg/mL) for 3 h at 37 °C/5% CO<sub>2</sub>. After incubation, 200 µL of DMSO was added to each well and absorbance at 570nm was measured on a SpectraMax M2 spectrometer (Molecular Devices). Each condition was repeated thrice and errors bar representing standard deviation are plotted as part of the assessment of cell viability in the hydrogel environment, with the cells grown in standard poly-L-Lysine coated plastic surface as control.

**ROS-generation Study.** Bacterial ROS generation in presence of the hybrid-hydrogel is probed using 2,7-Dichlorofluorescein Diacetate which emits at 535 nm when excited at 485 nm in its activated form. Samples are prepared by first taking 1mL of bacteria suspension from a liquid culture in micro-centrifuge tubes. The samples are centrifuged at 6000 rpm for 5 minutes to observe pellet formation at the bottom of the tube. The broth is discarded and replaced by Hank's Balanced Salt Solution (HBSS). The new suspension is then treated with various quantity of hybrid-hydrogels. 2m 2,7-Dichlorofluorescein Diacetate stock is prepared by dissolving 1 mg of the dye in 1mL DMSO. 10 µL of stock solution is added to each micro-centrifuge tube 10 minutes before taking fluorescence readings. Readings are recorded with a Fluoromax-3 instrument (Horiva Jovin Yvon).

**Antimicrobial Studies.** Well diffusion method is utilized to check the antimicrobial activity of the samples. 90 mm sterile plastic plates were used to prepare the gel-bed made of 1.5% luria agar. 50 µL of bacteria suspension was spread on the plate before making wells to pour in 50-60 µL of the sample hydrogels. The plates were incubated for 16 hours at 37°C and the zone of inhibition was measured. The minimum inhibitory concentration (MIC) for different species was found using standard protocol of serial half-dilutions of the sample concentration. In this protocol Mueller Hinton broth was used throughout. Initially bacteria were grown in MH broth suspension from culture plates. From this suspension 20 µL was added to each vial containing the sample dissolved in MH broth. The vials are incubated for 16 hours at 37°C and the optical density

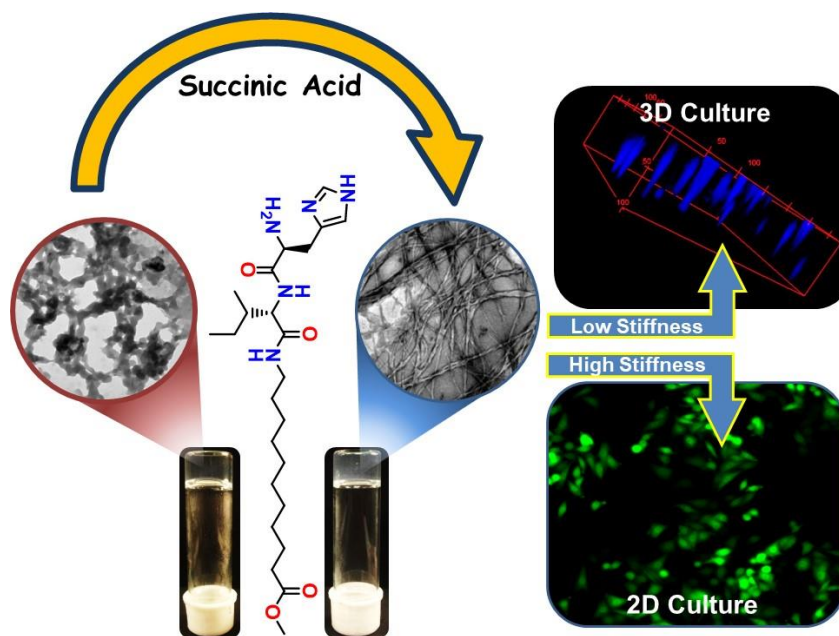
(OD) of the vials was measured at 600 nm with a Cary Varian 50 scan UV-Vis optical spectrometer. The minimum sample concentration at which OD became close to zero, was designated as the MIC.

### 2.9. References

- (1) A. I. Vogel, *A Text Book of Practical Organic Chemistry*, 4th Eds. ELBS, Longmans, 1978I.
- (2) M. Brenner and W. Hubber, *Helv. Chim. Acta.*, 1953, **36**, 1109-1115.
- (3) E. Schnabel, *Ann. Chem.*, 1967, **702**, 188-196.
- (4) M. Bodanszky and A. Bodanszky, *The Practice of Peptide Synthesis*, Springer-Verlag, Berlin, Heidelberg, New York, Tokyo, 1984, 1-282.
- (5) Mosmann, T. Rapid Colorimetric Assay for Cellular Growth and Survival: Application to Proliferation and Cytotoxicity Assays. *J. Immunol. Methods* 1983, **65**, 55-63.

## CHAPTER 3

# Self-Assembling Peptide-Based Hydrogel: Regulation of Mechanical Stiffness and Thermal Stability and 3D Cell Culture of Fibroblasts





### 3.1 Introduction

Self-assembling small molecule soft materials have continued to create interest over the years, due to their diverse applications<sup>1-5</sup> and easy tunability.<sup>6,7</sup> Usage of self-assembling peptides as functional materials has numerous advantages, namely, low fabrication cost, good biocompatibility and control over functionality. Amphiphilic peptides are good candidates for self-association to form gels under suitable conditions. Current improvement of bio-medical technology demands gel-like soft materials for efficient culture of stemcells,<sup>8</sup> therapeutics,<sup>9,10</sup> immune modulation,<sup>11</sup> in vitro diagnostics,<sup>12</sup> wound healing,<sup>13-15</sup> creation of synthetic extracellular matrix,<sup>16-19</sup> anti-bacterial agents,<sup>20-25</sup> drug delivery<sup>26-28</sup> and many others.<sup>29</sup> For such applications, gel-forming peptides have great potential, due to their inherently biocompatible nature and low toxicity compared to conventional polymer-based materials.<sup>30</sup> Moreover, it is challenging to tune the physical properties of covalent polymers, whereas supramolecular assemblies are more flexible, and they are easily stabilized by various non-covalent interactions including H-bonding, van der Waals interactions and  $\pi$ - $\pi$  stacking. Design of nanofibrous gel scaffolds is one of the key components in the field of regenerative medicine.<sup>31-34</sup> In a tissue system, the relation between the cells and the surrounding matrix plays a crucial role in proliferation, differentiation and migration of the cells for tissue repair. Hydrogels provide an excellent environment for cell growth and tissue regeneration due to their high oxygen, nutrient and metabolite permeability. Various research groups over the globe have designed and utilized peptide-based hydrogels as cell culture scaffolds. Ulijn and co-workers have reported fluorenylmethoxycarbonyl-protected peptide-based hydrogels for 3D culture of bovine chondrocytes.<sup>35</sup> Tomasini and co-workers have developed a non-cytotoxic pseudo-peptide-based hydrogel that can be used for regenerative medicine.<sup>36</sup> These peptides produce a perfect environment upon assembly which mimics the extracellular matrix as a perfect platform for the cell growth. Recently Langhans and co-workers have reported a series of  $\beta$ -hairpin gelator peptides for 3D cell culture.<sup>37</sup> Gazit and co-workers have reported a peptide-based self-healing and conductive hydrogel which supported the growth of electrogenic cells, cardiomyocytes.<sup>38</sup>

In the context of cell culture, the mechanical properties of the matrix are important to realize cell adhesion and proliferation. The extracellular matrix is a dynamic system with specific mechanical properties and a rationally

designed synthetic scaffold must successfully mimic the *in vivo* situation. Different types of cells demand matrices of different stiffness to grow.<sup>39</sup> Discher and co-workers have shown that it is possible to grow neuronal, muscle, and bone cells from human mesenchymal stem cells by culturing them in gels of varying elastic modulus.<sup>40</sup> Variation of gel stiffness is generally done by varying the concentration of gelator.<sup>41</sup> However, it has been reported that mechanical rigidity can be increased by adding hydrophobic amino acids in the peptide sequence, or by creating chemical cross-linking through oxidation of cysteine side chains or by using multi-component systems.<sup>42</sup>

The comprehensive goal of this work was to develop a cheap, non-cytotoxic, nanofibrous hydrogel, which can act as a scaffold for adherence and proliferation of cells. We demonstrate that it is possible to regulate gel stiffness (mechanical strength) and thermal stability by incorporating different dicarboxylic acids (oxalic acid, succinic acid, glutaric acid and octanedioic acid) as they promote extended non-covalent interaction between the histidine containing, N-termini free peptide molecules. By tuning the elasticity of dicarboxylic acid incorporated peptide hydrogel through the variation of gelator concentration and chain length of dicarboxylic acids, a successful scaffold for mammalian fibroblast cell culture has been achieved. Among all the acids tested, succinic acid leads to the highest gel thermal stability and mechanical stiffness at a given concentration, thus peptide-succinic acid hydrogels at physiological pH (7.5) have been selected as our material of choice. Interestingly, it has been observed that the extended interaction through succinic acid spacer changes the morphology of the hydrogel to a nanofibrous one, which mimics the extracellular matrix protein more than the native peptide gel with a nano-spherical morphology. In this study, 3D cell culture was possible in the hydrogel with a storage modulus of 4 kPa, whereas for a stiffer gel with storage modulus of 9.7 kPa, only 2D culture was possible on the surface of the hydrogel. Thus, a two-component hydrogel with a suitable gel stiffness can serve as a successful cell culture scaffold for mouse fibroblasts and this holds future promise in the field of short peptide based regenerative medicine and tissue engineering.



## 3.2 Result and Discussion

The L-histidine containing C-terminal protected tripeptide NH<sub>2</sub>-His-Ile-AUDA-COOMe (AUDA = 11-aminoundecanoic acid) **P1** (Figure 3.2a) was synthesized in solution phase and subsequently purified and characterized.

### Gelation Study

The gelation property of **P1** was tested in the full spectrum of pH of phosphate buffer solutions (PBS) and it was found that a transparent hydrogel was formed between pH 5.5 to 8.5. For each gelation study, 4 mg of the solid peptide was taken in a glass vial and dissolved in 1 mL of PBS by heating with a hot-gun until a clear solution was obtained. The solution was allowed to equilibrate at room temperature (27 °C) and it turned translucent as it was cooled down within 60 seconds. Interestingly, it became transparent as hydrogel formation took place. The gel melting temperature of the peptide hydrogel at pH 7.46 was found to be 44 °C (0.5 % w/v i.e. 10.75 mM). To strengthen the network of the hydrogel, we have incorporated various dicarboxylic acids into the peptide gel network. For each gelation experiment 4 mg (8.6 μmol) of solid peptide was placed in 950 μL of PBS (pH 7.46), dissolved by careful heating with a hot-gun and 50 μL of 85 mM (4.3 μmol) dicarboxylic acid solution (oxalic acid, succinic acid, glutaric acid and octanedioic acid) was added to it to obtain the peptide-dicarboxylic acid based two-component hydrogels. There was no significant change in the appearance of the gel as the pH changed from 5.5 to 8.5 (Figure 3.1). Neither did the addition of dicarboxylic acid of different chain lengths showed any significant change in the appearance of two-component hydrogels (Figure 3.1).

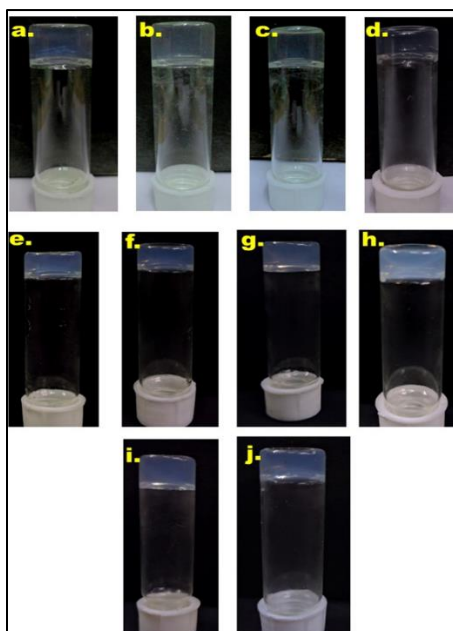


**Figure 3.1:** Images of hydrogels of P1 at 0.5 % w/v (10.75 mM) in (a) pH 5.5, (b) pH 6.5, (c) pH 7.5, (d) pH 8.5. Images of two component hydrogels at 0.5 % w/v (10.75 mM) of P1 consisting of (e) P1+oxalic acid, (f) P1+succinic acid, (g) P1+glutaric acid, (h) P1+octanedioic acid. (i) Hydrogel optimized for 3D cell culture experiments (P1+succinic acid with 21.5 mM P1) and (j) Hydrogel optimized for 2D cell culture experiments (P1+succinic acid with 43 mM P1)

It was observed that the gel melting temperature significantly increased upon the addition of dicarboxylic acids (Table 3.1). The most prominent improvement was shown for peptide-succinic acid gel, which showed a  $T_{\text{gel}}$  of 62 °C (0.5 % w/v). The native hydrogel, as well as the gels obtained after the addition of succinic acid, were found to be transparent and suitable for microscopic studies (Figure 3.2c). A comparative study of gel melting temperature versus concentration of gelator, between native peptide gel and the peptide-succinic acid gel shows the improvement of thermal stability overall concentration range. It is noted that  $T_{\text{gel}}$  values become essentially independent of concentration above 1% w/v for both the hydrogels (Figure 3.2b).

**Table 3.1:** Details of various hydrogels of P1 and dicarboxylic acids including gels used for cell culture

Gel	Melting Temperature (°C)	pH	Concentration of P1 (mM)
Peptide	44	7.5	10.75
Peptide+ <b>Oxalic Acid</b> (n=0)	53	7.5	10.75
Peptide+ <b>Succinic Acid</b> (n=2)	62	7.5	10.75
Peptide+ <b>Glutaric Acid</b> (n=3)	57	7.5	10.75
Peptide+ <b>Octanedioic Acid</b> (n=8)	56	7.5	10.75
Peptide+ <b>Succinic Acid</b> (for 3D culture)	65	7.5	21.50
Peptide+ <b>Succinic Acid</b> (for 2D culture)	67	7.5	43.00

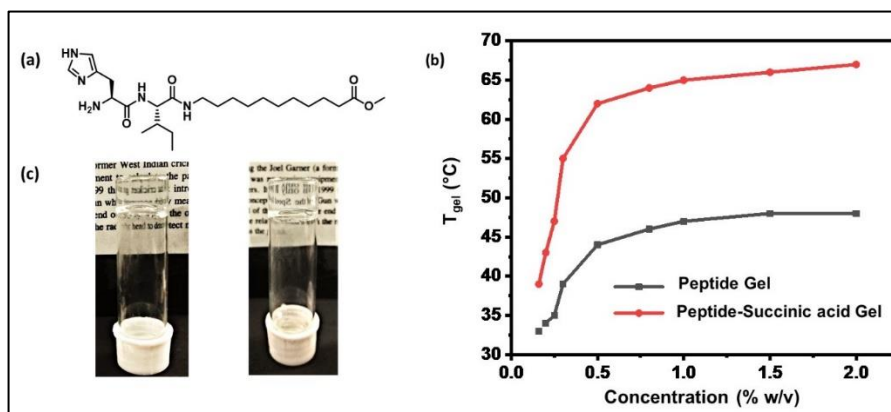


**Figure 3.2.** (a) Chemical structure of peptide P1; (b) Gel melting temperature ( $T_{gel}$ ) of hydrogel obtained from P1 and hydrogel obtained from P1 added with succinic acid, plotted against various concentrations; (c) Inverted vial images of peptide gel (left) and Peptide-succinic acid gel (right).

### Morphology

High resolution transmission electron microscopic (HR-TEM) studies were performed to examine the morphologies of the gelators in different assembled states (aggregated non-gel and gel states). Samples of **P1** hydrogels were made at two different concentrations to understand the nature of the aggregation. The HR-TEM images obtained from the dilute solution reveals the formation of nanospheres (Figure 3.3a). The radii of the nanospheres vary from 80 nm to 100 nm. The radii are plotted in a frequency distribution histogram (Figure 3.4a) and the average radius is found to be 90 nm. In the non-gel state, the nanospheres are obtained from the aggregation of gelator molecules and these nanospheres are aligned in a regular fashion forming a network-like arrangement (Figure 3.3b). Although this is a rare phenomenon, a few examples have been observed for the spherical morphology in gels formed by assembly of small molecules.<sup>44, 45</sup> The three-dimensional porous network structure formed by adhered interconnecting nanospheres shows a beads-on-a-string-like morphology in the concentrated gel phase (Figure 3.3c). This cage-like porous structure can entrap a lot of water molecules into it to form a self-supporting hydrogel. Interestingly, a change in the morphology is observed in the two-component gel consisting of the peptide gelator P1 and succinic acid. In presence of the acid, a well-resolved interconnected helical nanofibrous network structure is obtained (Figure 3.3d). The width of the gel forming fibers ranges from 40 nm to 60 nm.

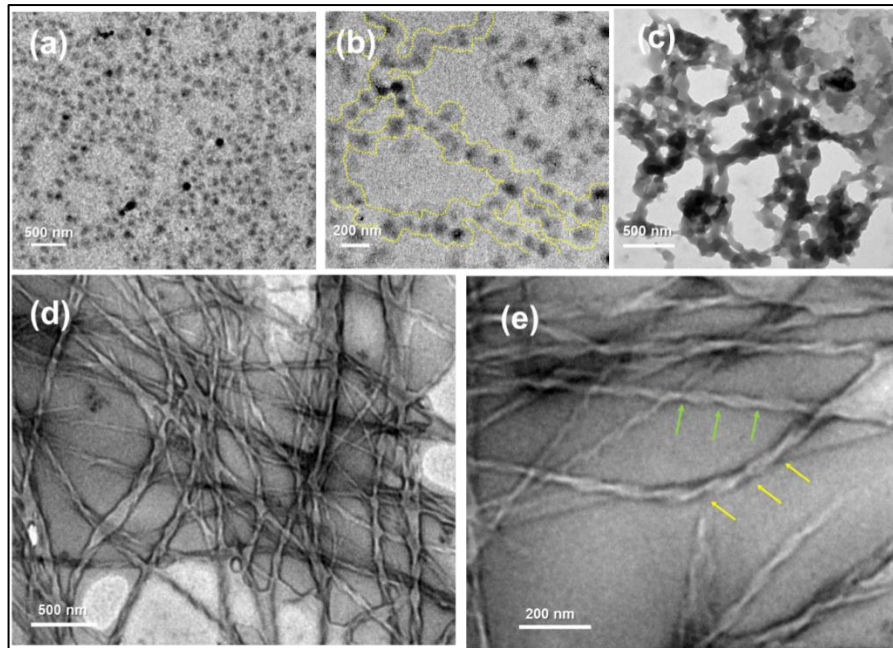


**Figure 3.3.** High Resolution Transmission Electron Microscopic images showing (a) nanospheres composing the peptide hydrogel; (b) magnified image of the nanospheres arranged in a network-like arrangement (yellow dotted line highlights the pattern); (c) 3D network assembly of the nanospheres showing beads-on-a-string-like morphology; (d) Helical fibrous morphology of peptide-succinic acid hydrogel, (e) Individual fibers of peptide-succinic acid gel. (Green arrows and yellow arrows show two different kinds of handedness in the helices.)

A histogram showing frequency distribution of widths (Figure 3.4b) of different fibers reveals that the average width of the fibers is 50nm. Widths of most of these fibers lie within the range from 50 nm to 55 nm. The network shows the presence of both right and left-handed helicity (Figure 3.3e). The nanofibrous network is well adapted to support the proliferation of mammalian cells. The images reveal a remarkable transition from a nanosphere (soluble aggregated non-gel state) to a beads-on-a-string morphology in the gel state. A few previous reports describe morphological transformations within hydrogel systems.<sup>46-48</sup> However, it is rare to observe a drastic change in morphology (interconnected nanospheres to helical nanofibers) from one gel phase (only peptide) to another gel phase (peptide + succinic acid).

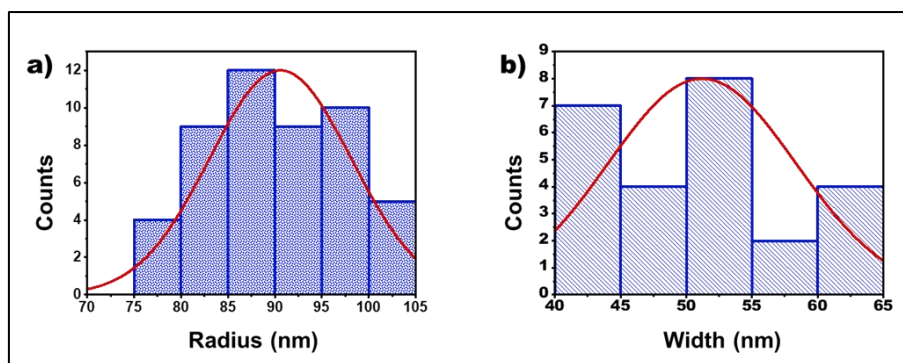


**Figure 3.4:** (a) Frequency distribution of radii of nanospheres found in hydrogel of P1, (b) Frequency distribution of the width of the fibers consisting P1-succinic acid gel.

### Fourier Transformed-Infrared (FT-IR) Spectroscopic Study

Intense peaks at  $3291\text{ cm}^{-1}$  corresponding to N-H stretching vibration,  $1637\text{ cm}^{-1}$  corresponding to amide C=O stretching (amide I) and  $1555\text{ cm}^{-1}$  (N-H bending), suggest a strongly hydrogen bonded network in the **P1** hydrogel at physiological pH (Figure 3.5).<sup>49</sup> Similar kind of IR signatures were found in two component gels with various dicarboxylic acids. Moreover, the decrease in the stretching frequency of ester C=O to  $1730\text{ cm}^{-1}$  suggests bond elongation, which indicates its participation in hydrogen bonding (the ester C=O stretching generally appears within the  $1735\text{--}50\text{ cm}^{-1}$  range).<sup>50</sup> A xerogel obtained from the two-component gel containing peptide and succinic acid shows symmetric and antisymmetric stretching of carboxylate anion of succinic acid at  $1420\text{ cm}^{-1}$  and  $1570\text{ cm}^{-1}$  respectively along with the other peaks observed for the peptide-only gel (Figure 3.5).

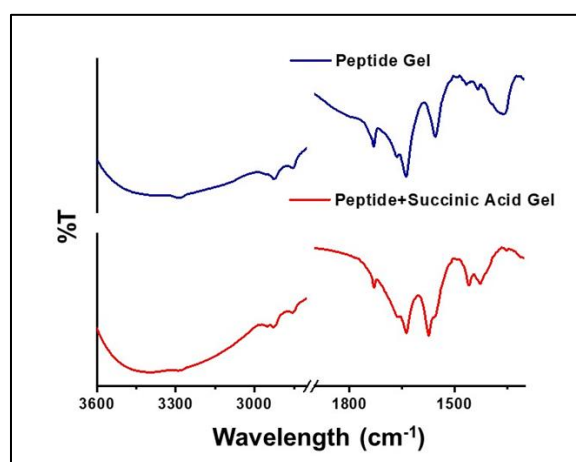


**Figure 3.5:** FTIR spectra comparison of Peptide P1 assembly and Peptide-Succinic acid aggregation

### Powder X-Ray Diffraction Studies

To probe the molecular packing within the gels, X-ray diffraction studies of powdered freeze-dried gels were performed. In the low angle diffraction pattern, for the peptide only gel, we observed a peak at  $D = 30.26 \text{ \AA}$  ( $2\theta = 2.84^\circ$ ), which can be attributed to the length of two peptide molecules interdigitated along the hydrocarbon chain (Figure 3.6a) (Estimated molecular length of **P1** is  $24.62 \text{ \AA}$ ). A similar packing was reported previously for a lipidated histidine dipeptide gelator.<sup>51</sup> In the wide-angle powder x-ray diffraction patterns, peaks at  $4.78 \text{ \AA}$  ( $2\theta = 18.05^\circ$ ) are ascribed to the distance between  $\beta$ -strands and the peak at  $9.87 \text{ \AA}$  ( $2\theta = 8.71^\circ$ ) corresponds to the distance between two stacked  $\beta$  sheets (Figure 3.6b).<sup>52</sup> Interestingly four peaks at  $5.48 \text{ \AA}$  ( $2\theta = 15.72^\circ$ ),  $4.39 \text{ \AA}$  ( $2\theta = 19.66^\circ$ ),  $3.74 \text{ \AA}$  ( $2\theta = 23.13^\circ$ ),  $3.33 \text{ \AA}$  ( $2\theta = 26.00^\circ$ ) correspond to  $D/6$ ,  $D/7$ ,  $D/8$  and  $D/9$  respectively. This indicates a lamellar type of packing arrangement.<sup>52</sup> Investigation of small angle diffraction pattern from succinic acid-peptide xerogels showed a peak at  $D' = 59.27 \text{ \AA}$  ( $2\theta = 1.45^\circ$ ). The total molecular length of two peptide molecules and a succinic acid ( $5.05 \text{ \AA}$ ) (estimated in Chem3D Pro 12.0 software) is  $54.3 \text{ \AA}$ . However, if the succinate anion and the peptide molecules are connected through hydrogen bonding between imidazole N-H and carboxylate O, the overall supramolecular unit length increases by twice that of N-H...O hydrogen-bond length<sup>53,54</sup> ( $2.7 \text{ \AA} \times 2 = 5.4 \text{ \AA}$ ) and it becomes  $59.69 \text{ \AA}$ , which is in accordance with the d-spacing found by XRD (Figure 3.6c). So, we can conclude that the two peptide molecules are interconnected by a centrally located succinic acid moiety through hydrogen bonding. Furthermore, three peaks at  $6.13 \text{ \AA}$  ( $2\theta = 14.05^\circ$ ),  $5.50 \text{ \AA}$  ( $2\theta = 15.67^\circ$ ),  $4.85 \text{ \AA}$  ( $2\theta = 17.81^\circ$ ) can be interpreted as  $D'/10$ ,  $D'/11$  and  $D'/12$ , and this suggests the length corresponding to two terminally located peptide molecules hydrogen bonded to a centrally positioned succinic acid moiety (Figure 3.6d). Another set of peaks was found at  $3.90 \text{ \AA}$  ( $2\theta = 22.22^\circ$ ),  $3.66 \text{ \AA}$  ( $2\theta = 23.62^\circ$ ),  $3.36 \text{ \AA}$  ( $2\theta = 25.82^\circ$ ), assigned as  $D'/15$ ,  $D'/16$  and  $D'/17$ . It shows that the peptide succinic acid gel packs in a lamellar fashion. Again, the d-spacing of  $4.78 \text{ \AA}$  ( $2\theta = 18.05^\circ$ ) is the distance between  $\beta$ -strands.



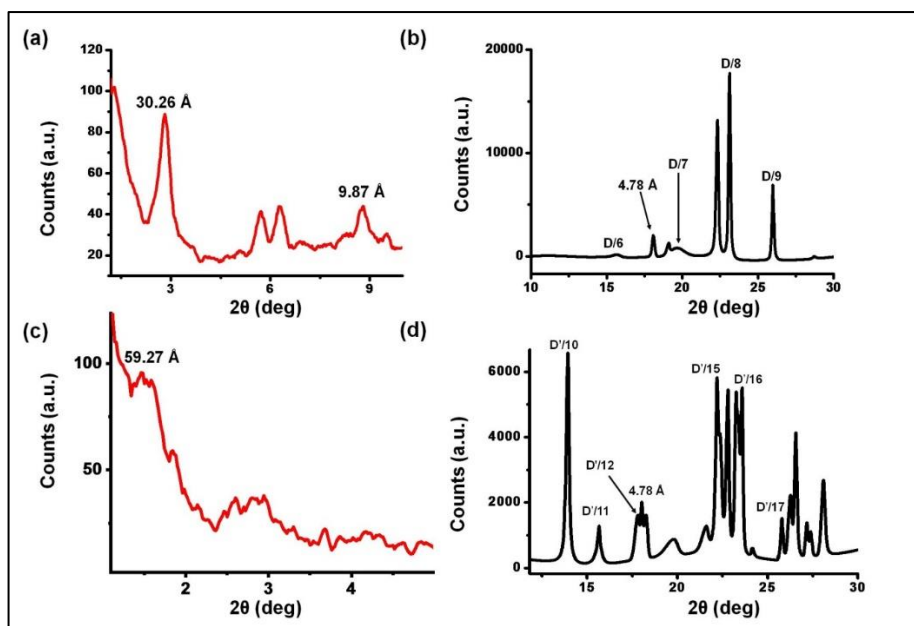


**Figure 3.6.** (a) Low-angle (b) Wide-angle X-ray diffraction pattern recorded for xerogel obtained from peptide hydrogel (c) Low-angle (d) Wide-angle X-ray diffraction pattern recorded for xerogel obtained from succinic acid-peptide hydrogel.

### Small-Angle X-ray Scattering (SAXS) Study

To visualize single molecular length and mode of packing of the peptide in the (undried) gel state, small angle X-ray scattering (SAXS) was carried out. The d-spacing of 30.2 Å (Figure 3.7) can be assigned to the length of a layered structure of two interdigitated peptides. This data supports the low angle powder XRD data of the dried peptide gel. On the basis of SAXS and PXRD and FT-IR studies, probable models for the molecular packing pattern of the gel phase has been constructed in Figure 3.8 for the native peptide gel and the two-component gel (obtained from peptide and succinic acid) respectively.

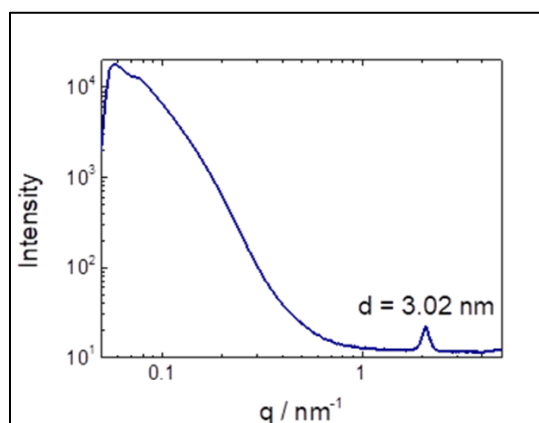


**Figure 3.7** SAXS intensity profile for peptide-only gel shows a d-spacing 30.2 Å.



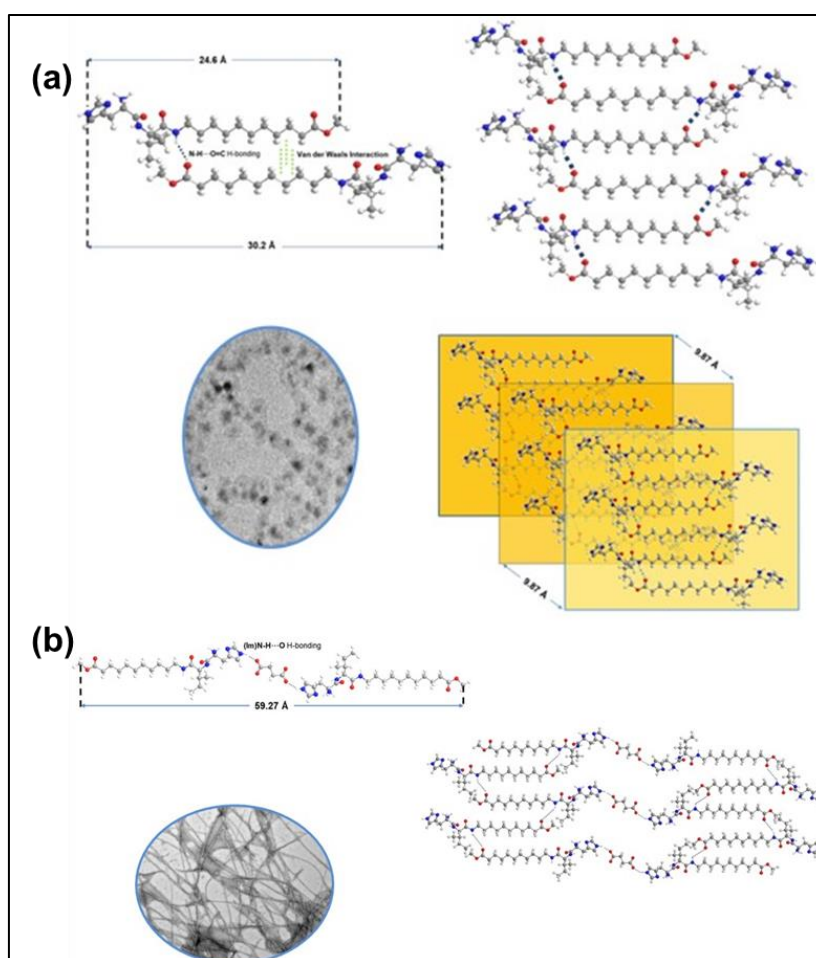


**Figure 3.8** Model for the probable mode of self-assembly of (a) the peptide hydrogel and (b) that of peptide-succinic acid two-component hydrogel.

### Rheological Study

The stiffness of the extracellular matrix is known to influence cell physiology, and thus, it is a crucial parameter to address when developing hydrogels as models for tissue systems. The degree of stiffness of the peptide hydrogels and peptide-dicarboxylic acid gels were systematically measured and compared to get an insight into how the incorporation of these acids affects the mechanical strength of the native gel. Time sweep rheology data of the peptide gel was also recorded to quantify the visible thixotropic property of the hydrogel. Firstly, the frequency sweep experiment was done for peptide hydrogel with gelator concentration 0.5% (w/v) (10.75 mM) where the two moduli, i.e. storage modulus ( $G'$ ) and loss modulus ( $G''$ ) were plotted against angular frequency ( $\omega$ ) ranging from 8-100 rad/s, at a constant strain of 0.1%. The moduli show an insignificant dependence on angular frequency (Figure 3.9a).

This indicates the formation of a stable gel. To attain higher stiffness, we increased the concentration of the gelator to 1.0% w/v (21.50 mM) and 1.5% w/v (32.25 mM). While doubling the concentration of the peptide increased the elastic modulus by a factor of two, tripling the concentration increased the elastic modulus tenfold. At  $\omega = 50$  rad/s,  $G'$  is 690 Pa, 1402 Pa and 7006 Pa for 0.5%, 1%, 1.5% w/v hydrogel respectively (Figure 3.9a). The time-dependent step-strain experiment was performed with a time step of 125 s. Initially, the strain was kept constant at 0.1% then the strain was increased to 30% at which point the gel ruptured. The reformation of the gel takes place as the strain is reduced to 0.1% at the next cycle. The process was continued to 3 cycles to show reproducibility (Figure 3.9b).

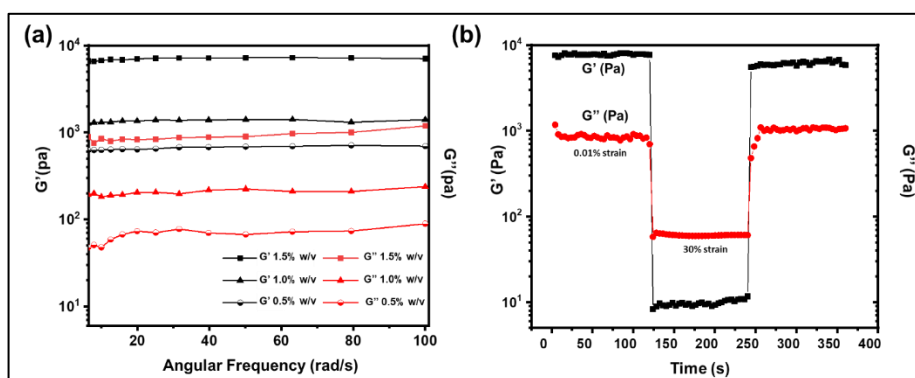


**Figure 3.9** (a) Elastic modulus  $G'$  and Loss modulus  $G''$  of hydrogels of peptide **PI** in three different concentrations 1.5% w/v, 1% w/v and 0.5% w/v; (b) Step strain experiment for 1.5% w/v of peptide **PI** hydrogel with 125 s step length, confirming thixotropic behavior of the hydrogel.

Dicarboxylic acids with varying chain lengths were incorporated with an expectation of extended supramolecular interactions between free carboxylic acid groups and peptide molecules with free N terminus, as well as the imidazole side chain of the histidine residue. Peptide-dicarboxylic acids at 1% w/v (21.50 mM) concentration of peptide and acids taken in 2:1 molar ratio indeed showed increased storage modulus, to different degrees, for different acids (Figure 3.10).

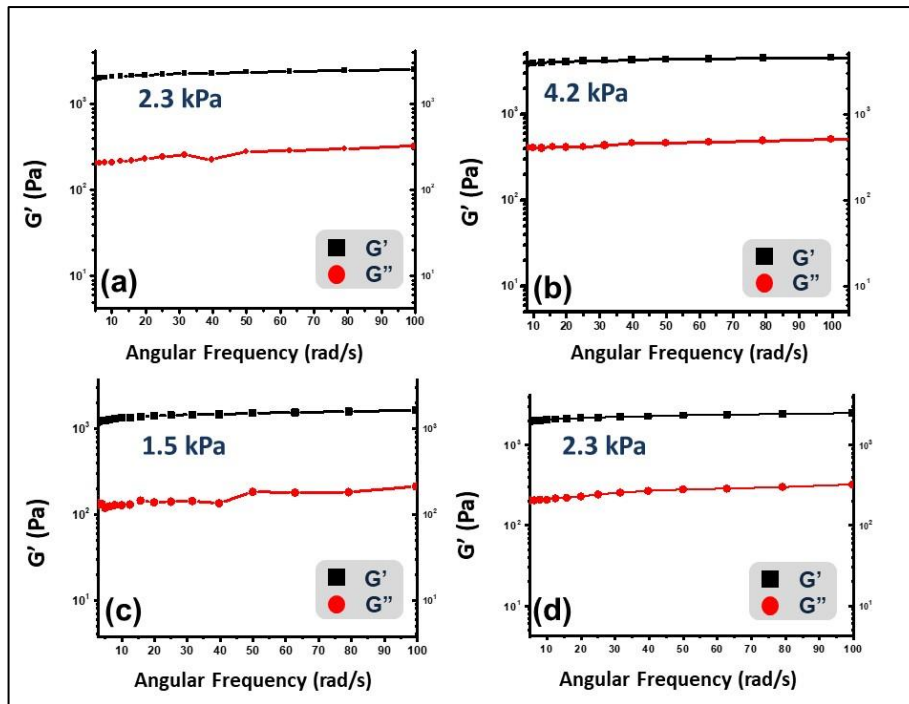


**Figure 3.10** Elastic modulus  $G'$  and Loss modulus  $G''$  of hydrogels of peptide **P1** with different additives, (a) oxalic acid, (b) succinic acid, (c) glutamic acid, (d) octanedioic acid, with value of  $G'$  at 50 rad/s indicated for each case. Peptide and dicarboxylic acid were taken in a 2:1 molar ratio with 1% (w/v) (21.50 mM) peptide in each hydrogel.

The most significant enhancement of mechanical strength was shown by the addition of succinic acid (Figure 3.10). Due to its optimal mechanical and thermal response, the transparent gels of peptide-succinic acid were used in cell culture. Stiffness tuning of the peptide-succinic acid gel could be achieved by varying the concentration from 0.5% to 2.0% w/v (Figure 3.11a-d). At  $\omega=50$  rad/s,  $G'$  is 879 Pa, 4340 Pa, 8357 Pa and 9729 Pa for 0.5%, 1%, 1.5% and 2% w/v hydrogel respectively. Step strain experiment was also performed for peptide-succinic acid hydrogel (Figure 3.11e) to confirm the thixotropic behavior which was observed visually. The reformation of gel phase takes place within 30 minutes.

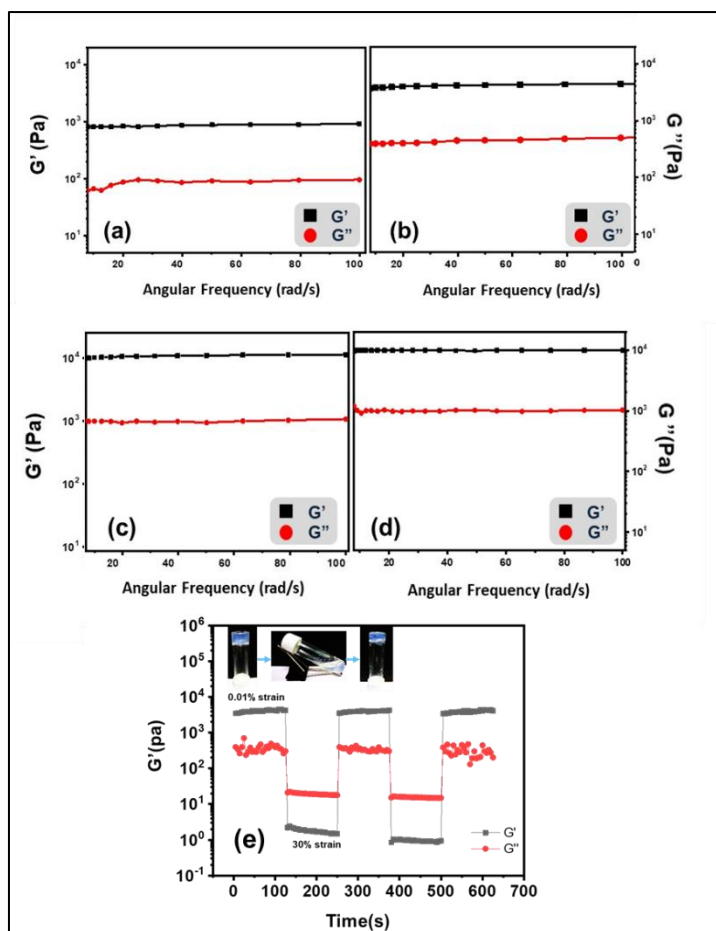


**Figure 3.11** Elastic modulus  $G'$  and Loss modulus  $G''$  of hydrogels of two component gel of peptide and succinic acid in different concentrations of peptide and succinic acid, (a) 0.5% w/v, (b) 1% w/v, (c) 1.5% w/v, (d) 2% w/v. (e) Step strain rheological data for peptide-succinic acid gel (1% w/v) showing recovery of gel phase after removal of mechanical force. (Inset image shows gel state transforms to sol after shaking and regains gel form as the mechanical force is withdrawn.)

### Cell culture Experiments

The histidine-based hydrogel is optically transparent, and it forms gels at a physiological pH of 7.5. Free  $\text{NH}_2$  groups give it a net positive charge at pH 7.5, which would facilitate adhesion of negatively charged cell membranes on the substrate. Moreover, the stiffness of the gel can be tuned by varying the gelator concentration. This makes our hydrogel system a good candidate as an extracellular matrix mimic. Due to transparency and good rheological response, the hydrogel of **P1** was initially used to investigate whether cells can grow on them or not. The fibroblast cell line NIH 3T3 was employed for cell culture experiments. Cell culture was attempted on the peptide gel (1.5% w/v) (32.25 mM) with the stiffness of 7 kPa, but it was found that the gel would disappear readily within 6 h at the incubator temperature of 37 °C. This

is because the gel melting temperature of the pure peptide gel at 1.5% w/v gelator concentration is 48 °C and this makes it slightly unstable at the physiological temperature of 37 °C. To primarily increase the thermal stability of the hydrogel, we incorporated several dicarboxylic acids along with the peptide gelator. As detailed above, the peptide-succinic acid gel gave the best thermal and mechanical response. The nanofibrous morphology of the peptide-succinic acid gel also encouraged us to investigate its possibility of acting as an extracellular matrix for cell growth and proliferation. Cell culture was performed on custom-made glass bottomed petri dishes. Cell culture was first attempted on 2% w/v (43 mM peptide+ peptide-succinic acid gel ( $G' = 9.7$  kPa). Cell growth was monitored for 36 h at 6 h intervals, after which the gel mass generally got detached from the glass surface, making microscopy difficult. Figure 3.12 a shows that the cells are able to grow on the two-component peptide-based gel surface for at least 36 h without any debilitating effect on viability. Cells did not exhibit a well spread morphology, possibly due to absence of stable focal adhesions.<sup>55-57</sup> Fibroblasts are also known to tune their internal stiffness to enable survival and proliferation on substrates with lower stiffness, which often results in a rounded morphology.<sup>58, 59</sup> The cells that did have elongated morphology could have secreted ECM proteins (locally) as typical of fibroblasts<sup>60</sup> (Figure 3.12a). When cells were cultured on a lower concentration 1% w/v gel of a lower  $G' = 4$  kPa, it was convincingly apparent that they could penetrate deep inside the gel (Figure 3.12c-e). To assess their viability, the cells were stained with Rhodamine 123, a green fluorescent dye that accumulates on respiring mitochondrial membrane. Cells nuclei were also stained with the blue fluorescent dye, Hoechst. Live cells exhibit both green and blue fluorescence, while dead cells without respiring mitochondria just have only blue fluorescence. In Figures 3.12 (a) and (b), the Rhodamine 123/Hoechst staining reveals the living and dead cells cultured on 2% (w/v) hydrogel and glass. Figures 3.12 (a)-(ii) and (b)-(ii), have the dead cells indicted with red arrows. It is known that contractile forces generated by cells on the culture substrate can influence the mechanical architecture of the substrate.<sup>61</sup> In the case of the P1-succinic acid gel, the cellular traction stress could have broken the gel in a localized manner, thus enabling the cells to travel inside by constantly dissolving the gel beneath them. The gel above the cells could then recover from solution state to reform the gel due to its thixotropic property, after some time. Figure 3.12c shows DIC images of cells grown on the surface of the 1% w/v hydrogel. General cell morphology is

rounder than the cells cultured on the 2% w/v, but Rhodamine 123/Hoechst staining Figure 3.12d shows that cells are alive and healthy post 36 h after seeding on the gel. By imaging the Rhodamine 123 fluorescence of cells at 22 focal planes starting from the gel surface, each plane being 2  $\mu\text{m}$  apart, a 2D maximum intensity projection of the 3D fluorescence was generated, which essentially means showing only the brightest pixel of a 3D voxel (Figure 3.12d-i).

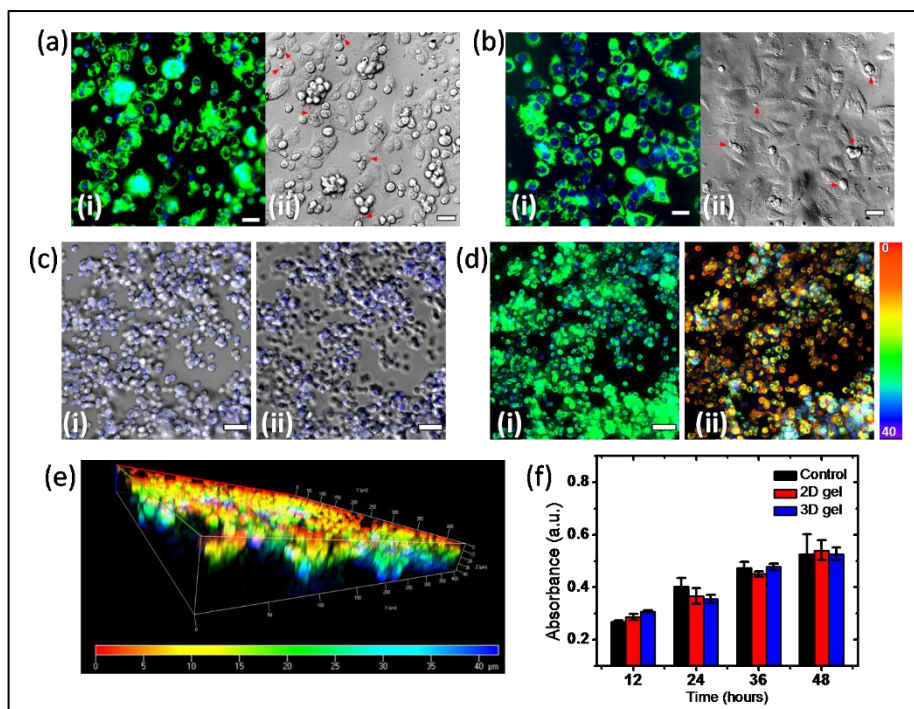


**Figure 3.12** (a)-(i) Fluorescence image of Rhodamine 123 (green) and Hoechst (blue) stained NIH 3T3 cells cultured on the surface of 2% (w/v) gel and (a)-(ii) is the corresponding Differential Interference Contrast (DIC) image (40x magnification) at 36h post seeding. Dead cells don't get stained by Rhodamine 123 but having their nuclei stained by Hoechst, they appear only blue. Dead cells have been pointed out in the DIC image using red arrows. (b)-(i) Fluorescence and (b)-(ii) DIC image of cells grown on glass at 36 h post seeding. Upon culturing cells on 1% (w/v) hydrogel, it was observed that cells were present at different depths inside the gel, post 36 h of seeding the cells on the surface. (c)-(i) shows DIC images (20X magnification) with the cell nuclei stained with Hoechst (blue) on the surface of the gel, (c)-(ii) shows cells at a depth of 20  $\mu\text{m}$  inside the gel. (d)-(i) Maximum Intensity Projection of fluorescence images of Rhodamine123/Hoechst-stained cells at 22 focal planes spanning a depth of 40  $\mu\text{m}$ . In (d)-(ii), the cells having Rhodamine 123 fluorescence were color coded according to their depth inside the gel in the Maximum Intensity Projection, with red indicating the gel surface. (e) 3D Volume Rendering of Rhodamine 123 stained cells (color bar indicates location of cell in the Z direction). (f) MTT assay comparing viability of cells on glass surface (black), 2% (w/v) gel for 2D culture (red) and 1% (w/v) gel for 3D culture (blue). Scale bars in (a)-(b) indicate 30 $\mu\text{m}$ , and in (c)-(d) indicate 50  $\mu\text{m}$



Depth color coding of the maximum intensity projection image reveals the distribution of the live cells along the height of the gel (Figure 3.12d-i), which is reiterated by the 3D volume rendering (Figure 3.12e) of the Rhodamine 123 stained cells. An MTT cell survival assay was performed to examine the influence of peptide-succinic acid hydrogel on cell viability over time. The assay reveals that the 2D or 3D environment provided by the peptide gel has no detrimental effect on cell viability (Figure 3.12f). This indicates that the peptide-based hydrogel obtained from gelator **P1** and succinic acid is not cytotoxic, and it can be used to mimic the extracellular matrix to culture fibroblasts in vitro up to two days at least.

We also did the cell growth experiments with the cell line RAW264.7 murine macrophages. This suggests that the hydrogel-based biomaterial is a good support for the growth of different types of cells in vitro. Details of that study can be found in the supporting information (Figure 3.13).

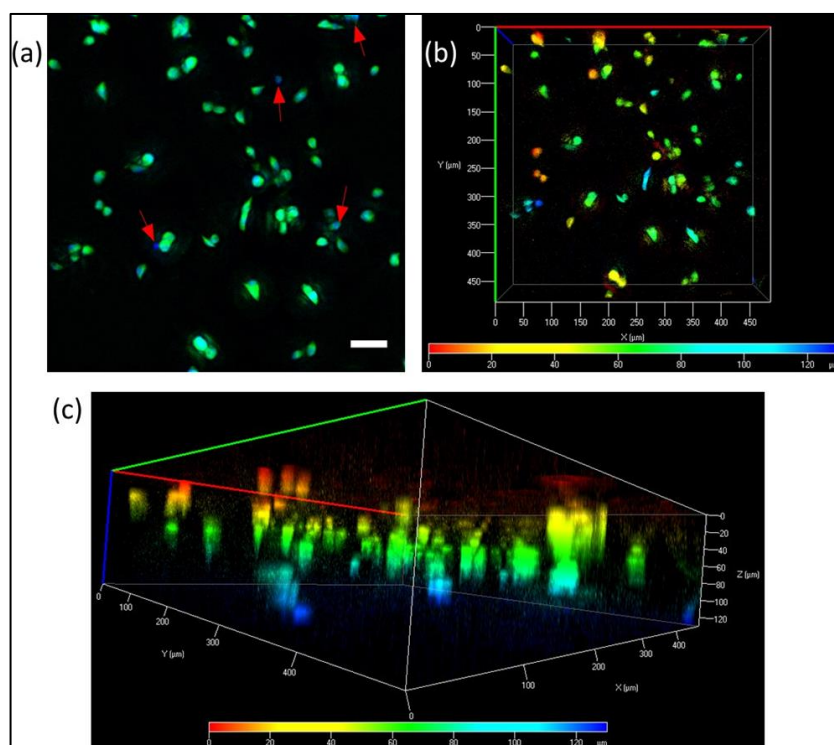


**Figure 3.13** (a) Maximum Intensity Projection of fluorescence images of Rhodamine123/Hoechst stained RAW 264.7 macrophages distributed throughout 100 $\mu\text{m}$  of 2% (w/v) gel depth. The dead cells have been marked with red arrows. In (b), the cells having Rhodamine 123/Hoechst fluorescence were color coded according to their depth inside the gel in the Maximum Intensity Projection, with red indicating the gel surface. (c) 3D Volume Rendering of Rhodamine 123/Hoechst

*stained cells (color bar indicates location of cell in the Z direction). Scale bar in (a) indicates 50 $\mu$ m*

The aforementioned study suggests that the tuning of the thermal stability of the hydrogel enhances the gel stability for a sufficiently long time that is needed for the cell culture. Moreover, the mechanical stiffness of the hydrogel can be modulated according to the traction stress generated by the cell type to choose the culture environment as 2D or 3D. Relatively less stiff gel ( $G' = 4$  kPa) is well suited for 3D culture, as it promotes selective penetration of cells into the gel phase material, while increasing the gel stiffness above the cellular traction stress provides a platform for 2D culture on the hydrogel surface. Here, gel stiffness was optimized for successful culture of NIH-3T3 cells in 2D and 3D environments.

### 3.3 Conclusion

We demonstrated the formation of a histidine-containing peptide-based hydrogel at pH 7.5. This study also convincingly demonstrates the tuning of mechanical stiffness and thermal stability of this peptide-based supramolecular hydrogel by incorporation of different dicarboxylic acids into the system, promoting hydrogen bonding and electrostatic interaction within the gel phase. We show for the first time that it is possible to improve the thermal and mechanical properties of a peptide hydrogel by introducing a dicarboxylic acid (succinic acid in 1:2 molar ratio) to promote acid base interaction in a two-component hydrogel system. Interestingly, the morphology of the native gel changes significantly in presence of succinic acid from bead-on-a-garland to a network of inter-connected helical nanofibers to form a two-component hydrogel. The increased gel stiffness, the enhanced gel melting temperature and a nanofibrous network have been successfully utilized for the 3D/2D culture of fibroblasts by using the two-component hydrogel as an extracellular matrix. This indicates that the tuning of mechanical strength, thermal stability and the morphology of the hydrogel promotes growth and nourishment of the cells in vitro pointing towards the future promise for peptide gel-based soft biomaterials in regenerative medicine.



### 3.4 Experimental Section

#### Synthesis of the peptide

The N-terminus and imidazole group of L-histidine were protected with Boc groups and the methyl ester protection strategy was taken to protect the C-terminus. Coupling was mediated by N,N-dicyclohexylcarbodiimide and 1-hydroxybenzotriazole monohydrate (DCC/HOBt.H<sub>2</sub>O). The Boc group from the N-terminal was removed by treating the protected peptide with 98-100% formic acid solution. The final compound was fully characterized by mass spectrometry, <sup>1</sup>H NMR spectroscopy and <sup>13</sup>C NMR spectroscopy

**Synthesis of Boc-Ile-OH[(CH<sub>3</sub>)<sub>3</sub>C-O-CONH-CH(C<sub>4</sub>H<sub>9</sub>)-COOH]:** 2.62 g (20 mmol) of L-Isoleucine (Ile) was taken in a 250 mL round bottomed flask and 20 mL 0.5(N) NaOH and equal volume of 1,4-dioxane were added to it to dissolve the amino acid completely. 4.60 g (21.1 mmol) di-tert-butyl dicarbonate (Boc anhydride) was added to the reaction mixture, cooled in an ice bath and stirred for 10 hours at room temperature. Then the solution volume was reduced to one third in a rotary evaporator. The resulting mixture was acidified with saturated KHSO<sub>4</sub> solution and the aqueous layer was extracted with ethyl acetate (3 x 40 mL). The ethyl acetate extract was dried over anhydrous sodium sulfate and evaporated in vacuum to obtain the sticky solid product.

Yield: 4.10 g (17.74 mmol, 88.70 %).

**Synthesis of Boc-Ile-AUDA-OMe [(CH<sub>3</sub>)<sub>3</sub>C-O-CONH-CH(C<sub>4</sub>H<sub>9</sub>)-CONH-(CH<sub>2</sub>)<sub>10</sub>-COOCH<sub>3</sub>]:** 4.10 g (17.74 mmol) of Boc-Ile-OH was dissolved in 12 mL dry N,N-dimethyl formamide (DMF) and cooled in an ice bath. H-AUDA-OMe (AUDA = 11-aminoundecanoic acid residue) was obtained by neutralization with saturated Na<sub>2</sub>CO<sub>3</sub> from its hydrochloride salt and subsequent extraction with ethyl acetate. The ethyl acetate solution was then concentrated to 10 mL and added to the DMF solution followed by 2.43 g (18.00 mmol) of 1-hydroxybenzotriazole monohydrate (HOBt.H<sub>2</sub>O) and 4.12 g (20 mmol) of N,N-dicyclohexylcarbodiimide (DCC). The reaction mixture was stirred for 24 hours in room temperature (27°C). The reaction mixture was diluted with ethyl acetate and filtered to separate N,N-dicyclohexyl urea (DCU). The ethyl acetate layer was washed with 1(N) HCl (3 x 30 mL), brine (2 x 30 mL), saturated sodium carbonate solution (2 x 30 mL) and brine (2 x

30 mL). The organic layer was dried over anhydrous sodium sulfate and the solvent was removed under reduced pressure. The crude reaction mixture was purified through silica gel column chromatography using petroleum ether/ethyl acetate (6:1) as eluent to obtain the pure white product.

Yield: 5.30 g (12.38 mmol, 69.78%).

$^1\text{H}$  NMR (500 MHz,  $\text{CDCl}_3$ , 25 °C):  $\delta$  6.05 (1H, br, NH), 5.08 (1H, br, NH), 3.83-3.87 (1H, m,  $\alpha$  CH of Ile), 3.64 (3H, s,  $-\text{OCH}_3$ ), 3.17-3.26 (2H, m,  $^{11}\text{CH}_2$ ), 2.28 (2H, t,  $J=7.5$  Hz,  $^2\text{CH}_2$ ), 1.83 (1H, s,  $\beta$  CH of Ile), 1.56-1.60 (2H, m,  $\gamma^1\text{CH}_2$  of Ile), 1.41-1.48 (13H, m, Boc- $\text{CH}_3$ ,  $^3\text{CH}_2$  and  $^{10}\text{CH}_2$ ), 1.25 (12H, m, chain  $\text{CH}_2$ ), 0.87-0.90 (6H, m,  $\gamma^2\text{CH}_3$  and  $\delta\text{CH}_3$  of Ile).  $^{13}\text{C}$  NMR (125 MHz,  $\text{CDCl}_3$ ):  $\delta$  174.41, 171.61, 155.97, 79.87, 59.58, 51.53, 39.55, 37.26, 34.21, 29.65, 29.53, 29.48, 29.44, 29.31, 29.22, 28.44, 26.97, 25.05, 24.90, 15.71, 11.49. HRMS (m/z): Calculated for  $\text{C}_{23}\text{H}_{44}\text{N}_2\text{O}_5$ : 428.33 Found: 429.80(M+H) $^+$ , 451.82(M+Na) $^+$ , 467.80(M+K) $^+$ . (Figure 3.14-3.16)

**Synthesis of H-Ile-AUDA-OMe[ $\text{H}_2\text{N}-\text{CH}(\text{C}_4\text{H}_9)-\text{CONH}-(\text{CH}_2)_{10}-\text{COOCH}_3$ ]:** To 5.30 g (12.38 mmol) of Boc-Ile-AUDA-OMe, 15 mL of formic acid was added to remove the Boc protection. The reaction was monitored using TLC. After 8 hours, formic acid was removed under vacuum using a liquid nitrogen trap. 10 mL of water is added, and the pH was balanced to 8-8.5 using  $\text{Na}_2\text{CO}_3$ . The product was extracted with ethyl acetate (3 x 40 mL). It was further purified using basic alumina column, chloroform and methanol (9:1) as eluent.

Yield: 3.65g (11.13 mmol, 89.90%)

$^1\text{H}$  NMR (400 MHz,  $\text{DMSO}-d_6$ , 25 °C):  $\delta$  7.76 (1H, t,  $J=5.2$  Hz, NH), 3.59 (3H, s,  $-\text{OCH}_3$ ), 3.09-3.01 (2H, m,  $^{11}\text{CH}_2$ ), 2.93 (1H, d,  $J=5.6$  Hz,  $\alpha$  CH of Ile), 2.29 (2H, t,  $J=7.6$  Hz,  $^2\text{CH}_2$ ), 1.50-1.59 (5H, m,  $\beta$  CH of Ile,  $\text{CH}_2$ ), 1.37-1.45 (2H, m,  $\gamma^1\text{CH}_2$  of Ile), 1.25 (12H, m,  $\text{CH}_2$ ), 0.79-0.83 (6H, m,  $\gamma^2\text{CH}_3$  and  $\delta\text{CH}_3$  of Ile).  $^{13}\text{C}$  NMR (100 MHz,  $\text{DMSO}-d_6$ ):  $\delta$  174.85, 173.80, 79.65, 59.85, 51.59, 38.96, 38.65, 33.75, 29.63, 29.38, 29.25, 29.16, 29.11, 28.91, 26.85, 24.89, 24.24, 16.29, 12.00. HRMS (m/z): Calculated for  $\text{C}_{18}\text{H}_{36}\text{N}_2\text{O}_3$ : 328.27 Found: 329.48 (M+H) $^+$ , 351.59 (M+Na) $^+$ . (Figure 3.17-3.19)

**Synthesis of di-BocHistidine[ (Boc) $_2$ -His-COOH]:** The synthetic procedure has been described in by Mirzahosseini et.al. previously. (Mirzahosseini, A.;

Hosztafi, S.; Tóth, G.; Noszál, B. A Cost-Effective Synthesis of Enantiopure Ovothiol A from L-Histidine, Its Natural Precursor. *Arkivoc* **2014**, 2014, 1-9.)

**Synthesis of (Boc)<sub>2</sub>-His-Ile-AUDA-OMe [(CH<sub>3</sub>)<sub>3</sub>C-O-CONH-CH(C<sub>9</sub>H<sub>13</sub>N<sub>2</sub>O<sub>2</sub>)-CONH-CH(C<sub>4</sub>H<sub>9</sub>)-CONH-(CH<sub>2</sub>)<sub>10</sub>-COOCH<sub>3</sub>]:**

4.62g(12.00mmol) of solid (Boc)<sub>2</sub>-His-COOH was dissolved in 15 mL of DMF and taken in an ice bath. To the stirring solution, 50 mL solution of 3.65g (11.13 mmol) of H-Ile-AUDA-OMe was added. It was followed by addition of 1.62g (12.00 mmol) of 1-hydroxybenzotriazolemonohydrate (HOBt.H<sub>2</sub>O) and 2.89 g (14mmol) of N, N-dicyclohexylcarbodiimide (DCC). The reaction mixture was stirred for 48 hours at room temperature (27°C). Subsequently, it was diluted with ethyl acetate and filtered to separate N, N- dicyclohexyl urea (DCU). The ethyl acetate layer was washed with brine (2 x 30 mL), saturated sodium carbonate solution (2 x 30 mL) and brine (2 x 30 mL). The organic layer was dried over anhydrous sodium sulphate and the solvent was removed under reduced pressure. The crude reaction mixture was purified through silica gel column chromatography using chloroform/methanol (9:1) as eluent to obtain a colourless solid.

Yield: 4.93 g (7.42 mmol, 66.67 %).

<sup>1</sup>H NMR (400 MHz, CDCl<sub>3</sub>, 25 °C): δ 8.13(1H, s, ε<sup>1</sup> CH of His), 7.67(1H, d, J=7.6 Hz, NH), 7.01 (1H, s, δ<sup>2</sup>CH of His), 6.20(1H, d, J=6.4 Hz, NH), 4.51-4.55(1H, m, α CH of His), 4.20-4.23 (1H, t, J=6.8 Hz α CH of Ile), 3.65 (3H, s, -OCH<sub>3</sub>), 3.11-3.25 (4H, m, β of His and <sup>11</sup>CH<sub>2</sub>), 2.28 (2H, t, J=14.8 Hz, <sup>2</sup>CH<sub>2</sub>), 1.92 (1H, m, β CH of Ile), 1.56-1.60 (2H, , m, γ<sup>1</sup>CH<sub>2</sub> of Ile), 1.37 (4H, m, CH<sub>2</sub>), 1.32 (18H, s, Boc-CH<sub>3</sub>) 1.20-1.25 (12H, m, chain CH<sub>2</sub>), 0.78-0.85 (6H, m, γ<sup>2</sup> CH<sub>3</sub> and δ CH<sub>3</sub> of Ile) <sup>13</sup>C NMR (100 MHz, CDCl<sub>3</sub>): δ 174.47, 171.37, 171.69, 142.59, 134.49, 130.96, 128.40, 125.90, 125.09, 118.59, 118.22, 111.13, 80.56, 59.10, 54.60, 51.53, 39.92, 36.79, 34.26, 29.55, 29.49, 29.45, 29.32, 29.25, 28.38, 28.08, 27.04, 25.09, 15.74, 11.38. HRMS (m/z): Calculated for C<sub>34</sub>H<sub>59</sub>N<sub>5</sub>O<sub>8</sub>: 665.44 Found: 666.75(M+H)<sup>+</sup>, 688.72 (M+Na)<sup>+</sup>. (Figure 3.20-3.22)

**Synthesis of H-His-Ile-AUDA-OMe [ $H_2N-CH(C_4H_5N_2)-CONH-CH(C_4H_9)-CONH-(CH_2)_{10}-COOCH_3$ ]:** To 4.93 g (7.42mmol) of Boc-Ile-AUDA-OMe, 10 mL of formic acid was added to remove the Bocgroup. The reaction was monitored using TLC. After 8 hours, formic acid was removed under vacuum using a liquid nitrogen trap. 10 mL water was added to the sticky residue remaining. 30% ammonia solution was then added dropwise to adjust the pH of the solution to 8. The solution was freeze dried and purified using basic alumina in chloroform, methanol (9:1) as eluent.  $^1H$  NMR (400 MHz, DMSO- $d_6$ , 25 °C):  $\delta$  11.77 (1H, br,  $\epsilon^2NH$  of His), 8.07(1H, s,  $\epsilon^1$  CH of His), 7.97(1H, d, J=8.8 Hz, NH), 7.53 (1H, s,  $\delta^2CH$  of His), 6.82 (1H, br, NH), 4.12 (1H, t, J=7.6 Hz,  $\alpha$  CH of His), 3.58 (3H, s,  $-OCH_3$ ), 3.39-3.42(1H, m,  $\alpha$  CH of Ile), 3.05-3.15 (1H, m,  $\beta$  of His), 2.95-3.01(1H, m,  $\beta$   $CH_2$  of His), 2.84-2.88 (2H, m,  $^{11}CH_2$ ), 2.27-2.30 (2H, t, J=7.6 Hz,  $^2CH_2$ ), 1.65-1.67 (1H, m,  $\beta$  CH of Ile), 1.49-1.51 (2H, , m,  $\gamma^1CH_2$  of Ile), 1.36-1.38 (4H, m,  $CH_2$ ), 1.23-1.25 (12H, m, chain  $CH_2$ ), 0.81-0.82 (6H, m,  $\gamma^2$   $CH_3$  and  $\delta$   $CH_3$  of Ile)  $^{13}C$  NMR (100 MHz, DMSO- $d_6$ ):  $\delta$  173.17, 172.77, 170.00, 134.13, 55.74, 54.43, 50.56, 37.77, 36.71, 32.70, 28.38, 28.33, 28.20, 28.07, 27.86, 25.76, 23.85, 23.61, 14.74, 10.60. HRMS (m/z): Calculated for  $C_{24}H_{43}N_5O_4$ : 465.33 Found: 466.41(M+H) $^+$ , 488.33 (M+Na) $^+$ . (Figure 3.23-3.25)

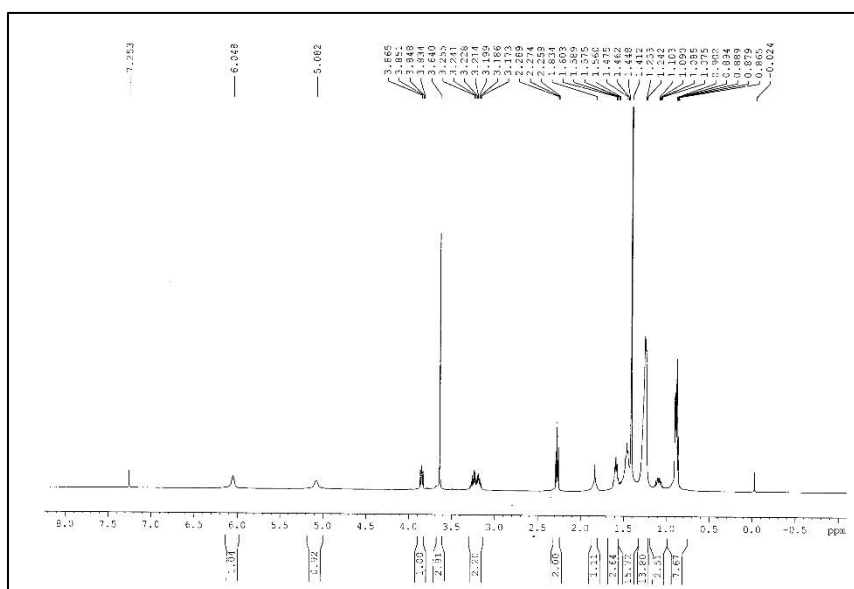


Figure 3.14 500 MHz  $^1H$  NMR spectrum of Boc-Ile-AUDA-OMe

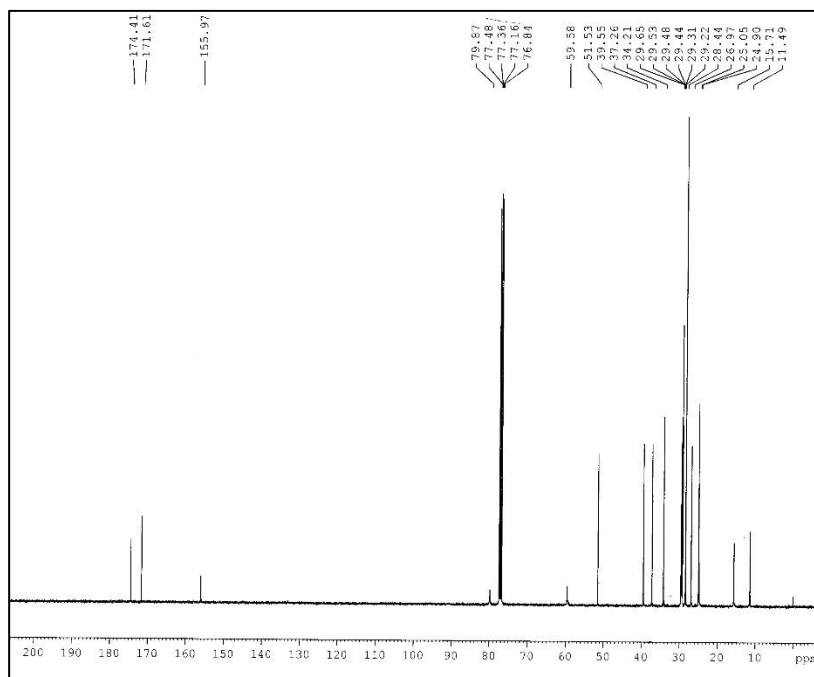


Figure 3.15 125 MHz  $^{13}\text{C}$  NMR spectrum of Boc-Ile-AUDA-OMe

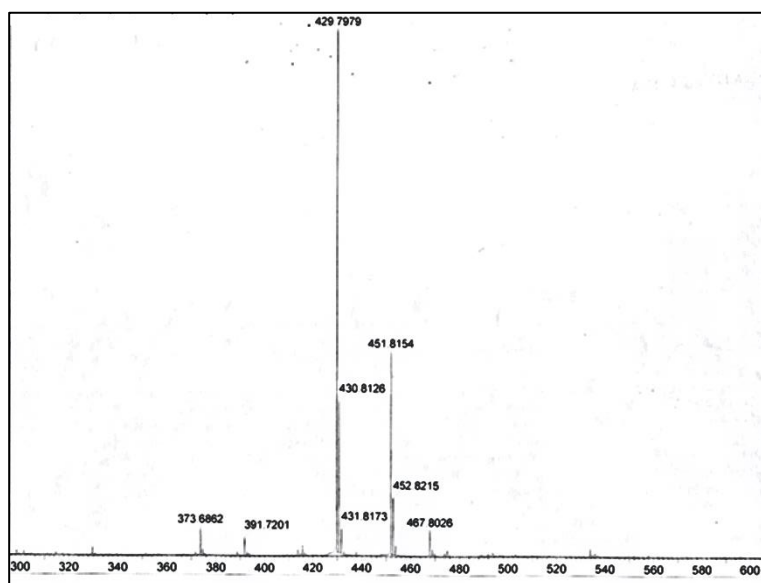


Figure 3.16 HRMS spectrum of Boc-Ile-AUDA-OMe



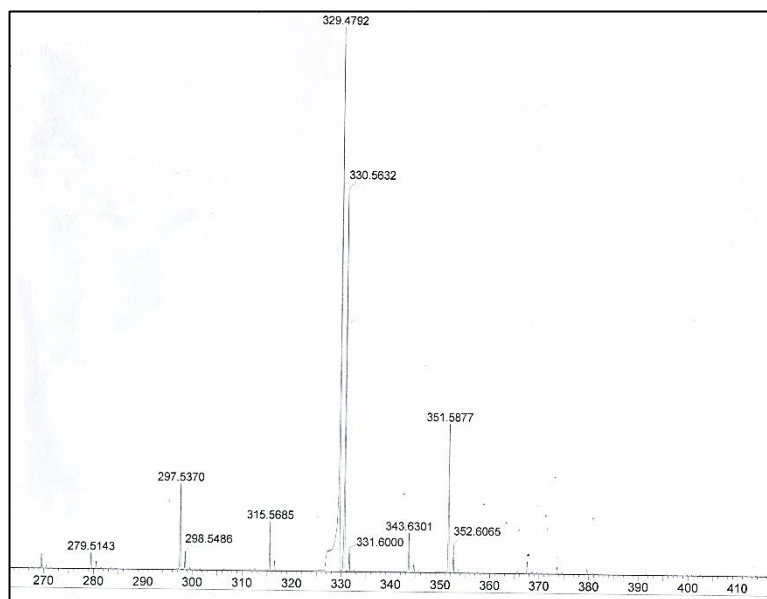


Figure 3.19 HRMS spectrum of H-Ile-AUDA-OMe in DMSO- $d_6$

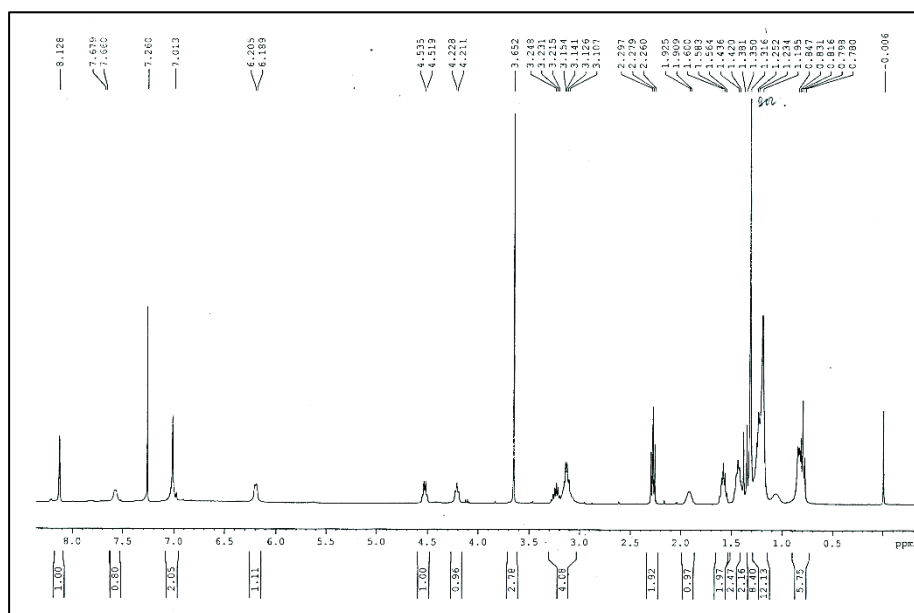


Figure 3.20 400 MHz  $^1\text{H}$  NMR spectrum of  $(\text{Boc})_2\text{-His-Ile-AUDA-OMe}$  in  $\text{CDCl}_3$

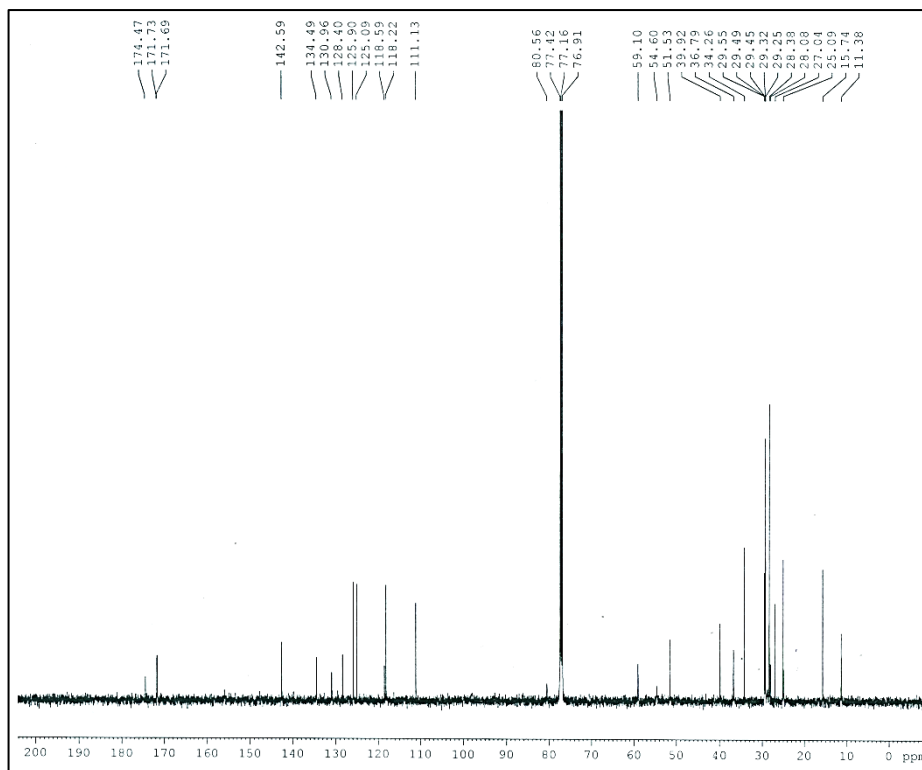


Figure 3.21 100 MHz  $^{13}\text{C}$  NMR spectrum of  $(\text{Boc})_2\text{-His-Ile-AUDA-OMe}$  in  $\text{CDCl}_3$

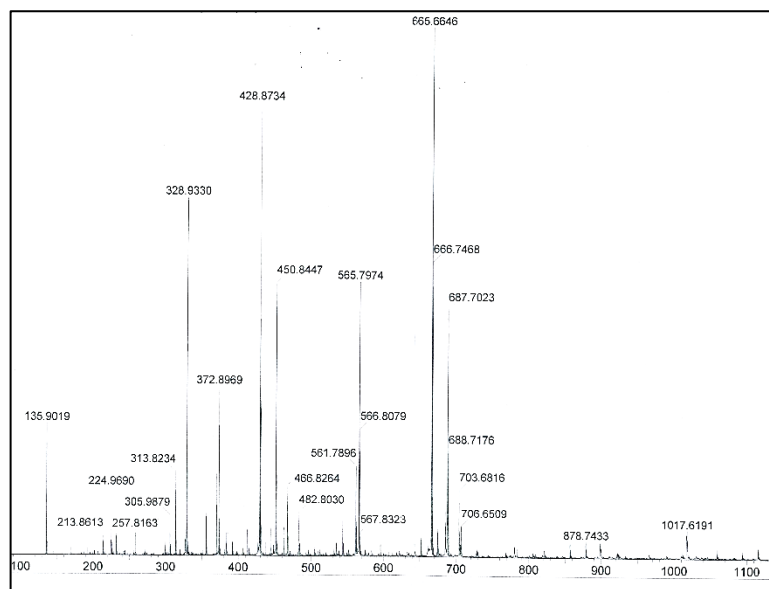


Figure 3.22 HRMS spectrum of  $(\text{Boc})_2\text{-His-Ile-AUDA-OMe}$





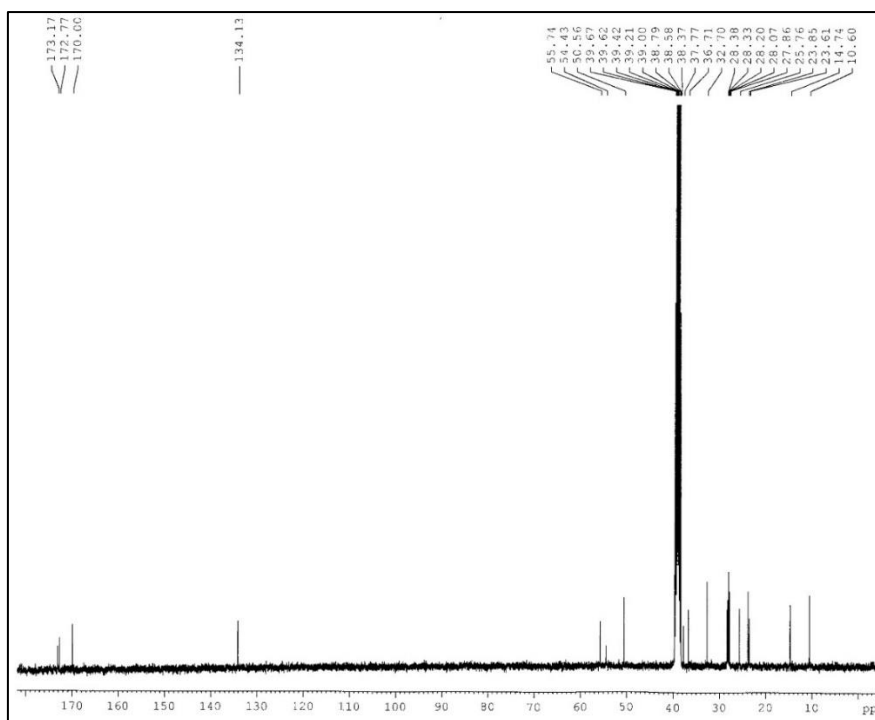


Figure 3.24 100 MHz  $^{13}\text{C}$  NMR spectrum of H-His-Ile-AUDA-OMe in  $\text{DMSO-}d_6$

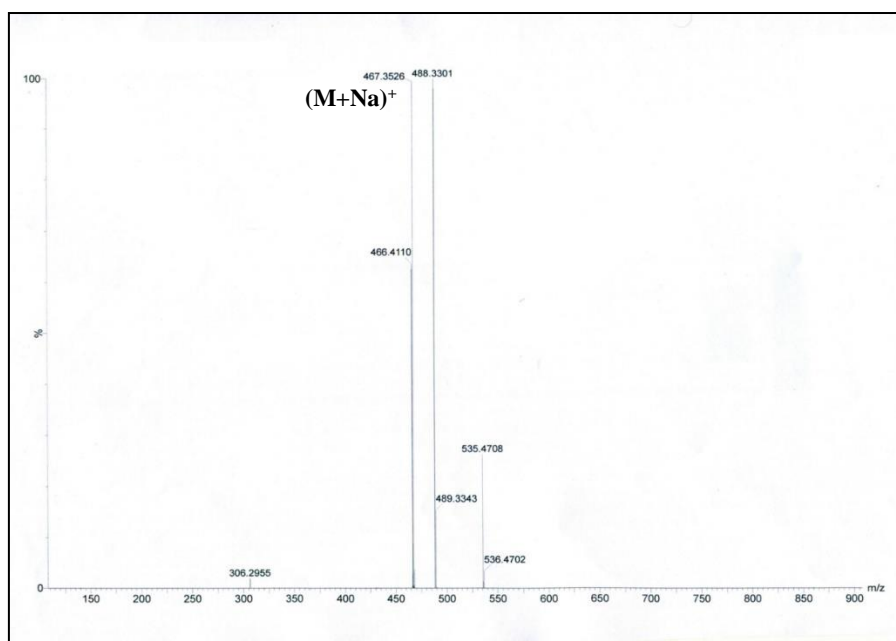


Figure 3.25 HR-MS spectrum of H-His-Ile-AUDA-OMe

### 3.5 References

1. X.-Q. Dou and C.-L. Feng, *Adv. Mater.*, 2017, **29**, 1604062.
2. J. Raeburn and D. J. Adams, *Chem. Commun.*, 2015, **51**, 5170–5180.
3. A. R. Hirst, B. Escuder, J. F. Miravet and D. K. Smith, *Angew. Chemie - Int. Ed.*, 2008, **47**, 8002–8018.
4. S. Datta, N. Dey and S. Bhattacharya, *Chem. Commun.*, 2017, **53**, 2371–2374.
5. S. S. Panda, H. E. Katz and J. D. Tovar, *Chem. Soc. Rev.*, 2018, **47**, 3640–3658.
6. M. Kumar, N. L. Ing, V. Narang, N. K. Wijerathne, A. I. Hochbaum and R. V. Ulijn, *Nat. Chem.*, 2018, **10**, 696–703.
7. A. Lampel, R. V. Ulijn and T. Tuttle, *Chem. Soc. Rev.*, 2018, **47**, 3737–3758.
8. K. S. Hellmund and B. Koksich, *Front. Chem.*, 2019, **7**, 172.
9. Y. Li, F. Wang and H. Cui, *Bioeng. Transl. Med.*, 2016, **1**, 306–322.
10. K. Sato, M. P. Hendricks, L. C. Palmer and S. I. Stupp, *Chem. Soc. Rev.*, 2018, **47**, 7539–7551.
11. J. K. Sahoo, A. S. Braegelman and M. J. Webber, *J Indian Inst Sci*, 2018, **98**, 69–79.
12. G.-B. Qi, Y.-J. Gao, L. Wang and H. Wang, *Adv. Mater.*, 2018, **30**, e1703444.
13. D. Stern and H. Cui, *Adv. Healthcare Mater.*, 2019, **8**, 1900104.
14. N. C. Carrejo, A. N. Moore, T. L. Lopez Silva, D. G. Leach, I.-C. Li, D. R. Walker and J. D. Hartgerink, *ACS Biomater. Sci. Eng.*, 2018, **4**, 1386–1396.
15. Q. Wei, J. Duan, G. Ma, W. Zhang, Q. Wang and Z. Hu, *J. Mater. Chem. B Mater. Biol. Med.*, 2019, **7**, 2220–2225.
16. F. Koch, A. Wolff, S. Mathes, U. Pieleles, S. S. Saxer, B. Kreikemeyer and K. Peters, *Int. J. Nanomedicine*, 2018, **13**, 6717–6733.
17. J. Kisiday, M. Jin, B. Kurz, H. Hung, C. Semino, S. Zhang and A. J. Grodzinsky, *Proc. Natl. Acad. Sci*, 2002, **99**, 9996–10001.
18. H. Wang and Z. Yang, *Nanoscale*, 2012, **4**, 5259–5267.
19. M. W. Tibbitt and K. S. Anseth, *Biotechnol. Bioeng.*, 2009, **103**, 655–663.
20. N. Nandi, K. Gayen, S. Ghosh, D. Bhunia, S. Kirkham, S. K. Sen, S. Ghosh, I. W. Hamley and A. Banerjee, *Biomacromolecules*, 2017, **18**, 3621–3629.

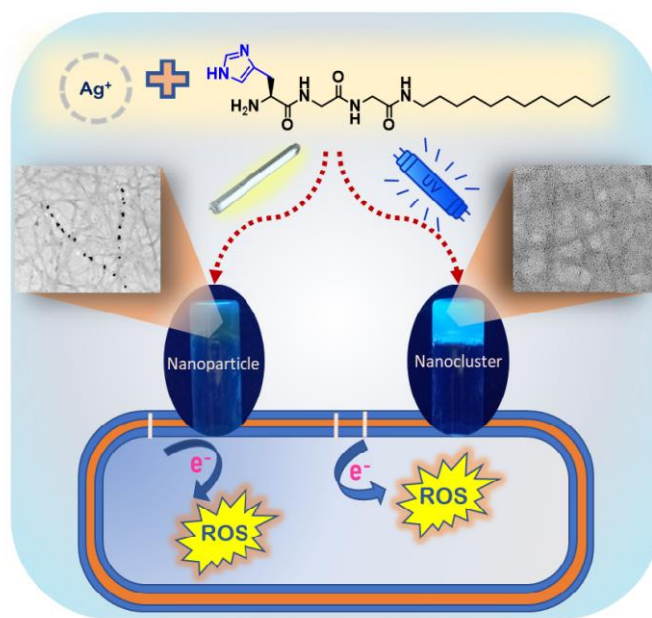
21. A. Baral, S. Roy, S. Ghosh, D. Hermida-Merino, I. W. Hamley and A. Banerjee, *Langmuir*, 2016, **32**, 1836–1845.
22. D. A. Salick, D. J. Pochan and J. P. Schneider, *Adv. Mater.*, 2009, **21**, 4120–4123.
23. A. S. Veiga, C. Sinthuvanich, D. Gaspar, H. G. Franquelim, M. A. R. B. Castanho and J. P. Schneider, *Biomaterials*, 2012, **33**, 8907–8916.
24. B. Hu, C. Owh, P. L. Chee, W. R. Leow, X. Liu, Y.-L. Wu, P. Guo, X. J. Loh and X. Chen, *Chem. Soc. Rev.*, 2018, **47**, 6917–6929.
25. V. Castelletto, C. J. C. Edwards-Gayle, I. W. Hamley, G. Barrett, J. Seitsonen and J. Ruokolainen, *ACS Appl. Mater. Interfaces*, 2019, **11**, 9893–9903.
26. R. Dimatteo, N. J. Darling and T. Segura, *Adv. Drug Deliv. Rev.*, 2018, **127**, 167–184.
27. J. E. P. Sun, B. Stewart, A. Litan, S. J. Lee, J. P. Schneider, S. A. Langhans and D. J. Pochan, *Biomater. Sci.*, 2016, **4**, 839–848.
28. D. M. Raymond, B. L. Abraham, T. Fujita, M. J. Watrous, E. S. Toriki, T. Takano and B. L. Nilsson, *ACS Appl. Bio Mater.*, 2019, **2**, 2116–2124.
29. N. Falcone and H. B. Kraatz, *Chem. - A Eur. J*, 2018, **24**, 14316–14328.
30. K. A. Black, B. F. Lin, E. A. Wonder, S. S. Desai, E. J. Chung, B. D. Ulery, R. S. Katari and M. V. Tirrell, *Tissue Eng. Part A*, 2015, **21**, 1333–1342.
31. I. Arioiz, O. Erol, G. Bakan, F. B. Dikecoglu, A. E. Topal, M. Urel, A. Dana, A. B. Tekinay and M. O. Guler, *ACS Appl. Mater. Interfaces*, 2018, **10**, 308–317.
32. S. Koutsopoulos, *J. Biomed. Mater. Res. A*, 2016, **104**, 1002–1016.
33. J. B. Matson and S. I. Stupp, *Chem. Commun.*, 2012, **48**, 26–33.
34. F. Yergoz, N. Hastar, C. E. Cimenci, A. D. Ozkan, T. Tekinay, M. O. Guler and A. B. Tekinay, *Biomaterials*, 2017, **134**, 117–127.
35. V. Jayawarna, M. Ali, T. A. Jowitt, A. F. Miller, A. Saiani, J. E. Gough and R. V. Ulijn, *Adv. Mater.*, 2006, **18**, 611–614.
36. N. Zanna, S. Focaroli, A. Merlettoni, L. Gentilucci, G. Teti, M. Falconi and C. Tomasini, *ACS Omega*, 2017, **2**, 2374–2381.
37. P. Worthington, K. M. Drake, Z. Li, A. D. Napper, D. J. Pochan and S. A. Langhans, *Anal. Biochem*, 2017, **535**, 25–34.
38. P. Chakraborty, T. Guterman, N. Adadi, M. Yadid, T. Brosh, L. Adler-Abramovich, T. Dvir and E. Gazit, *ACS Nano*, 2019, **13**, 163–175.

39. I. Levental, P. C. Georges and P. A. Janmey, *Soft Matter*, 2007, **3**, 299–306.
40. A. J. Engler, S. Sen, H. L. Sweeney and D. E. Discher, *Cell*, 2006, **126**, 677–689.
41. S. Boothroyd, A. Saiani and A. F. Miller, *Biopolymers*, 2014, **101**, 669–680.
42. A. Scelsi, B. Bochicchio, A. Smith, V. L. Workman, L. A. Castillo Diaz, A. Saiani and A. Pepe, *J. Biomed. Mater. Res. A*, 2019, **107**, 535–544.
43. T. Mosmann, *J. Immunol. Methods*, 1983, **65**, 55–63.
44. A. Srivastava, S. Ghorai, A. Bhattacharjya and S. Bhattacharya, *J. Org. Chem.*, 2005, **70**, 6574–6582.
45. X. Cai, Y. Wu, L. Wang, N. Yan, J. Liu, X. Fang and Y. Fang, *Soft matter*, **9**, 5807–5814.
46. F. Ye, S. Chen, G. Tang and X. Wang, *Colloids Surf. A Physicochem. Eng. Asp.*, 2014, **452**, 165–172.
47. Y. Zhou, M. Xu, T. Yi, S. Xiao, Z. Zhou, F. Li and C. Huang, *Langmuir*, 2007, **23**, 202–208.
48. J. Nanda, A. Biswas and A. Banerjee, *Soft Matter*, 2013, **9**, 4198.
49. D. Haldar and M. G. B. Drew, *Tetrahedron*, 2006, 2006, **62**, 6370–6378.
50. Y. Liu, T. Wang and M. Liu, *Chem. - A Eur. J.*, 2012, **18**, 14650–14659.
51. V. Castelletto, G. Cheng, C. Stain, C. J. Connon and I. W. Hamley, *Langmuir*, 2012, 2012, **28**, 11599–11608.
52. A. Baral, S. Roy, A. Dehsorkhi, I. W. Hamley, S. Mohapatra, S. Ghosh and A. Banerjee, *Langmuir*, 2014, **30**, 929–936.
53. L. F. Pacios, O. Gálvez and P. C. Gómez, *J. Chem. Phys.*, 2005, **122**, 214307.
54. M. A. Trachsel, P. Ottiger, H. M. Frey, C. Pfaffen, A. Bihlmeier, W. Klopper and S. Leutwyler, *J. Phys. Chem. B*, 2015, **119**, 7778–7790.
55. W.-H. Guo, M. T. Frey, N. A. Burnham and Y.-L. Wang, *Biophys. J.*, 2006, **90**, 2213–2220.
56. J. Li, D. Han and Y.-P. Zhao, *Sci. Rep.*, 2014, **4**, 3910.
57. G. Vertelov, E. Gutierrez, S.-A. Lee, E. Ronan, A. Groisman and E. Tkachenko, *Sci. Rep.*, 2016, **6**, 1–6.
58. J. Solon, I. Levental, K. Sengupta, P. C. Georges and P. A. Janmey, *Biophys. J.*, 2007, **93**, 4453–4461.
59. S.-Y. Tee, J. Fu, C. S. Chen and P. A. Janmey, *Biophys. J.*, 2011, **100**, L25-7.

60. M. T. Scherzer, S. Waigel, H. Donninger, V. Arumugam, W. Zacharias, G. Clark, L. J. Siskind, P. Soucy and L. Beverly, *PLoS One*, 2015, **10**, e0138065.
61. K. A. Jansen, R. G. Bacabac, I. K. Piechocka and G. H. Koenderink, *Biophys. J.*, 2013, **105**, 2240–2251.

## CHAPTER 4

# In-situ Formation of a Nano-Hybrid of Silver Nano-Dots and Peptide Nanofibers in a Silver-Based Metallogel: Elucidating Their Potential for Antimicrobial Activities



Manuscript under revision in *ACS Appl. Nano Mater.*





## 4.1 Introduction

Research on peptide-based soft materials has burgeoned in the last two decades due to diverse applicability of these materials.<sup>1-2</sup> Materials formed due to self-aggregation of peptides and peptide-amphiphiles possess high tunability, functional diversity and bio-compatibility. It is often more practical to use a low molecular weight gelator (LMWG) peptide to realize the potentials of self-aggregation as LMWGs are easier to synthesize than peptide oligomers. Moreover, these peptide-based LMWGs not only form interesting nano-structures but also form gel under suitable physico-chemical conditions. Hydrogels are known for their diverse applications in the fields of nano-hybrid materials,<sup>3-5</sup> templated synthesis of nanoparticles,<sup>6-7</sup> environmental remediation,<sup>8-9</sup> catalysis,<sup>10</sup> delivery of biologics,<sup>11-13</sup> regenerative medicine,<sup>14</sup> cell culture<sup>15</sup> and novel antibiotics.<sup>16-18</sup> These gelators utilize several non-covalent interactions to self-assemble into bigger supramolecular structures. An elegant pathway to create non-covalent cross-linking between the peptide gelators to induce gel formation is to use metal ions.<sup>19-20</sup> Histidine, aspartic acid, glutamic acid, cysteine and methionine are known to act as ligand utilizing their functional side chains. In natural peptides, more specifically in proteins, the metal-amino acid interactions are widely utilized to change protein conformation to bind specific substrates or to form supramolecular structure.<sup>21</sup> Peptides are designed to exploit these natural ligands to promote self-assembly on binding with the metal ions and form extended supramolecular networks subsequently. These networks come together to form nanofibers of the hydrogel system. Although there are many examples of metal ion incorporation in a self-assembled gel system,<sup>20</sup> there are only a handful of examples, where hydrogel formation takes place with the aid from metal ion coordination. Ulijn and coworkers demonstrated coordination of  $\text{Cu}^{2+}$  to form metallogel with two tripeptides F-F-D and G-H-K.<sup>22</sup> Banerjee and co-workers, in 2018, showed a L-histidine-based peptide amphiphile only forms gel upon coordination with  $\text{Hg}^+$  and  $\text{Fe}^{3+}$  ions in different molar ratios.<sup>23</sup> Another L-Histidine based peptide amphiphile which formed precipitate in aqueous media, was shown to form metallogel only in presence of  $\text{Fe}^{3+}$  designed by Chen *et al.*<sup>24</sup> Using Fmoc protected amino acids, Song *et al.* have recently prepared silver-based metallogels which forms in-situ nanoparticles that can kill Gram positive bacteria.<sup>25</sup>

Bacterial infection is one of the major concerns in the public health sector. Discovery of novel antibiotics is accompanied by mutation in bacteria strains for multidrug-resistance. Thus, significant research efforts behind finding new class of anti-microbial agents have yielded cationic polymers, nanoparticle and peptide-based antibacterial hydrogels.<sup>26</sup> Although polymers show good bactericidal properties, their non-degradable long chains cannot be cleared from living system through excretion. As broad-spectrum antibacterial agent metal nanoparticles, especially silver nanoparticles (Ag NPs) as well as silver nanoclusters (Ag NCs) show excellent results.<sup>27-28</sup> Silver salts has been used for wound and burn dressing for ages. But unfortunately, their cytotoxicity has limited the application for internal usages.<sup>29</sup> Extended exposure to silver nanomaterials can lead to the deposition of silver as an insoluble compound under skin leading to diseases like argyria.<sup>30-31</sup> As silver-based nanoparticles (Ag NPs) and nanoclusters (Ag NCs) tend to aggregate to form bulk silver, the strategies of growing them in a closed network system started evolving.<sup>32-35</sup> Silver nanoparticles protected by small molecules may show high antimicrobial effects but possess threat of accumulation and toxicity as excretion of these materials from our body is difficult. On the other hand, despite excellent biocompatible nature of peptide-based antibacterial gels, they do not generally exhibit broad-spectrum bacteria killing and possesses high MIC values.<sup>36-37</sup> Nanoparticles with efficient broad-range antibacterial activity can be combined with peptide-based hydrogel which shows minimum cytotoxicity. Among peptide hydrogel and silver nanoparticle composite system, Fmoc protected amino acids and peptides are previously explored.<sup>25, 38</sup> Few more examples of peptide amphiphile or unnatural amino acid containing peptide sequences helping ordered array of silver nanoparticle formation in the peptide nano-architectures, exist in literature.<sup>39-41</sup>

In the present work a histidine-containing peptide amphiphile is utilized to form metallohydrogel, when aqueous solution of  $\text{AgNO}_3$  is added to hot aqueous solution of the amphiphile in 2:1 metal salt to amphiphile molar ratio. This transparent hydrogel consists of nano-fibrous networks. We successfully photo-reduce this metallohydrogel under two different conditions to develop two different hybrid hydrogels, viz., silver nanocluster containing hydrogel and silver nanoparticle containing hydrogels. To the best of our knowledge, controlled formation of nanoclusters and nanoparticles from the same source material is an

unprecedented phenomenon. The presence of each nanomaterial is confirmed by optical spectroscopy, X-ray photoelectron spectroscopy as well as MALDI-TOF mass analysis. Morphological analysis of individual hybrid hydrogels elucidates that the nanoclusters grow along the peptide nanofibers and they have an average diameter of 2.3 nm. It is observed in the nanoparticle containing gel that, although there are some growths of nanoparticles outside the fibers, most of them form along the network consisting of the gelator. The rheological measurements clarify the increase in hydrogel strength with the growth of silver nanomaterials as their crosslinking ability strengthens the hydrogel matrix further. Knowing the antimicrobial potential of silver nanomaterials and biocompatibility of peptide amphiphile hydrogels, we ventured to develop new antimicrobial materials using this hybrid system. It is observed that both the hybrid hydrogels effectively kill Gram negative as well as Gram positive bacteria. Lower MIC value and more biocompatibility of nanocluster containing hydrogel makes it a better candidate for potential antibacterial agent that can be used in mammalian systems. The elevated levels of reactive oxygen species (ROS) found in the bacteria in presence of the hybrid hydrogels establish that generation of ROS is the primary reason of bacterial cell death.

## 4.2 Result and Discussion

The L-histidine containing tripeptide-based amphiphile  $\text{H}_2\text{N-His-Gly-Gly-(CH}_2\text{)}_{11}\text{-CH}_3$  **P1** (Figure 4.1a) is synthesized in solution phase and subsequently purified and characterized (Supporting Information).

### Gelation Study

The histidine-based amphiphile **P1** has been subjected to gelation studies in aqueous medium (pH 7.0, 27 °C). We have taken 5 mg of **P1** white powder in a glass vial containing 1 mL of Mili-Q water and carefully heat using a hot-gun. On heating the powder dissolves, but as it cools down it appears as a white precipitate (Figure 4.1b) at the bottom of the vial. This indicates that **P1** cannot form hydrogel alone. As the imidazole moiety of the histidine residue is known to chelate metal cations in metalloproteins, various transition metal cations, *viz.*,  $\text{Mn}^{2+}$ ,  $\text{Fe}^{2+}$ ,  $\text{Fe}^{3+}$ ,  $\text{Co}^{2+}$ ,  $\text{Ni}^{2+}$ ,  $\text{Cu}^{2+}$ ,  $\text{Zn}^{2+}$ ,  $\text{Cd}^{2+}$ ,  $\text{Hg}^{2+}$  and  $\text{Ag}^+$  are added to the hot solution of **P1** to

check possibilities of gel formation through extended coordination of the cations through **P1**. It is interesting to note that addition of only  $\text{Ag}^+$  shows successful gelation with gradual cooling of the warm solution (Figure 4.1b). At 2:1 molar ratio of **P1** to  $\text{AgNO}_3$  the hydrogel forms but at higher salt quantity soluble aggregate is observed, whereas decreasing the salt ratio brings back the precipitation. When the vial containing the metallogel is kept under UV torch emitting 365 nm light, for 30 minutes, a bright blue fluorescence can be observed (Figure 4.2a). This fluorescent hydrogel is further characterized as a hydrogel containing silver nanoclusters. On the other hand, when the as prepared metallogel is turned into solution through shear-thinning and kept in ambient light, the gel forms back with orange coloration (Figure 4.1b) after 12-14 hours. Further investigations confirms that this is a hybrid of hydrogel and silver nanoparticles.

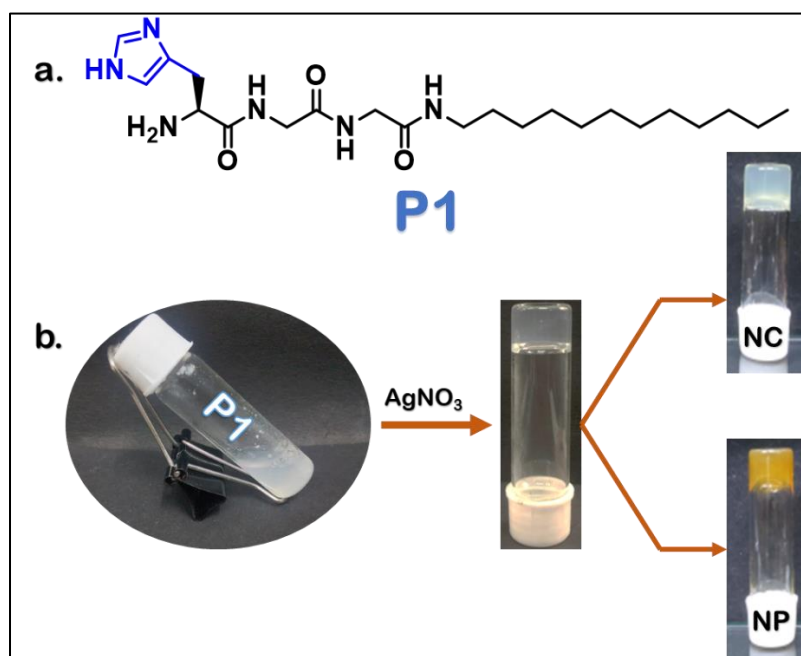


**Figure 4.1.** (a) Chemical structure of the peptide amphiphile **P1**. (b) Schematic representation of metallogel formation upon addition of  $\text{AgNO}_3$  and subsequent synthesis of Ag NC containing gel and Ag NP containing gel from the same source of the hydrogel.

## Optical Studies

The hybrid hydrogels containing silver nanoclusters and silver nanoparticles are examined for their UV-Vis absorption properties. The hydrogels are diluted with Mili-Q water and pipetted into the cuvette. The nanocluster containing hydrogel does not show any strong absorbance signature but the hydrogel containing nanoparticle shows absorbance maxima at 420 nm (Figure 4.2b) which is the characteristic of silver NPs due to surface plasmon resonance.<sup>42</sup> Moreover, an intense absorption peak with narrow distribution indicates monodispersity of the nanoparticles formed. Absence of shoulder peaks at longer wavelengths nullifies the possibility of bigger Ag nanoparticles, Ag nanorod or Ag anisotropy ellipsoid formation.<sup>43</sup>

Under 365 nm UV torch the NC containing gel shows strong fluorescence which was missing in case of NP containing gel. Encouraged by this primary observation emission studies of these samples are done. When excited with 370 nm source, NC containing gel shows emission maxima at 445 nm (Figure 4.2a). As the size of NCs are so tiny that it approaches Fermi wavelength of metals, the continuous energy levels become discrete in nature. Thus, NCs behave more like molecules and due to presence of discrete molecular levels luminescence property emerges in case of NCs.<sup>44</sup>

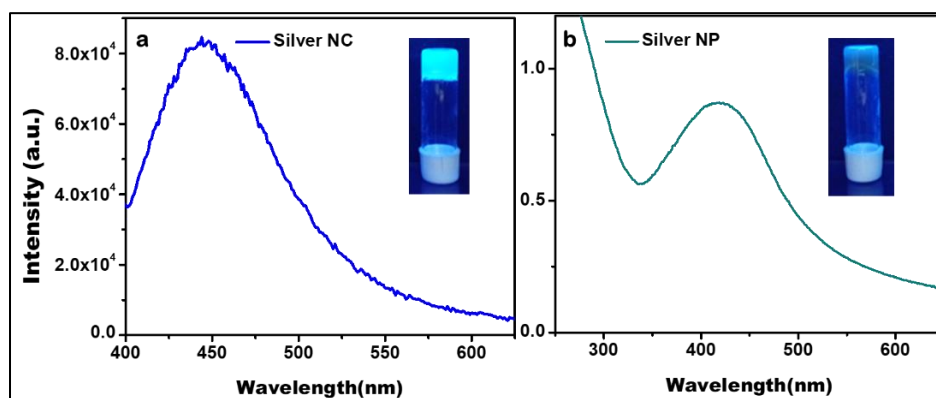


**Figure 4.2.** (a) Photoluminescence spectra of silver nanocluster formed in the hydrogel matrix shows a maximum at 445 nm when excited at 370 nm. In the inset inverted vial image of nanocluster containing hydrogel under 365 nm UV lamp. (b) UV-visible absorbance spectrum of the silver nanoparticle-containing hydrogel shows absorbance maximum at 420 nm due to surface plasmon resonance of the nanoparticles. In the inset inverted vial image of nanoparticle containing hydrogel under 365 nm UV lamp.

### Morphology

Transmission electron microscopic (TEM) study was performed to examine the morphologies of the gelators in aggregated gel state and hydrogels containing silver nanomaterials formed in-situ. The morphological analysis of silver-based metallohydrogel in its dried form shows twisted nanofibrous assembly (Figure 4.3a) where the fibers have an average width of 50-60 nm. The gelator peptide amphiphile coordinates with  $\text{Ag}^+$  to form extended network which further self-assemble through van der Waal's forces and hydrogen bonding to form nanofibrous assembly and this can hold the solvent water molecules entrapped inside the network. The fluorescent hydrogel prepared through 30 minutes' exposure of the native metallohydrogel under UV light, is found to be consisting of nanofibrous network with nanocluster grown along them (Figure 4.3b). The nanoclusters (Figure 4.3c) are found to possess an average diameter of 2.3 nm (Figure 4.4a). It is fascinating to see that all the nanoclusters are grown on the nanofibers and this indicates that the metal ions are embedded inside the nanofibers and some of them are mineralized to form  $\text{Ag}^0$  nanoclusters when irradiated to right reduction condition.

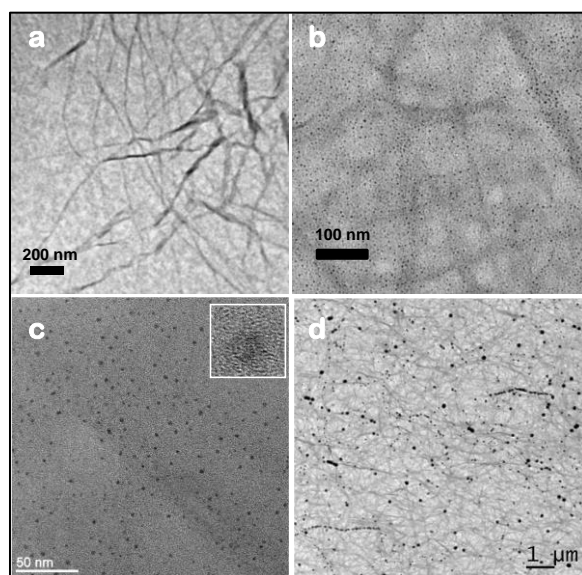


**Figure 4.3.** Transmission electron microscopic images of (a)  $\text{PI-AgNO}_3$  metallohydrogel showing twisted nanofibrous morphology, (b) formation of silver nanoclusters can be seen growing predominantly on hydrogel nanofibers, (c) magnified image of the nanoclusters (in inset a single nanocluster is presented), (d) formation of nanoparticles in the hydrogel takes place both along the nanofibers and outside of it.

The morphological analysis of the non-fluorescent orange-coloured hybrid hydrogel demonstrates formation of bigger nanoparticles (Figure 4.3d) which results from aggregation of smaller nanoclusters. There are two types of nanoparticles are found in the TEM analysis. The majority of them have an average particle diameter of 52.4 nm (Figure 4.4c) and arranged in array of nanofibers. A few of bigger sized nanoparticles are also found outside the nanofibrous network (Figure 4.3d). They have an average diameter of 117.3 nm (Figure 4.4c). They are formed by two adjoining smaller nanoparticles. The formation of nanoclusters is aided by densely packed fibrous network of the metallohydrogel which resists the agglomeration of reduced silver into bigger nanoparticles. In the case of nanoparticle formation, the solution phase of the hybrid system as well as the longer reduction time helps to grow bigger nanoparticles. It should be noted that during solution phase the system does not lose its nanofibrous morphology. That is why nanoparticles too are found mostly in an ordered arrangement along the hydrogel network.

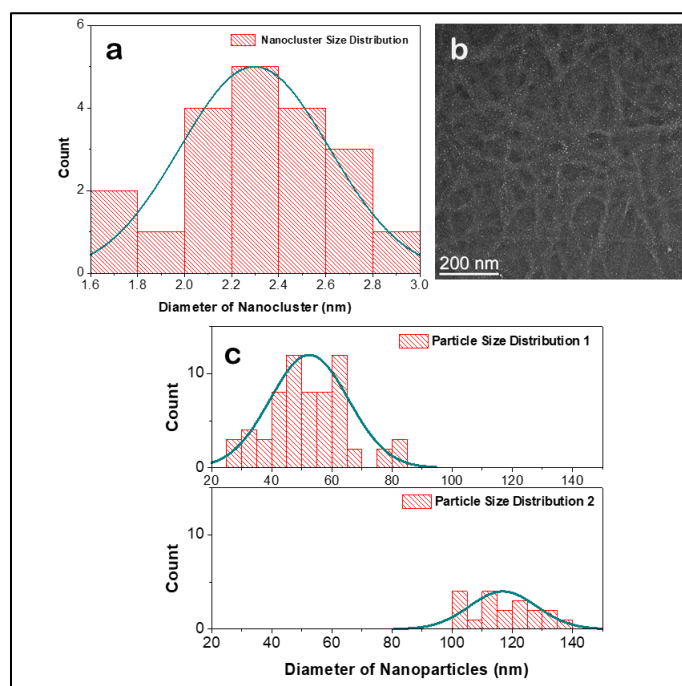


**Figure 4.4** (a) Particle size distribution of the nanoclusters formed inside the metallohydrogel. The gaussian distribution provides an average particle diameter of 2.3 nm. (b) Reserve phase transmission electron microscopic image of Figure 3b, clearly showing growth of nanoclusters along the fibrous network. (c) Particle size distribution of silver nanoparticles grown inside the metallohydrogel matrix. The distribution is bimodal hence it is divided in two different gaussian distribution and overlaid together.



### Characterization of Nanocluster

The nanoclusters formed inside the gel matrix is further characterized using MALDI-TOF and X-ray photoelectron spectroscopy (XPS) analysis. MALDI-TOF mass analysis of the nanocluster species tells us about the composition of the core of the nanocluster, i.e., we can tell how many silver atoms are present in the nanocluster and how many ligands are protecting it from the surrounding. The MALDI-TOF experiment was performed multiple times with different matrices such as alpha-cyano-4-hydroxycinnamic acid and 2,5-Dihydroxybenzoic acid, but only sinapinic acid formed stable adduct with the Ag NC containing hydrogel and the mass was found in LP (Linear Positive) mode. MALDI-TOF MS analysis profile of the nanocluster is provided in Figure 4.5a. Here the peak at  $m/z$  value of 1202 for Cu NC corresponds to  $(Ag_3P_2 + 5H)^+$  ion while the peak at  $m/z$  value of 1239 can be assigned for  $(Ag_3P_2 + 3H + K)^+$  confirming formation of a three atom-centred silver nanocluster. P denotes the peptide amphiphile ( $H_2N$ -His-Gly-Gly- $(CH_2)_{11}$ - $CH_3$ ) which acts as a protecting ligand to the cluster as well as being the hydrogelator (Figure 4.5a).

XPS is a sophisticated tool to gain insight of the binding energy of electronic state of individual elements of a system. Core-level XPS analysis of the nanocluster containing hydrogel, lets us know the oxidation state of the silver species in the nanocluster. The presence of 3d peaks (Figure 4.5b) of silver at 367.8 eV ( $3d_{5/2}$ ) and 373.8 eV ( $3d_{3/2}$ ) are attributed to Ag (0) species.<sup>45-46</sup> This signifies that the silver nanoclusters are completely formed by metallic silver.

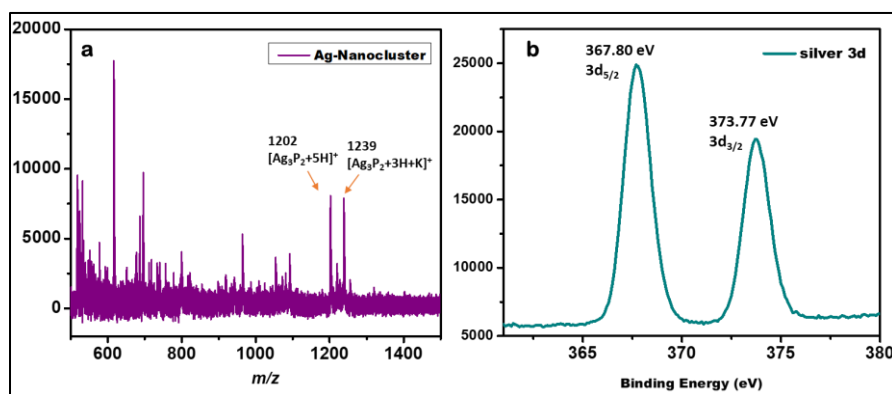


**Figure 4.5.** (a) MALDI-TOF mass analysis of the silver nanoclusters in sinapinic acid matrix and (b) X-Ray photoelectron spectrum for binding energy of silver 3d state suggesting presence of only Ag (0) species in the nanocluster containing hydrogel.



### Powder X-ray Diffraction (PXRD) Study

The X-ray diffraction analysis of the powder sample obtained from freeze-drying of the hydrogels are performed to investigate the nature of internal packing and secondary supramolecular structures adopted by the hydrogelator. The dried powder of aggregated peptide amphiphile is found to be amorphous. The small-angle X-ray diffraction of silver nanocluster containing hydrogel gives a molecular length of  $D = 55.1 \text{ \AA}$  corresponds to  $2\theta = 1.56^\circ$  (Figure 4.6a). The estimated length of the peptide amphiphile is measured to be  $25.7 \text{ \AA}$  (Obtained from Chem3D Pro 12.0 software). Thus, the probable length of  $D$  is coming from two peptide amphiphiles are attached through coordinating an  $\text{Ag}^+$  cation. In the wide-angle X-ray diffraction pattern of the same sample, the peak at  $10.3 \text{ \AA}$  ( $2\theta = 8.36^\circ$ ) corresponds to the inter-sheet distance of two  $\beta$ -sheets<sup>47</sup> and the peak at  $4.8 \text{ \AA}$  ( $2\theta = 17.96^\circ$ ) corresponds to the distance between two  $\beta$ -strands<sup>47</sup> (Figure 4.6b). The XRD pattern confirms  $\beta$ -sheet formation in the nanocluster containing hydrogel. The peak at  $3.9 \text{ \AA}$  ( $2\theta = 22.08^\circ$ ) proves the presence of strong intermolecular  $\pi$ - $\pi$  interaction between two imidazole groups of histidine residues (Figure 5b).<sup>23</sup> The powder sample of nanoparticle containing hydrogel shows very similar  $D$  value ( $2\theta = 1.54^\circ$ ) in its small-angle X-ray diffraction pattern (Figure 4.6c) confirming that the core hydrogel structure remains unchanged, while nanoclusters are conglomerate to bigger sized nanoparticles. In the wide-angle region peaks of  $9.7 \text{ \AA}$  ( $2\theta = 8.92^\circ$ ) and  $4.1 \text{ \AA}$  ( $2\theta = 20.87^\circ$ ) corresponds respectively to inter-sheet distance and  $\pi$ - $\pi$  stacking distance of the self-assembly system (Figure 4.6d).

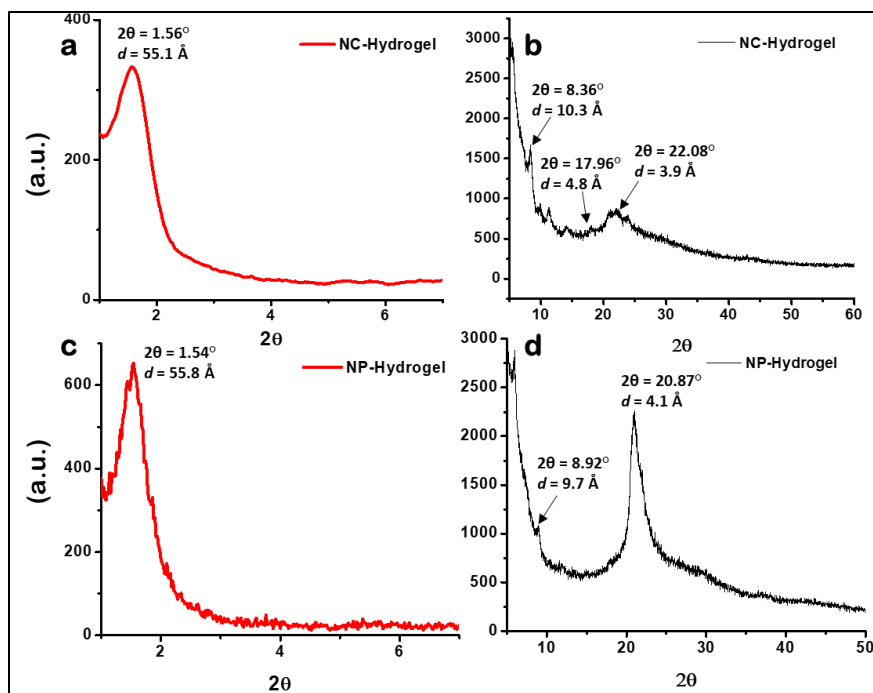


**Figure 4.6.** (a) Small-angle X-ray diffraction pattern and (b) Wide-angle X-ray diffraction pattern for dried nanocluster containing hydrogel. (c) Small-angle X-ray diffraction pattern and (d) Wide-angle X-ray diffraction pattern for dried nanoparticle containing hydrogel.

### Fourier Transform Infrared (FT-IR) Analysis

Fourier Transform Infrared (FT-IR) spectroscopic analysis of the hydrogels in their dried powdered form gives us the idea of hydrogen bonding nature of the aggregated system. The metallohydrogel formed shows peaks at  $1559 \text{ cm}^{-1}$  for amide II (amide N-H bending), at  $1650 \text{ cm}^{-1}$  for amide I (amide C=O stretching) and at  $3297 \text{ cm}^{-1}$  corresponding to N-H stretching vibrations (Figure S5).<sup>48</sup> It is interesting to note that there is no peak at  $3400 \text{ cm}^{-1}$  for non-hydrogen bonded amide N-H groups. Amide I signal lower than  $1660 \text{ cm}^{-1}$  is considered strongly hydrogen bonded. Thus, it can be concluded that the  $\beta$ -sheet arrangement of the hydrogel is formed via intramolecular amide hydrogen bonds.<sup>49</sup> It should also be noted that formation of nanoclusters or nanoparticles within the gel matrix does not interfere with the H-bonded network (Figure 4.7).

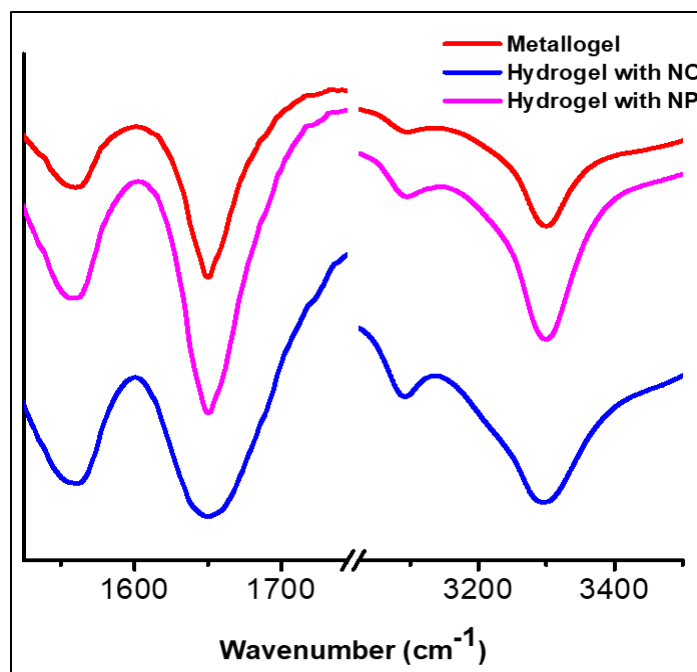


**Figure 4.7.** The solid state FTIR response of the metallohydrogel, hydrogel containing silver nanoclusters (NC) and hydrogel containing silver nanoparticle (NP).

### Rheology.

Rheological measurement of the hydrogels helps us to know how much stress the gel matrix can sustain before it breaks. To measure the mechanical strengths of the metallohydrogel and the nanomaterials containing hydrogel, 10 mg of the peptide amphiphile and 2 mg of  $\text{AgNO}_3$  was used to make 2 mL hydrogels. The hydrogels are subsequently reduced (The process is mentioned previously) to obtain nanoclusters or nanoparticles inside the gel matrix. Firstly, the frequency sweep experiment was done for freshly prepared metallohydrogel with gelator concentration 11.5 mM, where the two moduli, i.e., storage modulus ( $G'$ ) and loss modulus ( $G''$ ) were plotted against angular frequency ( $\omega$ ) ranging from 1-100 rad/s, at a constant strain of 0.1%. The moduli show an insignificant dependence on angular frequency (Figure 4.8, black line). This indicates the formation of a stable metallohydrogel with a storage modulus ( $G'$ ) of 980 Pa At  $\omega = 50$  rad/s. All these hydrogel samples show that there is no crossover between loss and storage modulus plot and it indicates that gels remain stable in the region of 1-100 rad/s of

angular frequency variation. It is interesting to note that the hydrogel containing silver nanoclusters show a significant improvement in mechanical property. It has  $G'$  of 7319 Pa (Figure 4.8, pink line). But the storage modulus of the hydrogel containing silver nanoparticles drops to 1505 Pa (Figure 4.8, orange line). Both enhancement<sup>50-52</sup> and loss<sup>53</sup> of mechanical strength due to addition of nanomaterials in gel matrix has been reported in literature. The morphological analysis clarifies that nanoclusters are grown uniformly on the nanofiber network (Figure 4.3b, Figure 4.4b). These nanoclusters protect the soft hydrogel thus improving the gel strength. Moreover, because of the affinity between hydrogel nanofibers and the nanoclusters, crosslinking through nanoclusters is formed inside the gel matrix, subsequently increasing the mechanical stiffness of this hybrid hydrogel further.<sup>52,54</sup> But in case of nanoparticles containing hydrogel, due to their bigger size, lower density and less uniform distribution (Figure 4.3d), additional crosslinkings are not formed, hence the rheological property is quite similar to that of fresh metallohydrogel.

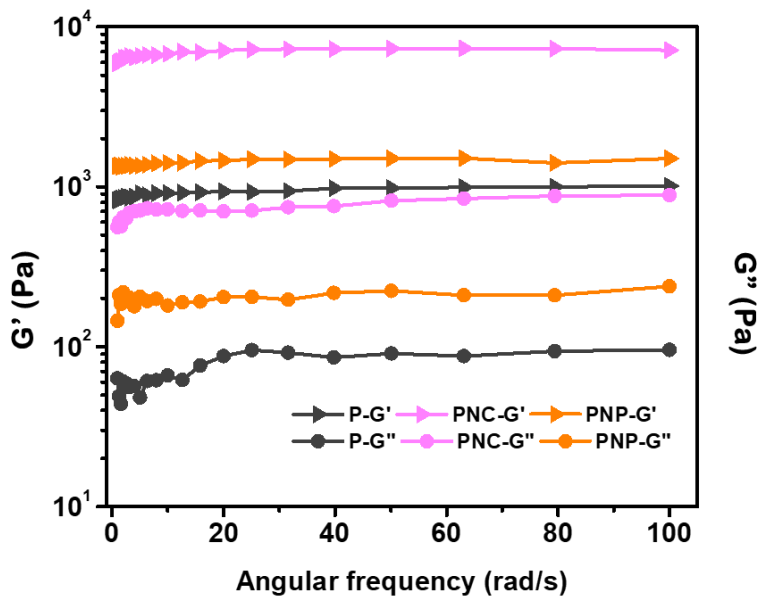


**Figure 4.8** Storage modulus  $G'$  and Loss modulus  $G''$  of hydrogels where P, PNP and PNC stand for pure metallohydrogel, hydrogel containing nanoclusters and hydrogel containing nanoparticles respectively.

### Antibacterial studies

We have investigated the potential for antimicrobial treatment of the nanomaterials containing hydrogels with only peptide amphiphile aggregate and water as controls. The initial study of antibacterial activity is conducted through a well-diffusion method. *Escherichia coli* and *Pseudomonas aeruginosa* are taken as Gram-negative, whereas *Bacillus subtilis* and *Staphylococcus aureus* are taken as Gram positive bacteria model. Wells are made on LB agar plates after spreading the bacteria solution on the gel surface. The pure peptide amphiphile aggregate (marked 'P' in Figure 4.9) did not show any antibacterial activity by itself. However, it is noted that both nanocluster containing hydrogel (marked as NC in the agar plates) and nanoparticle containing hydrogel (marked as NP in the agar plates) shows potential antibiotic activity for all the four types of bacteria used for the studies. The zone of inhibition values for NC and NP for all the bacteria species are tabulated in Table 1. Encouraged by the diffusion studies, minimum inhibitory concentrations (MIC) of the hydrogels have been measured to quantify their antimicrobial activities (Table 4.1). Although both the hydrogels show the same MIC for *E. coli* (23-34  $\mu\text{g}$ ), NC containing hydrogel shows better results in inhibiting bacterial growth in other three models (Table 4.1). The results show that silver nanomaterial-based hybrid hydrogels are effective antibacterial agent. We used the MTT assay to examine the cytotoxicity of the hybrid-hydrogels on the eukaryotes. For the experiment, mouse skin-derived NIH-3T3 cells are used. Silver nitrate solution shows more significant toxicity (34% cell viability) compared to the silver nanomaterials containing hydrogels (NC, NP cell viability 90% and 72% respectively). The pure peptide amphiphile shows maximum cell viability (97%) compared to the control (Figure 4.10). This shows that the hybrid hydrogels are more biocompatible than  $\text{AgNO}_3$  in the MIC range. This is consistent with previous works as well.<sup>55-56</sup>



**Figure 4.9** Images of the culture plates for zone of inhibition study by well-diffusion method. Each culture plate contains different bacterial strain. (a) *P. aeruginosa*, (b) *E. coli*, (c) *B. subtilis*, (d) *S. aureus*.

**Table 4.1** List of bacterial inhibition zone (diameter) and minimum inhibitory concentrations of the hybrid hydrogels

Bacteria	MIC for NC-Hydrogel (µg)	Zone of Inhibition for NC-Hydrogel (mm)	MIC for NP-Hydrogels (µg)	Zone of Inhibition for NP-Hydrogel (mm)
<i>B. Subtilis</i>	23-34	12	34-46	14
<i>E. Coli</i>	23-34	12	23-34	14
<i>S. Aureus</i>	17-23	13	34-46	15
<i>P. Aeruginosa</i>	9-17	12	23-34	14

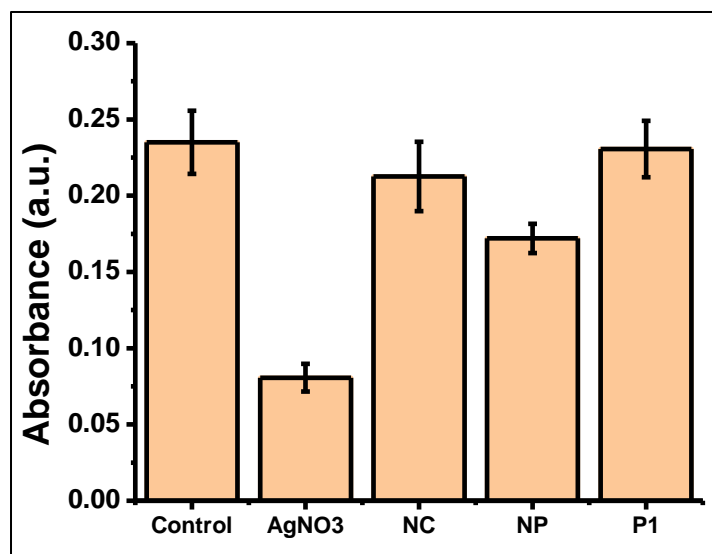


**Figure 4.10** The cell viability study (MTT assay) of  $\text{AgNO}_3$  solution, nanocluster containing gel (NC), nanoparticle containing gel (NP) and pure peptide amphiphile **P1** for NIH-3T3 cell-line incubated for 24 h.

### Reactive Oxygen Species generation study

To understand the effectiveness of the nanoclusters and the nanoparticles as antibiotic agents, a study is designed to quantify reactive oxygen species (ROS) generated inside the bacteria cell in presence of the hybrid-hydrogels. For the aforementioned study *B. subtilis* is used as the model bacteria and DCFDA as the probe. The study shows that reactive oxygen species produced inside the bacteria cell increases with increasing amount of silver nanocluster containing hydrogel (Figure 4.11a). The cellular ROS level of *B. subtilis* increases 83% upon addition of only 10  $\mu\text{g}$  of NC containing hydrogel to the bacteria suspended in Hank's balanced salt solution (HBSS). Addition of 25  $\mu\text{g}$  of the same hydrogel produces a 431% increase in ROS as probed by DCFDA dye which is activated only after diffusing inside the cell (Figure 4.11a). The nanocluster containing hydrogel shows increasing amount of ROS generation as the concentration of the hydrogel is increased. The curve tends to reach a saturation amount at higher concentrations of the hydrogel (Figure 4.11b). It is also clear from Figure 4.11b that at every concentration, amount of ROS generated in presence of nanoclusters is higher than ROS generated in the presence of nanoparticles. This observation convincingly

demonstrates why the nanocluster containing hydrogel shows better efficiency in inhibiting bacteria growth. The peptide amphiphile **P1** with a free amine group, contains positive charge at physiological pH. Thus, the nanofibrous network of the hydrogel can interact with negatively charged cell wall of bacteria. In this manner they can transport the nanomaterials to get through the cell wall so that they can interact with the electron transport chain of the phospholipid membrane. Interaction of silver nanomaterials with phospholipid is one of the key causes of increased ROS generation in bacteria.<sup>57</sup> It is hypothesized that due to rearrangement of phospholipids, electron leaks out inside cytoplasm to reduce cellular oxygen molecules forming ROS.<sup>58-59</sup> In this study, nanoclusters show more effectiveness in bacteria killing due to their ultra-small size which supports easy diffusion of the nanoclusters inside the cell membrane. Better microbial activity from smaller silver nanomaterial has been mentioned previously in literature.<sup>60</sup>

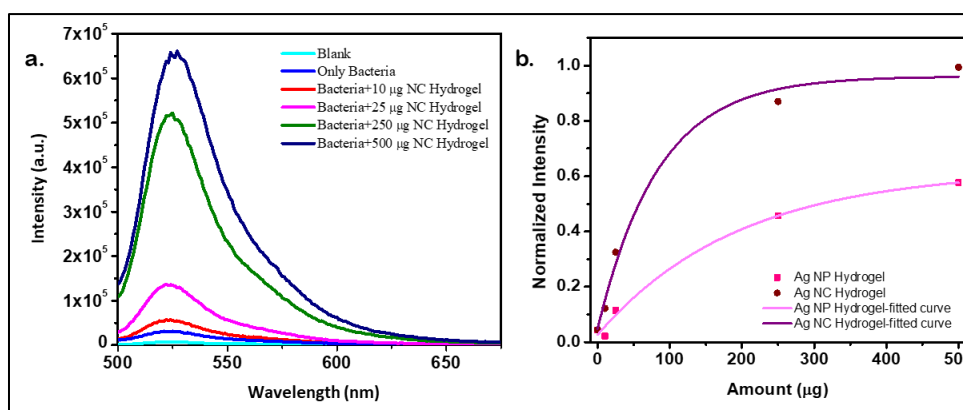


**Figure 4.11** (a) The fluorescence spectra of 2',7'-dichlorofluorescein (DCF) probing the intra-cellular ROS generation in *B. subtilis* when subjected to different concentration of NC containing hydrogel in Hank's Balanced Salt Solution. (b) The comparative analysis of intra-cellular ROS generated in *B. subtilis* in presence of NC and NP containing hydrogels. The intensity is normalized with respect to the highest intensity point of the experiment.

### 4.3 Conclusion

We illustrate silver ion induced hydrogelation of a histidine-based peptide amphiphile **P1** in Mili-Q water (pH 7.0). However, **P1** fails to form any hydrogel otherwise. The metallohydrogel can be photo-reduced in two different conditions



to obtain two different hybrid hydrogels: (i) blue light emitting silver nanocluster containing gel, (ii) non-fluorescent silver nanoparticle containing gel. The XPS and MALDI-TOF mass analysis helps in characterizing the nanoclusters. PXRD and FTIR analysis helps us to conclude that the hydrogel is formed via a  $\beta$ -sheet arrangement. Morphological analysis of the hydrogels reveal that nanomaterials are formed along the nanofibrous network thus, enabling cross-linking between the peptide fibers. The consequence of the cross-linking is evident from the rheological measurements. The mechanical rigidity of the original metallogel improves from 980 Pa to 7319 Pa of the Ag nanocluster containing gel. It happens because the nanoclusters increase the number of connections between the nanofibers. Interestingly, these nanohybrid gels show potent antimicrobial activity against both Gram-positive and Gram-negative bacteria. The synergy between the peptide amphiphile and the silver nanomaterials make them non-cytotoxic to eukaryotes. Finally, from the ROS generation study it can be concluded that the efficient killing of bacteria is primarily resulting from intra-cellular ROS generation which damages the bacterial DNA. It is also understood that the nanocluster containing hydrogel shows better antibacterial effect because of its ultra-small size and better dispersity. Thus, this study holds future promise for the development of new class of antibacterial drugs fighting the drug-resistance of bacteria.

## 4.4 Experimental section

### Synthesis of the peptide amphiphile

The N-terminus and imidazole group of L-histidine were protected with Boc groups. Coupling was mediated by N,N-dicyclohexylcarbodiimide and 1-hydroxybenzotriazole monohydrate (DCC/HOBt.H<sub>2</sub>O). The Boc group from the N-terminal was removed by treating the protected peptide with 98-100% formic acid solution. The final compound was fully characterized by mass spectrometry, <sup>1</sup>HNMR spectroscopy and <sup>13</sup>C NMR spectroscopy

### Synthesis of Boc-Gly-Gly-OH [(CH<sub>3</sub>)<sub>3</sub>C-O-CONH-CH<sub>2</sub>-CONH-CH<sub>2</sub>-COOH]:

2.62g (20 mmol) of L-Isoleucine (Ile) was taken in a 250mL round bottomed flask and 20 mL 0.5(N) NaOH and equal volume of 1,4-dioxane were added to it to

dissolve the amino acid completely. 4.60g (21.1 mmol) di-tert-butyl dicarbonate (Boc anhydride) was added to the reaction mixture, cooled in an ice bath and stirred for 10 hours at room temperature. Then the solution volume was reduced to one third in a rotary evaporator. The resulting mixture was acidified with saturated  $\text{KHSO}_4$  solution and the aqueous layer was extracted with ethyl acetate (3 x 40 mL). The ethyl acetate extract was dried over anhydrous sodium sulfate and evaporated in vacuum to obtain the white solid product.

Yield: 4.10 g (17.74 mmol, 88.70 %).

**Synthesis of Boc-Gly-Gly- $\text{C}_{12}$  [ $(\text{CH}_3)_3\text{C-O-CONH-CH}_2\text{-CONH-CH}_2\text{-CONH-}(\text{CH}_2)_{11}\text{-CH}_3$ ]:** 4.10 g (17.74 mmol) of Boc-Gly-Gly-OH was dissolved in 12mL dry N,N-dimethyl formamide (DMF) and cooled in an ice bath. 80mL of Ethyl acetate was added to it. It was followed by addition of 2.43g (18.00mmol) of 1-hydroxybenzotriazolemonohydrate (HOBt.H<sub>2</sub>O) and 3.70 g of dodecylamine (20mmol). 4.12 g (20mmol) of N,N-dicyclohexylcarbodiimide (DCC) was added after all the reagents are properly dissolved. The reaction mixture was stirred for 24 hours in room temperature (27°C). The reaction mixture was diluted with ethyl acetate and filtered to separate N,N- dicyclohexyl urea (DCU). The ethyl acetate layer was washed with 1(N) HCl (3 x 30 mL), brine (2 x 30 mL), saturated sodium carbonate solution (2 x 30 mL) and brine (2 x 30 mL). The organic layer was dried over anhydrous sodium sulfate and the solvent was removed under reduced pressure. The crude reaction mixture was purified through silica gel column chromatography using chloroform/methanol (97:3) as eluent to obtain the pure white product.

Yield: 5.82g (14.55 mmol, 82.02%).

$^1\text{H}$  NMR (400 MHz,  $\text{CDCl}_3$ , 25 °C):  $\delta$  6.91 (1H, br, NH), 6.38 (1H, br, NH), 5.26-5.28 (1H, t, J=5.0 Hz, NH), 3.92-3.94 (2H, d, J=5.6,  $\alpha$ -CH<sub>2</sub> of Gly), 3.80-3.82 (2H, d, J=5.6,  $\alpha$ -CH<sub>2</sub> of Gly), 3.20-3.25 (2H, m,  $\alpha$ -CH<sub>2</sub> of acyl chain), 1.74 (2H, s,  $\beta$ -CH<sub>2</sub> of acyl chain), 1.45-1.51 (11H, m, chain CH<sub>2</sub>), 1.25-1.27 (18H, m, chain CH<sub>2</sub> and Boc-CH<sub>3</sub>), 0.86-0.89 (3H, t, J=6.4 Hz, chain CH<sub>3</sub>).  $^{13}\text{C}$  NMR (100 MHz,  $\text{CDCl}_3$ ):  $\delta$  170.06, 168.57, 156.42, 80.79, 44.68, 43.25, 39.89, 32.05, 29.78, 29.76, 29.74, 29.67, 29.59, 29.48, 29.42, 28.44, 27.03, 22.82, 14.23. HRMS (m/z): Calculated for  $\text{C}_{21}\text{H}_{41}\text{N}_3\text{O}_4$ : 399.31 Found: 422.27(M+Na)<sup>+</sup>, 438.24(M+K)<sup>+</sup>. (Figure 4.12-4.14)

**Synthesis of H-Gly-Gly-C<sub>12</sub> [(H<sub>2</sub>N-CH<sub>2</sub>-CONH-CH<sub>2</sub>-CONH-(CH<sub>2</sub>)<sub>11</sub>-CH<sub>3</sub>):** To 5.82g (14.55 mmol) of Boc-Gly-Gly-C<sub>12</sub>, 15 mL of formic acid was added to remove the Boc protection. The reaction was monitored using TLC. After 8 hours, formic acid was removed under vacuum using a liquid nitrogen trap. 10 mL of water is added, and the pH was balanced to 8-8.5 using Na<sub>2</sub>CO<sub>3</sub>. Subsequent addition of ethyl acetate precipitates out the beige crude product. The filtrate was dried and further purified using basic alumina column, chloroform and methanol (9:1) as eluent.

Yield: 4.10g (13.68mmol, 94.02%).

<sup>1</sup>H NMR (400 MHz, DMSO-d<sub>6</sub>, 25 °C): δ 8.06 (1H, br, NH), 7.79-7.81 (1H, t, J=5.2 Hz, NH), 3.68 (2H, s, α-CH<sub>2</sub> of Gly), 3.32 (2H, s, α-CH<sub>2</sub> of Gly), 3.02-3.07 (2H, m, α-CH<sub>2</sub> of acyl chain), 1.37-1.40 (2H, m, β-CH<sub>2</sub> of acyl chain), 1.25 (18H, m, chain CH<sub>2</sub>), 0.84-0.88 (3H, t, J=6.8 Hz, chain CH<sub>3</sub>). <sup>13</sup>C NMR (100 MHz, DMSO-d<sub>6</sub>): δ 173.00, 168.40, 44.66, 41.70, 38.43, 31.21, 29.02, 28.97, 28.92, 28.67, 28.62, 26.29, 22.00, 13.85. HRMS (m/z): Calculated for C<sub>16</sub>H<sub>33</sub>N<sub>3</sub>O<sub>2</sub>: 299.26 Found: 300.26 (M+H)<sup>+</sup>, 322.21 (M+Na)<sup>+</sup>. (Figure 4.15-4.17)

**Synthesis of (Boc)<sub>2</sub>-His-Gly-Gly-C<sub>12</sub> [(CH<sub>3</sub>)<sub>3</sub>C-O-CONH-CH(C<sub>9</sub>H<sub>13</sub>N<sub>2</sub>O<sub>2</sub>)-CONH-CH<sub>2</sub>-CONH-CH<sub>2</sub>-CONH-(CH<sub>2</sub>)<sub>11</sub>-CH<sub>3</sub>):** 1.78 g (5 mmol) of (Boc)<sub>2</sub>-His-COOH and 0.60 g (5.22 mmol) N-Hydroxysuccinimide was dissolved in 50 mL of THF. To this solution 1.20 g (5.83 mmol) of DCC is added. After 24 hours, the reaction mixture is filtered to remove DCU precipitate and to this fresh solution, 1.50 g (5 mmol) of H-Gly-Gly-C<sub>12</sub> was suspended and stirred vigorously for 48 hours. Subsequently the solvent is removed under vacuum and the desired product is purified using a silica gel column and chloroform/methanol (94:6) as eluent to obtain the pure glassy product.

Yield: 1.3g (2.03 mmol, 40.63%).

<sup>1</sup>H NMR (400 MHz, CDCl<sub>3</sub>, 25 °C): δ 9.04 (1H, br, NH), 7.57 (1H, s, ε<sup>1</sup> CH of His), 6.97 (1H, br, NH), 6.83 (1H, s, δ<sup>2</sup>CH of His), 5.55 (1H, br, NH), 4.43 (1H, s, α CH of His), 3.81-3.89 (4H, m, α-CH<sub>2</sub> of Gly), 3.22-3.25 (1H, m, β-CH<sub>2</sub> of His), 2.95-3.00 (1H, m, β-CH<sub>2</sub> of His), 3.10-3.15 (2H, m, α-CH<sub>2</sub> of acyl chain), 1.42 (12H, m, chain CH<sub>2</sub>), 1.22 (20H, m, chain CH<sub>2</sub> and Boc-CH<sub>3</sub>), 0.84-0.88 (3H, t, J=6.8 Hz, chain CH<sub>3</sub>). <sup>13</sup>C NMR (100 MHz, CDCl<sub>3</sub>): δ 173.75, 170.04, 169.76,



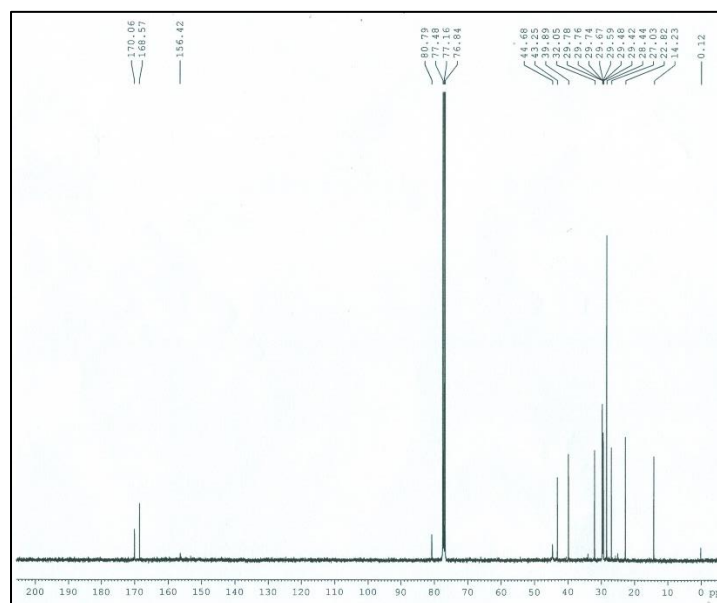


**Figure 4.13** 100 MHz  $^{13}\text{C}$  NMR spectrum of Boc-Gly-Gly- $\text{C}_{12}$  in  $\text{CDCl}_3$

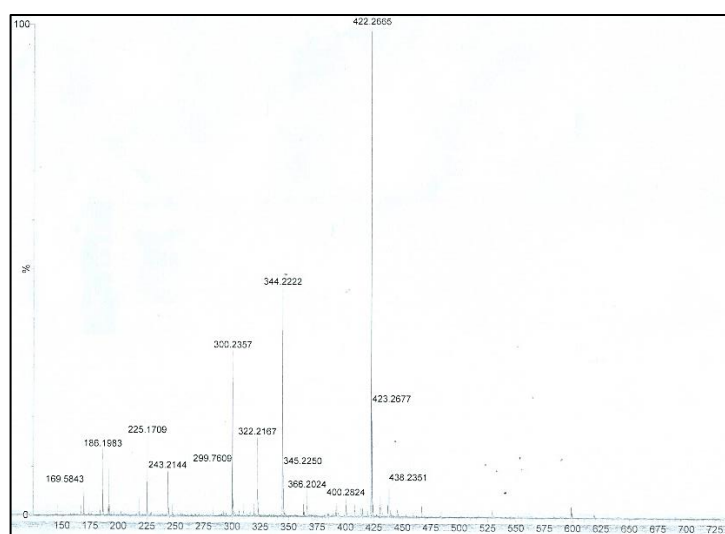


**Figure 4.14** HRMS spectrum of Boc-Gly-Gly- $\text{C}_{12}$

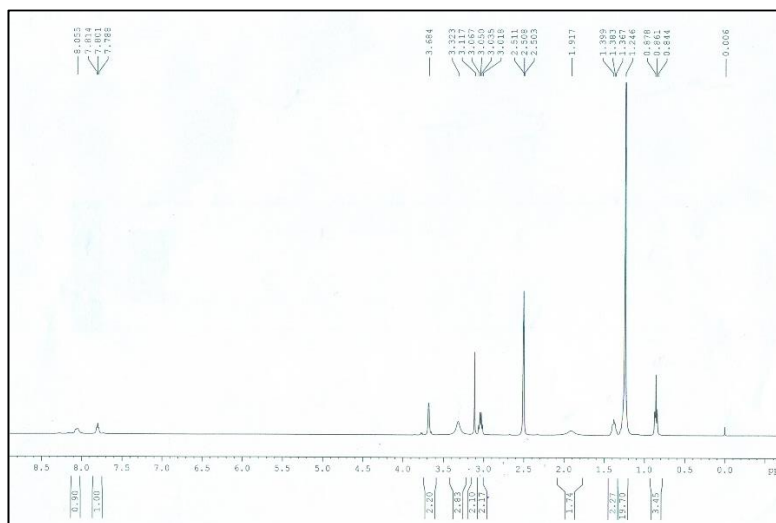


Figure 4.15 400 MHz  $^1\text{H}$  NMR spectrum of H-Gly-Gly- $\text{C}_{12}$  in  $\text{DMSO-d}_6$

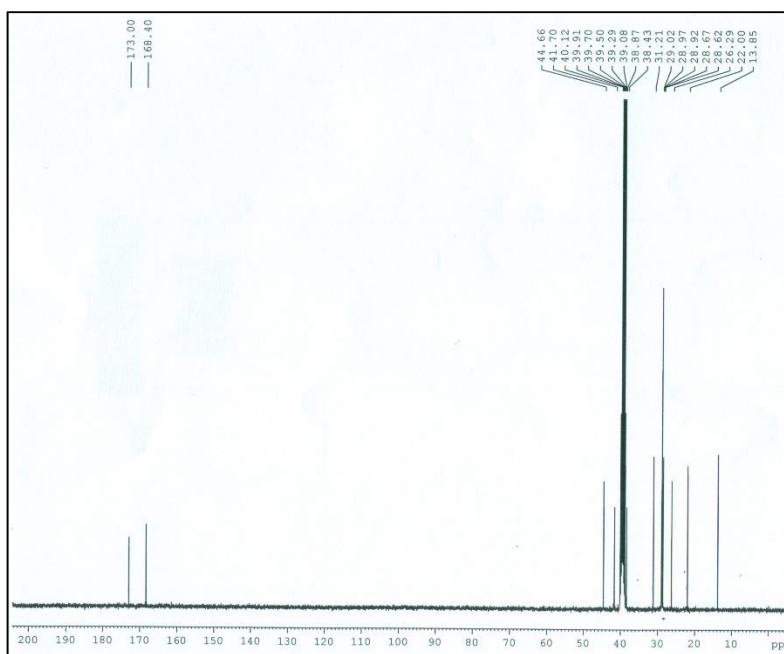
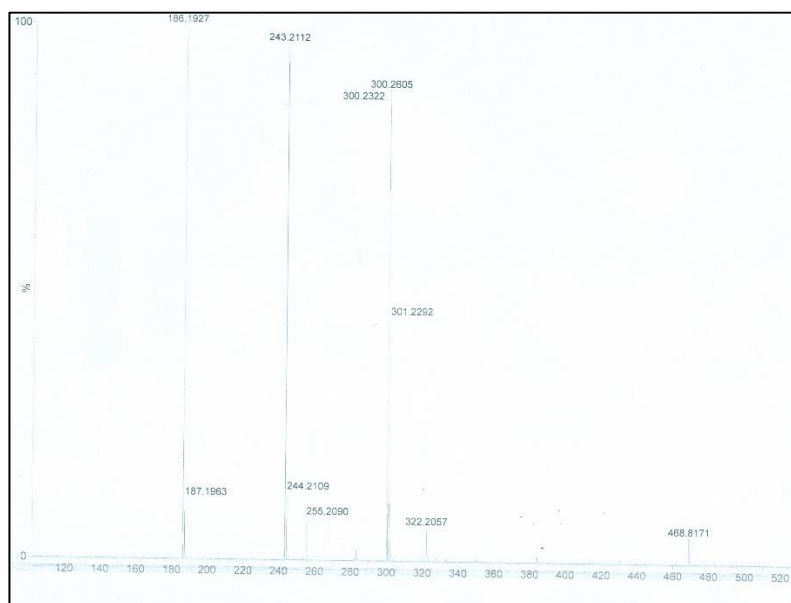
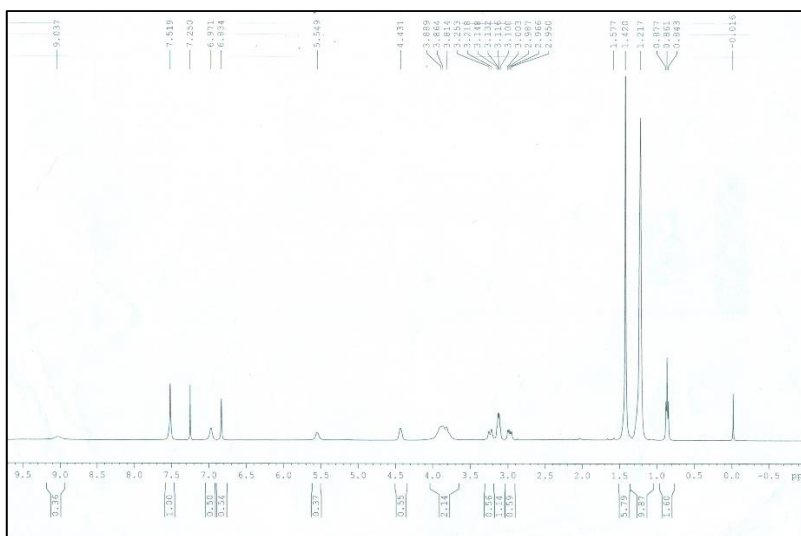


Figure 4.16 100 MHz  $^{13}\text{C}$  NMR spectrum of Boc-Gly-Gly- $\text{C}_{12}$  in  $\text{DMSO-d}_6$



**Figure 4.17** HRMS spectrum of *H*-Gly-Gly-*C*<sub>12</sub>



**Figure 4.18** 400 MHz <sup>1</sup>H NMR spectrum of (Boc)<sub>2</sub>-His-Gly-Gly-*C*<sub>12</sub> in CDCl<sub>3</sub>

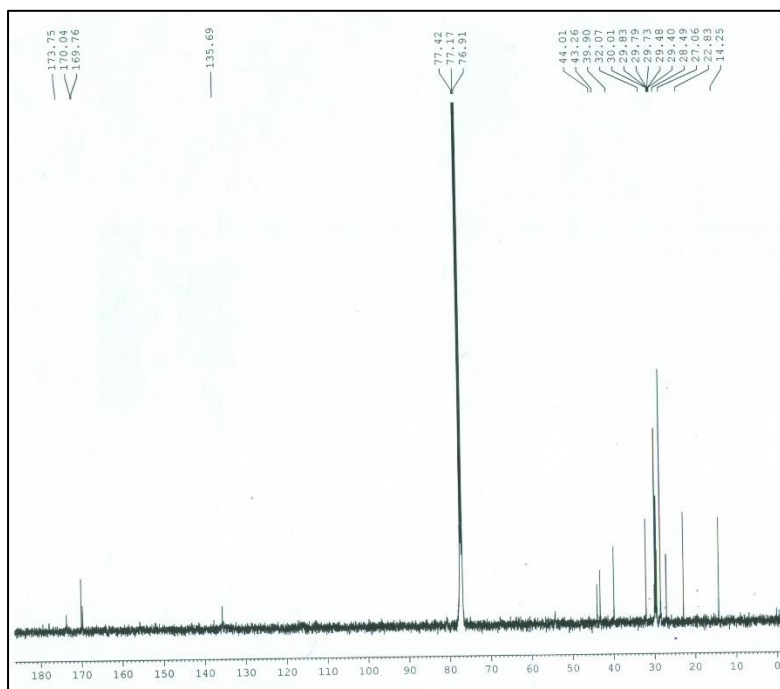


Figure 4.19 100 MHz  $^{13}\text{C}$  NMR spectrum of  $(\text{Boc})_2\text{-His-Gly-Gly-C}_{12}$  in  $\text{CDCl}_3$

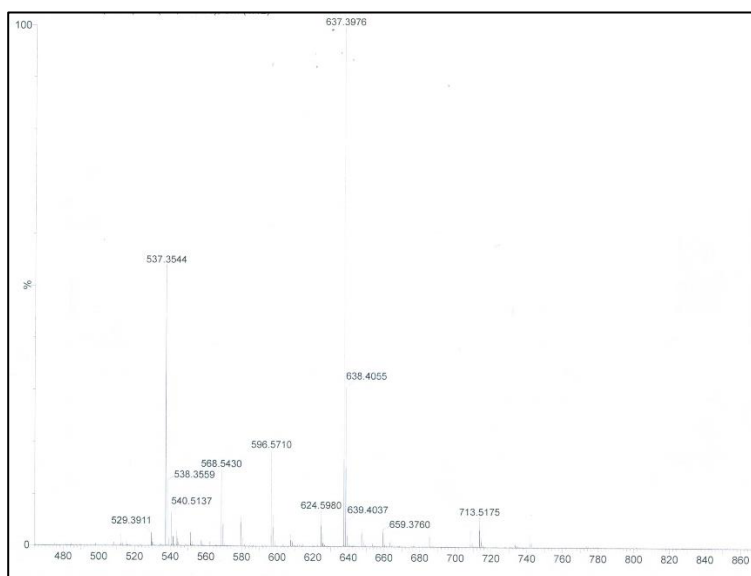
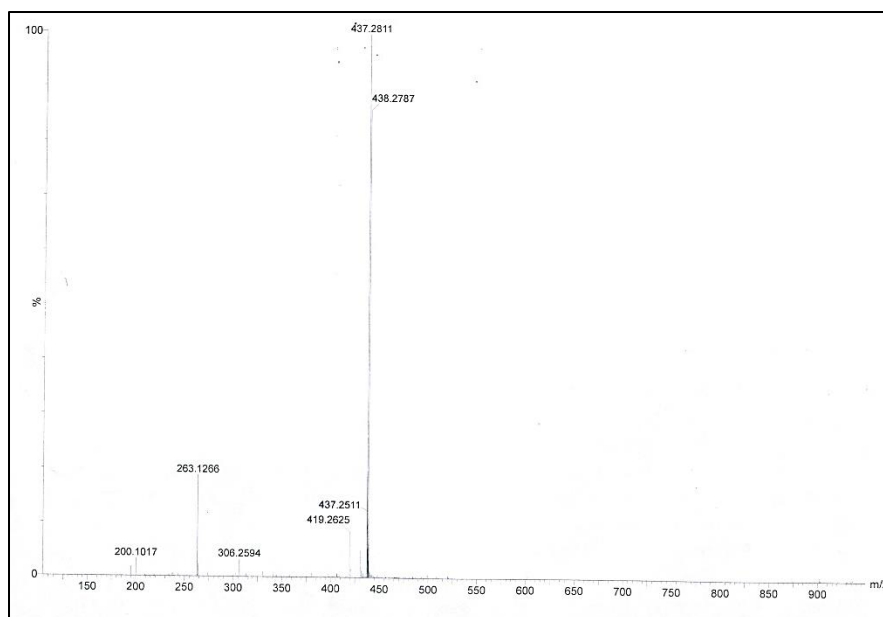


Figure 4.20 HRMS spectrum of  $(\text{Boc})_2\text{-His-Gly-Gly-C}_{12}$







**Figure 4.23** HRMS spectrum of H-His-Gly-Gly-C<sub>12</sub>

## 4.5 References

1. C. Yan and D. J. Pochan, *Chem. Soc. Rev.*, 2010, **39**, 3528-3540.
2. M. Amit, S. Yuran, E. Gazit, M. Reches and N. Ashkenasy, *Adv. Mater.*, 2018, **30**, 1707083.
3. S. Paul, K. Basu, K. S. Das and A. Banerjee, *ChemNanoMat*, 2018, **4**, 882-887.
4. S. Roy, K. Basu, K. Gayen, S. Panigrahi, S. Mondal, D. Basak and A. Banerjee, *J. Phys. Chem. C*, 2017, **121**, 5428-5435.
5. C. Ligorio, A. Vijayaraghavan, J. A. Hoyland and A. Saiani, *Acta Biomater.*, 2022, **143**, 145-158.
6. O. Bellotto, M. C. Cringoli, S. Perathoner, P. Fornasiero and S. Marchesan, *Gels*, 2021, **7**, 14.
7. C. C. Piras, A. G. Kay, P. G. Genever, J. Fitremann and D. K. Smith, *Chem. Sci.*, 2022, **13**, 1972-1981.

8. B. Mondal, D. Bairagi, N. Nandi, B. Hansda, K. S. Das, C. J. C. Edwards-Gayle, V. Castelletto, I. W. Hamley and A. Banerjee, *Langmuir*, 2020, **36**, 12942-12953.
9. P. J. Knerr, M. C. Branco, R. Nagarkar, D. J. Pochan and J. P. Schneider, *J. Mater. Chem.*, 2012, **22**, 1352-1357.
10. R. Martí-Centelles, J. Rubio-Magnieto and B. Escuder, *Chem. Commun.*, 2020, **56**, 14487-14490.
11. B. L. Abraham, E. S. Toriki, N. D. J. Tucker and B. L. Nilsson, *J. Mat. Chem. B*, 2020, **8**, 6366-6377.
12. R. Martí-Centelles, I. Dolz-Pérez, J. De la O, I. Ontoria-Oviedo, P. Sepúlveda, V. J. Nebot, M. J. Vicent and B. Escuder, *ACS Appl. Bio Mater.* 2021, **4**, 935-944.
13. P. Worthington, S. Langhans and D. Pochan, *Adv. Drug Del. Rev.*, 2017, **110-111**, 127-136.
14. B. O. Okesola, Y. Wu, B. Derkus, S. Gani, D. Wu, D. Knani, D. K. Smith, D. J. Adams and A. Mata, *Chem. Mater.*, 2019, **31**, 7883-7897.
15. A. Scelsi, B. Bochicchio, A. Smith, V. L. Workman, L. A. Castillo Diaz, A. Saiani and A. Pepe, *J. Biomed. Mater. Res. A*, 2019, **107**, 535-544.
16. O. Bellotto, S. Semeraro, A. Bandiera, F. Tramer, N. Pavan and S. Marchesan, *Pharmaceutics*, 2022, **14**, 446.
17. E. R. Cross, S. M. Coulter, A. M. Fuentes-Caparrós, K. McAulay, R. Schweins, G. Lavery and D. J. Adams, *Chem. Commun.*, 2020, **56**, 8135-8138.
18. C. C. Piras, C. S. Mahon, P. G. Genever and D. K. Smith, *ACS Biomater. Sci. Eng.*, 2022, **8**, 1829-1840.
19. V. K. Pal and S. Roy, *Macromol. Biosci.*, 2022, **22**, 2100462.
20. T. Shao, N. Falcone and H.-B. Kraatz, *ACS Omega*, 2020, **5**, 1312-1317.
21. C. M. Micklitsch, P. J. Knerr, M. C. Branco, R. Nagarkar, D. J. Pochan and J. P. Schneider, *Angew. Chem. Int. Ed.*, 2011, **50**, 1577-1579.

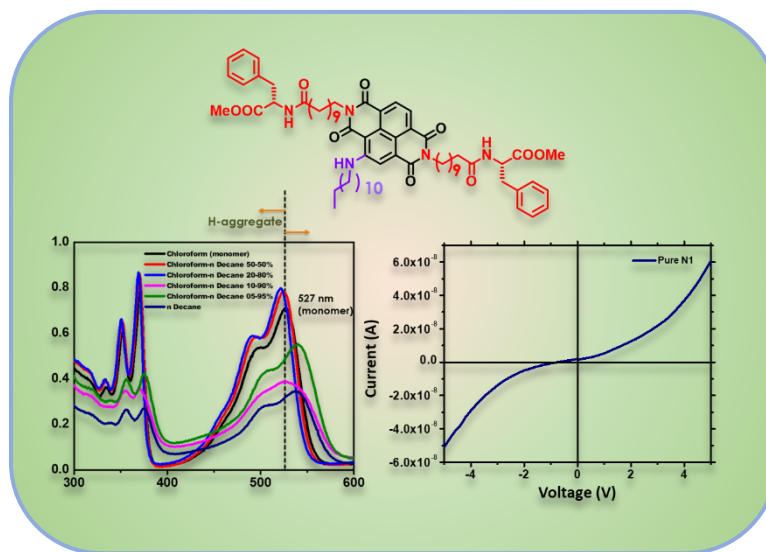
22. Y. M. Abul-Haija, G. G. Scott, J. K. Sahoo, T. Tuttle and R. V. Ulijn, *Chem. Commun.*, 2017, **53**, 9562-9565.
23. K. Gayen, K. Basu, D. Bairagi, V. Castelletto, I. W. Hamley and A. Banerjee, *ACS Appl. Bio Mater.*, 2018, **1**, 1717-1724.
24. J. Chen, T. Wang and M. Liu, *Inorg. Chem. Front.*, 2016, **3**, 1559-1565.
25. J. Song, C. Yuan, T. Jiao, R. Xing, M. Yang, D. J. Adams and X. Yan, *Small*, 2020, **16**, 1907309.
26. Z. Cao, Y. Luo, Z. Li, L. Tan, X. Liu, C. Li, Y. Zheng, Z. Cui, K. W. K. Yeung, Y. Liang, S. Zhu and S. Wu, *Macromol. Biosci.*, 2021, **21**, 2000252.
27. S. Tang and J. Zheng, *Adv. Healthcare Mater.*, 2018, **7**, 1701503.
28. J. Xu, M. Ramasamy, T. Tang, Y. Wang, W. Zhao and K. C. Tam, *J. Colloid Interface Sci.*, 2022, **623**, 883-896.
29. I. Khansa, A. R. Schoenbrunner, C. T. Kraft and J. E. Janis, *Plast Reconstr Surg Glob Open*, 2019, **7**, e2390-e2390.
30. S. P. Deshmukh, S. M. Patil, S. B. Mullani and S. D. Delekar, *Mater. Sci. Eng. C*, 2019, **97**, 954-965.
31. V. Burmistrov, A. Burmistrov, G. Odegova, A. Pestryakov, R. Luna-Vázquez-Gómez and N. Bogdanchikova, *Coatings*, 2022, **12**, 532.
32. Y. Wang, L. Cao, S. Guan, G. Shi, Q. Luo, L. Miao, I. Thistlethwaite, Z. Huang, J. Xu and J. Liu, *J. Mater. Chem.*, 2012, **22**, 2575-2581.
33. J.-S. Shen, Y.-L. Chen, J.-L. Huang, J.-D. Chen, C. Zhao, Y.-Q. Zheng, T. Yu, Y. Yang and H.-W. Zhang, *Soft Matter*, 2013, **9**, 2017-2023.
34. M. R. Reithofer, A. Lakshmanan, A. T. K. Ping, J. M. Chin and C. A. E. Hauser, *Biomaterials*, 2014, **35**, 7535-7542.
35. Z. Zhang, T. He, M. Yuan, R. Shen, L. Deng, L. Yi, Z. Sun and Y. Zhang, *Chem. Commun.*, 2015, **51**, 15862-15865.
36. N. Nandi, K. Gayen, S. Ghosh, D. Bhunia, S. Kirkham, S. K. Sen, S. Ghosh, I. W. Hamley and A. Banerjee, *Biomacromolecules*, 2017, **18**, 3621-3629.

37. A. S. Veiga, C. Sinthuvanich, D. Gaspar, H. G. Franquelim, M. A. R. B. Castanho and J. P. Schneider, *Biomaterials*, 2012, **33**, 8907-8916.
38. S. Roy and A. Banerjee, *Soft Matter*, 2011, **7**, 5300-5308.
39. N. K. Mishra, V. Kumar and K. B. Joshi, *Nanoscale*, 2015, **7**, 20238-20248.
40. Y. Wang, X. Yang, T. Liu, Z. Li, D. Leskauskas, G. Liu and J. B. Matson, *J. Am. Chem. Soc.*, 2020, **142**, 9158-9162.
41. E. Pazos, E. Sleep, C. M. Rubert Pérez, S. S. Lee, F. Tantakitti and S. I. Stupp, *J. Am. Chem. Soc.*, 2016, **138**, 5507-5510.
42. X. Gao, Y. Lu, S. He, X. Li and W. Chen, *Anal. Chim. Acta*, 2015, **879**, 118-125.
43. M. Annadhasan, T. Muthukumarasamyvel, V. R. Sankar Babu and N. Rajendiran, *ACS Sustain. Chem. Eng.*, 2014, **2**, 887-896.
44. T.-Q. Yang, B. Peng, B.-Q. Shan, Y.-X. Zong, J.-G. Jiang, P. Wu and K. Zhang, *Nanomaterials*, 2020, **10**, 261.
45. X. Wang, Y. Shen, A. Xie and S. Chen, *Mater. Chem. Phys.*, 2013, **140**, 487-492.
46. R. Sharma, A. Dhillon and D. Kumar, *Sci. Rep.*, 2018, **8**, 5189.
47. J. Naskar, G. Palui and A. Banerjee, *J. Phys. Chem. B*, 2009, **113**, 11787-11792.
48. A. Paikar, M. Debnath, D. Podder, S. Sasmal and D. Haldar, *Org. Biomol. Chem.*, 2017, **15**, 4218-4225.
49. C. Toniolo, G. M. Bonora, F. Marchiori and G. Borin, *J. Am. Chem. Soc.*, 1984, **106**, 1455-1457.
50. A. Memic, H. A. Alhadrami, M. A. Hussain, M. Aldhahri, F. Al Nowaiser, F. Al-Hazmi, R. Oklu and A. Khademhosseini, *Biomed. Mater.*, 2015, **11**, 014104.
51. M. Biondi, A. Borzacchiello, L. Mayol and L. Ambrosio, *Gels*, 2015, **1**, 162-178.

52. P. Thoniyot, M. J. Tan, A. A. Karim, D. J. Young and X. J. Loh, *Adv. Sci.*, 2015, **2**, 1400010.
53. J. Nanda, B. Adhikari, S. Basak and A. Banerjee, *J. Phys. Chem. B*, 2012, **116**, 12235-12244.
54. C. Ferrag, S. Li, K. Jeon, N. M. Andoy, R. M. A. Sullan, S. Mikhaylichenko and K. Kerman, *Colloids Surf. B.*, 2021, **197**, 111397.
55. O. Brandt, M. Mildner, A. E. Egger, M. Groessler, U. Rix, M. Posch, B. K. Keppler, C. Strupp, B. Mueller and G. Stingl, *Nanomedicine*, 2012, **8**, 478-488.
56. A. Yusuf and A. Casey, *Apoptosis*, 2020, **25**, 120-134.
57. Z. Lu and J. A. Imlay, *mBio*, 2017, **8**, e01873-16.
58. M. Yekani, H. B. Baghi, S. Z. Vahed, H. Ghanbari, R. Hosseinpur, R. Azargun, S. Azimi and M. Y. Memar, *Res. Microbiol.*, 2021, **172**, 103798.
59. S. Y. Kim, C. Park, H. J. Jang, B. O. Kim, H. W. Bae, I. Y. Chung, E. S. Kim and Y. H. Cho, *J. Microbiol.*, 2019, **57**, 203-212.
60. Y. Dong, H. Zhu, Y. Shen, W. Zhang and L. Zhang, *PLoS One*, 2019, **14**, e0222322.

## CHAPTER 5

# Peptide-Appended Core-substituted Naphthalenediimides: Exploration of Aggregation and Semiconducting Property



[Manuscript in Communication]





## 5.1 Introduction

Naphthalenediimides (NDIs) belong to the class of  $\pi$ -conjugated molecules. It is a hotspot of research activity for the past decade.<sup>1-5</sup> NDIs are a special class of  $\pi$ -conjugated molecules having a plethora of functional and beneficial properties such as thermal stability, electron affinity and molecular planarity. They find applications in wide variety of fields including solar cells,<sup>6,7</sup> photovoltaic cells,<sup>8</sup> light emitting diodes<sup>9</sup> and supramolecular chemistry<sup>10,11</sup> There are two types of NDI derivatives depending on the position where substituents attach on the naphthalene dianhydride (NDA) molecule namely imide-substituted NDIs<sup>12-14</sup> and the other is core-substituted NDIs.<sup>15-17</sup> The core substituted NDIs have one or more electron donors substituted at the core position of NDA thus leading to a collection of NDI molecules emitting full range of visible colors and have high quantum yield up to 0.8.<sup>18</sup> The NDIs are known for their self-assembling property and they form a variety of nanostructures with tunable functionality. The examples of such nanostructures include nano sheet, nano ribbons, nano tube, nano fibers.<sup>12,19,20</sup> The property of NDI in solvent system is studied with the help of amino acid substitution or synthetic peptide at the periphery of the NDI core.<sup>21-25</sup> The attached amino groups or synthetic peptides are biodegradable and biocompatible in nature and helps in the formation of hydrogen bond.<sup>26-28</sup> The self-assembly of these substituted NDI is influenced by the nature of the solvent,<sup>29</sup> pH of the medium,<sup>30</sup> and nature of the substituent<sup>31</sup> as they self-assemble using  $\pi$ - $\pi$  interaction, hydrogen bonding and van der Waals interaction. The self-assembly of the NDIs occurs in two ways- edge to edge interaction which is known as J aggregation and face to face interaction known as H aggregation<sup>32</sup> and both of them exhibit different electrical and optical properties.<sup>32,33,34</sup> The optical properties of the NDI remain unaltered as the substituted imide has no direct connection to the naphthalene rings harbouring the  $\pi$ - electron cloud.<sup>1,35</sup> The core substitution of the NDI provides an opportunity to manipulate the optical properties as the unit(s) is attached directly to the naphthalene ring. The HOMO and LUMO energy levels are finely tuned if the substituent at the core position has electron donating group such as nitrogen, oxygen and sulphur and they core substituted NDIs have wide absorption over the entire visible range and have high quantum yield also.<sup>18</sup> The

phenomenon of self-assembly also serves as a valuable tool for fine tuning of the optoelectronic properties of  $\pi$ -conjugated organic molecules.<sup>36-38</sup>

In the current work, we report a newly synthesized core-substituted NDI which is studied under various solvent systems to investigate its self-assembly behaviour. It is observed that the molecule remains in monomer state in chloroform but starts to aggregate as non-polar hydrocarbon solvents such as n-hexane, n-decane or methyl cyclohexane are added to it. Interestingly, the H-type aggregation is initially observed but finally J-aggregation takes place at higher percentage of the non-polar solvent. Fluorescence spectroscopy shows no significant change in peak position. However, the intensity of fluorescence keeps on decreasing with the aggregation. The aggregation patterns can be explained by the nature of hydrogen bonding in the self-assembly. The extent of hydrogen bonding is understood from the FT-IR studies. The morphological analysis clearly shows different nanostructure formation in J and H aggregated systems. The NDI system is known to act as a semiconductor. We have used several benzene derivatives to make hybrid with the NDI molecule to find significant current gain, keeping the semiconducting nature intact.

## 5.2 Results and Discussion

A peptide-appended, core-substituted NDI **N1** has been synthesized, purified and characterized thoroughly using NMR and MALDI-TOF analysis. Self-assembly of the molecule is studied in the presence of hydrophobic solvents n-hexane, methyl cyclohexane (MCH), n-decane in different ratios with chloroform. The compound remains in monomer state in chloroform. The compound **N1** aggregate *via*  $\pi$ - $\pi$  interaction between the naphthyl rings, inter-molecular hydrogen bonds between the amide groups present in the peptides and Van der Waals interactions between hydrocarbon chains present in the core position of the molecule. This compound is highly fluorescent in the monomeric state. The aggregation process yields non-fluorescent supramolecular assembly.



xylene, dimethyl sulfoxide (DMSO) and methanol, very fine blue shift is observed. The absorbance peaks of **NI** in presence of DMSO are 353 nm, 371 nm, 495 nm, 523 nm. These shifts are negligibly small thus no further studies were done in polar solvents. To observe the gradual change in aggregation upon addition of the hydrocarbon solvents, absorbance values are noted with various ratio of chloroform and n-decane/n-hexane/MCH keeping the concentration of the compound constant for every sample. Aggregation of **NI** is observed starting from 50:50 chloroform: n-hexane. In this solvent ratio blue shift (3 nm) is observed indicating H-aggregation. In 20:80 chloroform: n-hexane it further blue-shifts by 7 nm. Interestingly, at 10:90 chloroform: n-hexane the aggregation pattern changes to “edge-to-edge”. This can be concluded from the fact that the absorbance peak shows at 539 nm (12 nm red shift). Similar observation of initial blue shift and finally red shift at higher percentage of non-polar solvents is found with n-decane and methyl cyclohexane too.

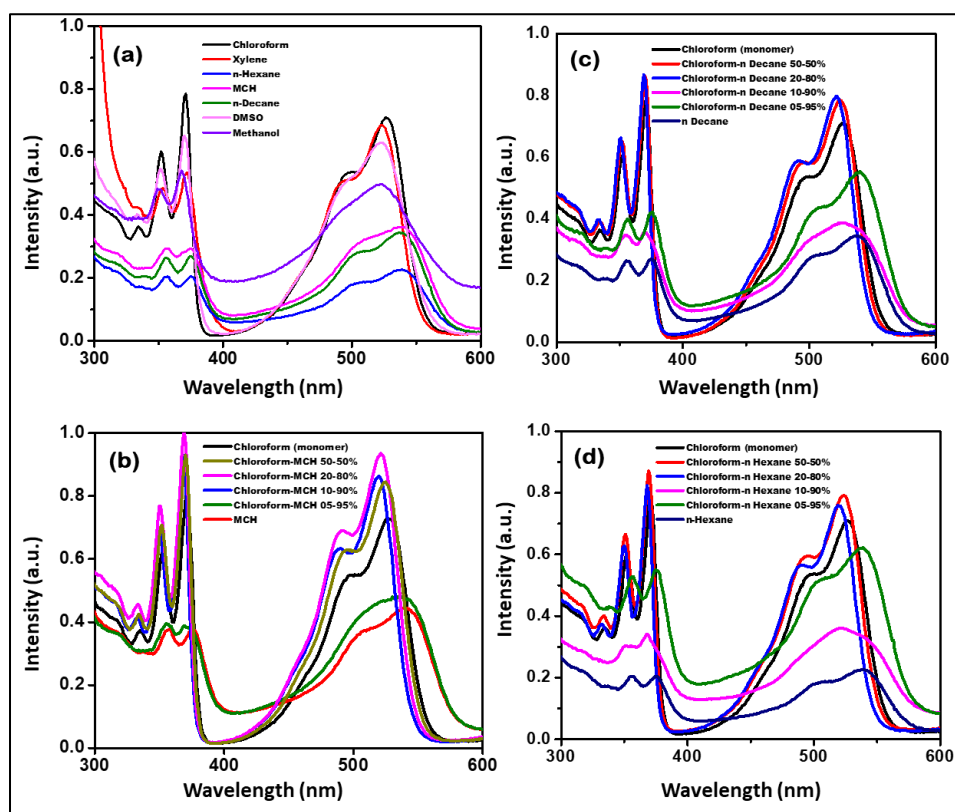


**Figure 5.2** (a) UV-Visible spectra of **NI** in various solvents. UV-visible spectral analysis of **NI** by gradual addition of anti-solvents (b) MCH, (c) n-decane and (d) n-hexane in monomeric solvent chloroform.

## Fluorescence Spectroscopy

Fluorescent spectroscopic studies are conducted to gain further insights of optical properties of **N1** in monomeric and aggregated state in different solutions. This compound shows intense yellow fluorescence in monomeric state (chloroform solution). In the fluorescence spectrum a sharp peak at 560 nm is observed when it is excited at 490 nm. The fluorescence of the monomer appears due to substitution in core position of the naphthyl ring. In the aggregated state (n-hexane/ n-decane/ MCH) the intensity of photoluminescence decreases significantly accompanied by broadening of the peaks. This is caused by aggregation caused quenching (ACQ) phenomena.<sup>40</sup> While systematically increasing the anti-solvent ratio, quenching does not happen until chloroform: n-hexane ratio reaches 10:90. This observation tells us the H-aggregated states are fluorescent and the J-aggregated states of **N1** are non-fluorescent.

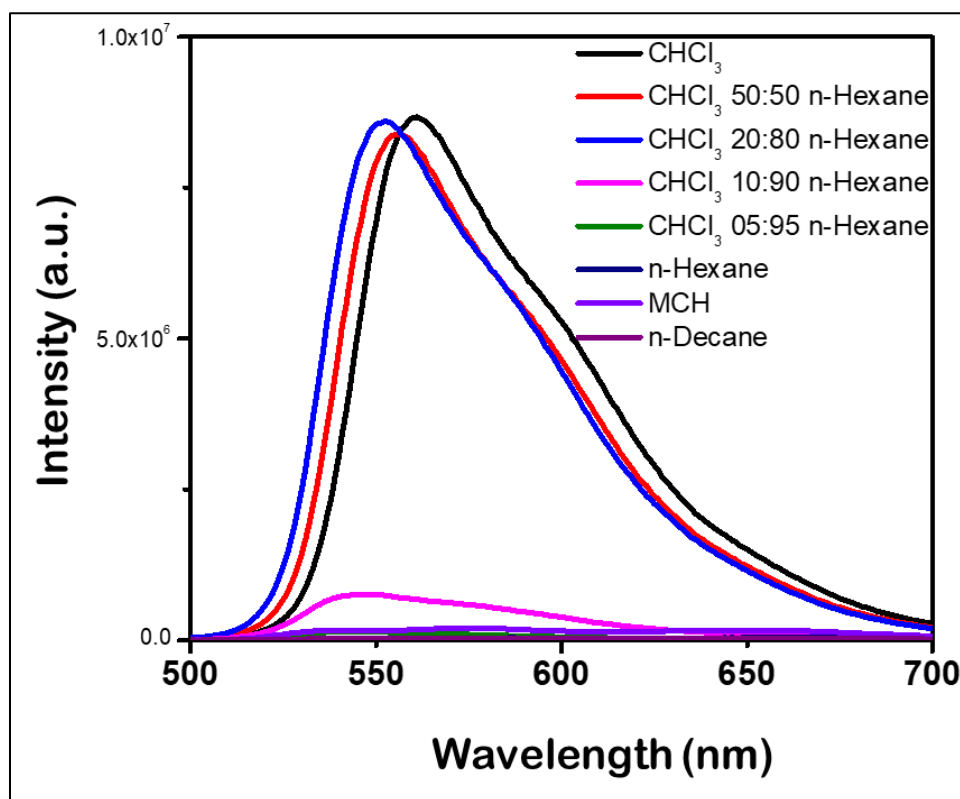


**Figure 5.3** The photoluminescence spectrum of **N1** in chloroform, anti-solvents such as MCH, n-decane, n-hexane and various ratios of chloroform and n-hexane.

### Fourier-Transform Infrared Spectroscopic (FT-IR) Analysis

Fourier-transformed infrared spectroscopy is utilized to analyze the hydrogen bonding between C=O and N-H groups between multiple **N1** molecules in monomer form as well as various aggregated forms. FT-IR analysis is done in solution phase to understand different hydrogen bonding interactions in monomer, H-aggregate and J-aggregated species. 1 mM concentration is maintained throughout all the samples. In chloroform, significant peaks observed in FT-IR are positioned at 3431  $\text{cm}^{-1}$ , 1740  $\text{cm}^{-1}$ , 1638  $\text{cm}^{-1}$ , 1588  $\text{cm}^{-1}$ . These peaks can be assigned to non-hydrogen bonded N-H stretching frequency, C=O stretching of ester group, C=O stretching of amide group and N-H bending respectively. The non-hydrogen bonded N-H stretching is expected as the molecules are non-aggregated and entrapped inside solvent cage. When 30-70% chloroform to n-hexane solvent is used, spectroscopic analysis suggests a H-type aggregation pattern. In the solution phase FT-IR studies, the prominent peaks are 3432  $\text{cm}^{-1}$ , 3312  $\text{cm}^{-1}$ , 1743  $\text{cm}^{-1}$ , 1640  $\text{cm}^{-1}$ , 1590  $\text{cm}^{-1}$ . These peaks can be attributed to non-hydrogen bonded N-H stretching, hydrogen-bonded N-H stretching, ester C=O stretching, amide C=O stretching and N-H bending respectively. In this form, most of the amide N-H groups cannot take part in hydrogen bonding but few hydrogen bonds are formed nevertheless. The face-to-face arrangement in H-aggregation hinders proper alignment of N-H...C=O hydrogen bonds. The FT-IR results tell us, H-aggregation happens *via*  $\pi$ - $\pi$  interactions and weakly H-bonded network. Finally, the analysis of aggregate found in 5:95% chloroform to n-hexane shows peaks at positions 3304  $\text{cm}^{-1}$ , 1740  $\text{cm}^{-1}$ , 1638  $\text{cm}^{-1}$  and 1585  $\text{cm}^{-1}$ . They can be attributed to strongly H-bonded N-H stretching, C=O stretching of ester linkage, C=O stretching of amide linkage and N-H bending of amide respectively. Absence of non-hydrogen bonded amide N-H stretching and presence of strongly hydrogen-bonded N-H at 3304  $\text{cm}^{-1}$  confirm strong N-H...C=O hydrogen bonds between amide groups present in the peptide chain present in NDI imide position. To form strong alignments, the naphthyl groups arrange themselves in slipped stacked manner. This gives rise to J-type aggregation which is confirmed in the absorbance spectroscopy.

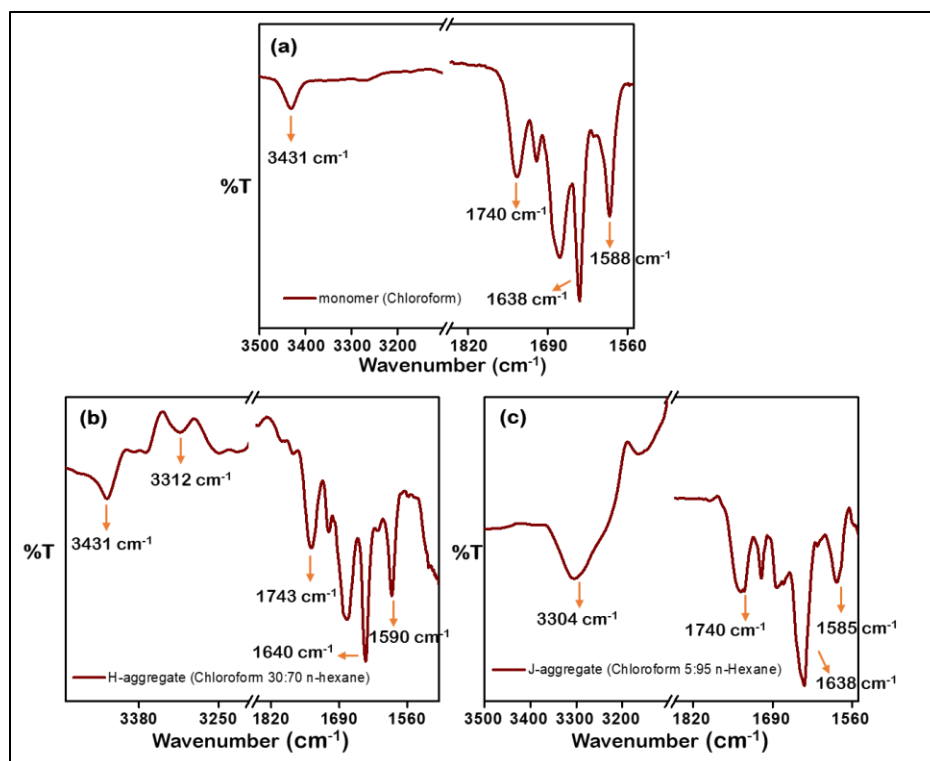


**Figure 5.4** Solution phase FT-IR spectra of **N1** in (a) chloroform (monomer form), (b) chloroform 30:70 *n*-hexane (H-aggregated form) and (c) chloroform 5:95 *n*-hexane (J-aggregated form).

## Morphology

In order to investigate the nanostructure of different aggregated state of **N1** microscopic imaging is done using high resolution transmission electron microscope (HR-TEM). 0.05 mM solution of **N1** in 30:70% chloroform: *n*-hexane is used to observe microstructure in H-aggregate and 0.05 mM solution of **N1** in *n*-Hexane is considered for imaging of the J-aggregate. Images from HR-TEM shows, the H-aggregate forms rigid nanorod structures which have a width of  $20 \pm 3$  nm. Length of the nanorods varies widely. The longest measurable nanorod is 1  $\mu\text{m}$  long. It should be noted that the nanorods remain individually without connecting to each other. The J-aggregate is observed to form network formation through twisted nanofibers having width of  $27 \pm 3$  nm. Although the J-aggregate do not form gel, an extended matrix formation is observed under HR-TEM.

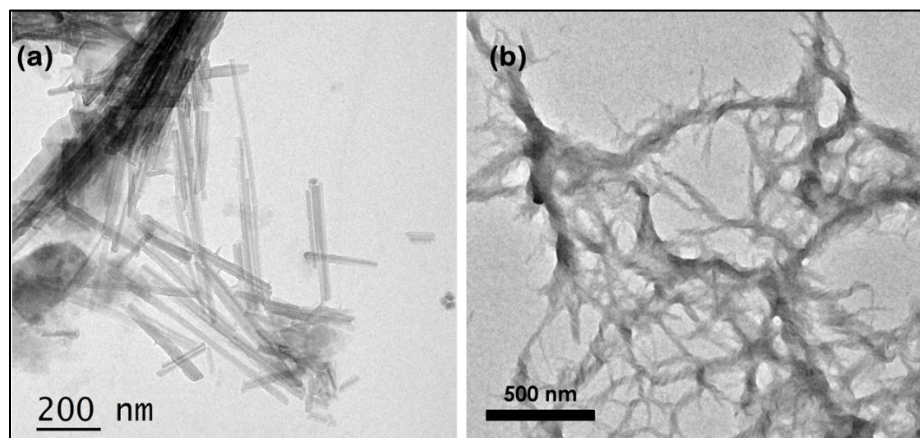


**Figure 5.5** High Resolution Transmission Electron Microscopic images of **N1** (a) in 70:30 *n*-Hexane:Chloroform aggregated as nanorods. In this solvent ratio **N1** shows *H* aggregation. (b) **N1** in *n*-Hexane aggregates as interconnecting twisted nanofibers. In this solvent system **N1** shows *J* aggregation.

### Current-voltage (I-V) studies

In order to investigate the electronic output of the core-substituted NDI molecule **N1** we obtain current output as voltage is varied from -5 to 5V. The samples are prepared using sandwich method. In this method the compound is drop-cast on indium-tin oxide coated glass (ITO glass) and covered with another ITO glass. The circuit is completed from one ITO glass slide to another with the test compound in between them. Pure **N1** characteristic Schottky diode like I-V curve with  $0.6 \times 10^{-7}$  A current response at 5V (Figure 5.6a). In order to tune that current response, we prepared several  $\pi$ -hybrid systems using simple aromatic compounds and **N1**. We have used three sets of benzene derivatives for the experiment. The 1<sup>st</sup> class contain benzene derivatives with electron withdrawing groups, the 2<sup>nd</sup> class is belonged to derivatives having both electron withdrawing and donating groups and the 3<sup>rd</sup> class consists of derivatives attached solely to electron donating groups. Thus, clearly  $\pi$ -electron density of these three classes follows the pattern, 3<sup>rd</sup> class > 2<sup>nd</sup> class > 1<sup>st</sup> class. All the hybrid systems are formed in 2:1 molar ratio of **N1** to benzene derivatives. The first hybrid system of **N1** and 3,5-dinitrobenzoic acid, the current response at 5 V is  $0.4 \times 10^{-7}$  A (Figure 5.6b) which is in comparable scale to **N1** aggregate. When 4-nitrotoluene and 4-nitrophenol are added to **N1**, the current increases moderately to  $0.5 \times 10^{-5}$  A and  $0.7 \times 10^{-5}$  A respectively (Figure 5.6c, d).



Thus, the 2<sup>nd</sup> class of additives increase the current response 100 times. Finally, addition of aniline and anisole to increase the current response at 5V to  $0.25 \times 10^{-4}$  A and  $0.3 \times 10^{-4}$  A. NDI and PBI chromophores are known to show semiconducting properties due to their  $\pi$ -electrons. The benzene derivatives added to the aggregation of **N1** are helping in enriching the electron density when electron donating substitution are made in it. The enhancement of current happens due to true  $\pi$ - $\pi$  interactions between the NDI core and the benzene core and the nanofibrous network of the aggregate helps the mobility of the generated electron-hole systems.

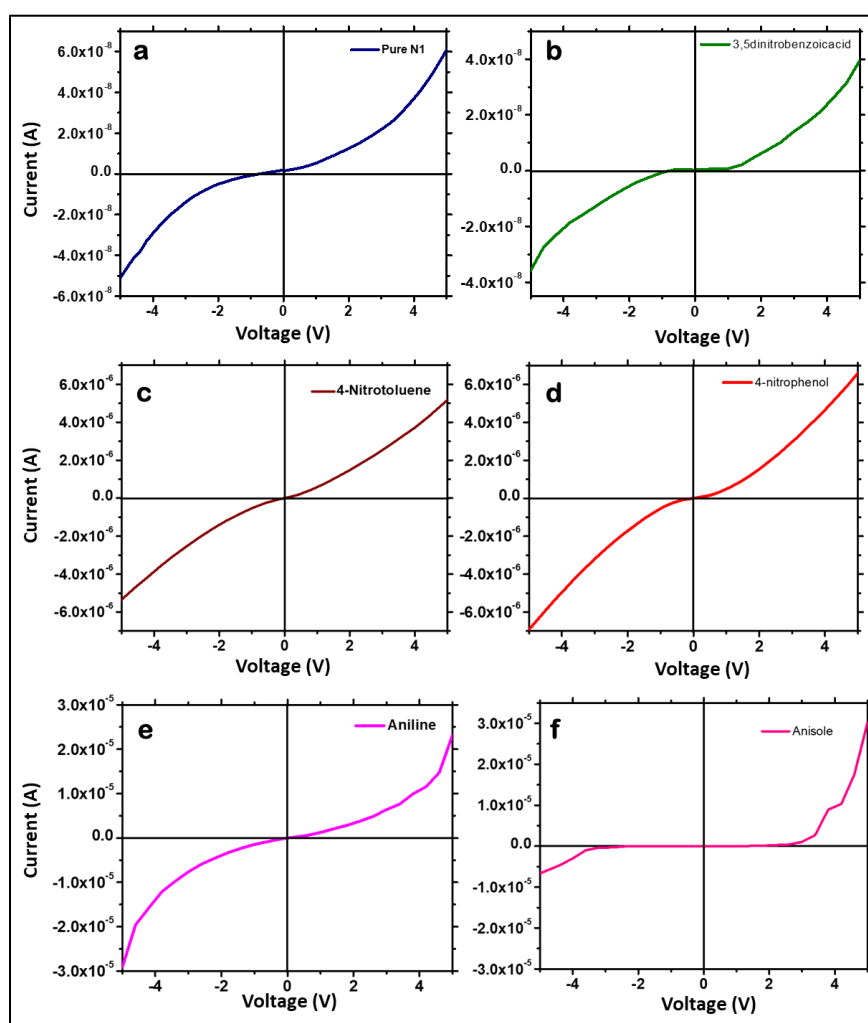


**Figure 5.6** Current-voltage plots of (a) aggregated **N1** only, (b) **N1** with electron deficient  $\pi$  system 3,5-dinitrobenzoic acid. **N1** with  $\pi$  system having both electron donor and acceptor groups demonstrates moderate current improvement shown in (c) with 4-nitrotoluene and (d) 4-nitrophenol. (e) **N1** with aniline and (f) **N1** with anisole shows high current enhancement in presence of electron rich  $\pi$  systems.

### 5.3 Conclusion

This is a unique study where both J and H types of aggregation are observed in same set of solvent system. The aggregation pattern is not only observed in optical spectroscopy but also in morphological analysis and FT-IR spectroscopic studies. The aggregation can be controlled by controlling the ratio of monomeric solvent and the anti-solvent. The primary H-aggregated state forms rigid nanorod structures but as the amount of anti-solvent increases the J-aggregation takes place which forms an extended network of nanofibers. The FT-IR studies help to conclude the strongly hydrogen-bonded amide group of imide chain of the NDI molecule **N1** arranges the molecules in slipped-stacked manner. Thus, a J-aggregated self-assembly is caused by stronger hydrogen bonding. The semiconducting nature is observed in I-V study with pure **N1**. In order to tune that current response, we prepared several  $\pi$ -hybrid systems using simple aromatic compounds and **N1**. It can be concluded that benzene derivatives with electron rich  $\pi$ -system helped in increasing the current response significantly.

### 5.4 Experimental section

#### Synthetic procedure:

**Synthesis of Boc-11-aminoundecanoic acid (Boc-AUDA-COOH):** 2.01g (10 mmol) of 11-aminoundecanoic acid (AUDA) was taken in a 250 ml round bottom flask. 10 ml 1(N) NaOH and 20 ml dioxane was added to it and cooled to 0°C. 2.20 g (10.1mmol) di-tert-butyl dicarbonate (Boc anhydride) was added to the reaction mixture and stirred for 8 hours at room temperature. Then dioxane was removed by reduced pressure. The resulting mixture was acidified with saturated KHSO<sub>4</sub> solution and the aqueous layer was extracted with ethyl acetate (3 x 50 mL). The ethyl acetate extract was dried over anhydrous sodium sulfate and evaporated in vacuum to obtain the colorless sticky product. Yield: 2.85g (9.5 mmol, 95%)

**Synthesis of Boc-AUDA-Phe-OMe :** 2.85 g (9.5 mmol) of Boc-AUDA-OH was dissolved in 10ml dry N,N-dimethyl formamide (DMF) and cooled in an ice bath. H<sub>2</sub>N-Phe-OMe (15mmol) was obtained by neutralization with saturated Na<sub>2</sub>CO<sub>3</sub> from its hydrochloride salt and subsequent extraction with ethyl acetate. The ethyl

acetate solution was then concentrated to 20 ml and added to the DMF solution followed by 1.35 g (10 mmol) of 1-hydroxy benzotriazole (HOBt) and 2.06 g (10 mmol) of N,N dicyclohexylcarbodiimide (DCC). The reaction mixture was allowed to come at room temperature and stirred for 24 hr. The reaction mixture was diluted with ethyl acetate and filtered to separate N,N- dicyclohexyl urea (DCU). The ethyl acetate layer was washed with brine (2 × 30 ml). The organic layer was dried over anhydrous sodium sulfate and evaporated to obtain the yellowish product. The product was purified through silica gel column chromatography using ethyl acetate: n-hexane (10-90) as eluent to obtain the pure product.

Yield: 3.24 g (7 mmol, 73.6 %).

$^1\text{H}$  NMR (500 MHz,  $\text{CDCl}_3$ , 25 °C):  $\delta$  7.08-7.29 (5H, m, aromatic proton), 5.85-5.87 (2H, d, NH), 4.88-4.92 (1H, m,  $\alpha$ -CH of Phe), 4.49 (1H, br, NH), 3.73 (3H, s, -OMe), 3.07-3.17 (4H, m,  $\beta$ -CH<sub>2</sub> of Phe and  $\alpha$ -CH<sub>2</sub> of AUDA), 2.15-2.18 (2H, t,  $J=7.5$  Hz), 1.44-1.64 (25H, m).  $^{13}\text{C}$  NMR (125 MHz,  $\text{CDCl}_3$ , 25 °C):  $\delta$  172.80, 136.08, 129.42, 128.71, 127.27, 53.07, 52.44, 38.11, 36.72, 30.23, 29.61, 29.49, 29.41, 29.31, 28.60, 26.93, 25.67. HRMS (m/z): Calculated for  $\text{C}_{26}\text{H}_{42}\text{N}_2\text{O}_5$  462.62. Found: 463.45 (M+H)<sup>+</sup>, 485.42 (M+Na)<sup>+</sup>. (Figure 5.7-5.9)

**Synthesis of H<sub>2</sub>N-AUDA-Phe-OMe:** To 2.31 g (5 mmol) of Boc-AUDA-Phe-OMe, 5 ml of 98% formic acid was added and the removal of the Boc group was monitored by TLC. After 6 h, formic acid was removed under vacuum. The residue was taken in water (8 ml) and pH of the aqueous solution was then adjusted to 8.0 with 30% aqueous NH<sub>3</sub>. The aqueous portion was evaporated under vacuum. A white material was obtained, purified using basic alumina in and methanol chloroform (1:9) as eluent.

Yield: 1.70 g (4.7 mmol, 94%).

$^1\text{H}$  NMR (500 MHz,  $(\text{CD}_3)_2\text{SO}$ , 25 °C):  $\delta$  7.97-7.99 (1H, d, NH), 7.13-7.28 (5H, m, aromatic proton), 5.57-5.59 (1H, m,  $\alpha$ -CH of Phe), 4.06 (2H, br, NH<sub>2</sub>), 3.59 (3H, s, -OMe), 2.84-3.04 (4H, m,  $\beta$ -CH<sub>2</sub> of Phe and  $\alpha$ -CH<sub>2</sub> of AUDA), 2.01-2.04 (2H, t,  $J=7.5$  Hz), 1.19-1.59 (16H, m, CH<sub>2</sub> of AUDA).  $^{13}\text{C}$  NMR ( $(\text{CD}_3)_2\text{SO}$ , 25 °C):  $\delta$  172.21, 172.17, 171.85, 171.13, 170.92, 156.57, 137.99, 137.29, 129.38, 129.04, 128.95, 128.09, 127.84, 126.38, 126.03, 79.12, 53.80, S6 53.29, 51.69, 48.54, 47.46, 36.62, 35.13, 34.91, 33.29, 31.77, 28.91, 28.83, 28.75,

28.71, 28.59, 28.42, 28.38, 26.24, 25.27, 25.14, 25.07, 24.40. HRMS (m/z): Calculated for C<sub>21</sub>H<sub>34</sub>N<sub>2</sub>O<sub>3</sub> 362.25. Found: 363.12 (M+H)<sup>+</sup>. (Figure 5.10-5.12)

**Synthesis of 2-bromo, N, N'(AUDA-Phe-OMe)-naphthalenediimide (Br-NDI):** Br1NDA (5mmol) and 20 ml acetic acid was taken in a 100ml round bottom flask. To the mixture 20 mmol H<sub>2</sub>N-AUDA-Phe-OMe was added and the reaction mixture was stirred at 120°C under nitrogen atmosphere. After cool down to room temperature the reaction mixture was poured into the ice water. The precipitate was filtered and dried to obtained orange solid. It was purified by column chromatography using n-hexane: ethyl acetate (98:2) as eluent.

Yield: 1.63 g (2.15 mmol, 43%).

<sup>1</sup>H NMR (500 MHz, CDCl<sub>3</sub>, 25 °C): δ 8.99 (2H, s, naphthyl proton), 7.07-7.29 (10H, m, H of Phe), 5.82-5.84 (2H, d, NH), 4.89-4.91 (2H, m, α-CH of Phe), 4.17-4.20 (4H, t, J=8Hz), 3.73 (6H, s, -OMe), 3.09-3.14 (4H, m, β-CH<sub>2</sub> of Phe), 2.146-2.177 (2H, m), 1.27-1.75 (32H, m aliphatic proton) <sup>13</sup>C NMR(125 MHz, (CDCl<sub>3</sub>, 25 °C): δ 172.76, 172.34, 160.93, 139.23, 136.08, 129.42, 128.71, 128.48, 127.27, 125.55, 124.30, 53.06, 52.44, 41.76, 38.12, 36.72, 29.57, 29.49, 29.40, 29.32, 28.06, 27.21, 25.68. MALDI-TOF MS (m/z): Calculated for C<sub>56</sub>H<sub>67</sub>BrN<sub>4</sub>O<sub>10</sub> 1036.40. Found: 1037.553 (M+H)<sup>+</sup>. (Figure 5.13-5.15)

**Synthesis of N1:** Dodecyl amine (66 mg, 0.36 mmol) and 2-bromo, N,N'(AUDA-Phe-OMe)- naphthalenediimide (200 mg, 0.19 mmol) were placed in a round-bottomed flask along with dry DMF (15 ml) and the reaction mixture was stirred for 12 h at 120 °C under N<sub>2</sub> atmosphere. The heating was stopped and the solution was allowed to cool to room temperature and added 50 ml diethyl ether and placed in the refrigerator for 30 min. red product came out as precipitate, which was filtered. The product was further purified by column chromatography using silica gel as stationary phase and ethyl acetate- n-hexane (1:9) as eluent.

Yield: 282 mg (0.25 mmol, 82%).

<sup>1</sup>H NMR (400 MHz, CDCl<sub>3</sub>, 25 °C): δ 10.10-10.13 (1H, t, NH attached with NDI), 8.64-8.57 (1H, d, NDI proton), 8.32-8.34 (1H, d, NDI proton), 8.21 (1H, s, NDI proton), 7.07-7.29 (5H, m, C-H of phe), 5.84-5.86 (2H, d, NH), 4.87- 4.92 (1H, m, α-CH of Phe), 4.13-4.20 (4H, t, J=8Hz), 3.72 (3H, s, -OMe), 3.54- 3.59 (2H, m, α-

CH of AUDA), 3.06-3.18 (4H, m,  $\beta$ -CH<sub>2</sub> of Phe), 2.15-2.19 (2H, t, J=8Hz), 1.25-1.82 (56H, m, chain proton), 0.85-0.89 (3H, t, J=6.8Hz). <sup>13</sup>C NMR (100 MHz, (CDCl<sub>3</sub>, 25 °C):  $\delta$  172.73, 172.34, 166.43, 163.56, 163.23, 163.21, 152.57, 136.07, 131.45, 129.74, 129.41, 128.69, 128.17, 127.25, 126.38, 124.58, 123.81, 119.99, 119.60, 100.04, 53.06, 52.42, 43.51, 41.07, 40.58, 38.11, 36.69, 32.06, 29.77, 29.74, 29.64, 29.58, 29.56, 29.52, 29.48, 29.43, 29.33, 28.24, 27.37, 27.25, 25.65, 22.82, 14.24. MALDI-TOF MS (m/z): Calculated for C<sub>58</sub>H<sub>93</sub>N<sub>5</sub>O<sub>10</sub> 1140.70; observed 1163.345 [M+Na]<sup>+</sup>, 1196.880 [M+2Na]<sup>+</sup>. (Figure 5.16-5.18)

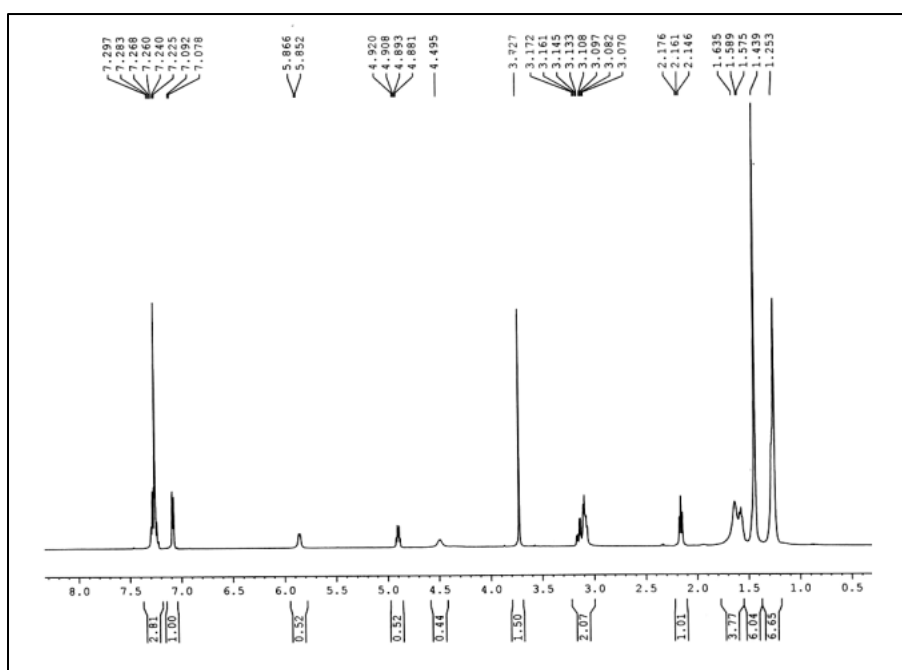


Figure 5.7 500 MHz <sup>1</sup>H NMR spectrum of Boc-AUDA-Phe-OMe

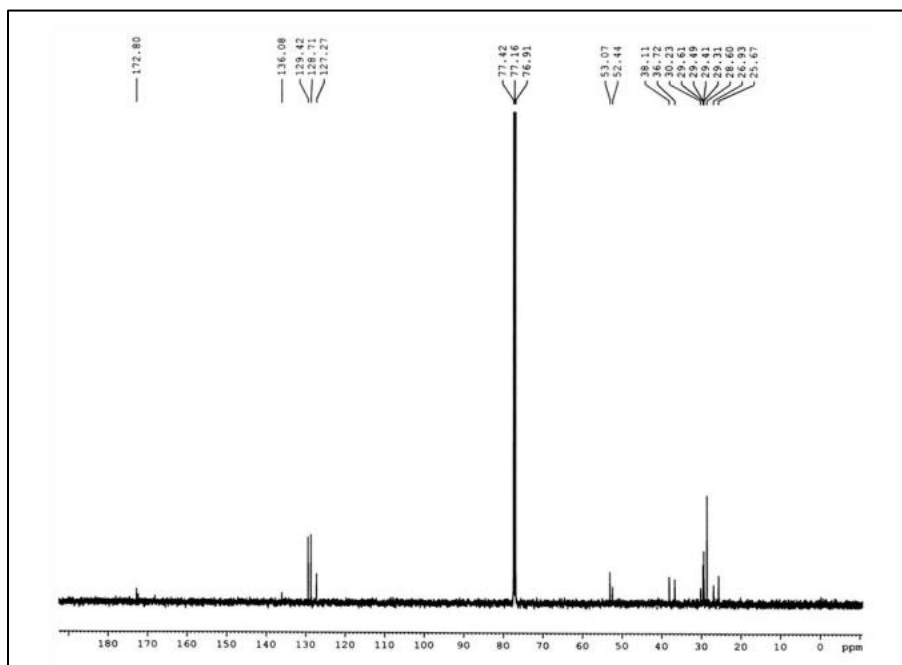


Figure 5.8 125 MHz  $^{13}\text{C}$  NMR spectrum of Boc-AUDA-Phe-OMe

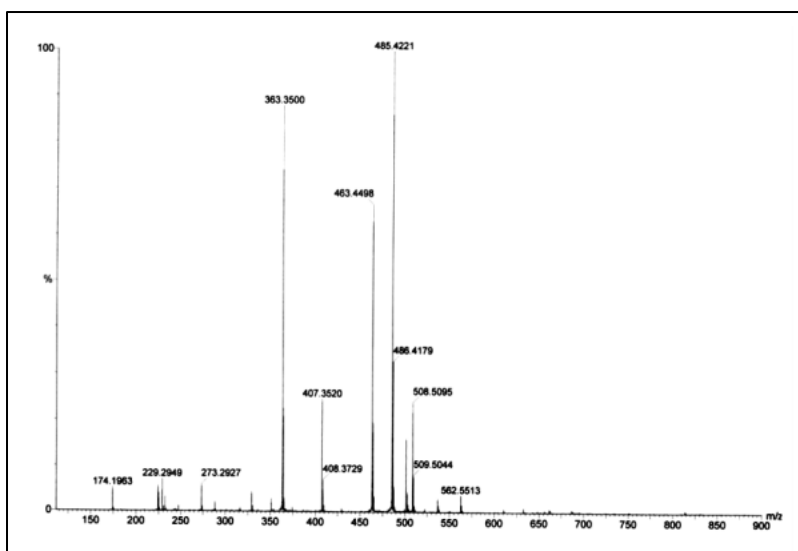


Figure 5.9 HRMS data for Boc-AUDA-Phe-OMe

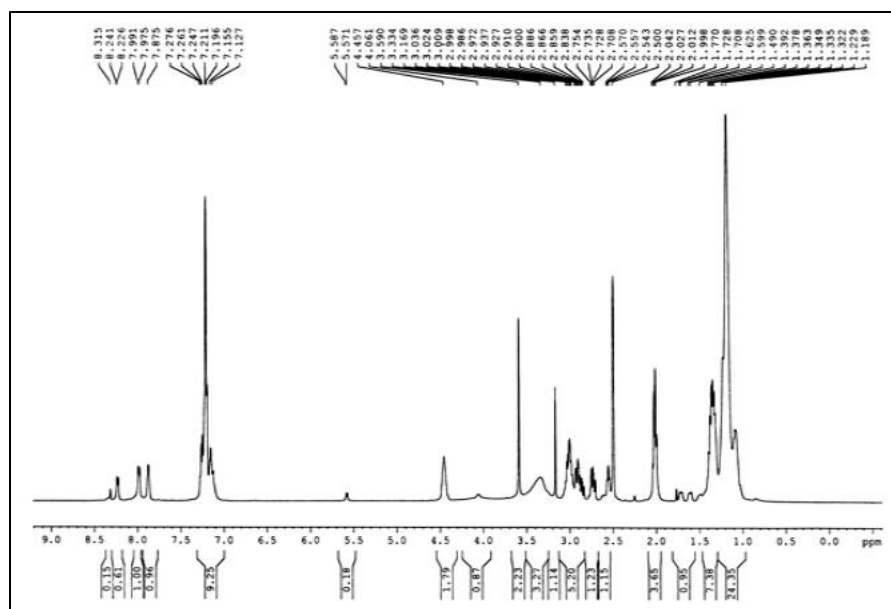


Figure 5.10 500 MHz  $^1\text{H}$  NMR spectrum of  $\text{H}_2\text{N-AUDA-Phe-OMe}$

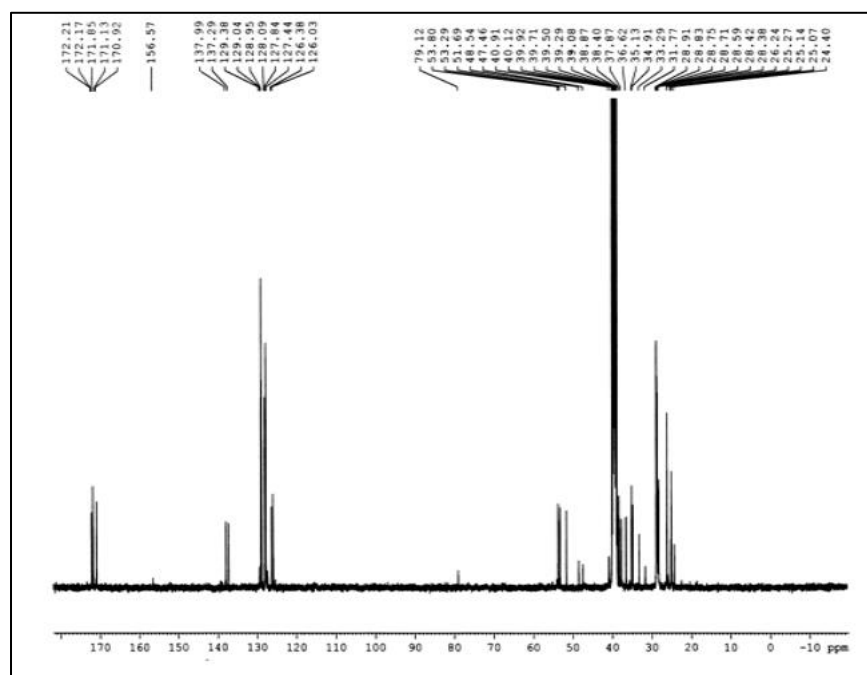


Figure 5.11 125 MHz  $^{13}\text{C}$  NMR spectrum of  $\text{H}_2\text{N-AUDA-Phe-OMe}$





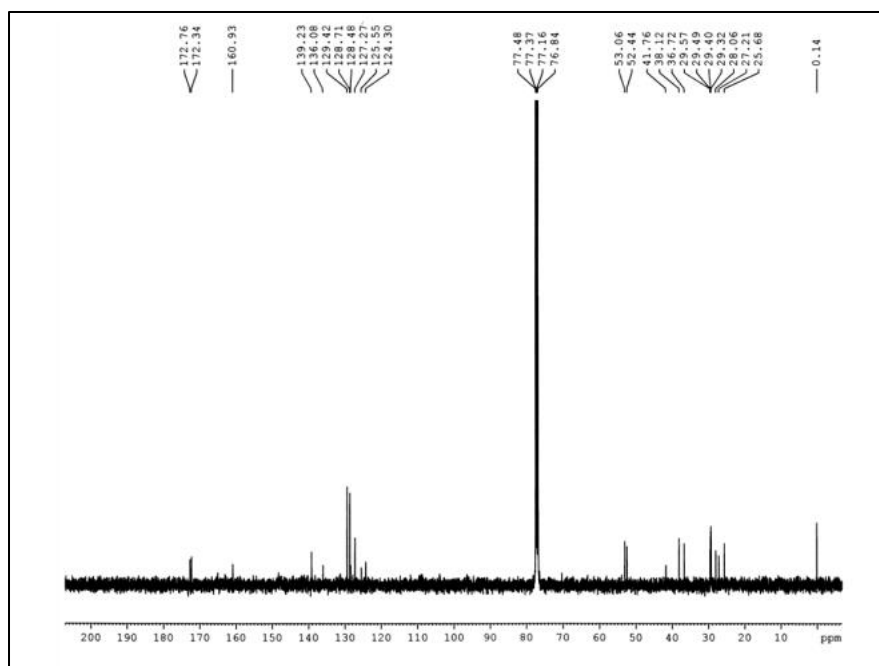


Figure 5.14 125 MHz  $^{13}\text{C}$  NMR spectrum of Br-NDI

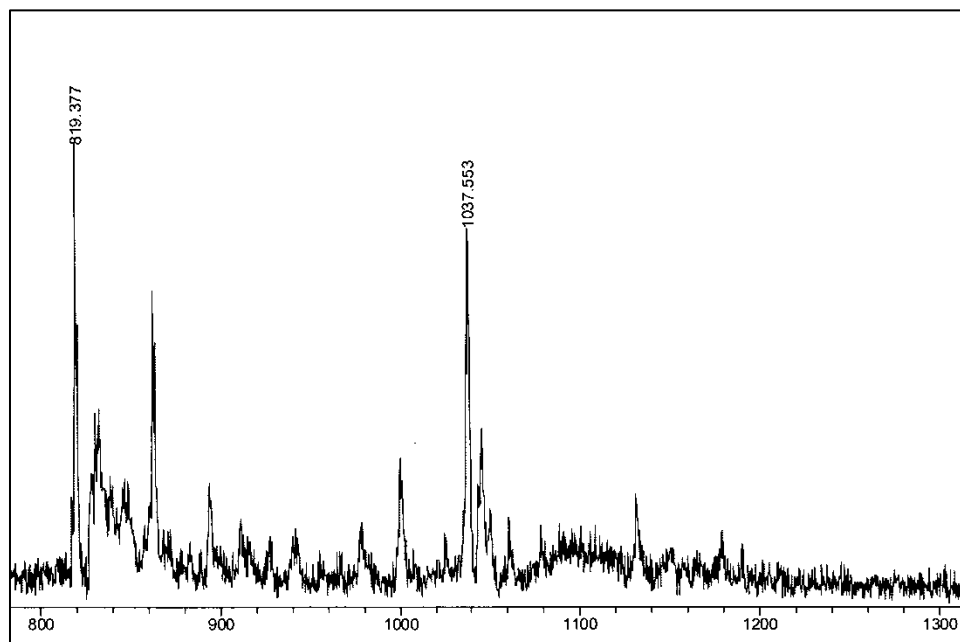


Figure 5.15 MALDI-TOF MS spectrum of Br-NDI

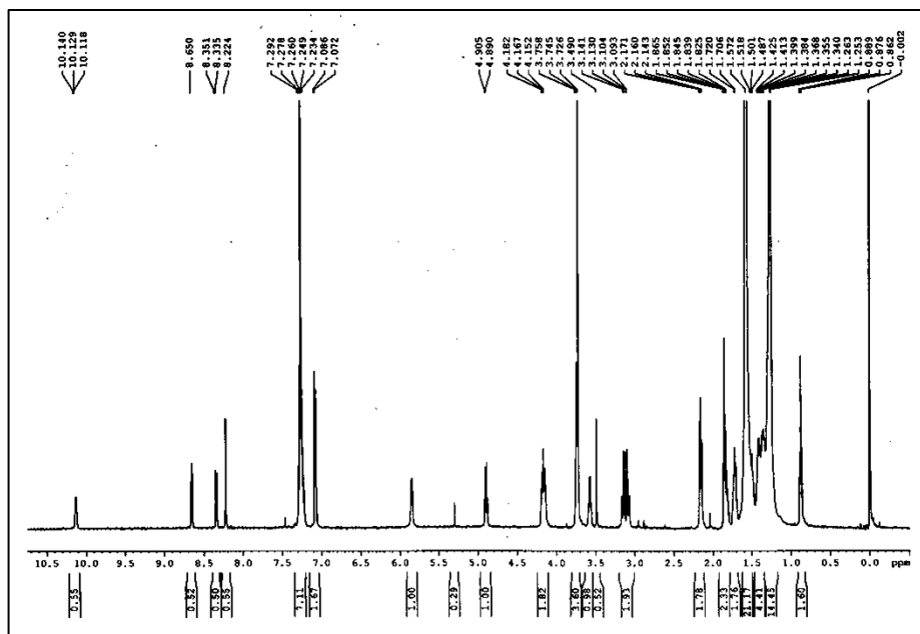


Figure 5.16 400 MHz  $^1\text{H}$  NMR spectrum of NI

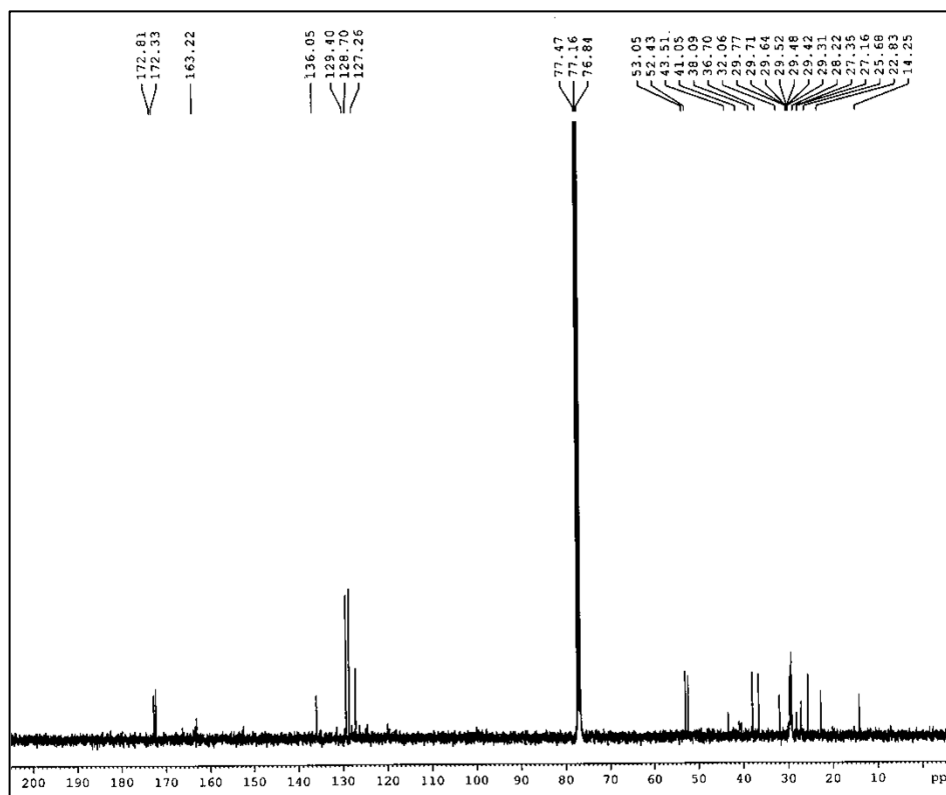


Figure 5.17 100 MHz  $^{13}\text{C}$  NMR spectrum of NI

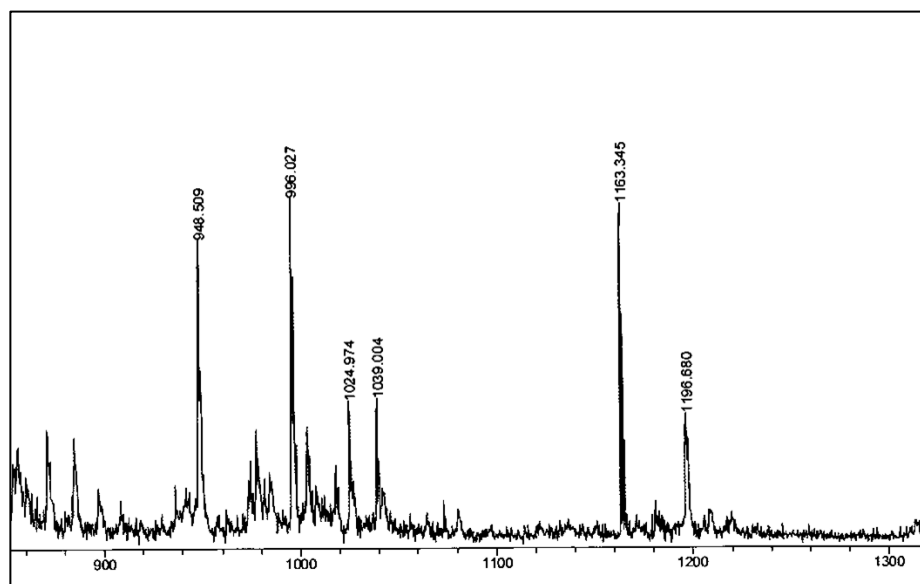


Figure 5.18 MALDI-TOF MS spectrum of N1

## 5.5 References

1. S.-L. Suraru and F. Würthner, *Angew. Chem. Int. Ed Engl.*, 2014, **53**, 7428–7448.
2. M. A. Kobaisi, S. V. Bhosale, K. Latham, A. M. Raynor and S. V. Bhosale, *Chem. Rev.*, 2016, **116**, 11685–11796.
3. M. C. Nolan, J. J. Walsh, L. L. E. Mears, E. R. Draper, M. Wallace, M. Barrow, B. Dietrich, S. M. King, A. J. Cowan and D. J. Adams, *J. Mater. Chem. A Mater.*, 2017, **5**, 7555–7563.
4. S. Maniam, H. F. Higginbotham, T. D. M. Bell and S. J. Langford, *Chem. Eur. J.*, 2019, **25**, 7044–7057.
5. S. S. Babu, V. K. Praveen and A. Ajayaghosh, *Chem. Rev.*, 2014, **114**, 1973–2129.

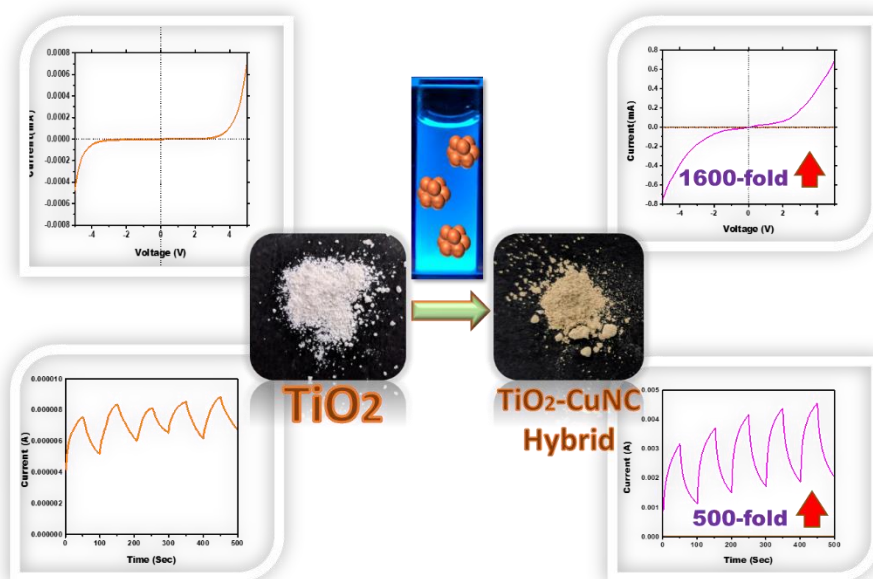
6. K. Rundel, S. Maniam, K. Deshmukh, E. Gann, S. K. K. Prasad, J. M. Hodgkiss, S. J. Langford and C. R. McNeill, *J. Mater. Chem. A Mater.*, 2017, **5**, 12266–12277.
7. S. W. Kim, Y. Wang, H. You, W. Lee, T. Michinobu and B. J. Kim, *ACS Appl. Mater. Interfaces*, 2019, **11**, 35896–35903.
8. Y. Liu, L. Zhang, H. Lee, H.-W. Wang, A. Santala, F. Liu, Y. Diao, A. L. Briseno and T. P. Russell, *Adv. Energy Mater.*, 2015, **5**, 1500195.
9. Y. Qin, G. Li, T. Qi and H. Huang, *Mater. Chem. Front.*, 2020, **4**, 1554–1568.
10. Q. Song, F. Li, Z. Wang and X. Zhang, *Chem. Sci.*, 2015, **6**, 3342–3346.
11. T. Jiao, K. Cai, J. N. Nelson, Y. Jiao, Y. Qiu, G. Wu, J. Zhou, C. Cheng, D. Shen, Y. Feng, Z. Liu, M. R. Wasielewski, J. F. Stoddart and H. Li, *J. Am. Chem. Soc.*, 2019, **141**, 16915–16922.
12. K. Gayen, K. Basu, N. Nandi, K. S. Das, D. Hermida-Merino, I. W. Hamley and A. Banerjee, *ChemPlusChem*, 2019, **84**, 1673–1680.
13. N. Singha, P. Gupta, B. Pramanik, S. Ahmed, A. Dasgupta, A. Ukil and D. Das, *Biomacromolecules*, 2017, **18**, 3630–3641.
14. Y. L. Wu, K. E. Brown, D. M. Gardner, S. M. Dyar and M. R. Wasielewski, *J. Am. Chem. Soc.*, 2015, **137**, 3981–3990.
15. A. Sarkar, S. Dhiman, A. Chalishazar and S. J. George, *Angew. Chem. Int. Ed Engl.*, 2017, **56**, 13767–13771.
16. Y. Hu, Z. Wang, X. Zhang, X. Yang, C. Ge, L. Fu and X. Gao, *Org. Lett.*, 2017, **19**, 468–471.

17. Z. Yuan, Y. Ma, T. Geßner, M. Li, L. Chen, M. Eustachi, R. T. Weitz, C. Li and K. Müllen, *Org. Lett.*, 2016, **18**, 456–459.
18. N. Sakai, J. Mareda, E. Vauthey and S. Matile, *Chem. Commun.*, 2010, **46**, 4225–4237.
19. T. Choisnet, D. Canevet, M. Sallé, E. Nicol, F. Niepceron, J. Jestin and O. Colombani, *Chem. Commun.*, 2019, **55**, 9519–9522.
20. K. Liu, Y. Yao, Y. Liu, C. Wang, Z. Li and X. Zhang, *Langmuir*, 2012, **28**, 10697–10702.
21. N. Nandi, S. Basak, S. Kirkham, I. W. Hamley and A. Banerjee, *Langmuir*, 2016, **32**, 13226–13233.
22. S. Basak, N. Nandi, S. Paul and A. Banerjee, *ACS Omega*, 2018, **3**, 2174–2182.
23. N. Ponnuswamy, G. D. Pantoş, M. M. J. Smulders and J. K. M. Sanders, *J. Am. Chem. Soc.*, 2012, **134**, 566–573.
24. H. A. M. Ardoña, E. R. Draper, F. Citossi, M. Wallace, L. C. Serpell, D. J. Adams and J. D. Tovar, *J. Am. Chem. Soc.*, 2017, **139**, 8685–8692.
25. Y. Wang, Y. Jiang, X. Zhu and M. Liu, *J. Phys. Chem. Lett.*, 2019, **10**, 5861–5867.
26. V. Castelletto, C. J. C. Edwards-Gayle, I. W. Hamley, G. Barrett, J. Seitsonen and J. Ruokolainen, *ACS Appl. Mater. Interfaces*, 2019, **11**, 9893–9903.
27. S. Kralj, O. Bellotto, E. Parisi, A. M. Garcia, D. Iglesias, S. Semeraro, C. Deganutti, P. D'Andrea, A. V. Vargiu, S. Geremia, R. De Zorzi and S. Marchesan, *ACS Nano*, 2020, **14**, 16951–16961.

28. K. Nagy-Smith, P. J. Beltramo, E. Moore, R. Tycko, E. M. Furst and J. P. Schneider, *ACS Cent. Sci.*, 2017, **3**, 586–597.
29. S. P. Goskulwad, V. G. More, M. A. Kobaisi, R. S. Bhosale, D. D. La, F. Antolasic, S. V. Bhosale and S. V. Bhosale, *ChemistrySelect*, 2019, **4**, 2626–2633.
30. E. R. Draper, B. J. Greeves, M. Barrow, R. Schweins, M. A. Zwijnenburg and D. J. Adams, *Chem. Eur. J.*, 2017, **2**, 716–731.
31. L. Cui, Y. Jiao, A. Wang, L. Zhao, Q. Dong, X. Yan and S. Bai, *Chem. Commun.*, 2018, **54**, 2208–2211.
32. M. Zangoli, M. Gazzano, F. Monti, L. Maini, D. Gentili, A. Liscio, A. Zanelli, E. Salatelli, G. Gigli, M. Baroncini and F. Di Maria, *ACS Appl. Mater. Interfaces*, 2019, **11**, 16864–16871.
33. K. Basu, B. Mondal, A. Das Mahapatra, N. Nandi, D. Basak and A. Banerjee, *J. Phys. Chem. C*, 2019, **123**, 20558–20566.
34. P. Rani, A. Husain, A. Shukla, N. Singla, A. K. Srivastava, G. Kumar, K. K. Bhasin and G. Kumar, *CrystEngComm*, 2021, **23**, 1859–1869.
35. S. Guha, F. S. Goodson, S. Roy, L. J. Corson, C. A. Gravenmier and S. Saha, *J. Am. Chem. Soc.*, 2011, **133**, 15256–15259.
36. F. S. Etheridge, R. Fernando, J. A. Golen, A. L. Rheingold and G. Sauve, *RSC Adv.*, 2015, **5**, 46534–46539.
37. J. R. Mulder, C. F. Guerra, J. C. Slootweg, K. Lammertsma and F. M. Bickelhaupt, *J. Comput. Chem.*, 2016, **37**, 304–313.
38. C. J. C. Edwards-Gayle, V. Castelletto, I. W. Hamley, G. Barrett, F. Greco, D. Hermida-Merino, R. P. Rambo, J. Seitsonen and J. Ruokolainen, *ACS Appl. Bio Mater.*, 2019, **2**, 2208–2218.
39. H. Kar, D. W. Gehrig, N. K. Allampally, G. Fernández, F. Laquai and S. Ghosh, *Chem. Sci.*, 2016, **7**, 1115–1120.
40. P. Li, D. Zhang, Y. Zhang, W. Lu, J. Zhang, W. Wang, Q. He, P. Théato and T. Chen, *ACS Macro Lett.*, 2019, **8**, 937–942.
41. K. Gayen, S. Paul, S. Hazra and A. Banerjee, *Langmuir*, 2021, **37**, 9577–9587.

## CHAPTER 6

# A Nanohybrid Containing Cyan-Emitting Copper Nanoclusters and TiO<sub>2</sub> Nanoparticles: Tuning of Optoelectronic Properties







## 6.1 Introduction

Few-atom fluorescent metal nanoclusters have gained considerable attention in the field of nano-research for their structural novelty and functional diversity.<sup>1-8</sup> Metal nanoclusters fill the void between few hundred atom nanoscale materials and individual atoms. They show novel optical, electronic and magnetic properties different than larger nanoparticles (NP). NPs can be differentiated from nanoclusters (NC) by their surface plasmon resonance (SPR) that spans from ultraviolet (UV) to near infrared (NIR) region of absorbance spectra.<sup>3</sup> The metal nanoclusters show discrete energy levels due to quantum confinement effect of small number of metal atoms present in the core of the NCs, much like individual atoms thus they show molecular electronic transition in the conduction level.<sup>6</sup> Novel Metal NCs especially copper nanoclusters (Cu NCs) are known to show various functionalities.<sup>9</sup> Their luminescent properties make them an excellent candidate for sensing<sup>10-16</sup>, bioimaging<sup>17, 18</sup> and LED<sup>19, 20</sup> applications whereas the tiny size and electronic properties push them as semiconducting materials<sup>21</sup> and diverse catalysts.<sup>22</sup> Copper based nanoclusters are sparsely found compared to their gold and silver counterparts because Cu(0) state is more prone to oxidation than Au(0) and Ag(0).<sup>11</sup> Although it is highly desirable to synthesize copper nanoclusters as they are significantly cheaper than their gold and silver alternatives and as functionally diverse as other coinage metal NCs, the lower redox stability has been a crucial barrier to explore copper nanoclusters to their fullest.<sup>19</sup>

Although copper-based NCs (Cu NCs) are very versatile in their applications, composite/hybrid materials made of Cu NC and other functional materials have made them more robust in application-oriented research. Since, stability of copper-based nanoclusters has been the main hurdle to use in various materials, hybrid materials often help to overcome the stability issue.<sup>23</sup> The synergistic effect of both the materials creates more opportunities for interesting novel properties and their applications. Lan *et al.* has stabilized highly reactive Cu NCs by graphitic carbon nitride and mesoporous silica to facilitate hydrogenation of levulinic acid to synthesize  $\gamma$ -valerolactone (GVL) with a 92% yield.<sup>24</sup> Wang and co-workers have synthesized a dual emission hybrid of sulfur doped carbon quantum dot and blue light emitting Cu NC that selectively senses dinotefuran with a detection limit of 7.04  $\mu$ M.<sup>25</sup> A luminescent Cu NC and egg shell membrane composite has been

fabricated in presence of dithiothreitol (DTT) as capping agent by Li *et al.*<sup>26</sup> The Cu NC gets stability and better dispersity via the egg shell membrane matrix and this composite is successfully used in visual detection of silver ions.<sup>26</sup> Gao *et al.* has incorporated Cu NC into an imidazole appended zeolite framework where the nanocluster has shown improved stability and fluorescence enhancement.<sup>27</sup> This hybrid material has been successfully used to sense ATP of aquatic food product with a detection limit of 0.67  $\mu\text{M}$ . Mu *et al.* has comprehensively reviewed hybrid materials of Cu NCs with RGO, QDs, zeolite, heparin, carbon dots etc. and their wide-range application in biosensing and imaging.<sup>23</sup> However, the diversity of application of Cu NC-based hybrid materials in optoelectronics, photovoltaics, hydrogen generation and other photocatalytic applications is much less reported than their applications in bio-analytics and catalysis.<sup>23</sup>

Since the discovery of photochemical water splitting using titania ( $\text{TiO}_2$ ) electrode in 1972,<sup>28</sup> this environmentally benign, cost-effective oxide has become the most used semiconducting material as photo-catalyst.<sup>29-31</sup> Due to its surface, electronic and photocatalytic properties it has been used in the fields of photochemical dye degradation<sup>32</sup>, fuel cell<sup>33-35</sup>, lithium ion batteries<sup>36</sup> and biosensors<sup>37</sup>. In the current study the anatase form of  $\text{TiO}_2$  has been preferred over its other polymorphs because of its highest electron mobility.<sup>38</sup> In this comprehensive work, an environment friendly synthetic method was devised to synthesize a cyan-emitting nanocluster having 7 copper atoms in the core. In order to demonstrate tuning of electronic properties of  $\text{TiO}_2$  using the copper nanocluster, a hybrid of the two materials was successfully formed. The electrostatic interaction between Lewis acidic pores of synthesized  $\text{TiO}_2$  nanoparticles and the copper nanocluster with negative surface charge held the tiny (2.14 nm average diameter) nanoclusters to  $\text{TiO}_2$ . TCSPC analysis revealed a possible photo-excited charge transfer from nanocluster to  $\text{TiO}_2$ . From the diffused reflectance spectroscopy (DRS) study, a clear red shift in absorbance of  $\text{TiO}_2$  was observed when copper nanocluster was added to it demonstrating band gap narrowing of  $\text{TiO}_2$ . Among hybrids made from different weight ratios of  $\text{TiO}_2$  and Cu nanoclusters, 10% w/w ratio of nanocluster: $\text{TiO}_2$  showed the highest current output keeping Schottky nature of the original  $\text{TiO}_2$  preserved. The same hybrid material showed the highest  $I_{ON}/I_{OFF}$  ratio too. The current gain can be attributed to a long-lived electron-hole separation in the hybrid material through an interfacial charge transfer from LUMO of

nanocluster to the conduction band of TiO<sub>2</sub>. Although there are a very few reports<sup>39,40</sup> on nano hybrids consisting of copper nanocluster and two dimensional TiO<sub>2</sub> nanosheets studying hydrogen evolution efficiencies, to best of our knowledge, no studies have been done consisting nano hybrid of copper nanoclusters and zero-dimension (nanoparticles) TiO<sub>2</sub> nanomaterials. Herein, a comprehensive study on the modulation of semiconducting property and photocurrent response of the hybrid made of anatase TiO<sub>2</sub> nanoparticles and cyan-emitting Cu NCs is presented for the first time.

## 6.2 Results and Discussion

### UV-VIS Spectroscopy

The synthesized and purified Cu NC in water showed cyan fluorescence when illuminated with a UV torch producing 365 nm wavelength. To confirm the formation of a few-atom copper nanocluster, the as-purified aqueous solution of the nanocluster was subjected to UV-VIS absorption study. There was no peak in the 500-600 nm region confirming the absence of formation of large nanoparticles. (Figure 6.1a) Nanoparticles are known to show intense absorption signature in that region due to surface plasmon resonance.<sup>19</sup> The Cu NC showed a weak absorbance peak at 406 nm in aqueous solution. The optical band gap energy of the Cu NC was calculated using a Tauc Plot drawn using the data obtained from the UV-visible spectroscopy data (Figure 6.2). The band gap was found to be 2.8 eV.

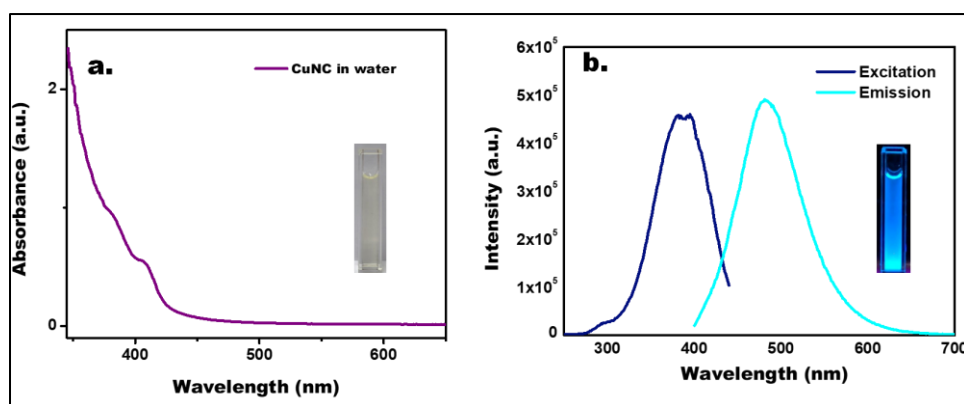


**Figure 6.1** (a) UV-Visible absorption spectra of the Cu NC in water shows weak absorption at 406 nm. Photograph of pure Cu NC aqueous solution in the inset. (b) Fluorescence excitation and emission spectra of the Cu NC showing maxima at 385 nm and 481 nm respectively. Visible cyan fluorescence of the Cu NC under 365 nm UV torch. (Inset).

## Fluorescence Spectroscopy

The nanocluster showed cyan fluorescence as seen under UV torch. It prompted us to study its fluorescence spectra. The excitation spectra showed a maximum at 385 nm which is in accordance with the absorption maxima (Figure 6.1b). The nanocluster emits at 481 nm with a symmetric emission distribution (Figure 6.1b) which indicates formation of a single species.<sup>41</sup> The Cu NC-TiO<sub>2</sub> composite was dispersed in water to measure its emission profile. Although the fluorescence maximum was found to be unchanged, a significant amount of quenching of fluorescence intensity was observed in the hybrid solution. The reduction in photoluminescence (PL) intensity signifies fast deactivation of excited Cu NC species.<sup>42, 43</sup>

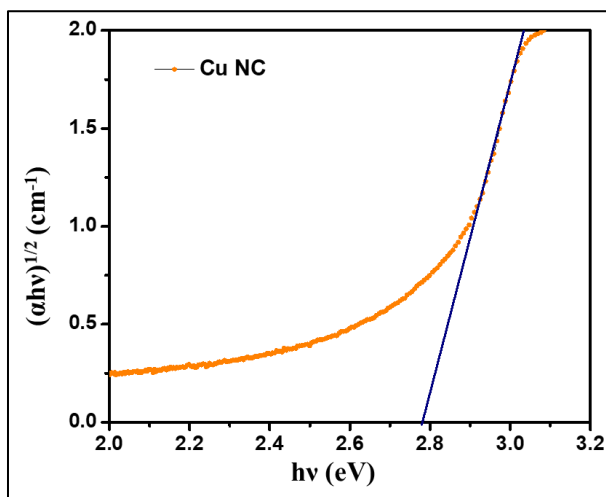


**Figure 6.2** The Tauc Plot for Cu NC found corresponding to the UV-visible absorption spectroscopy, shows the nanoclusters have an optical band gap of 2.8 eV.

## Detailed Quantum Yield Calculation

Relative Quantum Yield  $\Phi_x$  of a substance x is given by the equation,

$$\Phi_x = \Phi_{St} (F_x \times f_{st}(\lambda_{ex}) \times \eta_x^2) / (F_{St} \times f_x(\lambda_{ex}) \times \eta_{St}^2)$$

Where,  $\Phi_{St}$  is the absolute quantum yield of the standard fluorophore and F stands for the integral photon flux, f stands for the absorbance factor and  $\eta$  stands for the refractive indices of the respective solvents. The indices 'x' and 'St' stand for the sample under investigation and the standard reference. The absorbance factor  $f(\lambda_{ex}) = 1 - 10^{-A(\lambda_{ex})}$ , where  $A(\lambda_{ex})$  is the absorbance value of the solutions at the excitation

wavelength  $\lambda_{ex}$ . Quinine sulfate in 0.1 M sulfuric acid is taken as the reference. 0.1 M sulfuric acid and water both shows refractive index of 1.33 that is why refractive index is not taken under consideration. While collecting fluorescence spectra of copper nanocluster (Cu-NC), 385 nm was used as the excitation wavelength and for Quinine Sulfate (QS) excitation wavelength was 350nm. Integration was done for the whole fluorescence spectra to calculate total photon flux for both Cu-NC and the reference.

$$A_{CuNC}(\lambda_{385}) = 0.08; A_{QS}(\lambda_{350}) = 0.65$$

$$\text{Hence, } f_{CuNC}(\lambda_{385}) = 1 - 10^{-0.08} = 0.17 \text{ and } f_{QS}(\lambda_{350}) = 1 - 10^{-0.65} = 0.78$$

Thus, the relative quantum yield of synthesized Cu-NC,

$$\begin{aligned} \Phi_{CuNC} &= \Phi_{QS} (F_{CuNC} \times f_{QS}(\lambda_{350})) / (F_{QS} \times f_{CuNC}(\lambda_{385})) \\ &= 0.546 \times (2.11 \times 10^7 \times 0.78) / (6.09 \times 10^8 \times 0.17) \\ &= 0.087 \text{ or } 8.7\% \end{aligned}$$

### TCSPC Measurements

To gain insight into the excited state behavior of the copper nanocluster and its hybrid with anatase titanium dioxide nanocrystals (TiO<sub>2</sub>) time correlated single photon counting experiment was done using 385 nm as excitation wavelength. Same excitation wavelength was used for both pure Cu NC and the hybrid as their excitation and emission maxima were same. Interestingly enough, the lifetime of the excited species was different in two cases. The Cu NC showed an average lifetime of 3.86 ns and a bi-exponential decay profile (Figure 6.3) with time constants 1.5 ns (69%) and 8.9 ns (31%). In the hybrid, excited Cu NC species decays faster with an average lifetime of 1.50 ns having a biexponential decay profile with time constants 0.45 ns (89%) and 9.2 ns (11%). The shortening of decay time can be attributed to either resonance energy transfer or electron transfer. As there is no significant overlap between donor (Cu NC) emission and acceptor (TiO<sub>2</sub>) absorption spectra, energy transfer was ruled out. Electron transfer takes place in the photo-excited composite and that is why one of the time constants of the hybrid system is as small as 450 ps.<sup>44</sup>

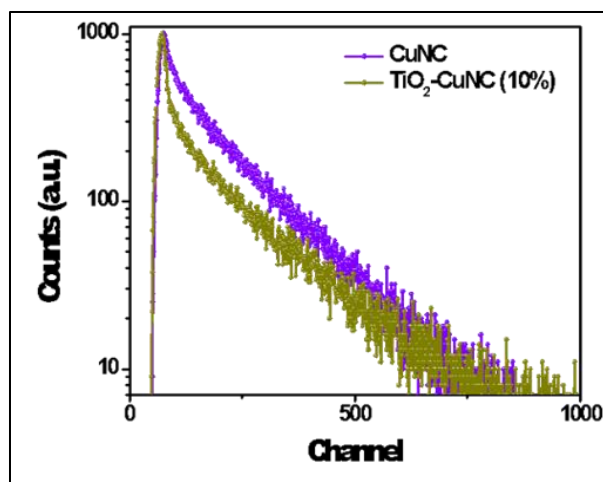


**Figure 6.3** The fluorescence excited state decay profile of Cu NC and  $\text{TiO}_2$ -Cu NC with respect to their emission at 481 nm. The estimated average lifetimes for the respective species are 3.86 ns and 1.50 ns.

**DRS Studies.** Diffused Reflectance Spectroscopy (DRS) was used to measure solid state absorbance of  $\text{TiO}_2$  and 10% w/w  $\text{TiO}_2$ -Cu NC hybrid. It was observed that  $\text{TiO}_2$  has a maximum at 315 nm (Figure 6.4a) and the hybrid shows a red shift of 29 nm from the pure  $\text{TiO}_2$ . The corresponding Tauc Plot was drawn using the DRS data to compare the optical band gap energy of the materials (Figure 6.4b). The energy band gap between the valence band and conduction band of titania was found to be 3.4 eV (Figure 6.4b) which is in accordance with the literature value.<sup>45-47</sup> The gap clearly diminished to 3.1 eV in case of the hybrid. The decrease in band gap energy encouraged us to study the hybrid materials' current output under a varied bias voltage.

### MALDI-TOF MS Analysis

The exact sizes of these copper nanoclusters or in other words the exact number of atoms and ligands present in the core of these clusters were characterized by positive mode MALDI-TOF MS analyses by using sinapinic acid as a matrix. This experiment was performed multiple times with other matrices like alpha-Cyano-4-hydroxycinnamic acid and 2,5-Dihydroxybenzoic acid but only sinapinic acid -Cu NC adduct was stable and the mass was found in LP (Linear Positive) mode. MALDI-TOF MS analysis profile of these Cu NCs is provided in Figure 4d. Here the peak at  $m/z$  value of 619 for Cu NC corresponds to  $(\text{Cu}_7\text{L}_2 + \text{Na})^+$  ion while

the peak at  $m/z$  value of 698 can be assigned for  $(\text{Cu}_7\text{L}_2 + \text{Na} + 2\text{K})$  + confirming formation of a seven-atom centred copper nanocluster (Figure 6.6d). L denotes the capping ligand cysteamine (2-aminoethanethiol).

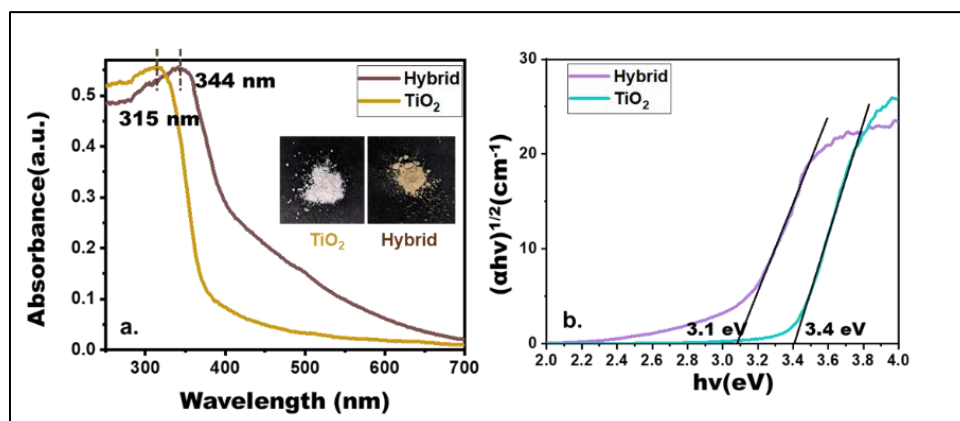


**Figure 6.4** (a) UV-Visible Diffuse Reflectance Spectroscopy (DRS) of solid powdered  $\text{TiO}_2$  nanocrystals and  $\text{TiO}_2$ -Cu NC hybrid showing absorbance maxima at 315 nm and 344 nm respectively. The powder materials are shown in inset. (b) The Tauc plot obtained from DRS spectra gives the optical band gap values of the same materials.

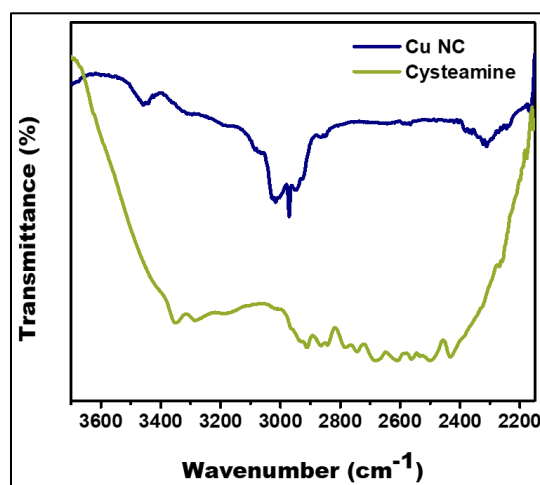


**Figure 6.5.** FT-IR Spectroscopy data obtained for the ligand cysteamine and the synthesized copper nanocluster.

### FT-IR analysis

To confirm the binding of thiol group on copper cluster, Fourier Transform Infrared Spectroscopy (FT-IR) studies of the nanoclusters and pure cysteamine

were done and compared with each other. The absence of a broad band of thiol S-H stretching from 2500-2600  $\text{cm}^{-1}$  in the IR spectra (Figure 6.5) of the nanoclusters which was earlier visible in cysteamine, confirms the participation of sulfides in capping of the  $\text{Cu}_7$  nanocluster. Presence of N-H stretching at 3442  $\text{cm}^{-1}$  for both the cases (Figure 6.5) suggests attachment of cysteamine ligands on the nanocluster. The peak at 3442  $\text{cm}^{-1}$  is attributed to the free amine groups of cysteamine.

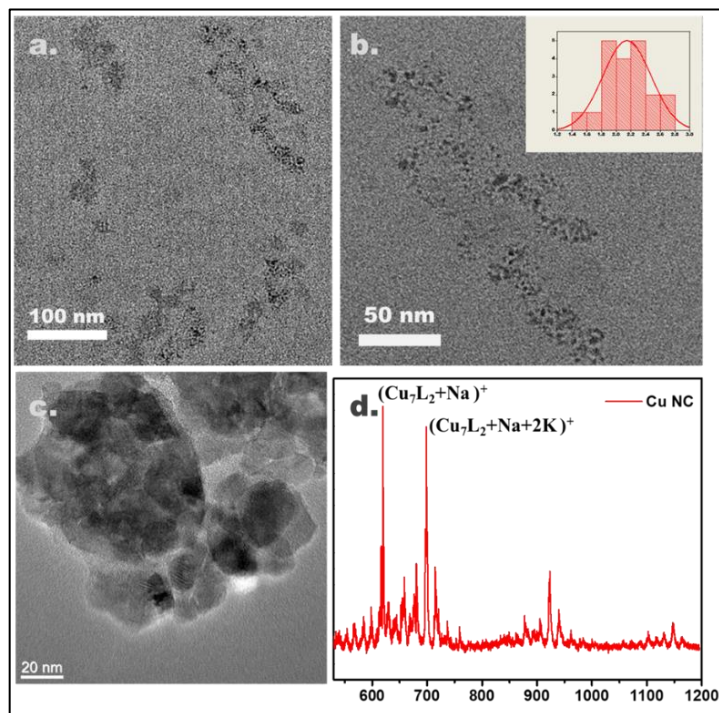


**Figure 6.6.** (a) Field Emission Gun Transmission Electron Microscope (FEG-TEM) image of Cu NC, (b) Portion of first image is magnified for clarity. The distribution of Nanocluster size is provided in the inset, (c) FEG-TEM image of  $\text{TiO}_2$  nanocrystal, (d) MALDI-TOF mass analysis of the Cu NC in sinapinic acid matrix.

### FEG-TEM Studies

Field Emission Gun Transmission Electron Microscopy (FEG-TEM) was used to determine the size and dispersity of the nanoclusters prepared. It was challenging to find the copper nanoclusters with proper contrast (Figure 6.6a) as the TEM grids themselves are made of copper. Figure 6.6b shows that the average nanocluster size is calculated to be 2.14 nm as most of the nanoclusters lie in the range of 1.8-2.2 nm. It is very common to find cluster size bigger than the original size as the



cluster consisting of organic capping ligands tend to aggregate under high intensity (more than 160 keV) electron beam.<sup>48, 49</sup> Anatase TiO<sub>2</sub> nanocrystals were imaged under Field Emission Gun Transmission Electron Microscopy (FEG-TEM) (Figure 6.6c). Lattice plane of (101) of anatase TiO<sub>2</sub> was assigned by measuring the lattice spacing  $d = 0.35$  nm as distance between two adjacent fringes<sup>50</sup>. The hybrid did not show Cu NC and TiO<sub>2</sub> together under FEG-TEM studies. As nanoclusters are extremely small in size and contrast of the image being a problem in case of imaging copper-based materials, they were not recognized along with TiO<sub>2</sub> nanocrystals.

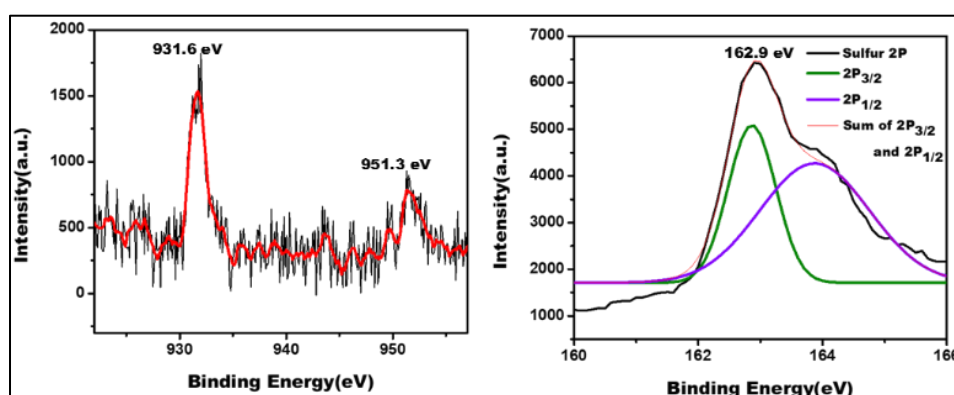


**Figure 6.7.** (a) X-Ray Photoelectron Spectroscopy (XPS) showing the binding energy of Cu 2P states in Cu NC, (b) XPS spectra of sulfur in Cu NC, coming from the cysteamine ligand.

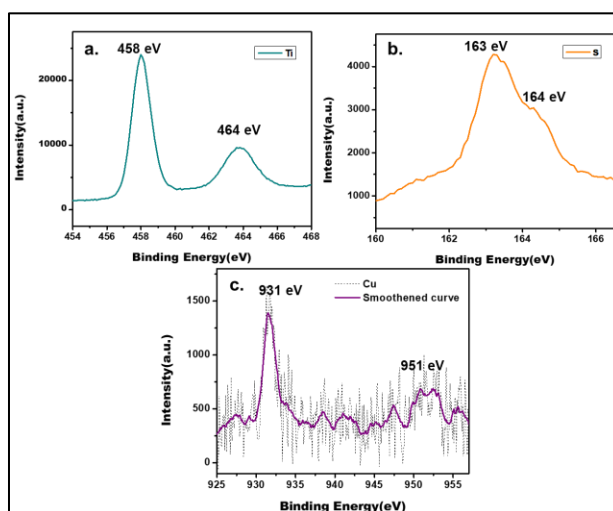


**Figure 6.8.** Core level XPS analysis of the Cu NC-TiO<sub>2</sub> hybrid shows (a) binding energy of Ti of TiO<sub>2</sub> nanoparticles and (b) binding energy of S and (c) Cu of the nanocluster.

**Zeta potential measurement** Zeta potential measurement of the Cu NC in water at 25 °C revealed that the nanoclusters possess a surface charge of -4.82 mV.

### X Ray photoelectron spectroscopy

X Ray photoelectron spectroscopy is a sophisticated tool to find electronic state information of elements present in a specific substance. Core-level XPS analysis of the Cu NC was done to gain insight into the oxidation states of the atoms present in the nanocluster. Binding energy peaks of 931.6 eV and 951.3 eV can be assigned to binding energies of Cu  $2P_{3/2}$  and Cu  $2P_{1/2}$  states respectively of Cu(0) (Figure 6.7a).<sup>51</sup> It should be noted that,  $2P_{3/2}$  and  $2P_{1/2}$  states of Cu(0) and Cu(I) vary only by 0.1 eV. That is why it cannot be concluded how many copper atoms are in Cu(0) state and how many are in Cu(I) state.<sup>44</sup> Absence of satellite peaks around 942 eV suggests absence of Cu(II) states in the nanocluster.<sup>44</sup> Thus, it can be concluded that complete reduction of starting material has taken place and the nanocluster consists of 0 and +1 states of copper. The 2P state of sulfur gives information about the binding of the ligand to the copper cluster. Deconvolution of XPS spectra for sulfur 2P peak shows more intense  $2P_{3/2}$  peak at 162.9 eV along with the less intense  $2P_{1/2}$  at 164 eV (Figure 6.7b). The binding energy of sulfur  $2P_{3/2}$  of unbound (physiosorbed) thiols lies in the region of  $163.6 \pm 0.2$  eV.<sup>52, 53</sup> In the present context, sulfur  $2P_{3/2}$  binding energy shifts to 162.9 eV as the unbound thiols of cysteamine get chemisorbed on copper nanoclusters.<sup>54</sup> The XPS analysis of TiO<sub>2</sub> showed peaks at 464 eV and 458 eV corresponding to Ti  $2P_{1/2}$  and Ti  $2P_{3/2}$  states respectively. The presence of Cu 2P peaks at 931 eV and 951 eV (Figure 6.8c), Ti 2P peaks at 464 eV and 458 eV (Figure 6.8a) and S 2P peaks at 163 eV and 164 eV (Figure 6.8b) found in core-level XPS analysis of the hybrid confirmed the formation of the hybrid. Although the unchanged binding energy of titanium nullifies the possibility of atomic-level interaction between TiO<sub>2</sub> and the copper nanocluster. Valence band XPS analysis of a material can be utilized to find valence band energy values of pure anatase TiO<sub>2</sub>, 10% TiO<sub>2</sub>-Cu NC hybrid, and HOMO energy state of pure copper nanoclusters They were found to be 1.90 eV, 1.50 eV and 0.67 eV respectively (Figure 6.9).

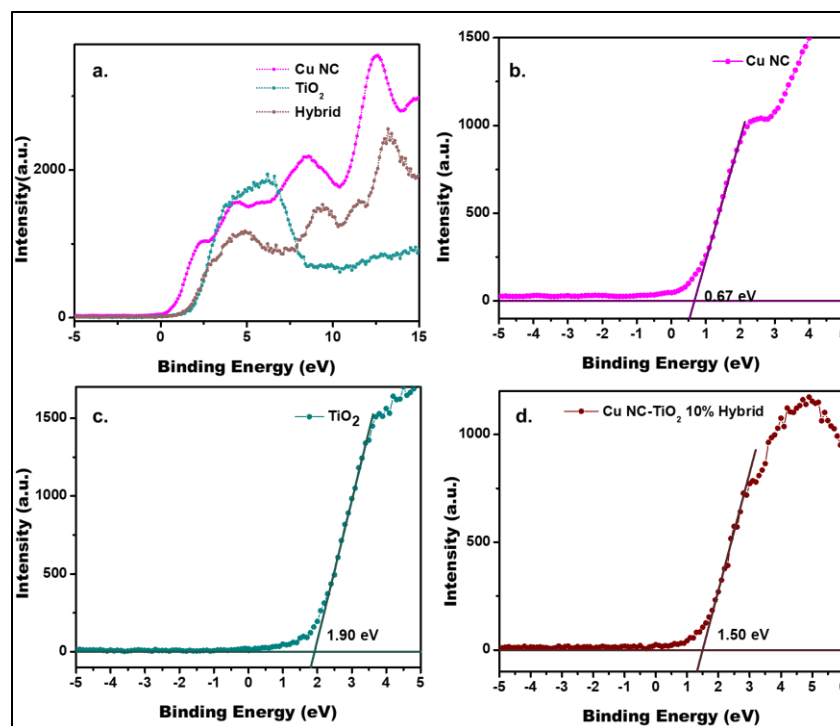


**Figure 6.9.** Valence Band XPS plot for (a) Cu NC, TiO<sub>2</sub>, Cu NC-TiO<sub>2</sub> Hybrid materials, close up of valence band XPS plot of (b) Cu NC, (c) TiO<sub>2</sub>, (d) Cu NC-TiO<sub>2</sub> Hybrid to show the valence band binding energy values.

### Current Voltage Measurement

Current-Voltage measurement of TiO<sub>2</sub>, TiO<sub>2</sub>-Cu NC hybrid in 2%, 5%, 10% and 15% w/w (where weight of TiO<sub>2</sub> was considered 100% each time) was done using sandwich method. In this method the samples are drop-casted on indium-tin oxide coated glass (ITO glass) and covered with another ITO glass. The circuit is completed from one ITO slide to another with the sample in between. The voltage was swept between -5V to 5V. Pure anatase TiO<sub>2</sub> showed a characteristic Schottky diode like I-V curve with 0.5  $\mu$ A current response at 5V (Figure 6.10), indicating the material's semiconducting nature. As the weight percentage of Cu NC was increased gradually the current increased dramatically without deviating from the Schottky diode like nature. The first hybrid sample (TiO<sub>2</sub> : Cu NC = 100:2) showed a ten-fold increase in current magnitude with 5  $\mu$ A at 5V. The current response of 5% w/w TiO<sub>2</sub>-Cu NC hybrid was 30  $\mu$ A (at 5V) (Figure 6.10) which is 60 times higher than the response of pure TiO<sub>2</sub>. At 10% w/w TiO<sub>2</sub>-Cu NC hybrid the current

response jumped to 800  $\mu\text{A}$  (Figure 6.10) which is 1600-fold increase of the current response from native  $\text{TiO}_2$ . It was found that further increase in Cu NC content did not change the amplitude of current significantly. It should also be noted that the current response by the film of pure Cu NC was feeble. Unlike  $\text{TiO}_2$  nanocrystals, the nanoclusters do not have any extended network among themselves. They are discreet entities with similar surface charge. Thus, despite formation of charge carriers, rapid recombination took place as mobility of electron and holes was very poor. But these nanoclusters having negative surface charge favorably interacts with Lewis acidic pores of  $\text{TiO}_2$ .<sup>50</sup> As a result nanoclusters utilized the extended three-dimensional network of  $\text{TiO}_2$  and worked synergistically with  $\text{TiO}_2$  to increase the mobility of the charge carriers and consequently increase the current. As the pores get saturated with Cu NC, in spite of addition of more Cu NC, the excess nanoclusters do not interact with  $\text{TiO}_2$ , thus the current response stops increasing even after increasing the Cu NC loading beyond 10% w/w  $\text{TiO}_2$ -Cu NC.

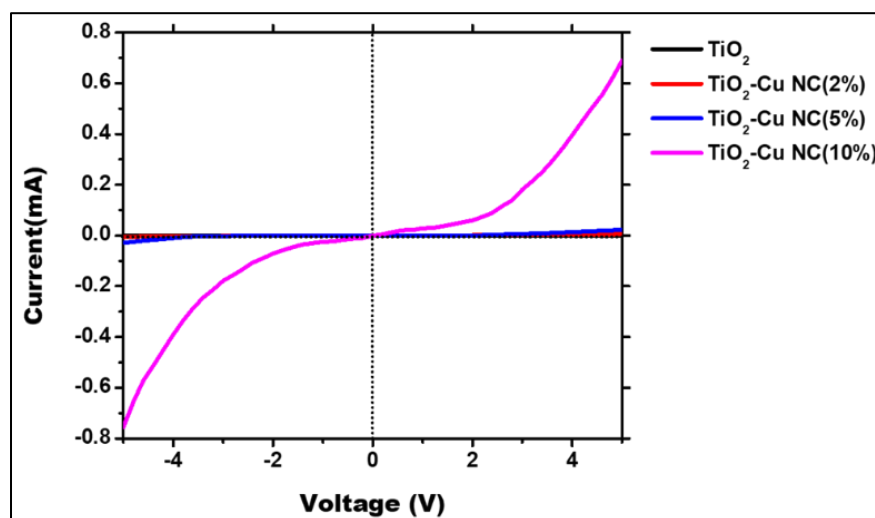


**Figure 6.10** Current signature plot for native  $\text{TiO}_2$ , and Hybrid of  $\text{TiO}_2$ -Cu NC with weight ratios 2%, 5% and 10% when voltage was cyclically varied from 5V to -5V

### Photocurrent Response

Photocurrent study is an important tool to know the light energy conversion efficiency of a particular sample. That is why it plays a vital part in optoelectronic applications. The photocurrent response of the samples was observed by switching on and off light source of intensity 1 sun while having each interval as 50 seconds (Figure 6.11). The dark current response follows the trend discussed in I-V response for all the samples. The Table. 1 indicates ratio of current output in presence of light to in absence of it ( $I_{ON}/I_{OFF}$ ) has increased to 2.7 in the case of TiO<sub>2</sub>-Cu NC (10%) whereas it was 1.43 in case of pure TiO<sub>2</sub>. Charge separation between electron and hole in the photo-excited species usually plays crucial role in generating photocurrent and its efficiency determines the photo response ability (light energy conversion) of a compound.<sup>55</sup> UV-visible spectroscopy studies yielded the band gap energies of the materials and the valence band XPS analysis gave the values of valence band (HOMO in case of Cu NC) energies. The conduction band (LUMO in case of Cu NC) energy was obtained by subtracting the energy band gap value from the valence band energy value. The nanoclusters are characterized by their discreet energy bands similar to molecules. The absorption spectra of the nanocluster highlighted the HOMO-LUMO transition (2.8 eV) in the visible region. Whereas TiO<sub>2</sub> has a large band gap of 3.4 eV which signifies that TiO<sub>2</sub> can only absorb in UV region. But in the hybrid system, the nanocluster absorbed photons in the visible range, to form excitons that dissociated in free charge carriers and the photo-excited electrons reach LUMO at -2.1 eV. The electrons were transported to CB (-1.5 eV) of TiO<sub>2</sub> through interfacial charge transfer.<sup>56, 57</sup> Thus, a long-lived electron- hole separation is created in the hybrid material where the electron is found in conduction band of TiO<sub>2</sub> and the holes reside in the HOMO of nanoclusters. Pure TiO<sub>2</sub> shows poor photocurrent response due to very fast recombination of electron and hole.<sup>58</sup> On the contrary, the hybrid material formed with Cu nanocluster showed enhanced photocurrent response (500 times increase in photocurrent in 10% w/w TiO<sub>2</sub>-Cu NC hybrid) (Table 1) due to long-lived electron hole separation and increased photon absorption in the visible spectrum.

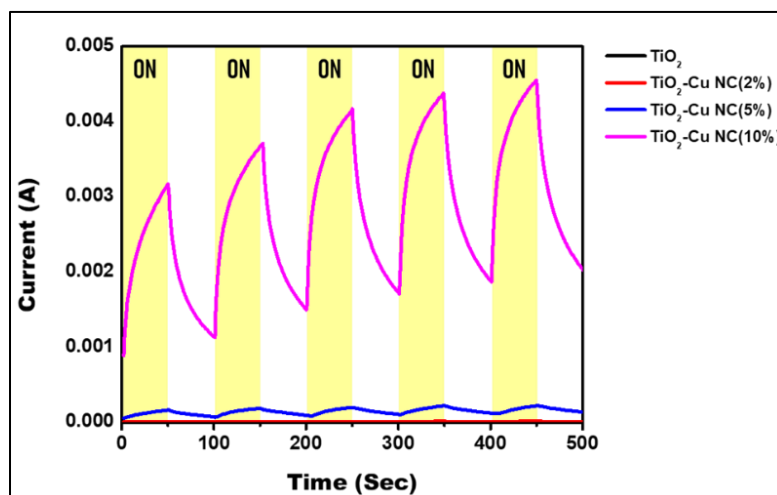


**Figure 6.11.** Photocurrent response plot for native TiO<sub>2</sub>, and Hybrid of TiO<sub>2</sub>-Cu NC with weight ratios 2%, 5%, 10%. Yellow highlighted regions denote periods of on phase of white light.

It is important to discuss photoelectrochemical activity of various Cu NC composites synthesized by other groups. Different research groups mostly focused on the various photocatalytic activity of the composite materials. Yu *et al.* has demonstrated photo-reduction of CO<sub>2</sub> to methanol by Cu-ZrO<sub>2</sub> composites,<sup>58</sup> whereas Deb *et al.* used Cu-halloysite nanotubes to degrade MB and MO dyes.<sup>58</sup> Hao *et al.* and, Kang and co-workers has reported photo-current response of their TiO<sub>2</sub>-Cu NC composites. Hao *et al.* observed a maximum of  $0.4 \times 10^{-3}$  mA of photocurrent in the composite system.<sup>58</sup> Kang and co-workers has found 0.05 mA·cm<sup>2</sup> photocurrent density in their most efficient photo-electrode.<sup>58</sup>

Thus, it is seen that the observed photocurrent values depend on bias voltage, excitation wavelength and device manufacturing processes. In the current study the measurements were done by drop-casting the materials on ITO plates, under 5V bias voltage. We observed a gradual increase from  $8.9 \times 10^{-3}$  mA to 4.1 mA in the 10 wt%. We report a result that is comparable to the literature and better than most of them.

**Table 1.** Photocurrent Response

<b>Material</b>	<b>Dark Current (mA)</b>	<b>Photo Current (mA)</b>	<b>I<sub>ON</sub>/I<sub>OFF</sub></b>
<b>TiO<sub>2</sub></b>	$6.2 \times 10^{-3}$	$8.9 \times 10^{-3}$	<b>1.43</b>
<b>TiO<sub>2</sub>-Cu NC (2%)</b>	$9.0 \times 10^{-3}$	$1.6 \times 10^{-2}$	<b>1.72</b>
<b>TiO<sub>2</sub>-Cu NC (5%)</b>	$1.0 \times 10^{-1}$	$2.2 \times 10^{-1}$	<b>2.1</b>
<b>TiO<sub>2</sub>-Cu NC (10%)</b>	<b>1.5</b>	<b>4.1</b>	<b>2.7</b>

### 6.3 Conclusion

This study convincingly demonstrates the formation of a new nanohybrid system consisting of cyan-emitting copper nanoclusters and anatase TiO<sub>2</sub> nanoparticles. Atomically precise Cu nanoclusters with negative surface charge interact favorably with the mesoporous TiO<sub>2</sub> nanoparticles with Lewis-acidic pores to form this hybrid. Interestingly, optoelectronic property of TiO<sub>2</sub> was wonderfully modulated in the nanohybrid in presence of Cu nanoclusters. The nanohybrid showed 1600-fold current improvement in the optimum weight ratio of Cu NC and TiO<sub>2</sub>. Enhancement of semiconducting current is an important advancement in the field of transistor development. To best of our knowledge, no other research group has demonstrated semiconducting current improvement of TiO<sub>2</sub> in presence of Cu nanoclusters in absence of light. The photo-switching property including photo current gain was improved significantly in the hybrid system compared to that of native TiO<sub>2</sub>. The photo-current curves demonstrated that the cooperation of copper nanoclusters help in reduction of the back reaction and rapid recombination of photo-generated electron-hole pairs. This nanohybrid shows promising results in improving the photovoltaic properties of TiO<sub>2</sub> in a very cost-effective manner thus holding future promises in designing cheap semiconducting devices.

## 6.4 Experimental Section

### Synthesis of TiO<sub>2</sub> Nanoparticle

TiO<sub>2</sub> nanoparticle was prepared following the previous method.<sup>50</sup> 1 g of l-glutamic acid (6.8 mmol) was put in 25 mL water and 1 M sodium hydroxide solution was periodically added to maintain the pH of the solution around 7. 1 mL of Ti(OiPr)<sub>4</sub> was added in 5 mL of isopropyl alcohol. This solution was added drop wise into the previous solution. The pH was further adjusted to 10 by adding an ammonia solution (25%). Stirring continued for two hours to observe a milky white precipitate. The nanoparticles were collected by centrifugation (10000 rpm, 15 min) and washed with water. The synthesized nanoparticles were dried in the oven overnight and then calcined at 250°C for one hour followed by 500°C for five hours.

### Synthesis of Cu nanocluster

As per our knowledge, there is only one literature where cysteamine (2-aminoethanethiol) was used as capping agent as well as reducing agent.<sup>41</sup> But the procedure in this work is different than that. The fluorescence emission maxima of the Cu NC were 380 nm for the nanocluster synthesized<sup>41</sup> by Boonmee et al. whereas Cu NC synthesized in this work shows emission maxima at 481 nm, so it can be said that it was a different cluster. but the procedure 1 mL of 10 mM Copper (II) acetate monohydrate solution in Mili-Q was placed in a 50 mL round bottom flask under stirring. 20 mg 2-aminoethanethiol was dissolved in 3 mL of water and slowly added to the flask at room temperature. The mixture was stirred for 30 mins at room temperature under the nitrogen atmosphere. After that the reaction mixture was refluxed at 120°C for 10 hours under the nitrogen atmosphere. The light-yellow colored supernatant solution containing Copper Nanocluster (Cu NC) was separated from the brown precipitates of copper oxides by centrifugation. (8000 rpm, 15 mins) Finally the mono-dispersed nanoclusters were separated from unreacted precursors by dialysis in Mili-Q water.

### Preparation of nanohybrid

The copper nanocluster was lyophilized to get sticky yellow solid with high fluorescence. Cu NC and TiO<sub>2</sub> nanoparticle are taken according to desired weight



ratio and 1 mL of water is added to the mixture. Cu NC redissolves in water whereas TiO<sub>2</sub> nanoparticle remained suspended in the solution. This solution was kept for 5 hours at 25°C and the change of color from white to beige in TiO<sub>2</sub> was noted. The beige colored powder was filtered, washed with water twice and dried overnight in a desiccator.

**Preparation of nanohybrid films for I-V and photocurrent measurements.**

0.5 mg of the nanohybrid powder was suspended in 100 µL water and drop-casted on Indium Tin oxide coated glass (ITO glass). The measurements were taken using the sandwich method.

## 6.5 References

1. Y. Du, H. Sheng, D. Astruc and M. Zhu, *Chem. Rev.*, 2020, **120**, 526-622.
2. L. Farzin, M. Shamsipur, L. Samandari, S. Sadjadi and S. Sheibani, *Talanta*, 2020, **214**, 120886.
3. R. Jin, C. Zeng, M. Zhou and Y. Chen, *Chem. Rev.*, 2016, **116**, 10346-10413.
4. Y. Tao, M. Li, J. Ren and X. Qu, *Chem. Soc. Rev.*, 2015, **44**, 8636-8663.
5. B. Wang, M. Zhao, M. Mehdi, G. Wang, P. Gao and K.-Q. Zhang, *Mater. Chem. Front.*, 2019, **3**, 1722-1735.
6. T.-Q. Yang, B. Peng, B.-Q. Shan, Y.-X. Zong, J.-G. Jiang, P. Wu and K. Zhang, *Nanomaterials*, 2020, **10**.
7. J. V. Rival, P. Mymoona, K. M. Lakshmi, Nonappa, T. Pradeep and E. S. Shibu, *Small*, 2021, **17**, 2005718.
8. A. Nag, P. Chakraborty, A. Thacharon, G. Paramasivam, B. Mondal, M. Bodiuzzaman and T. Pradeep, *J.Phys.Chem. C*, 2020, **124**, 22298-22303.
9. S. Shahsavari, S. Hadian-Ghazvini, F. Hooriabad Saboor, I. Menbari Oskouie, M. Hasany, A. Simchi and A. L. Rogach, *Mater. Chem. Front.*, 2019, **3**, 2326-2356.

10. B. Adhikari and A. Banerjee, *Chem. Mater.*, 2010, **22**, 4364-4371.
11. Y.-S. Lin, Y.-F. Lin, A. Nain, Y.-F. Huang and H.-T. Chang, *Sens. Actuator. Rep.*, 2021, **3**, 100026.
12. Z. Liu, X. Jing, S. Zhang and Y. Tian, *Anal. Chem.*, 2019, **91**, 2488-2497.
13. B.-J. Shi, L. Shang, W. Zhang, L.-P. Jia, R.-N. Ma, Q.-W. Xue and H.-S. Wang, *Sens. Actuator. B*, 2021, 130291.
14. A. Baral, K. Basu, S. Roy and A. Banerjee, *ACS Sustain. Chem. Eng.*, 2017, **5**, 1628-1637.
15. A. Dutta, U. Goswami and A. Chattopadhyay, *ACS Appl. Mater. Interfaces*, 2018, **10**, 19459-19472.
16. S. Pramanik, L. Khamari, S. Nandi and S. Mukherjee, *J.Phys.Chem. C*, 2019, **123**, 29047-29056.
17. K. Basu, K. Gayen, T. Mitra, A. Baral, S. S. Roy and A. Banerjee, *ChemNanoMat*, 2017, **3**, 808-814.
18. N. K. Das, S. Ghosh, A. Priya, S. Datta and S. Mukherjee, *J.Phys.Chem. C*, 2015, **119**, 24657-24664.
19. Z. Wang, B. Chen and A. L. Rogach, *Nanoscale Horizons*, 2017, **2**, 135-146.
20. P. Das and A. Chattopadhyay, *J.Phys.Chem. C*, 2022, DOI: 10.1021/acs.jpcc.1c07839.
21. A. Baral, K. Basu, S. Ghosh, K. Bhattacharyya, S. Roy, A. Datta and A. Banerjee, *Nanoscale*, 2017, **9**, 4419-4429.
22. K. Basu, S. Paul, R. Jana, A. Datta and A. Banerjee, *ACS Sustain. Chem. Eng.*, 2019, **7**, 1998-2007.
23. J. Mu, Y. Peng, Z. Shi, D. Zhang and Q. Jia, *Microchimica Acta*, 2021, **188**, 384.
24. F. Lan, J. Aarons, Y. Shu, X. Zhou, H. Jiao, H. Wang, Q. Guan and W. Li, *Appl. Catal. B*, 2021, **299**, 120651.

25. Y. Yang, Q. Wei, T. Zou, Y. Kong, L. Su, D. Ma and Y. Wang, *Sens. Actuator. B*, 2020, **321**, 128534.
26. C. Li, C. Shao, L. Li, X. Liu and M. Liu, *Photochem. Photobiol. Sci.*, 2019, **18**, 2942-2951.
27. X. Gao, J. Liu, X. Zhuang, C. Tian, F. Luan, H. Liu and Y. Xiong, *Sens. Actuator. B*, 2020, **308**, 127720.
28. A. Fujishima and K. Honda, *Nature*, 1972, **238**, 37-38.
29. J. Schneider, M. Matsuoka, M. Takeuchi, J. Zhang, Y. Horiuchi, M. Anpo and D. W. Bahnemann, *Chem. Rev.*, 2014, **114**, 9919-9986.
30. K. Hashimoto, H. Irie and A. Fujishima, *Jpn. J. Appl. Phys.*, 2005, **44**, 8269-8285.
31. B. Bakbolat, C. Daulbayev, F. Sultanov, R. Beissenov, A. Umirzakov, A. Mereke, A. Bekbaev and I. Chuprakov, *Nanomaterials*, 2020, **10**.
32. C. Thambiliyagodage, *Environ. Nanotechnol., Monit. Manag.*, 2021, **16**, 100592.
33. M. Ismael, *Fuel*, 2021, **303**, 121207.
34. E. Antolini, *Appl. Catal.*, 2018, **237**, 491-503.
35. C. Shi, W. Yuan, K. Qu, J. Shi, M. Eqi, X. Tan, Z. Huang, F. G. Gãndara, D. Pan, N. Naik, Y. Zhang and Z. Guo, *Eng. Sci.*, 2021, **16**, 374-386.
36. T. N. Pham, V. K. H. Bui and Y.-C. Lee, *Int. J. Energy Res.*, 2021, **45**, 17532-17562.
37. C. Zhao, T. Jing, J. Tian, J. Guo, M. Wu, D. Shi, Z. Zhao and Z. Guo, *J. Nanostruct. Chem.*, 2021, DOI: 10.1007/s40097-021-00455-0.
38. T. Luttrell, S. Halpegamage, J. Tao, A. Kramer, E. Sutter and M. Batzill, *Sci. Rep.*, 2014, **4**, 4043.
39. Y.-D. Cao, H.-P. Hao, H.-S. Liu, D. Yin, M.-L. Wang, G.-G. Gao, L.-L. Fan and H. Liu, *Nanoscale*, 2021, **13**, 16182-16188.

40. F. Yu, L. Chen, X. Li, X. Shen, H. Zhao, C. Duan and Q. Chen, *ACS Appl. Mater. Interfaces*, 2021, **13**, 18619-18626.
41. C. Boonmee, V. Promarak, T. Tuntulani and W. Ngeontae, *Talanta*, 2018, **178**, 796-804.
42. B.-R. Hyun, A. C. Bartnik, L. Sun, T. Hanrath and F. W. Wise, *Nano Lett.*, 2011, **11**, 2126-2132.
43. H. Matsumoto, T. Matsunaga, T. Sakata, H. Mori and H. Yoneyama, *Langmuir*, 1995, **11**, 4283-4287.
44. S. Maity, D. Bain, K. Bhattacharyya, S. Das, R. Bera, B. Jana, B. Paramanik, A. Datta and A. Patra, *J. Phys. Chem. C*, 2018, **122**, 13354-13362.
45. C. Moslah, G. A. Mousdis, M. Kandyla, G. Petropoulou, M. Ksibi, in *Nanostructured Materials for the Detection of CBRN*, Springer Dordrecht, 2018, pp. 71-89.
46. M. B. Poudel, C. Yu and H. J. Kim, *Catalysts*, 2020, **10**.
47. T. Lan, J. Tu, Q. Zou, X. Zeng, J. Zou, H. Huang and M. Wei, *Electrochimica Acta*, 2019, **319**, 101-109.
48. S. Roy, A. Baral, R. Bhattacharjee, B. Jana, A. Datta, S. Ghosh and A. Banerjee, *Nanoscale*, 2015, **7**, 1912-1920.
49. X. Liu, C. Shao, T. Chen, Z. He and G. Du, *Sens. Actuator. B*, 2019, **278**, 181-189.
50. S. De, S. Dutta, A. K. Patra, A. Bhaumik and B. Saha, *J. Mater. Chem.*, 2011, **21**, 17505-17510.
51. Q.-Q. Huang, M.-Y. Hu, Y.-L. Li, N.-N. Chen, Y. Li, Q.-H. Wei and F. Fu, *Chem. Commun.*, 2021, **57**, 9890-9893.
52. S. Kumar, J. T. van Herpt, R. Y. N. Gengler, B. L. Feringa, P. Rudolf and R. C. Chiechi, *J. Am. Chem. Soc.*, 2016, **138**, 12519-12526.
53. O. Ivashenko, J. T. van Herpt, B. L. Feringa, P. Rudolf and W. R. Browne, *Langmuir*, 2013, **29**, 4290-4297.

- 
54. Y. Wang, J. Im, J. W. Soares, D. M. Steeves and J. E. Whitten, *Langmuir*, 2016, **32**, 3848-3857.
55. M. Zhang, Y. Duan, H. Jia, F. Wang, L. Wang, Z. Su and C. Wang, *Catal. Sci. Tech.*, 2017, **7**, 452-458.
56. Y. Duan, J. Luo, S. Zhou, X. Mao, M. W. Shah, F. Wang, Z. Chen and C. Wang, *Appl. Catal. Bl*, 2018, **234**, 206-212.
57. X. Wang and C. Li, *J Photochem. Photobiol. C*, 2017, **33**, 165-179.
58. S. Veziroglu, A.-L. Obermann, M. Ullrich, M. Hussain, M. Kamp, L. Kienle, T. Leibner, H.-G. Rubahn, O. Polonskyi, T. Strunskus, J. Fiutowski, M. Es-Souni, J. Adam, F. Faupel and O. C. Aktas, *ACS Appl. Mater. Interfaces*, 2020, **12**, 14983-14992.



1. **A Nanohybrid Containing Cyan-Emitting Copper Nanoclusters and TiO<sub>2</sub> Nanoparticles: Tuning of Optoelectronic Properties.** Dipayan Bairagi, Soumyajit Hazra, Kingshuk Basu and Arindam Banerjee, *ChemistrySelect*, 2022, **7**, e202201701.
2. **Peptide-Based Gel in Environmental Remediation: Removal of Toxic Organic Dyes and Hazardous Pb<sup>2+</sup> and Cd<sup>2+</sup> Ions from Wastewater and Oil Spill Recovery.** Biplab Mondal, Dipayan Bairagi, Nibedita Nandi, Biswanath Hansda, Krishna Sundar Das, Charlotte J. C. Edwards-Gayle, Valeria Castelletto, Ian W. Hamley and Arindam Banerjee, *Langmuir*, 2020, **36**, 12942-12953.
3. **Self-Assembling Peptide-Based Hydrogel: Regulation of Mechanical Stiffness and Thermal Stability and 3D Cell Culture of Fibroblasts.** Dipayan Bairagi, Parijat Biswas, Kingshuk Basu, Soumyajit Hazra, Daniel Hermida-Merino, Deepak Kumar Sinha, Ian W. Hamley and Arindam Banerjee, *ACS Appl. Bio Mater.*, 2019, **2**, 5235-5244.
4. **Amino-Acid-Based Metallo-Hydrogel That Acts Like an Esterase.** Kousik Gayen, Kingshuk Basu, Dipayan Bairagi, Valeria Castelletto, Ian W. Hamley and Arindam Banerjee, *ACS Appl. Bio Mater.*, 2018, **1**, 1717-1724.